Effects of Heterogeneities on Fluid Flow and Borehole Permeability Measurements

by

Xiaomin Zhao

B.S., Beijing University (1982)
M.S., Graduate School of the Chinese Academy of Sciences (1984)
M.S., Boston College (1990)

Submitted to the Department of Earth, Atmospheric, and Planetary Sciences
in partial fulfillment of the requirements for the degree of

Doctor of Philosophy

at the

MASSACHUSETTS INSTITUTE OF TECHNOLOGY

May 1994

Signature of Author .....
Department of Earth, Atmospheric, and Planetary Sciences
May, 1994

Certified by .....
M. Nafi Toksöz
Professor of Geophysics
Thesis Supervisor

Accepted by .....
Thomas H. Jordan
Chairman
Department of Earth, Atmospheric, and Planetary Sciences

Effects of Heterogeneities on Fluid Flow and Borehole Permeability Measurements

by

Xiaomin Zhao

Submitted to the Department of Earth, Atmospheric, and Planetary Sciences
on May, 1994, in partial fulfillment of the
requirements for the degree of
Doctor of Philosophy

Abstract

One of the prominent features of a porous formation is the presence of heterogeneities of various scales. The effects of these heterogeneities on the fluid transport properties are of primary concern for basic scientific studies, petroleum production, ground water hydrology, and environmental characterization. This thesis is concerned with the effects of porous formation heterogeneities on the steady, transient, and dynamic fluid flow behavior, and their influence on borehole permeability measurements.

From the fluid flow point of view, heterogeneity and anisotropy are two closely related properties. We model steady fluid flow in media with different heterogeneities, especially the lineated continuous and discontinuous permeability heterogeneities. It is found that the lineation of heterogeneities results in macroscopic permeability anisotropy. The permeability contrast between the low- and high-permeability regions is the key factor controlling the degree of permeability anisotropy. Strong anisotropy exists only when the contrast is large. The effects of the heterogeneity scale on permeability anisotropy are also studied. Numerical simulation indicates that large size heterogeneities along the lineation direction produce strong anisotropy. The anisotropy decreases with decreasing heterogeneity scale sizes.

In the laboratory transient tests, both the early time and the late time portions of the pressure transient are used to obtain rock permeability. Our numerical simulation results show that the early time behavior of the transient pressure pulse is controlled by the rock heterogeneity and can be used to characterize the permeability heterogeneity of the rock, while the late time behavior is mainly controlled by the effective permeability of the sample. As in the steady fluid flow case, lineation of permeability heterogeneity results in anisotropy. The degree of anisotropy is controlled by the contrast between low- and high-permeability regions in the porous media.

This thesis is primarily concerned with dynamic (or frequency-dependent) fluid transport properties in heterogeneous porous media and its application to acoustic

logging in heterogeneous porous formations. The theory of dynamic permeability is modified by introducing spatially varying permeability into the theory. As a result, a complex permeability as a function of both spatial coordinates and frequency is used to describe the dynamic fluid transport properties in heterogeneous porous media. An iterative finite difference technique is developed to compute the fluid motion in the frequency domain.

The important application of the dynamic fluid flow modeling is in the study of borehole Stoneley wave propagation in heterogeneous permeable porous formations. By formulating the finite difference scheme for the cylindrical coordinates, we have modeled the effects of radial and azimuthal permeability heterogeneity variation on borehole Stoneley wave propagation. Our models show that random permeability variation has only minimal effects on the Stoneley wave propagation. However, in the case of a damaged borehole wall, where the wall has much higher permeability than the surrounding formation, the effects of the heterogeneity can be detected by the significant delay in Stoneley wave arrival and the attenuation peak in the frequency range of common Stoneley wave measurements. The modeling results provide a theoretical basis for determining the borehole wall damage from measuring the Stoneley wave propagation characteristics.

To further study the problem of acoustic logging in heterogeneous porous formations, we look at the case where the formation permeability varies in the borehole axial and radial directions. This is a very important problem because vertical heterogeneity variations are commonly encountered in acoustic logging applications. Our numerical simulation results show that the continuous permeability variations in the formation have only minimal effects on the Stoneley wave propagation, whereas the discontinuous variation can have significant effects on the Stoneley wave propagation. However, when the Stoneley wavelength is considerably larger than the scale of heterogeneity variations, the Stoneley wave is sensitive only to the overall fluid transmissivity of the formation. To demonstrate the effects of heterogeneity on the Stoneley propagation, an experimental data set (Winkler *et al.*, 1989) has been modeled using randomly layered permeability models. The heterogeneous permeability model results agree with the data very well.

The numerical technique for calculating Stoneley wave propagation across permeability heterogeneities has been applied to interpret the acoustic logging data across a heterogeneous fracture zone (Paillet, 1984). The modeling technique, in conjunction with variable permeability models, successfully explains the non-symmetric patterns of the Stoneley wave attenuation and reflection at the top and bottom of the fracture zone, whereas it is difficult to explain these patterns using a homogeneous permeable zone model. The technique developed in this study can be used as an effective means for characterizing permeability heterogeneities using borehole Stoneley waves.

Thesis Supervisor: M. Nafi Toksöz
Title: Professor of Geophysics

Acknowledgments

I would like to thank my advisor, Prof. M. Nafi Toksöz, for his advice, guidance, and help throughout this endeavor. Without his encouragement from the very beginning, this work would not be possible. I appreciate his patience and valuable suggestions in many discussions. I thank Yves Bernabé for his many helpful suggestions and discussions concerning the fluid flow modeling problem. His extensive knowledge on permeability measurements is a ready source to consult. Thanks also go to the other committee members, Dr. Dale Morgan, Dr. Dan Rothman, and Dr. Dennies McLaughlin, for sharing their experiences with me in many aspects of this thesis and for their helpful suggestions. Another person from whom I benefited a lot is Dr. Arthur Cheng. His knowledge on borehole acoustic logging had helped me connect fluid flow modeling to borehole acoustic waves.

The Earth Resources Laboratory of MIT provided an encouraging environment for my thesis research. Dr. Zhu's borehole models in the water tank, Ningya Cheng's fantastic 3-D borehole wave propagation graphics, Roger Turppening's time to time reminding of the real data analysis, and the Consortium's crave for formation permeability from Stoneley waves, all seemed to indicate that I could not get out of ERL without doing something on the borehole logging problems. As a result, a large portion of this thesis is concerned with acoustic propagation in heterogeneous porous boreholes.

I would like to thank Sara Brydges, Naida Buckingham, Liz Henderson, and Sue Turbak for all their help over the past several years and for making the Lab a much more enjoyable and family-like place. I thank Delaine Reiter and Jane Maloof for their help with many technical problems and for their friendship. I enjoyed sharing office with Andrea Benco and Shirley Rieven. I had bothered them too much with spellings, grammars, America cookings, and so forth. I would also like to thank Carol Caravana, Chuck Doll, and Joe Matarese for their help in many things.

I thank my Chinese fellow scholars and students, Ningya Cheng, Wenjie Dong, Yingping Li, Chengbin Peng, Wenqun Shi, Jie Zhang, Tiepeng Zhou, and Zhenya Zhu. Their friendship and company made life a lot easier.

I am most grateful to my family. I thank my husband, Xiaoming Tang, for his encouragement and support through these years. His interest in my work has made the graduate study a little easier for me. I thank my children, Tony and Vivian, for being such lovely kids. The tiredness, the depression, and the pressures I brought home from a long working day would be dissolved in their smiling, their laughing, and even their crying. I thank my parents for their continuous love and encouragement. I thank my brothers and sister for allowing me escaping from the direct responsibility of taking care of my elderly father and mother. Finally, I am truly thankful for my parent-in-laws. They had come thousands miles to help me take care of the children

and the family. Without their encouragement, understanding, and sacrifice, this thesis work would last much longer.

This research was supported by the Borehole Acoustic and Logging Consortium at M.I.T. and by Department of Energy Grant DE-FG02-86ER13636.

Contents

Chapter 1

Introduction

1.1 Thesis Objective

Many rocks in the upper crust are characterized as porous, permeable media. The most important parameter controlling fluid transport in the subsurface is permeability. A common feature of a porous formation is the presence of heterogeneities of various scales. The determination of fluid transport properties and the characterization of the effects of heterogeneity on the transport properties are of great importance for basic scientific studies, petroleum production, ground water hydrology, and environmental characterization. Current techniques used to measure the porous medium transport properties include: (1) The steady flow test (such as the borehole slug or pump test), which uses the steady (or time-invariant) fluid flow to measure formation hydraulic conductivity or permeability; (2) The transient technique (such as the borehole pressure pulse test or laboratory pulse decay technique), which utilizes the transient behavior of the fluid pressure pulse to measure porous medium flow properties; (3) The dynamic wave propagation method (such as acoustic logging in permeable porous formations), which applies the dynamic wave pulse to excite fluid motion in a porous formation and derives the fluid transport properties from the interaction between the wave propagation and the pore fluid motion. In all these

techniques, the presence of medium heterogeneity poses a serious problem. For example, in the measurement of permeability using pressure tests in a single borehole, the presence of permeability heterogeneities places limitations on the use of the test data because the permeability values are measured only for the immediate vicinity of the borehole and only in a direction more or less perpendicular to the borehole.

The primary objective of this thesis is to investigate the effects of formation heterogeneities on the steady, transient, and dynamic fluid flow behaviors. This is accomplished by carrying out numerical studies to model the pore fluid flow behavior in heterogeneous porous media under steady, transient, and dynamic conditions.

The second objective of this thesis is to apply the numerical modeling approach to study the problem of acoustic logging in heterogeneous permeable porous formations. Obtaining formation permeability from borehole acoustic logging measurements is a very important task that has been of concern for decades, and the problems associated with formation heterogeneities have not yet been systematically studied. In conjunction with the recent development of the theory of dynamic permeability and the theory of borehole Stoneley wave propagation, this thesis develops an iterative finite difference method for the cylindrical coordinates system to simulate dynamic pore fluid flow in a variety of formation heterogeneities. Using the finite difference approach, such heterogeneities as random permeability variation, damaged zones, permeable and non-permeable sequences, multiple permeable zones, *etc.*, can be readily modeled, and their effects on borehole Stoneley wave propagation can be analyzed. The modeling results provide a theoretical basis for developing methods to characterize the heterogeneities using acoustic logging measurements.

The final objective of this thesis is to apply the modeling technique to actual laboratory and field data. The important reason for doing this is that by applying the numerical modeling to the real data, one can demonstrate the sensibility of flow to parameters of medium heterogeneities. In the steady fluid flow problem, a set of experimental data measured from materials with anisotropic permeability (Bernabé,

1992) has been modeled to predict the measured permeability anisotropy. In transient fluid flow problem, a data set from Kamath *et al.* (1990) has been modeled to show the heterogeneity effects in the pressure transient. To demonstrate the effects of formation heterogeneity on borehole acoustic wave propagation, an experimental data set (Winkler *et al.*, 1989) is modeled using random layer permeability models. The numerical technique for calculating Stoneley wave propagation across permeability heterogeneities is also applied to the field acoustic logging data across a heterogeneous fracture zone (Paillet, 1984). The modeling technique, in conjunction with a variable permeability model, successfully explains the non-symmetric pattern of the Stoneley wave attenuation and reflection at the top and bottom of the fracture zone. This non-symmetric pattern cannot be explained by a homogeneous permeable zone model. This example demonstrates the effectiveness of the numerical modeling approach in characterizing permeability heterogeneities using borehole Stoneley wave measurements.

1.2 Background

The flow of pore fluid is seriously affected by their heterogeneous and/or anisotropic structures of reservoirs. The study of heterogeneity/anisotropy effects is very important because major production problems occur in many oil and gas reservoirs with strongly heterogeneous and/or anisotropic structures.

From the fluid flow point of view, heterogeneity and anisotropy are two closely related properties. The origin of anisotropic transport properties of rocks was recently discussed by Lake (1988). One conclusion is that the lineation or directionality of small scale heterogeneities may produce permeability anisotropy. However, the permeability anisotropy, like permeability heterogeneity, is scale-dependent. Lake (1988) found that the lineation of pore structure (i.e. preferred orientation of microcracks or

non-spherical grains) at small scale only produces moderate permeability anisotropy. Strong permeability anisotropy is more likely to be found from the large scale lineation of heterogeneities with high permeability contrast. Examples of highly anisotropic formations include sand-shale sequences (Haldorsen and Lake, 1984; Desbarats, 1987; Deutsch, 1989; Begg *et al.*, 1989) and jointed or fractured rock masses (Long *et al.*, 1982; Oda, 1985). Bernabé (1992) showed that the experimental data obtained from heterogeneous synthetic porous materials agree with the numerical results of a homogeneous but anisotropic model. The search for the relationship between permeability heterogeneity and permeability anisotropy has produced strong motivation for carrying out numerical studies, which, by simulating fluid flow in heterogeneous porous media and measuring the global fluid transport properties, will help determine the key factors controlling permeability anisotropy in heterogeneous porous media.

In a heterogeneous medium, the heterogeneities are generally distributed in an irregular manner in space. To describe the spatial variability of the heterogeneities, space random functions are commonly used in connection with ground water flow problems (Dagan, 1986). In the past decade, the statistical approach has been applied increasingly to ground water studies, in which the spatial covariance or correlation function is used to characterize the heterogeneity scale of the porous medium (Dagan, 1986; Ababou, 1988). Given the statistical distribution of the porous medium heterogeneities, numerical techniques can then be applied to simulate ground water flow in the heterogeneous systems (Dagan, 1986; Ababou, 1988; Kwicklis and Healy, 1993). The results are then analyzed against the medium statistical parameters such as the heterogeneity scale length (i.e. correlation length) and standard deviation of the heterogeneity variation (Ababou, 1988; Smith and Freeze, 1979). Therefore, by following the statistical approach commonly used in ground water flow literature, space correlation functions will be used in this thesis to describe the heterogeneity variation of porous media.

Traditional procedures for measuring formation permeability include steady-state

and transient analyses. In the steady-state analysis, permeability is usually determined from measurements of the fluid flow rate through a laboratory sample (Bernabé, 1987, 1992), or into the formation surrounding a well bore (Hvorslev, 1951; Zeigler, 1976) under a time invariant pressure gradient. In oil and gas reservoirs and ground water aquifers, the steady-state fluid flow condition is applicable because the flow has taken place over a long period of time and has become stablized. The pressure transient method for permeability measurements has been used in both field (Bredehoeft and Papadopulos, 1980; Melville *et al.*, 1991) and laboratory. In the laboratory, the pulse decay method has been the primary application of pressure transient testing of core permeability. The pulse decay method was originated by Brace *et al.* (1968). Kamath *et al.* (1990), by implementing the technique with a laboratory experimental system, has demonstrated the effects of permeability heterogeneity on the time-history of a pressure transient. The experiment data of Kamath *et al.* (1990) provide a very good example that can be used to guide the interpretation of the numerical simulation results of the pressure transient in heterogeneous porous media.

Because permeability is such a very important parameter, technologies are needed to measure it in-situ. The borehole pressure pump test and the tracer test are direct ways to measure it but are expensive and time consuming. In this regard, borehole acoustic logging provides a particularly useful technique for measuring formation permeability. This has been a topic of intensive research for decades, in which borehole Stoneley waves have primarily been used. The basic theory relating borehole acoustic waves to formation permeability is Biot's poroelastic theory (Biot, 1956a, 1956b). Rosenbaum (1974) was the first to apply Biot's theory to study the effects of formation permeability on high frequency acoustic wave train. This model is called Biot-Rosenbaum model. Since then, numerous researchers have made substantial efforts on this topic. Using the Biot-Rosenbaum model, Burns and Cheng (1986) inverted in-situ permeability from borehole Stoneley waves. Cheng *et al.* (1987) applied this model to study the effects of permeability on field Stoneley wave data. Using wavenum-

ber integration technique, Schmitt *et al.* (1988) calculated the wave propagation in homogeneous porous formation. Schmitt (1989) investigated the more complicated model of a borehole surrounded by multiple porous layers with anisotropy in both elastic constants and permeabilities. The first important experimental verification of the Biot-Rosenbaum theory was given by Winkler *et al.* (1989), who performed laboratory model experiments on borehole Stoneley wave propagation to evaluate the applicability of the Biot' theory to acoustic logging in porous formations and found excellent agreement between theory and experiment (out of 4 cases, agreement was found for 3 cases; the only case where the agreement was not observed was due to medium heterogeneity and will be studied in detail in Chapter 5).

In most of these studies, formation permeability was treated as homogeneous and the effects of formation heterogeneity have not yet been seriously considered. In reality, however, formation permeability is rarely homogeneous. A common example are the sand (permeable) - shale (non-permeable) sequences found in sedimentary rocks. Borehole fracture and fracture zones are also examples of (high) permeability heterogeneities. Therefore, it is necessary to understand the effects of formation permeability heterogeneity on borehole acoustic wave propagation for the better determination of formation permeability and characterization of its heterogeneity variations. At present, however, numerical analysis of borehole acoustic wave propagation in a heterogeneous porous formation using the Biot-Rosenbaum theory has not yet been developed, although there have been some efforts towards solving this problem using finite difference methods (Stephen *et al.*, 1985; Cheng, personal communication). The numerical difficulty seems to lie in the dispersive nature of the Biot's slow wave (Biot, 1956a, 1956b) and the coupling of this wave with the fast (compressional and shear) waves.

Two recent developments have made it possible to model the effects of formation permeability heterogeneities on borehole Stoneley wave propagation. One such development is the theory of dynamic permeability (Johnson *et al.*, 1987), and the other

is the simplified Biot-Rosenbaum model for Stoneley wave propagation in porous boreholes (Tang *et al.*, 1991b).

Basically, Biot's theory predicts three distinct types of waves in a fluid saturated porous medium (Biot, 1956a, 1956b): the "fast" compressional and shear waves, and the slow compressional wave. The fast waves are similar to the P and S waves in an elastic solid, while the slow wave is a dilatational wave primarily associated with the pore fluid motion. The slow wave exhibits strong frequency-dependent behavior. At very low frequency, the slow wave is essentially the steady or transient pore fluid flow motion which is well described by Darcy's law. At high frequencies, however, this wave becomes a propagating wave. The theory of dynamic permeability provides a simple way to calculate the frequency-dependent (or dynamic) fluid transport properties associated with the slow wave. In the simplified Biot-Rosenbaum model for Stoneley wave propagation, Tang *et al.* (1991b) showed that the interaction of a borehole Stoneley wave with a porous formation can be decomposed into two parts. The first is the interaction with an equivalent elastic formation in which only the fast waves are considered. The second is the interaction with the slow wave. Tang *et al.* (1991b) also showed that, as far as the borehole Stoneley wave is concerned, it is adequate to neglect the coupling between the slow and fast waves. Extending this approach to a heterogeneous porous medium, one can see that as long as the slow wave motion in the heterogeneous medium can be modeled (independent of the elastic problem), the combination of the equivalent elastic formation solution and the porous fluid flow solution will give the solution for the Stoneley wave propagation in the heterogeneous formation. In this way, the modeling of dynamic fluid transport properties of heterogeneous porous media is directly applicable to the important problem of acoustic logging in heterogeneous porous formations. The detailed solution procedure and numerical techniques involved will be described in Chapters 4 and 5, and Appendices A, B, and C.

Following this approach, the problem of acoustic logging with various formation

permeability heterogeneities can be readily modeled to analyze their effects on borehole Stoneley wave propagation. For example, borehole fractures or fracture zones are important applications of these modeling studies. Although Tang and Cheng (1993) have used a homogeneous permeability layer to model a borehole fracture zone, their theory cannot model the heterogeneity structure within the zone. With the heterogeneity modeling approach, such effects as multiple fractures, sand-shale sequences, *etc.* can be readily handled. In Chapter 5, laboratory and field Stoneley wave data across heterogeneous formations will be used to test the numerical modeling technique and to demonstrate the effectiveness of the technique in handling formation heterogeneities.

1.3 Thesis Outline

This thesis is divided into six chapters. Chapter 1 defines the objectives of the thesis, reviews the background work related to the thesis research, and outlines the studies covered by the thesis.

In Chapter 2, we first describe some random medium models that are used to model permeability heterogeneities. These heterogeneous models are classified under two categories: continuous and discontinuous models. In the continuous models, permeability variation from low- to high-permeability regions is continuous. In the discontinuous models the variation is discontinuous and there is a significant permeability contrast between low- and high-permeability regions. The procedures for generating these models are also described.

Then we investigate the steady-state fluid flow in heterogeneous porous media. The governing equations for fluid flow are reviewed and the finite difference scheme using the Successive Over-Relaxation (SOR) method is described. This chapter concentrates on the study of the relationship between permeability heterogeneity and

anisotropy. In order to test the numerical technique and verify the results of the numerical studies, a set of experimental permeability data measured from materials with anisotropic permeability (Bernabé, 1992) is modeled.

Also in this chapter, transient fluid flow in heterogeneous porous media is modeled. The numerical method uses an Alternating Direction Implicit (ADI) finite difference formulation, instead of the commonly used forward time-central space finite difference method. In addition, the effects of fluid storage capacity relative to that of the fluid reservoir of the measurement system are also studied to analyze its role in the determination of rock permeability and heterogeneity. These effects are demonstrated by modeling a laboratory data set from Kamath *et al.* (1990). These effects are demonstrated by modeling a laboratory data set from Kamath *et al.* (1990). Furthermore, the effects of permeability lineation on the pressure transient behavior is also studied.

In chapter 3, numerical studies are carried out to investigate dynamic (or frequency-dependent) fluid motion in heterogeneous porous media. The theory of dynamic permeability of Johnson *et al.* (1987) is modified by introducing spatially varying permeability into the theory. As a result, a complex permeability (i.e. dynamic permeability) as a function of both spatial coordinates and frequency is used to describe the dynamic fluid transport properties in heterogeneous porous media. Because the fluid motion is strongly dispersive (which can be diffusive and propagational depending on frequency and permeability), an iterative finite difference technique is developed based on the ADI algorithm. By using the numerical technique, we simulate the dynamic fluid transport as a function of frequency for various heterogeneities. In particular, we model the dynamic fluid flow through a single fracture with rough surfaces. The effects of fracture permeability heterogeneity due to surface roughness on the dynamic fluid transport through a single fracture are discussed.

The study of dynamic fluid flow in heterogeneous porous media is directly applicable to the important problem of acoustic logging in heterogeneous permeable porous formations. This problem is addressed in Chapters 4 and 5. Because borehole

Stoneley waves have been employed as a major means for permeability studies, we discuss the effects of formation heterogeneity on the Stoneley wave propagation. The simplified Biot-Rosenbaum theory for Stoneley wave propagation (Tang *et al.*, 1991b) is first reviewed to illustrate how we can incorporate the effects of dynamic fluid flow into the Stoneley wave propagation theory. Then the finite difference simulation procedure is developed for the cylindrical coordinates system to compute the dynamic fluid flow in the formation. Because it is time consuming to compute Stoneley wave propagation in a formation with three dimensional heterogeneity variations, we model the effects of the 3-D heterogeneities using two procedures which employ two types of 2-D heterogeneity models. The first is the case where permeability varies only in the radial and azimuthal directions. In the second procedure, the permeability varies along the direction of wave propagation, as well as in the radial direction. Chapter 4 deals only with radial and azimuthal permeability variations. The effects of various permeability heterogeneities on the Stoneley wave propagation are modeled.

Chapter 5 studies the effects of formation permeability heterogeneity that can vary along the borehole axial direction. This case can have a broad range of applications because Stoneley wave propagation across borehole heterogeneities like fractures, sand-shale sequences, *etc.*, is frequently encountered. Using the finite difference approach, the effects due to such heterogeneities as random permeability variation, multiple fracture zones, or sand-shale sequences are modeled and the results are presented.

To demonstrate the effects of heterogeneity on the Stoneley wave propagation, we model an experimental data set of Winkler *et al.* (1989). Using randomly layered formation permeability models, the numerical simulation results agree excellently with the experimental data, while the data disagree with the results of homogeneous permeability models.

Numerical studies are also performed to calculate Stoneley wave propagation across various permeability heterogeneities, including random permeability hetero-

geneity, multiple fractures, sand-shale sequences *etc.* The numerical modeling technique for calculating Stoneley wave propagation across permeability heterogeneities is applied to interpret the acoustic logging data across a heterogeneous fracture zone. This example demonstrates that the numerical modeling technique can be used as an effective means for characterizing permeability heterogeneities using borehole Stoneley waves.

Finally, in Chapter 6, we conclude this thesis by summarizing the major results and contributions of the thesis work. Some relevant future directions are also mentioned.

Chapter 2

Steady-state and Transient Fluid Flow in Heterogeneous Porous Medium

2.1 Introduction

The transport properties of fluids in reservoirs are controlled by the permeability of the medium. Due to the complexity of geological structures, the distribution of the permeability is usually heterogeneous. The situation becomes more complicated when the reservoir contains numerous aligned structures such as lineated flow channels, microcracks, fractures, joints, and faults. In the presence of the aligned structures, anisotropy in permeability usually occurs because fluid flow takes place preferentially in the direction of alignment. In fact, from fluid flow point of view, heterogeneity and anisotropy are two closely related properties of heterogeneous media. However, different heterogeneities will produce different degree of anisotropy. As studied by Lake (1988), the lineation of small structures, such as microcracks or non-spherical grains, only produces moderate permeability anisotropy. Whereas large scale heterogeneities with high permeability contrast (e.g. sand-shale sequences) is more likely

to produce high permeability anisotropy (Haldorsen and Lake, 1984). The effects of these heterogeneous and aligned structures on the anisotropic transport properties of the porous media containing these structures will be investigated in this chapter.

Because of the importance of the heterogeneous permeability distribution, considerable effort has been placed on the numerical modeling. Brown (1987, 1989) has modeled the transport properties of rock joints with surface roughness, in which he assumed that the local permeability of the joint is controlled by the aperture of the local distance between the two rough surfaces. Because the aperture varies with the roughness throughout the joint, the distribution of permeability is heterogeneous over the joint. Recently, by applying the method of cellular-automata to modeling fluid flow in arbitrarily heterogeneous porous media, Rothman (1988) has successfully modeled the fluid flow in porous media and confirmed the validity of Darcy's law for the heterogeneous media. Thompson (1991) presented the numerical results for flow and solute migration in a rough walled fracture with heterogeneous permeabilities. These studies, however, primarily studied the effects of heterogeneous permeability on the fluid transport. The anisotropic effect in the flow was not a major issue. In the case of lineated permeable structures, the flow will depend on the direction of lineation, resulting in anisotropy of fluid flow. Gibson and Toksöz (1990) showed that, in the case of lineated fractures (this would result from the preferential closure of cracks subjected to a uniaxial stress), the permeability of such aligned fracture system varies as a function of the orientation with respect to the alignment. The major goals of the fluid flow modeling are to numerically test whether or not such alignment of flow channels would result in significant permeability anisotropy, and to investigate the important parameters that control the degree of anisotropy. In a recent article, Bernabé (1992) published the results of permeability measurements on anisotropic laboratory samples. He performed a set of permeability measurements using synthetic samples made from a stack of identical flat porous plates with high permeability channels and low permeability coating. Two sets of experimental results

are of particular interest to this study. In one case, high permeability channels are sandwiched between the less-permeable porous plates, but the permeability contrast between the two types of flow layers is not large. In the other case, thin impermeable coating materials are sandwiched between the high permeability channels and the porous plates. These data sets, coupled with the numerical modeling results, will be used to demonstrate that the permeability contrast is the key factor controlling the degree of anisotropy.

Time-dependent fluid flow in permeable porous media is important both in the laboratory and field. In the field, the decay of pressure pulse with time in boreholes is used to measure permeability or fluid transport properties of formation (Melville *et al.*, 1991). In the laboratory, pressure transients are commonly used to determine the permeability of low permeable samples (Brace *et al.*, 1968; Kamath *et al.*, 1990; Bernabé, 1987). In both situations, a commonly encountered problem is the effects of heterogeneous porous media on the transient flow characteristics. In the field, heterogeneities of different scales exist in the reservoirs. In these cases, the scale size of the heterogeneities relative to the penetration of the transient flow may control the flow field. Down to the laboratory scale of a few centimeters, the effect of heterogeneities still plays an important role in affecting the behavior of pressure transients. Kamath *et al.* (1990) showed that, due to the presence of sample heterogeneities, the effective permeability calculated from the pressure transient test could change with the direction of pressure gradient, and could differ significantly from the effective steady-state values. To understand the effects of heterogeneities on pressure transients in porous medium, we carry out a numerical study to investigate the effects of scale size and the distribution of a heterogeneous porous media on the transient fluid flow.

In this chapter, we first describe the procedures for generating the random models. These models will be extensively used later in the forward modeling. We apply finite difference techniques to model the the static and transient flow in porous media. We will describe a Successive Over-Relaxation (SOR) scheme for solving the steady-

state fluid flow problem. This technique will be applied to model fluid flow in various heterogeneous media and Bernabé's (1992) laboratory data and measure the degree of anisotropy. For the transient flow, we apply an Alternating Direction Implicit (ADI) technique to model the time dependent fluid flow in heterogeneous porous media. As an application, we use the finite difference methods to simulate the experimental pressure transient for measuring the permeability of laboratory core samples. Finally, we apply the finite difference techniques to model the butted sample experimental data of Kamath (1990).

2.2 Random Field Models for Formation Permeability Heterogeneities

In a geological medium, the distribution of permeability is usually heterogeneous. The variations of the heterogeneities are often irregularly distributed and can often be modeled as stochastic or random processes (Charrette, 1991). Basically, there are two types of heterogeneity variations, which, according to Kerner (1992), are called transitional and cyclic variations, respectively. In the transitional heterogeneity, the permeability variation is everywhere continuous. An example of transitional permeability variation is the fracture permeability due to fracture surface roughness, as studied by Brown (1987, 1989) and Thompson (1991). In this situation, the local permeability in the fracture is controlled by the aperture of the local distance between the two rough surfaces, the permeability changing continuously with the surface roughness throughout the fracture. In the cyclic heterogeneity, the permeability variations are usually discontinuous. An example of the cyclic change of permeability can be seen in sand-shale sequences commonly found in sedimentary formations. A sandstone can have permeability of one Darcy, while the permeability of shales maybe a milli-Darcy or lower. As will be shown later in this thesis, continuous and discontinuous random permeability variations have very different effects on the fluid transport

properties.

2.2.1 Continuous Random Fields

A random field provides a statistical description of a physical phenomenon that varies spatially according to the laws of probability. The stochastic model used here is a stationary Gaussian random field with mean $\bar{\varepsilon}$ and standard deviation σ. The spatial auto-correlation function of the random field is

$$C_{\varepsilon\varepsilon}(\vec{\mathbf{x}}) = < \varepsilon(\vec{\mathbf{x_1}})\varepsilon(\vec{\mathbf{x_1}} + \vec{\mathbf{x}}) > \ , \tag{2.1}$$

where $< -- >$ is the expected value and $\vec{\mathbf{x}}$ is the lag vector or spatial offset. The power spectrum of the Gaussian field $\varepsilon(\vec{\mathbf{x}})$ is the Fourier transform of the correlation function (Bracewell, 1978), and its phase spectrum is a random process uniformly distributed between 0 and 2π (Priestly, 1981). In this thesis, we use two correlation functions

$$C_{\varepsilon\varepsilon}(\vec{\mathbf{x}}) = e^{-\hat{r}^2} \tag{2.2}$$

$$C_{\varepsilon\varepsilon}(\vec{\mathbf{x}}) = K_0(\hat{r}) \ , \tag{2.3}$$

where $e^{-\hat{r}^2}$ is a Gaussian function and $K_0(\hat{r})$, the zero order modified Bessel function, represents the zero order von Kármán correlation function (Frankel and Clayton, 1986; Charrette, 1991), and $\hat{r}$ is a dimensionless norm. In the case of a two-dimensional (2-D) isotropic distribution, $\hat{r}$ is

$$\hat{r} = \frac{r}{a} = \frac{\sqrt{x^2 + y^2}}{a} \ , \tag{2.4}$$

where a is the correlation length of the heterogeneities. As shown in Frankel and Clayton (1986), as well as by Charrette (1991), the spatial frequency spectrum of the Gaussian function decays exponentially with the wavenumber k_r, varying as $e^{-k_r^2 a^2/4}$. Thus the Gaussian heterogeneity lacks high frequency or short wavelength components, and the heterogeneity variations are smooth. In the 2-D case, the spectrum

of von Kármán function decays with wavenumber k_r as k_r^{-2} [or $k_r^{-(7-2D)}$, where D is fractal dimension, (Brown, 1987)], giving a fractal dimension of $D = 2.5$. This represents a self-similar distribution for the heterogeneities (Frankel and Clayton, 1986). Thus the heterogeneity variation persists down to very small scales (short wavelength or large wavenumbers).

The case of directionality or anisotropy in the heterogeneity distribution can be modeled by introducing two different correlation lengths a_1 and a_2 in the 2-D case. The azimuthal variation can be expressed in terms of the ellipsoidal norm

$$\hat{r}(\vec{\mathbf{x}}) = \sqrt{\frac{(x\cos\theta + y\sin\theta)^2}{a_1^2} + \frac{(y\cos\theta - x\sin\theta)^2}{a_2^2}} \quad , \tag{2.5}$$

where θ is the angle between the vector $\vec{\mathbf{x}}$ and the x-axis. With the use of this dimensionless norm, Equation (2.2) or (2.3) defines an elliptically-shaped 2-D correlation function, whose semi-major axis is aligned in θ direction, and the semiaxes are a_1 and a_2, respectively, yielding an aspect ratio a_1/a_2 for the lineation of the heterogeneities. Figure 2-1 shows examples of isotropic (top figure) and lineated (anisotropic, bottom figure) correlation functions calculated using the Gaussian function (Equation 2.2). Figure 2-2 shows examples of isotropic (top figure) and anisotropic correlation functions calculated using the von Kármán function (Equation 2.3). In the isotropic cases, $a_1/a_2 = 1$ for both Gaussian and von Kármán correlation functions. In the anisotropic cases, $a_1 = 5a_2$, and $\theta = 45°$. In the extreme case as $a_1/a_2 \longrightarrow \infty$, the heterogeneous distribution does not vary in the θ- direction and becomes one-dimensional (1-D) distribution along the $\theta + 90^o$ direction. Compare Figure 2-1 and Figure 2-2, we see that the von Kármán correlation function shows more significant peakedness than the Gaussian correlation function. The peakedness of the correlation function leads to a wide spectral representations. As will be shown, the random distribution characterized by the von Kármán function contains significantly more high frequency variations (or roughness) compared to that characterized by the Gaussian function.

The generation of a heterogeneous distribution (Gaussian or von Kármán) is based on the linear filter theory applied to Gaussian random processes whose probability

distribution is defined as

$$\text{Prob}\{p(x,y)\} = \frac{exp\{-[p(x,y) - p_0]/2\sigma\}}{\sqrt{2\pi\sigma}} \quad , \tag{2.6}$$

where p_0 is the mean of $p(x,y)$, and σ is the standard deviation of the random variation. The 2-D heterogeneities are generated by filtering a 2-D random distribution drawn from the Gaussian distribution (Equation 2.6) in which the 2-D correlation function of a given type (Gaussian or von Kármán) and given parameters (a_1,a_2, and θ) is used as the 2-D filter, as in the following operation

$$H(x,y) = \int_{-\infty}^{+\infty} \int_{-\infty}^{+\infty} p(x',y') C_{\varepsilon\varepsilon}(x'-x, y'-y) dx' dy' \quad , \tag{2.7}$$

where $H(x,y)$ is the generated 2-D heterogeneous distribution. Equation (2.7) can be performed using 2-D digital filtering algorithm (Oppenheim, 1978). Figure 2-3 shows a realization of the heterogeneous variations generated using the Gaussian correlation function. The correlation length $a = 10$ and model size is 256×256. In Figure 2-4, another heterogeneous distribution is shown for the same correlation length and model size as in Figure 2-3, except that the correlation function is the von Kármán function. As discussed earlier, the von Kármán function falls off at short wavelengths much slower than the Gaussian correlation function, thus the realization of the von Kármán function shows more roughness than the one using the Gaussian correlation function. As an example of lineated heterogeneous distribution shown in Figure 2-5, an elliptically shaped Gaussian correlation function, for which $a_1 = 20$, $a_2 = 2$, and $\theta = 45°$, is used. In Figure 2-5, the heterogeneous variation is significantly elongated along the $\theta = 45°$ direction. The preferred orientation of the fluctuation may produce a "effective" or "apparent" anisotropy.

2.2.2 Discontinuous Models

In the continuous heterogeneous distribution models, the variation from high (low) to low (high) permeability regions is continuous. In contrast to the continuous models,

in the discontinuous models the permeability variation from high to low (or low to high) values is discontinuous. In this section, we discuss two types of discontinuous models. In one type, the discontinuity exists in multiple-dimensional space, which can be used to simulate various flow channels, such as a fracture network. In the other type, the discontinuity is primarily along one direction, which can be used to simulate the layered permeability structure of sedimentary rocks, such as the sand-shale sequences.

The first type of discontinuous model can be generated from the lineated continuous distributions (e.g., Figure 2-5) as follows. We choose the aspect ratio $a_1/a_2 >> 1$ so that the heterogeneity distribution is highly lineated. In order to produce the discontinuity, we set a threshold, which can be a fraction of the maximum value of the distribution. Those values of the distribution that are smaller (greater) than this threshold are set to a constant number, and values greater (smaller) than this threshold are kept unchanged. Furthermore, the background value can be set to a very small number such that high permeability contrast is generated between regions with high (low) permeability and the low (high) permeability background. Figure 2-6 shows an example of a discontinuous flow channel model. In this model, the correlation lengths are $a_1 = 20$ and $a_2 = 2$, the model size is 256×256, and the threshold is set to be 60% of the maximum value.

The 1-D layered permeability structure is modeled using the Poisson process, which can describe a layered structure whose permeability variation is not transitional, but cyclic. The medium has two rock constituents (e.g., sandstone and shale). Each constituent can have its own permeability distribution given by the transitional variation model, with a mean $\bar{\kappa}$ and standard deviation σ.

In the Poisson process $p(y)$, the occurrence of an interface between the two constituents is controlled by the parameter a (analogous to correlation length), which describes the average "waiting times" (layer thickness) of the layers. $p(y)$ takes on the value of $+1$ or -1 which are associated with the two constituents. The permeability

distribution is

$$\kappa(y) = \begin{cases} \kappa_1(y) & p(y) = +1 \\ \kappa_2(y) & p(y) = -1 \end{cases} , \tag{2.8}$$

where the subscripts 1 and 2 denote medium 1 and 2, respectively. The Poisson process also has an exponential auto-correlation function (Jenkins and Watts, 1968), with a being the average thickness of the laminar.

For the Poisson process, the probability distribution is

$$\text{Prob}\{t\} = \frac{a^{[t]}e^{-a}}{[t]!} , \tag{2.9}$$

where t is the random layer thickness and $[t]$ denotes the integer part of t. The mean value of the distribution is a.

The procedure for generating the random layer structure using Poisson distribution is as follows. Let origin $y = 0$ be situated in either medium 1 or 2. A thickness t_0 is drawn from the Poisson distribution given by Equation (2.9). The spatial distance y is set to $y = t_0$. At distance y, which equals the thickness of the first layer, the model permeability jumps from medium 1 (2) to medium 2 (1). Then another thickness t_1 value is drawn from the probability function [Equation (2.9)], and y is set to $t_0 + t_1$, at which the medium permeability jumps back from medium 2 (1) to medium 1 (2). This process is repeated until the entire model length is filled with permeability values. Because the thickness values are drawn from the Poisson distribution, the mean value of the thickness is the average layer thickness a.

Figure 2-7 shows an example of a laminar structure generated by a random medium using the Poisson process. The structure has two constituents. The mean permeabilities of the two constituents of the formation component are 1 and 0.01 (arbitrary unit), respectively. Each constituent has its own 1-D transitional random variation modeled using the von Kármán correlation function with a correlation length of 4. The model size is 256×256. The standard deviation for both constituents is 5% of the mean values. The permeability variation in Figures 2-6 and 2-7 are distinctly different from that of the convolutional model (Figures 2-3, 2-4, and 2-5).

2.3 Formulation of Fluid Flow in Heterogeneous Media

2.3.1 Governing equation

In many applications, fluid flow in porous media is assumed to be laminar and is governed by the Darcy's law (Bear, 1972),

$$\vec{\mathbf{q}} = -\frac{\kappa}{\mu} \nabla P \ , \tag{2.10}$$

where $\vec{\mathbf{q}}$ is the volume flow rate through unit area, κ is permeability, μ is fluid viscosity, and ∇P is pressure gradient. The equation of continuity is

$$\frac{\partial}{\partial t}(\rho\phi) + \nabla \cdot (\rho\vec{\mathbf{q}}) = 0 \ , \tag{2.11}$$

where ϕ is the porosity of the medium, and ρ is the fluid density.

When a pore fluid pressure P is applied, the pore fluid density becomes

$$\rho = \rho_0(1 + \frac{P}{K_f} + \frac{P}{K_p}) \ , \tag{2.12}$$

where K_f is the fluid incompressibility and K_p is the porous matrix incompressibility (Brace *et al.*, 1968). Here we neglect the term P/K_p, assuming fluid is much more compressible than rock. Substituting of Equation (2.12) into Equation (2.11) and assuming that $P/K_f \ll 1$, we have

$$\frac{\partial P}{\partial t} = \nabla \cdot (\alpha \nabla P) \ , \tag{2.13}$$

where $\alpha = (\kappa K_f)/(\phi\mu)$ is the pore fluid diffusivity that can vary spatially when the permeability κ is heterogeneous. In many reservoir applications, we deal with pressure field that is steady over time, i.e. $\frac{\partial P}{\partial t} = 0$. In this case, Equation (2.13) becomes

$$\nabla \cdot (\alpha \nabla P) = 0 \ . \tag{2.14}$$

In the present study, we are concerned with the two dimensional (2-D) case, i.e. $\frac{\partial}{\partial z} = 0$. Thus, Equation (2.14) can be written as

$$\frac{\partial}{\partial x}\left[\alpha(x,y)\frac{\partial P}{\partial x}\right] + \frac{\partial}{\partial y}\left[\alpha(x,y)\frac{\partial P}{\partial y}\right] = 0 \ . \tag{2.15}$$

Accordingly, Darcy's law in the 2-D case is

$$q_x = -\frac{\kappa}{\mu}\frac{\partial P}{\partial x} \tag{2.16}$$

$$q_y = -\frac{\kappa}{\mu}\frac{\partial P}{\partial y} \ . \tag{2.17}$$

Using these equations, we study the fluid flow through a 2-D rectangular of length x_0 and width y_0. Fluid pressure is held constant along two opposite sides ($x = 0$ and $x = x_0$). A pressure gradient is set up across the area by setting the pressure on each side to different values. For the other two sides, we assume a zero fluid flux boundary condition by setting the pressure gradient perpendicular to these boundaries to zero. In summary, the boundary conditions are given as

$$\begin{cases} P|_{(x=0,y)} = P_0 \\ P|_{(x=x_0,y)} = 0 \end{cases} \tag{2.18}$$

and

$$\left.\frac{\partial P}{\partial y}\right|_{(x,y=0)} = \left.\frac{\partial P}{\partial y}\right|_{(x,y=y_0)} = 0 \ . \tag{2.19}$$

2.3.2 Finite difference implementation for static flow

We use finite difference technique to solve Equation (2.15). Discretizing the rectangular domain $x_0 \times y_0$ into $M \times N$ grids, we have

$$\begin{cases} x = m\Delta x & m = 0, 1, 2, \cdots, M-1 \\ y = n\Delta y & n = 0, 1, 2, \cdots, N-1 \end{cases} \tag{2.20}$$

and

$$\alpha_{m,n} = \alpha(m\Delta x, n\Delta y) \ . \tag{2.21}$$

Using the forward difference, Equation (2.15) can be written as

$$P_{m,n} = \frac{1}{A_1 + A_2 + d(A_3 + A_4)} \left[A_1 P_{m+1,n} + A_2 P_{m-1,n} + dA_3 P_{m,n+1} + dA_4 P_{m,n-1}\right] \quad , \tag{2.22}$$

where

$$\begin{cases} A_1 = \alpha_{m+1,n} + \alpha_{m,n} \\ A_2 = \alpha_{m,n} + \alpha_{m-1,n} \\ A_3 = \alpha_{m,n+1} + \alpha_{m,n} \\ A_4 = \alpha_{m,n} + \alpha_{m,n-1} \end{cases} \tag{2.23}$$

and $d = \Delta x^2 / \Delta y^2$. This results in M×N simultaneous equations. Because M and N can be large, direct solutions using matrix inversion technique is costly and iteration methods are often used for the solution of Equation (2.22). A simple iterative procedure can be constructed based on Equation (2.22):

$$P^{k+1}_{m,n} = \frac{1}{A_1 + A_2 + d(A_3 + A_4)} \left[A_1 P^k_{m+1,n} + A_2 P^k_{m-1,n} + dA_3 P^k_{m,n+1} + dA_4 P^k_{m,n-1}\right] \quad . \tag{2.24}$$

The grids for this iteration scheme are shown in Figure 2-8a. The iteration begins by assigning an arbitrary pressure distribution over the area. Equation (2.24) is then used to iterate until convergence is achieved. In the iteration for the boundary points, boundary conditions are always used.

Gauss-Seidel method (Ferziger, 1981) can be used to accelerate the iteration. This consists of changing Equation (2.24) into

$$P^{k+1}_{m,n} = \frac{1}{A_1 + A_2 + d(A_3 + A_4)} \left[A_1 P^k_{m+1,n} + A_2 P^{k+1}_{m-1,n} + dA_3 P^k_{m,n+1} + dA_4 P^{k+1}_{m,n-1}\right] \quad . \tag{2.25}$$

The grids for this iteration are shown in Figure 2-8b. Compared with Figure 2-8a, this iteration makes use of the results of two neighboring points obtained from the current step (if the iteration starts from left to right and from bottom to top). Because the results of the current step are generally closer to the true results than the results of the previous step, the Gaussian-Seidel iteration converges faster than

the simple iteration [Equation (2.24)]. The convergence can further be accelerated by using the Successive Over-Relaxation (SOR) technique (Ferziger, 1981), as given by the following formula:

$$P_{m,n}^{k+1} = \omega Q(m,n,k) + (1-\omega) P_{m,n}^{k} \quad , \tag{2.26}$$

where $Q(m,n,k)$ is the right hand side of Equation (2.25), and ω is the optimum relaxation constant given by

$$\omega_{opt} = \frac{2}{1+\sqrt{1-|\lambda|^2}} \quad , \tag{2.27}$$

where

$$\lambda = \frac{1}{2}\left(\cos\frac{\pi}{M} + \cos\frac{\pi}{N}\right) \quad . \tag{2.28}$$

The SOR technique is much faster than the simple iteration [Equation (2.24)] (Ferziger, 1981). Using the algorithm of iterative procedure, the finite difference system [Equation (2.22)] can be solved fast and efficiently.

2.4 Numerical Results for Steady Flow

The major purpose of these simulations is to study the effects of heterogeneities on the flow through porous media. The flow simulations are done as follows. First, the distribution of the fluid diffusivity $\alpha(x,y)$ is generated over the rectangular area $0 \leq x \leq x_0$, $0 \leq y \leq y_0$, using the random field models described earlier in this chapter. For the given $\alpha(x,y)$ and the boundary conditions, the pressure field $P(x,y)$ is computed by solving the finite difference equation [Equation (2.22)] using the SOR iterative procedure.

The calculated pressure field is differentiated and used in the Darcy's law to compute the volume flow rate vector field, whose components are given in Equations (2.16) and (2.17). Plots of these vectors represent the flow field in the 2-D porous medium.

The total flow across the $x = x_0$ boundary is given by

$$Q_x = \int_0^{y_0} q_x(x_0, y)dy \ . \tag{2.29}$$

The total flow is divided by y_0 to give the flow per unit length

$$\overline{q}_x = Q_x/y_0 \ . \tag{2.30}$$

The effective permeability $\overline{\kappa}$ of the 2-D medium can be measured using the Darcy's law [Equation (2.16)]

$$\overline{q}_x = -\frac{\overline{\kappa}}{\mu}\frac{\Delta P}{x_0} \ , \tag{2.31}$$

where ΔP is the difference between the pressures at the two ends of the 2-D model, and $\Delta P/x_0$ represents the macroscopic pressure gradient across the model length x_0 parallel to the no-flow boundaries. In the following calculations, we assume that the pore fluid is water with $\mu = 1.14 \times 10^{-3}$(Pa s) and $K_f = 2.25$GPa.

The validity and accuracy of the numerical fluid flow solution in a heterogeneous medium can be checked using Equation (2.14). Integrating Equation (2.14) over a heterogeneous volume (or area in the 2-D case) and using Gauss theorem, we have

$$\int_A \nabla \cdot (\alpha \nabla P)dA = \oint_C \vec{\mathbf{q}} \cdot \vec{\mathbf{n}}dC = 0 \ ,$$

where A is the area occupied by the heterogeneous medium, C is the contour enclosing A, and $\vec{\mathbf{n}}$ is the unit vector pointing out perpendicularly to C.

We use the above equation to check our finite difference solution. For example, for the heterogeneous model shown in the top figure of Figure 2-9, we take a small square area of any size ($\leq 128 \times 128$) at any location within the 128×128 model, the net fluid flux into and out of the square area are computed. The sum of the fluxes is very close to zero (generally less than 3% of the in- or out-flow flux). This numerical testing confirms the validity of our finite difference modeling.

2.4.1 Isotropic distribution

We first study the effects of different heterogeneities on the flow and the effective permeability $\overline{\kappa}$ of the medium. The top figures of Figure 2-9 and Figure 2-10 plot two distributions of $\alpha(x, y)$, one is generated using Gaussian correlation function (top figure in Figure 2-9), the other is generated using von Kármán function (top figure in Figure 2-10). The distributions are isotropic and have a correlation length $a = 3$. The mean value and standard deviation of the distribution are 1 Darcy and 30%, respectively. The model lengths are $x_0 = y_0 = 128$.

The von Kármán correlation function distribution (self-similar) is much rougher than the distribution using Gaussian correlation function. The simulated flow fields for the two cases are shown in the bottom figures of Figures 2-9 and 2-10. Although the two heterogeneous distributions modify the local flow, the difference between the overall effects of the two flow fields is minimal. Figure 2-11 shows the average flow *vs.* pressure gradient calculated using Equation (2.30) for a number of ΔP values. The slope of the line gives the average permeability $\overline{\kappa}$. It can be seen that Darcy's law still holds despite the heterogeneities and that the average permeabilities for the two distributions are very close, although the result for the von Kármán random variations shows a slightly higher $\overline{\kappa}$ value. This result shows that the total flow is not sensitive to the details of the heterogeneous distribution (i.e. roughness of the random variation distribution). This agrees with the result obtained by Brown (1987), who showed that the total flow through a joint does not vary significantly with the fractal dimension used to characterize the joint roughness. However, this conclusion is valid only when the correlation length is small compared with the model length. When the ratio of the two lengths a/x_0 increases, the difference between the $\overline{\kappa}$ values of the two distributions will increase. Figures 2-12a and 2-12b show the flow *vs.* pressure gradient for two successively larger a/x_0 ratios, $a/x_0 = 0.047$ (Figure 2-12a), and $a/x_0 = 0.078$ (Figure 2-12b) ($a/x_0 = 0.023$ in Figure 2-11). The permeability difference for the two cases are about 4% and 9%, respectively (it is only 1% in

Figure 2-11). This demonstrates that with increasing heterogeneity size *vs.* model size, the roughness in the von Kármán distribution begins to obstruct the fluid flow, resulting in a lower effective permeability.

2.4.2 Aligned distribution

Using the ellipsoidal norm given in Equations (2.2), (2.3), and (2.5), we can generate aligned distribution for the heterogeneities. In examples shown in Figure 2-13, we use the same model length, standard deviation, and mean value as those in the previous isotropic case. The correlation lengths in the semimajor axial and semiminor axial directions are $a_1 = 20$ and $a_2 = 2$, respectively (top figures in Figure 2-13). The correlation function is Gaussian [Equation (2.2)]. For $\theta = 0°$, $\theta = 45°$, and $\theta = 90°$, the calculated flow fields are also shown in Figure 2-13 (bottom figures). Because of the permeability lineation, the flow tends to channel through high permeability regions. This is clearly shown in the $\theta = 45°$ case, where the lineation of high and low permeability strips makes the flow field have a trend to deflect towards the lineation of high permeability region. Figure 2-14 shows the calculated average flow *vs.* θ. The permeability is the maximum along $\theta = 0°$, and becomes minimum along $\theta = 90°$. We define the permeability anisotropy as

$$\frac{\kappa_{0°} - \kappa_{90°}}{(\kappa_{0°} + \kappa_{90°})/2} \times 100\% \ . \tag{2.32}$$

The anisotropy for this case is about 10%. For comparison, the case of isotropic Gaussian ($a = 20$) is also shown (solid line). By varying the correlation lengths a_1 and a_2, the degree of anisotropy can not significantly exceed this value. This is due to the continuous random medium model used here. In this model, a region with moderate and low permeabilities is sandwiched between two adjacent high permeability regions. Therefore, flow can always cross the less permeable region without having to flow around the region. Thus, due to the presence of background permeability, the

lineation of continuous random heterogeneities can not result in anisotropic permeabilities that are order of magnitude difference. In order to produce such a strong permeability anisotropy, the background permeability must be removed. This will be the case of discontinuous permeability variation models (Section 2.2.2) studied in the following.

2.4.3 Flow channel model

Since permeability channels in reservoirs, such as fractures, could contribute significantly to the reservoir permeability, it is important to model their effects on the permeability. As shown by Gibson and Toksöz (1990), a primary effect of fracture is anisotropy in permeability. Because of the alignment of flow channels or fractures, the permeability can vary with orientation by orders of magnitude. The primary interest of this section is to model the effects of flow channels in reservoirs on the flow fields. The major features of the flow channel models are that the background has negligible permeability, and that the flow is highly concentrated along the flow channels. This situation can be modeled using discontinuous flow channel models. Figure 2-15 shows the $\alpha(x, y)$ distributions that resemble a natural fracture network. The procedure for generating this model is described in section 2.2.2. In this model, we have used a threshold of 60% of the maximum value of $\alpha(x, y)$. Values smaller than the threshold is set to a small number. The correlation lengths are $a_1 = 20$, $a_2 = 2$. The model size is 128×128. The permeability contrast between the fracture and the background is 600:1. Although the background permeability may still be large compared to typical fractured rocks (granite, limestone, *etc.*), the highly conductive channels (fractures) conduct most of the flow so that the background flow is small. In this way, the flow in the fracture network is simulated. The calculated flow fields along and perpendicular to the fracture alignment are also shown in Figure 2-15 (bottom figures). The flow patterns for the three orientations are quite different. As expected, the flow is highly

channeled along fractures. The connectivity of the fractures plays a very important role controlling the flow field. As shown in these figures, fractures that are not connected with the $x = 0$ and $x = x_0$ boundaries have very little flow, while fractures connected with the boundaries conduct most of the flow. For the $\theta = 90°$ case, the flow has to wind around the junctions of the fractures. While in the $\theta = 0°$ case, flow takes place along the straight channel. These result in significant permeability difference for the two cases. We have performed the calculation for various orientations. The calculated average flow as a function of the orientation θ is shown in Figure 2-16. In this figure, the permeability is maximum along fractures and minimum perpendicular to them, same as the previous case of aligned heterogeneities. However, the permeability difference between $\theta = 0°$ and $\theta = 90°$ is 184% in the present case. This numerical modeling result confirms the prediction of Gibson and Toksöz (1990) that aligned fractures can have very significant anisotropy.

In above example, the major flow channels (fractures) connect the model boundaries and are comparable to the model length. as in the case assumed by Gibson and Toksöz (1990). In the field, fractures between two wells have limited extent, and the fractures may not be well connected. Long and Witherspoon (1985) pointed out the importance of fracture network connectivity on permeability. Here we model how the anisotropy of permeability changes when the connectivity decreases. We first generate the lineated heterogeneities with $a_1 = 5$, $a_2 = 1$, the model length is still 128. The lineated fractures are shown in Figure 2-17. Compared with the fracture system shown in Figure 2-15, fractures in this case have a much lower degree of connectivity. Figure 2-17 also includes the simulated flow fields for $\theta = 0°$, $\theta = 45°$, and $\theta = 90°$ cases. For $\theta = 0°$, the average permeability is only 25 mD, much decreased compared to the well connected case of Figure 2-15, in which the average permeability at $\theta = 0°$ is about 2.5D. Because of the decreased connectivity due to shorter fracture lengths, flow can take a "shorter cut" winding around fractures in the $\theta = 90°$ case. As a result, anisotropy is not as significant as the well connected case of Figure 2-15.

Figure 2-18 shows the calculated average flow *vs.* θ. The anisotropy is still present, but the difference between $\theta = 0°$ and $\theta = 90°$ is now about 87%, much lower than the previous case of 184% (Figure 2-16). This example demonstrates that not only the fracture orientation, but also the scale size of the heterogeneities are important in controlling the anisotropy of permeability.

To test the effects of model scale on the permeability, we carried out a set of numerical experiments. A lineated flow channel model with $a_1 = 10$, $a_2 = 1$ and model length 128 is generated (Figure 2-19). Numerical simulation results give an anisotropy value of 134% for this model. We then reduce the model size by using a 64×64 model taken from the lower left corner of the original 128×128 model. The anisotropy value for this case is about 140%. We further reduce the model size to 32×32, again taken from the lower left corner of the original model. The anisotropy value for this case is 160%. From these numerical experiments, we see that the anisotropy values for heterogeneities of the same scale length but different model length are of the same order. We also performed similar experiments on the model ($a_1 = 5$, $a_2 = 1$, model length = 128) as shown in Figure 2-17. The results also show that the degree of anisotropy does not vary significantly with model size. The results of these experiments indicate that the model size, as long as it is larger than the heterogeneity scale size, will not change the order of permeability anisotropy measured from the numerical simulations. Furthermore, comparing the values of permeability anisotropy measured from models with different heterogeneity scale sizes, we see a decrease of permeability anisotropy with decreasing heterogeneity scale sizes. This is an important conclusion from the numerical studies.

2.4.4 Flow barrier model

The above flow channel model shows that strong permeability anisotropy exists in lineated heterogeneous porous media only when the permeability contrast between

the permeable channels (fractures) and the less permeable background is large. It is interesting to study the case where the background becomes permeable while the flow channels are sealed (impermeable). This situation may exist in a sandstone reservoir with interplaced shales. This model can be generated from the previous lineated heterogeneity model, in the same way as the above fracture model. We set a threshold, 40% of the maximum permeability value of the model. The regions whose permeability is less than this threshold is assigned to a very small value (about 1/600 of the maximum permeability). Figure 2-20 shows heterogeneity models for the angle of lineation $\theta = 0^o$, 45^o, and 90^o cases, together with the simulated flow field. Because of the no-flow barriers in the heterogeneous distribution, the flow has to wind around these barriers. For the $\theta = 0^o$ case, the flow takes place along the lineation of the barriers, while for the $\theta = 90^o$ case, the flow has to penetrate the junctions between the barriers and the flow paths are longer than in the $\theta = 0^o$ case. Therefore, flow fields along and perpendicular to the aligned barriers are very different. This results in significant permeability anisotropy. Figure 2-21 shows the calculated average flow as a function of the angle of lineation θ. The permeability difference between $\theta = 0^o$ and $\theta = 90^o$ is about 175%, the same order as the previous flow channel model. From the flow berriers model, we again see the importance of permeability contrast in controlling the anisotropy.

2.5 Comparison With Experimental Data Measured From Materials With Anisotropic Permeability

Bernabé (1992) showed the experimental results of permeability measurements on anisotropic materials. These experiments were performed to evaluate the validity

of the tensor form of Darcy's law in anisotropic porous media. In that study a 2-D finite difference simulation using the anisotropic tensor form Darcy's law was also performed. Good agreement was found between the numerical analysis and the experiment.

The experiments were performed on anisotropic porous medium samples made from a stack of identical flat porous plates. In the sample, the space between two adjacent plates was deliberately left open. It was hoped that these openings would act as high permeability channels, analogous to fractures. However, it turned out that the ratio of permeabilities measured perpendicular and parallel to the plates was only about 0.6, the material obtained being only moderately anisotropic. In fact, these experimental results are quite consistent with our modeling results for the aligned permeability distributions (Figure 2-14), which shows that the lineation of high permeability channels (analogous to the openings between the plates) surrounded by a less permeable background (analogous to the synthetic porous plates) cannot result in significant permeability anisotropy.

As described in Bernabé's (1992) paper, in order to provide a highly anisotropic permeability model, a large percentage of the top surface of each plate was coated with a thin layer of impermeable silicone rubber so that the flow perpendicular to the plates was largely reduced. This time a permeability ratio of 0.02 for $\theta = 0°$ and 90° was obtained. To determine the variation of permeability measured along different directions, the synthetic materials of both cases (i.e., permeability ratios of 0.6 and of 0.02) were cut at 0°, 15°, 30°, 45°, 60°, 75°, and 90° with respect to the direction parallel to the plates. Permeabilities along these directions were measured, with other sides of the (cubic) sample that are parallel to the measurement direction sealed with a jacket (no flow boundaries). The experimental results are replotted in Figure 2-22 (crosses). The anisotropic finite difference modeling results of Bernabé (1992) are also represented in the same figure (triangles). It is seen that strong permeability anisotropy is produced by the model with the ratio of permeabilities

measured perpendicular and parallel to the plates being 0.02. We model the experimental results quantitatively using our finite difference technique and show that a macroscopically anisotropic permeability medium can result from a microscopically isotropic but heterogeneous medium.

Figure 2-23 shows our finite difference model composed of stacked plates. The permeability of the plates and that of the opening are denoted by κ_p and κ_0, respectively. A thin region with permeability κ_c is used to model the less permeable layer due to the silicone rubber coating. The three permeabilities are determined as follows. In the first, we determine κ_p and κ_0 in the absence of the κ_c region. Given the measured permeabilities at $\theta = 0°$ and $\theta = 90°$, κ_p and κ_0 can be uniquely determined. For the model shown in Figure 2-23, $\kappa_p = 1$ (dimensionless unit) and $\kappa_0 = 0.1$. This is the case with the permeability ratio equal to 0.6. In the second step, the κ_c region is introduced between κ_p and κ_0 regions and the value of κ_c is adjusted to obtain the measured permeability ratio of 0.02 for $\theta = 90°$ and 0°. This value is found to be 4×10^{-4}. From the model of Figure 2-23, square models were cut at $\theta = 0°$, 15°, 30°, 45°, 60°, 75°, and 90° with respect to the direction parallel to the plates. Each model includes 16 plates. For the models with given θ values, finite difference modeling was carried out and the average permeability for each θ was calculated. The results are given in Figure 2-22 (solid dots), together with the experimental results and those from the anisotropic finite difference modeling (Bernabé, 1992). Clearly, the results from our finite difference modeling agree well with both results. The agreement with experimental results verifies the validity of our heterogeneous finite difference formulation. More important, the agreement with Bernabé's (1992) anisotropic finite difference results indicates that the permeability anisotropy on a macroscopic scale can result from heterogeneities composed of microscopically isotropic materials, and that permeability contrast in a porous medium controls the degree of anisotropy.

2.6 Modeling of Laboratory Pressure Transient Measurements

The pulse decay method for measuring the permeability of cores is a widely used laboratory technique. The pulse decay experiment is shown in Figure 2-24. Before zero time $t = 0$, the pressures of the upper and lower reservoirs P_u and P_d are equal. At $t = 0$, a pressure difference ΔP is applied at the upper reservoir by adjusting the valve of the upper reservoir. Then the up-stream pressure, P_u, will decrease and the down-stream pressure, P_d, will increase with time and they will approach a common value at a later time. The decay characteristics of P_u depends on the permeability (and permeability heterogeneity), the dimensions of the sample, and the compressive fluid storage of the upper and lower reservoirs, as well as on the storage capacity of the sample. In this section we investigate the effects of the permeability heterogeneities of the sample on the pulse decay characteristics.

We use a 2-D distribution to describe the permeability heterogeneities. In conventional laboratory measurements, rock samples are shaped into cylinders with a circular or square cross-section. In the 2-D distribution, the permeability is assumed to vary in $x \sim y$ plane (x is the axial direction) and invariant in z direction in a square cylinder, while for a circular cylinder, the 2-D heterogeneous distribution may describe the variation along and perpendicular to the axial direction. Since the effects of heterogeneities are to cause the flow behavior to deviate from that of the one-dimensional case, the use of the 2-D distribution is to capture the characteristics of the heterogeneous flow which is fundamentally a multi-dimensional phenomenon. Therefore, the results of 2-D modeling will provide physical insight into the multi-dimensional phenomenon.

Earlier in this chapter, we have derived the governing equation for time-dependent pore fluid pressure [Equation (2.13)]. For a 2-D heterogeneity, this equation can be

written as

$$\frac{\partial}{\partial x}\left[\alpha(x,y)\frac{\partial P}{\partial x}\right]+\frac{\partial}{\partial y}\left[\alpha(x,y)\frac{\partial P}{\partial y}\right]=\frac{\partial P}{\partial t}\quad . \tag{2.33}$$

We choose to non-dimensionalize this equation by using

$$\begin{aligned} x &= L_x x' \qquad 0 \le x' \le 1 \\ y &= L_y y' \qquad 0 \le y' \le 1 \\ \kappa &= \kappa_0 \kappa'(x',y') \qquad 0 \le \kappa' \le 1. \end{aligned}$$

Where L_x and L_y are model lengths along x and y directions, respectively, and κ_0 is the maximum permeability over the 2-D model. Equation (2.33) now becomes:

$$\frac{\partial P}{\partial t'}=\frac{\partial}{\partial x'}\left[\kappa'(x',y')\frac{\partial P}{\partial x'}\right]+\frac{\partial}{\partial y'}\left[\kappa'(x',y')\frac{\partial P}{\partial y'}\right]\quad , \tag{2.34}$$

where the dimensionless time t' is

$$t = Tt' \tag{2.35}$$

with the characteristic time T given by

$$T=\frac{L^2\phi\mu}{\kappa_0 K_f} \tag{2.36}$$

(here we assume $L_x = L_y = L$). The initial condition is that at $t = 0$,

$$\begin{aligned} P|_{t=0}(x,y) &= 0 \qquad 0<x<L;\ \ 0<y<L \\ P|_{t=0}(0,y) &= \Delta P \qquad 0<y<L\ , \end{aligned} \tag{2.37}$$

or using the dimensionless quantities,

$$\begin{aligned} P'|_{t'=0}(x',y') &= 0 \qquad 0<x'<1;\ \ 0<y'<1 \\ P'|_{t'=0}(0,y') &= 1 \qquad 0<y'<1\ . \end{aligned} \tag{2.38}$$

(Without losing generality, we set the initial upper and down stream reservoir pressures to zero.) The boundary conditions are that the decrease (increase) of fluid volume in the upper (lower) reservoir per unit time equals the fluid flux flowing into (out of) the upper (lower) core boundary:

$$C_u V_u \frac{\partial P}{\partial t}=\int_A \frac{\kappa}{\mu}\frac{\partial P}{\partial x}dA \qquad x=0 \tag{2.39}$$

$$C_d V_d \frac{\partial P}{\partial t} = -\int_A \frac{\kappa}{\mu} \frac{\partial P}{\partial x} dA \quad x = L \ , \tag{2.40}$$

where $C_u V_u$ ($C_d V_d$) is the compressive fluid storage of the upper (lower) reservoir. For example, if the reservoir is a steel container filled with fluid, then C_u is the fluid compressibility $C_f = 1/K_f$ and V_u is the volume of the container. A is the cross area of the sample (for the 2-D problem, $dA = dy * L_z$, where L_z = unit length along the z-direction). Following Kamath *et al.* (1990), we use the dimensionless quantities

$$\beta = \frac{AL\phi C_f}{C_u V_u} \tag{2.41}$$

$$\beta^* = \frac{AL\phi C_f}{C_d V_d} \tag{2.42}$$

to denote the ratio of fluid storage of the sample to that of the upper (β) and lower (β^*) reservoirs. Using Equations (2.39) to (2.42), the dimensionless boundary conditions are written as

$$\frac{\partial P'}{\partial t'} = \beta \int_0^1 \kappa'(0, y') \frac{\partial P'}{\partial x'} dy' \ , \quad x' = 0 \tag{2.43}$$

$$\frac{\partial P'}{\partial t'} = -\beta^* \int_0^1 \kappa'(1, y') \frac{\partial P}{\partial x'} dy' \ , \quad x' = 1 \ . \tag{2.44}$$

As described in Appendix A, the governing equation [Equation (2.34)] can be solved using the ADI method if the boundary conditions are appropriately specified. We prescribe the no-flow boundaries at $y' = 0$ and $y' = 1$, i.e.

$$\frac{\partial P'}{\partial y'} = 0 \qquad \begin{cases} y' = 0 \\ y' = 1 \end{cases} \ . \tag{2.45}$$

For the boundary conditions at $x' = 0$ and $x' = 1$, we discretize Equations (2.43) and (2.44) using

$$\frac{\partial P'}{\partial t'} = \frac{P'^{n+1}(0, y') - P'^{n}(0, y')}{\Delta t'}$$

$$\frac{\partial P'}{\partial x'} = \frac{P'^{n}(\Delta x', y') - P'^{n}(0, y')}{\Delta x'} \ .$$

Then we have

$$P'^{n+1}(0, y') = \frac{\Delta t'}{\Delta x'} \beta \sum_j \kappa'(0, j)[P'^{n}(1, j) - P'^{n}(0, j)] + P'^{n}(0, j)$$

$$x' = 0 \quad (2.46)$$

$$P'^{n+1}(L, y') = -\frac{\Delta t'}{\Delta x'}\beta^* \sum_j \kappa'(L, j)[P'^n(L, j) - P'^n(L - \Delta x', j)] + P'^n(L, j) \qquad x' = 1 \quad (2.47)$$

If the pressure P' at time step n is known, then Equations (2.46) and (2.47) represent the first kind boundary condition for P' at time step $n+1$. In addition, for the boundary condition at $n = 0$, the initial condition Equation (2.38) is also used. Solving the finite difference form of Equation (2.34) (see Appendix A) with the given initial [Equation (2.38)] and boundary [Equations (2.43), (2.44), and (2.45)] conditions, the pressure decay characteristics can be investigated for any permeability distributions across the sample.

2.7 Numerical Results for Transient Flow

In this section, we present the transient flow modeling results for various distributions of permeability heterogeneities. The isotropic and anisotropic heterogeneous distributions are generated using the method described in Section 2.2. The anisotropic effects in the heterogeneity distribution will then be studied using the numerical technique. Because most laboratory pulse decay methods analyze the core permeability assuming homogeneity of the sample, it is useful to describe the theoretical basis for the analysis. The theoretical solution will later be compared with our numerical modeling results to demonstrate the effects of heterogeneity.

2.7.1 Analytical solution for homogeneous core sample

In laboratory measurements of core samples, the permeability of the sample is regarded as constant. The following 1-D analytical solution is employed to derive core

permeability from the pulse decay measurements (Kamath *et al.*, 1990):

$$P'(x',t') = \frac{1}{1+\beta+\gamma} + 2\sum_{m=1}^{\infty} \frac{\exp(-t'\phi_m^2)[\cos\phi_m x' - (\frac{\gamma\phi_m}{\beta})\sin\phi_m x']}{(1+\beta+\gamma-\gamma\phi_m^2/\beta)\cos\phi_m - \phi_m(1+\gamma+2\gamma/\beta)\sin\phi_m} \quad ,(2.48)$$

where ϕ_m are the roots of the equation

$$\tan\phi = \frac{(\gamma+1)\phi}{\gamma\phi^2/\beta - \beta} \tag{2.49}$$

and $\gamma = \frac{(C_d V_d)}{(C_u V_u)}$ is the ratio of the compressive fluid storage of the lower reservoir to that of the upper reservoir. In practice, the early time and late time portions of the pressure decay curves are used. The early time portion corresponds to the time interval where the down stream boundary has not been felt and the core appears infinite. The early time solution can be shown to obey the following differential equation (Kamath *et al.*, 1990):

$$\sqrt{t'}\frac{dP'}{dt'} = \beta^2 P'\sqrt{t'} - \frac{\beta}{\sqrt{\pi}} \quad . \tag{2.50}$$

Therefore, the group $(\sqrt{t'}dP'/dt')$ is a linear function of the group $(P'\sqrt{t'})$, with a slope β^2 and intercept $-\beta/\sqrt{\pi}$. Returning to real time domain using $t' = t/T$, we have

$$\text{slope (early time)} = \frac{\beta^2}{T} = \frac{\kappa_0\beta^2}{\mu\phi C_f L^2} \tag{2.51}$$

$$\text{intercept} = -\frac{\beta}{\sqrt{\pi T}} = -\beta\sqrt{\frac{\kappa_0}{\pi\mu\phi C_f L^2}} \quad . \tag{2.52}$$

Thus, knowing the ratio of the fluid storage of the sample to that of the upper reservoir β and μ, ϕ, C_f, and L, Equation (2.50) can be used to determine the core permeability κ_0.

At the late time, the terms in the series in Equation (2.48) decay to zero, and only the first term is important. It is readily shown that the late time solution at $x' = 0$ obeys the equation

$$\frac{dP'}{dt'} = -\phi_1^2\left(P' - \frac{1}{1+\beta+\gamma}\right) \tag{2.53}$$

or

$$\ln\left(P' - \frac{1}{1+\beta+\gamma}\right) = -\phi_1^2 t' + \text{constant} \quad . \tag{2.54}$$

This shows that the pressure at the upper reservoir decays exponentially with time. If $\ln(P' - 1/(1+\beta+\gamma))$ is plotted against t', the slope of the line is $-\phi_1^2$, where ϕ_1 is the first root of Equation (2.49). Back to real time using $t' = t/T$, we see that

$$\text{slope (late time)} = -\phi_1^2 \frac{\kappa_0}{\mu\phi C_f L^2} \quad . \tag{2.55}$$

Thus the core permeability can also be determined from the slope of the late time pressure transient curves. In fact, this is the theoretical background for the pulse decay method used by Brace *et al.* (1968).

When the core permeability is heterogeneous across the sample, the 1-D analytic solution [Equation (2.48)] is still used to determine core permeability, despite the permeability variation across the sample. The permeability so determined is the effective permeability of the heterogeneous sample. Our primary interest here is to investigate how the heterogeneities affect the measured effective permeability.

2.7.2 Gaussian *vs.* homogeneous distributions

Two groups of calculations were carried out. The first group is a heterogeneous Gaussian distribution (Figure 2-3). The second group is a homogeneous distribution, whose permeability is the average value of the Gaussian distribution over the 2-D grids, i.e., $\kappa' = 0.5$, if $\kappa'(x', y')$ $(0 < \kappa' < 1)$ is given by the Gaussian distribution. The calculations were performed for $\beta = 0.001$, 0.1, 1, and 10 ($\gamma = 1$). The results are plotted in Figure 2-25. The pulse decay curves ($P' \sim \log_{10} t'$) for the constant distributions fit almost exactly with the 1-D analytical solutions for the various β values (see also Kamath *et al.*, 1990). The results for the Gaussian distribution (dashed curves) differ from the constant permeability only for larger β values ($\beta = 1$, and 10). This result is in agreement with the result of Kamath *et al.* (1990). That

is, when the core fluid compressive storage is very small compared to the storage of the reservoir, the pressure transients measured from a heterogeneous and from a homogeneous core with the same (average) permeability are effectively the same. The effects of reservoir storage on pressure transient will be further demonstrated when we model an experimental data set of Kamath *et al.* (1990) measured from a heterogeneous core sample.

We now compare the early time results from the Gaussian and from the homogeneous distributions. Using Equation (2.50), the results for $\beta = 0.1$, 1, and 10 are plotted in Figures 2-26a, 2-26b, and 2-26c. It can be seen that the slopes of the curves determined by Equation (2.50) are different for the two distributions. The slopes for the Gaussian distribution are always greater than those of the constant distribution. If we treat the Gaussian case as a constant distribution with an effective permeability using Equation (2.48), the permeability for the Gaussian case appears to be greater than its average permeability. However, with increasing β values, the difference becomes smaller. For $\beta = 10$, the slopes of the two cases are quite close (Figure 2-26c).

The late time solution of the curves in Figure 2-25 are plotted in Figure 2-27 using Equation (2.54). It is seen that the Gaussian and homogeneous solutions have similar slopes for the linear part of the $\ln[P' - 1/(1 + \beta + \gamma)] \sim t'$ relationship. This means that the effective permeability measured using the late time solution will be approximately the same for the two distributions if we apply the analytical solution [Equation (2.48)] to the linear portion of the curves to derive the permeability.

To explain the physical process involved in the early time and late time solutions, we plot the pressure fields for $t' = 0.1$ [early time, Figure 2-28 (top figure)] and $t' = 3$ [late time, Figure 2-28 (bottom figure)] for $\beta = 1$. For the early time solution, the front of the pressure pulse (i.e., the zero pressure contour) has not reached the down stream boundary. Thus the decay is largely controlled by the permeability distribution near the upper boundary. Whereas in the late time, the fluid pressure has completely

penetrated the core sample and the pressure pulse decay is controlled by permeability distribution across the whole sample. In this case, the decay is not sensitive to the details of the distribution, but is controlled by the average (i.e., effective) permeability over the entire sample. Therefore, the late time solution offers a method for measuring the effective permeability of the core sample along the direction of measurement, while the early time solution can be used to detect the heterogeneity of the sample. The numerical modeling results are in agreement with the conclusion of Kamath *et al.* (1990) drawn from laboratory tests.

2.7.3 Gaussian *vs.* von Kármán distributions

To investigate the effects of fine structures of the heterogeneous distribution on transient flow, we generate a rough heterogeneity distribution using the von Kármán correlation function (Frankel and Clayton, 1986) (Figure 2-4), with the same correlation length as the Gaussian case used in section 2.6.2. The up and down stream pressure response curves calculated for the two distributions are shown in Figure 2-29 for $\beta = 1$ and $\beta = 10$. Despite the roughness of the von Kármán distribution, the pressure curves for the rough heterogeneity case (dashed curves) are almost identical to those for the smooth (Gaussian) case (solid curves), showing that the pressure transient is insensitive to the details of the heterogeneous distribution. This is also the case for steady fluid flow as studied earlier in this chapter.

2.7.4 Aligned distributions

For the steady flow case, the permeability of the core sample as a function of the direction ($0^o < \theta < 90^o$) of the alignment was modeled in section 2.4.2. For the transient fluid flow case, we model the pressure transient using the same distribution as shown in Figure 2-13. The pressure decay curves are calculated for various θ

values varying from 0^o to 90^o. The decay curves calculated for $\beta = 1$ are shown in Figure 2-30. By measuring the slope of the late time solution using Equation (2.54), the permeability as a function of θ can be determined. The permeability is the maximum along $\theta = 0^o$ and becomes minimum along $\theta = 90^o$. The permeability anisotropy [defined as $(\kappa_0 - \kappa_{90})/(\kappa_0 + \kappa_{90})/2$] for this case is about 10%. The degree of anisotropy for the transient flow case is similar to that of the steady flow case. The reason for this small anisotropy is that in the aligned heterogeneous Gaussian model a region with moderate and low permeabilities is sandwiched between two adjacent high permeability regions, but the permeability contrast between the high permeability region and the background is not very large. As a result, the flow (steady or transient) can always cross the less permeable region without having to flow around the region. Therefore, as in the steady flow case, due to the presence of background permeability the lineation of random heterogeneities cannot result in permeability anisotropy that is order of magnitude difference. In order to produce a strong permeability anisotropy, the permeability contrast between the background and the high permeability regions must be very large. This will be the case of fractures or flow channels studied in the following section.

2.7.5 Aligned fracture model

We calculated the transient pressure decay curves for the flow channel model shown in Figure 2-6. The calculations are performed for various angle of alignment θ from 0^o to 90^o. Figure 2-31 shows the decay curves for $\theta = 0^o$, $\theta = 45^o$, and $\theta = 90^o$ ($\beta = 1$). As we can see from this figure, from 0^o to 90^o, the pressure decay curve has increasingly higher values at the late time portion of the curves, showing a decreasing decay rate with increasing θ values. This indicates that the pressure transient shows smaller effective permeability across the model as θ increases. In this case, the measured effective permeability can differ significantly from the averaged permeability over

the 2-D grids, depending on the θ values. The explanation of this permeability anisotropy is similar to the steady state flow modeling result. That is, in the aligned fracture case flow takes a longer path to reach the down stream boundary when $\theta > 0$ than when $\theta = 0$. Because the late time solution offers a way to measure the effective permeability of the model along the x-direction, we use Equation (2.54) to determine the effective permeability *vs.* θ using the late time solution. The results are shown in Figure 2-32. In this figure, the permeability is the maximum along fracture alignment direction and the minimum perpendicular to the fractures. The permeability anisotropy is about 180%. This order of permeability anisotropy is in agreement with the steady flow case modeled in section 2.4.3.

2.7.6 Simulation of laboratory pressure transient data

In this section, we apply our finite difference technique to model a pressure transient data set (Kamath *et al.*, 1990) measured from a heterogeneous sample. The sample was made from two cores of different permeabilities (0.02 mD and 0.657 mD) and lengths (7.35 cm and 7.5 cm). The two cores were butted together to simulate a core with longitudinal heterogeneity. Figure 2-33a shows the experimental pressure transient response of the butted core (solid curves) compared to the analytical solution (dashed curves) for a homogeneous core with permeability equal to the effective steady state value (0.04 mD). The upper reservoir is connected to the low permeability core (0.02 mD). As the vessel sizes decrease (β increases), the measured and analytical responses deviate because of the effects of heterogeneity. This is similar to what we have shown in Figure 2-25.

We simulate the measured pressure transient data using our finite difference modeling technique. We compute the pressure transient responses for various β values given in Figure 2-33a for the butted core sample. The results are plotted in Figure 2-33b, together with the simulation results for a homogeneous sample with the length

of 14.85 cm and an effective permeability of 0.04 mD. The homogeneous model results agree with those shown in Figure 2-33a. Our curves for $\beta = 0.01$ match Kamath *et al.*'s (1990) $\beta = 0.001$ curves almost exactly. We therefore suspect that $\beta = 0.001$ is a typo error and should be 0.01. For the responses measured from the butted sample (solid curves in Figure 2-33a), our simulation results show very good agreement (solid curves in Figure 2-33b). The responses for the heterogeneous sample (in both Figure 2-33 a and b) agree with homogeneous sample results at small β values and deviate from them as β value increases.

This modeling example supports a major conclusion of Kamath *et al.* (1990) drawn from the experimental observations. That is, the large vessels can be used to calculate the effective permeability of a heterogeneous core, and the smaller vessels to study the permeability heterogeneity of the core sample.

2.8 Conclusions

In this chapter, we have outlined the procedures for the generation of random heterogeneity permeability models. These models are divided into two categories, the continuous and discontinuous models. Although both models possess random variation in the heterogeneous distribution, they have distinctly different features. In the continuous models, there is no significant permeability contrast because of the continuous variation from low to high permeability regions. In the discontinuous models, however, the permeability contrast can be very significant. As seen in the steady-state and transient fluid flow modeling, these two types of heterogeneities have very different effects on fluid transport properties.

We have used effective finite difference algorithms to model fluid flow in arbitrarily heterogeneous porous media. The modeling results in both static and transient situations show that the flow is not sensitive to the small scale roughness of the

distribution, but may be affected by the lineation in the permeability distribution. However, due to the presence of background permeability, the lineation of highly permeable regions and less permeable surroundings does not result in anisotropy of an order of magnitude. Nevertheless, when there is large permeability contrast in the heterogeneities of different permeability, such significant anisotropy does exist. This has been demonstrated in our numerical simulation of flow channel and flow barriers models. Another important parameter controlling anisotropy is the scale size of the heterogeneities. In general, large size heterogeneities tend to produce strong permeability anisotropy. Our modeling results support the conclusion of Lake (1988) that small scale heterogeneities (e.g., micro cracks, elongated grains) can not produce large permeability anisotropy, while large scale heterogeneities (e.g., sand-shale sequences, large scale flow channels, *etc.*) with large permeability contrast generate strong permeability anisotropy.

In addition, transient modeling with heterogeneous permeability core samples indicates that the early time portion of the transient pulse decay curve can be used to characterize the permeability heterogeneity of the core sample. The late time portion can be used to measure the effective permeability of the core sample, especially when the fluid storage of the core sample is small compared to that of the upper stream reservoir. This conclusion is supported by the finite difference modeling of an experimental pressure transient data set measured by Kamath *et al.* (1990).

The comparison between numerical modeling results with the experimental data of Bernabé (1992) further supports the conclusions that permeability contrast in heterogeneous porous media is the important parameter controlling the degree of permeability anisotropy, and that large scale permeability anisotropy can also result from the lineation of heterogeneities in an isotropic medium.

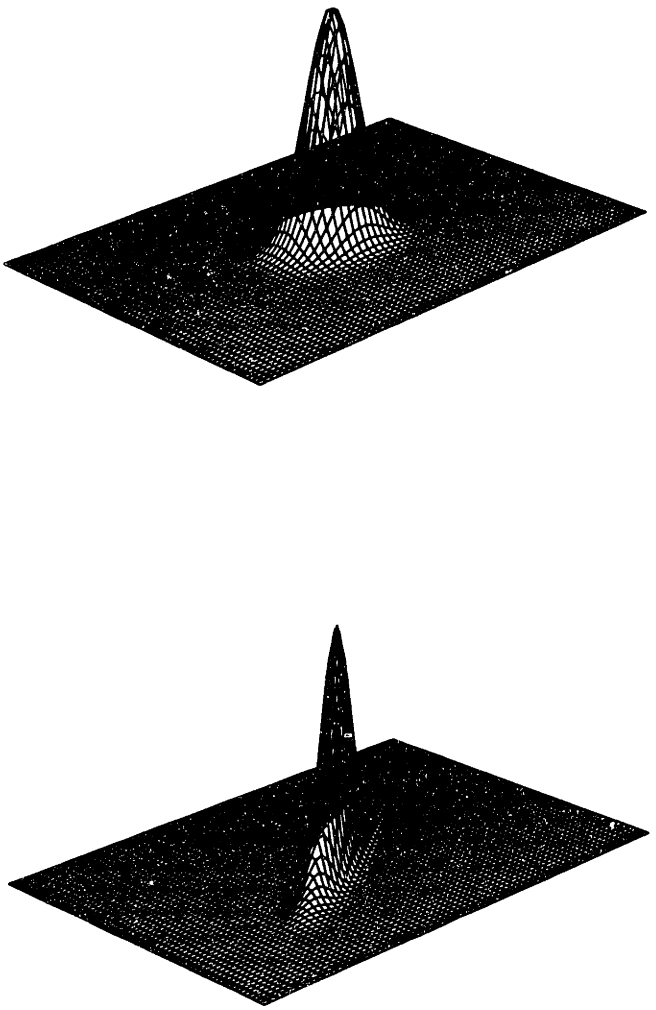

Figure 2-1: Examples of isotropic (top figure) and and anisotropic (bottom figure) Gaussian correlation functions.

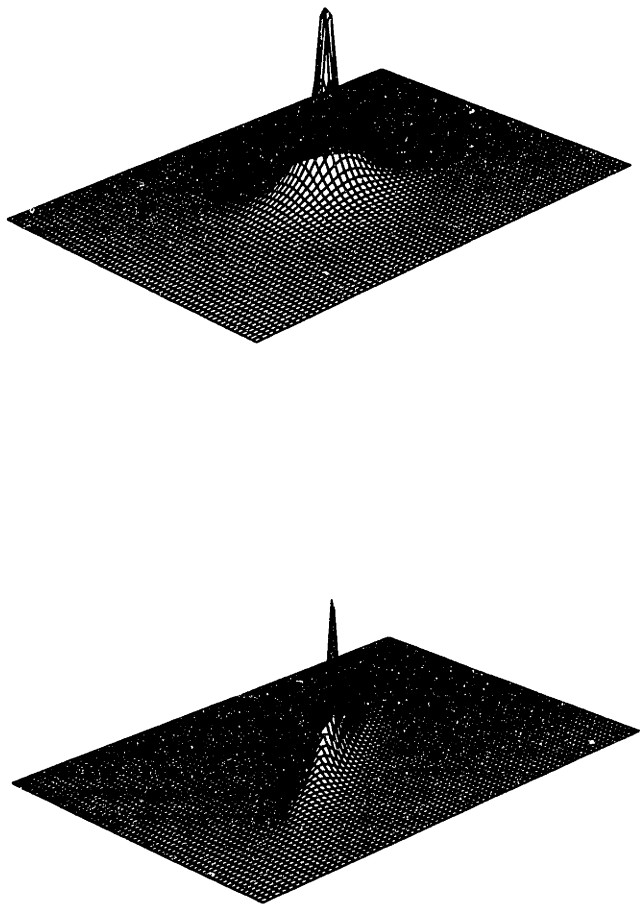

Figure 2-2: Examples of isotropic (top figure) and anisotropic (bottom figure) von Kármán correlation functions.

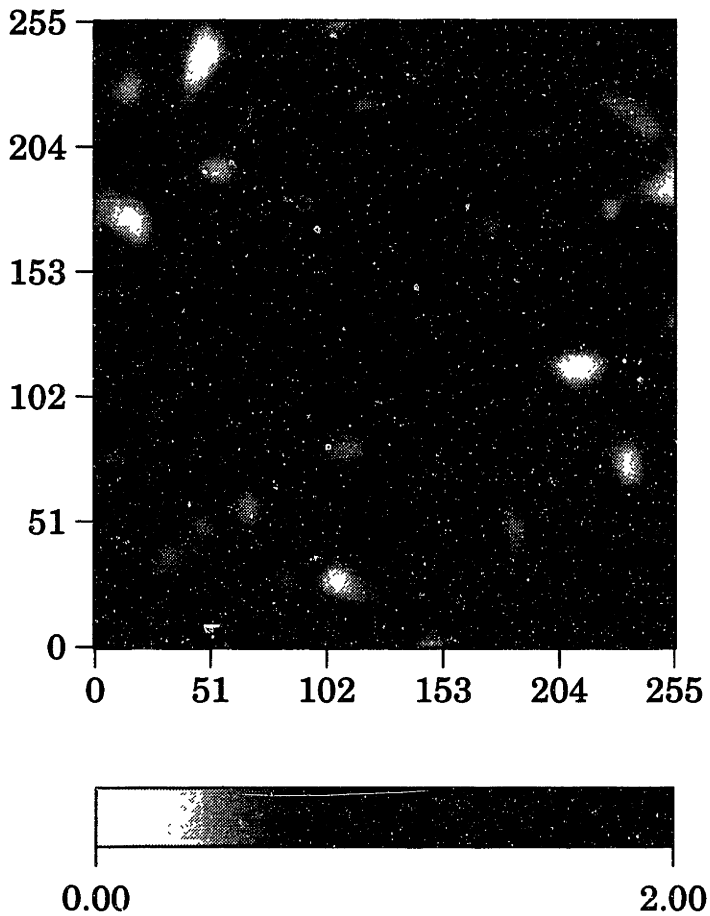

Figure 2-3: Heterogeneous random medium generated using Gaussian correlation function. The correlation lengths are $a_1 = a_2 = 10$ and the model size is 256×256.

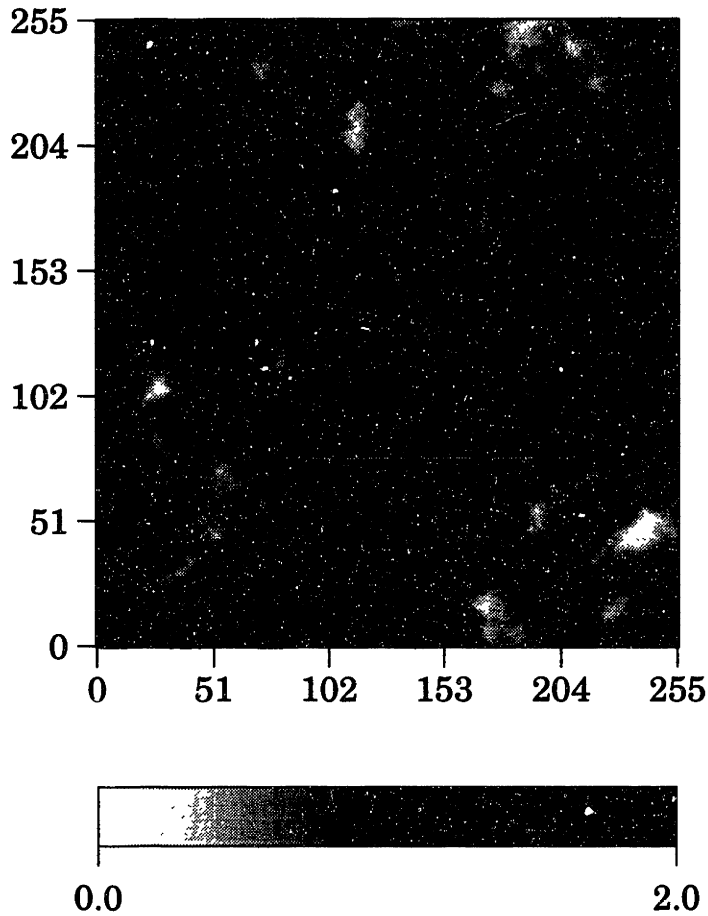

Figure 2-4: Heterogeneous random medium generated using von Kármán correlation function. The correlation lengths are $a_1 = a_2 = 10$ and the model size is 256×256.

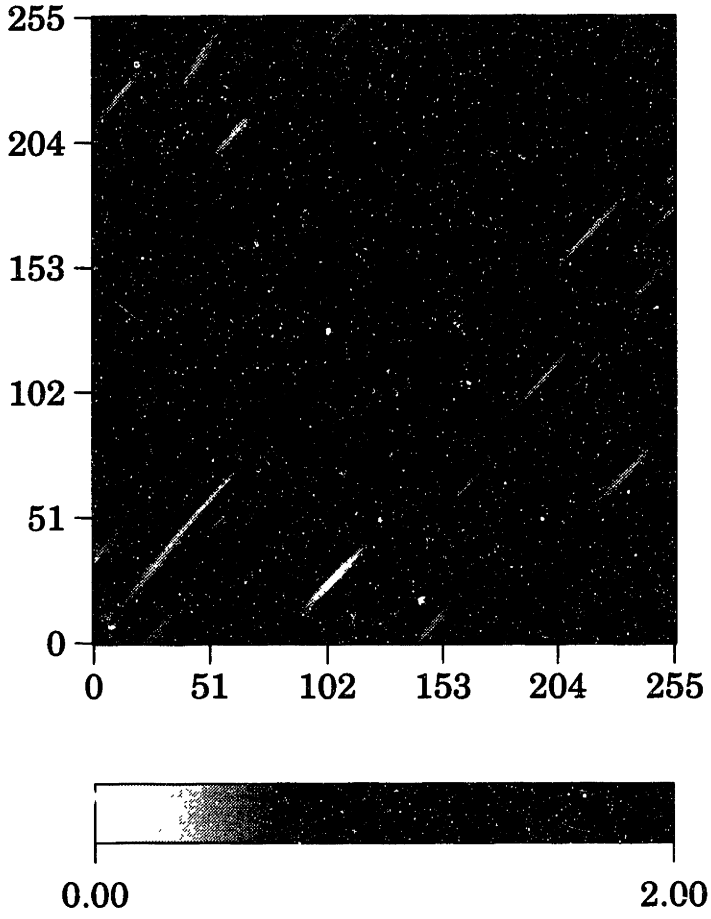

Figure 2-5: Lineated heterogeneous random distribution generated using anisotropic Gaussian correlation function, with semimajor axis aligned at $\theta = 45°$ from the horizontal axis. The correlation lengths are $a_1 = 20$, $a_2 = 2$, and the model size is 256×256.

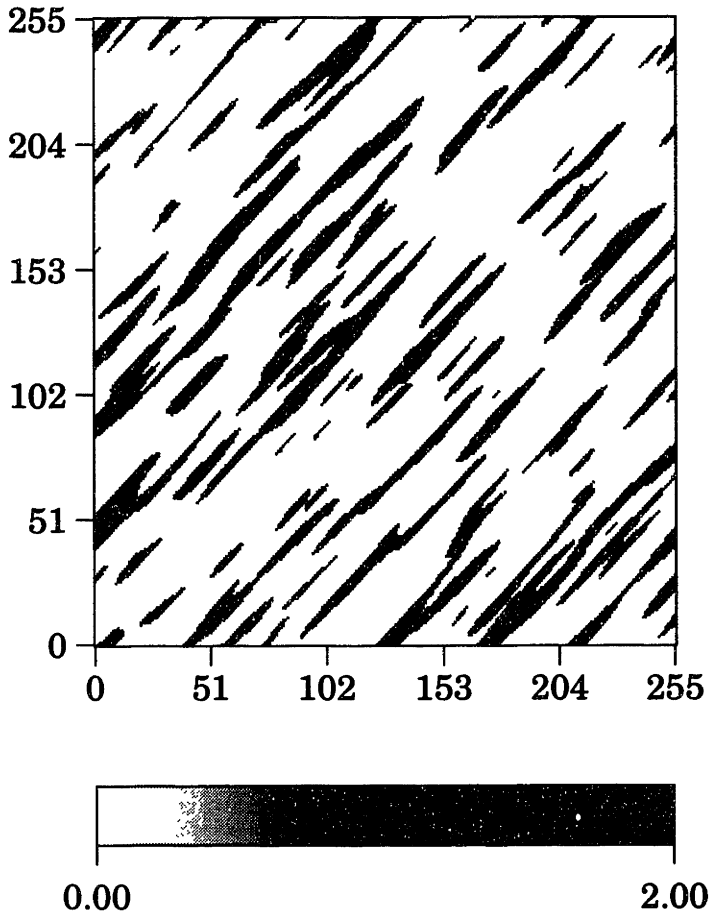

Figure 2-6: 2-D discontinuous random field generated based on a lineated Gaussian random distribution.

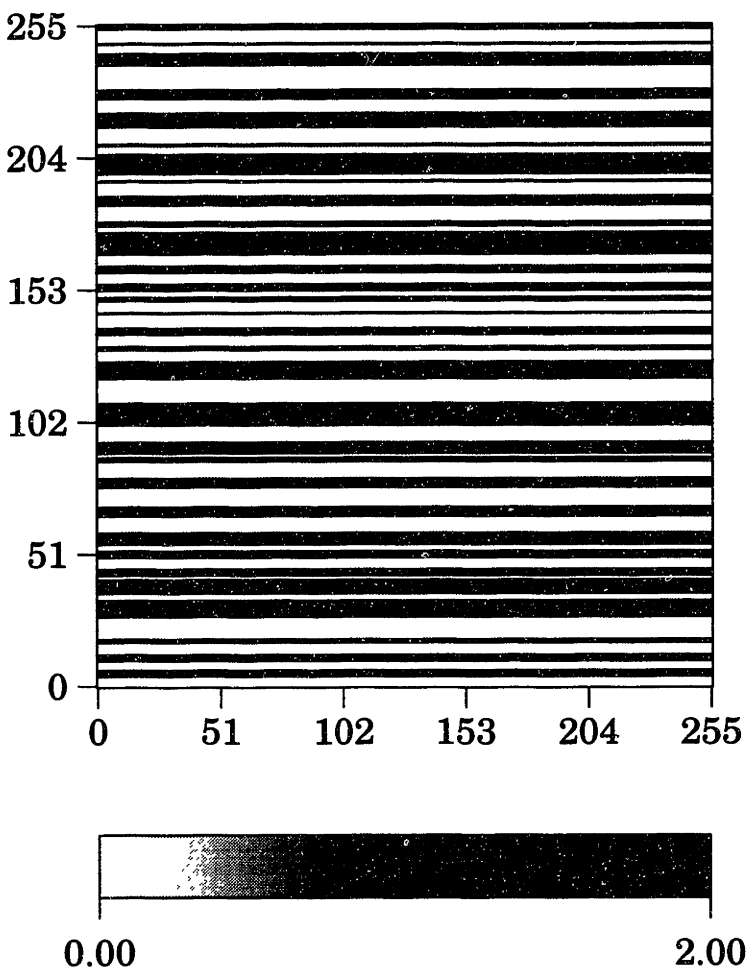

Figure 2-7: 1-D cyclic random medium generated using Poisson process.

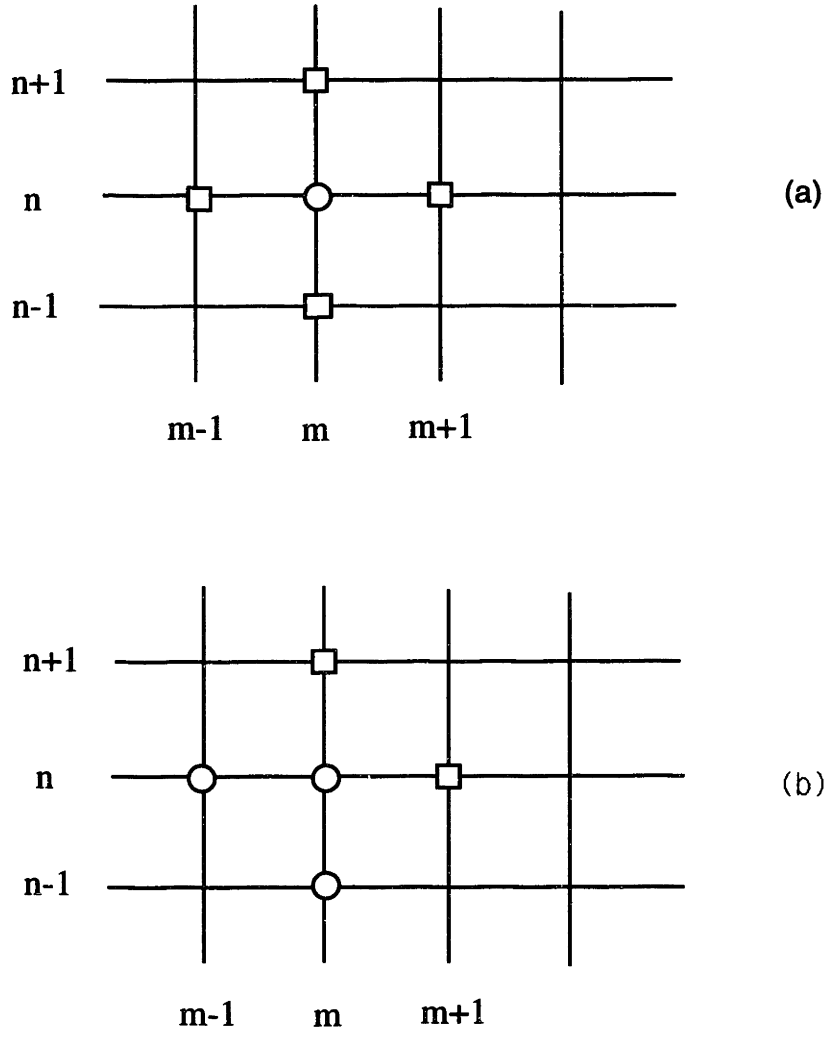

Figure 2-8: Finite difference grids for the simple iteration (a) and for Gauss-Seidel iteration (b). In both cases, open circles denotes current step and open squares denote previous step.

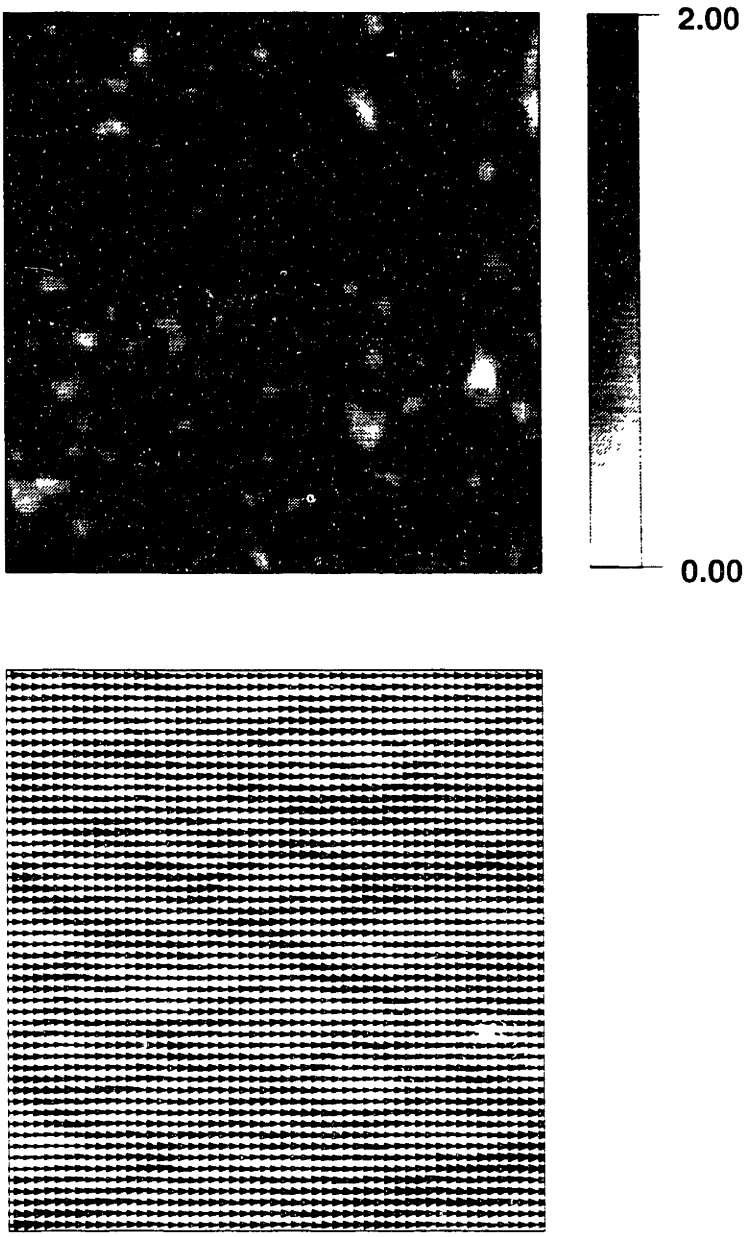

Figure 2-9: Isotropic permeability distribution generated by Gaussian correlation function (top) and the simulated fluid flow field for the random field (bottom). The correlation lengths of the distribution are $a_1 = a_2 = 3$, and the model size is 128×128.

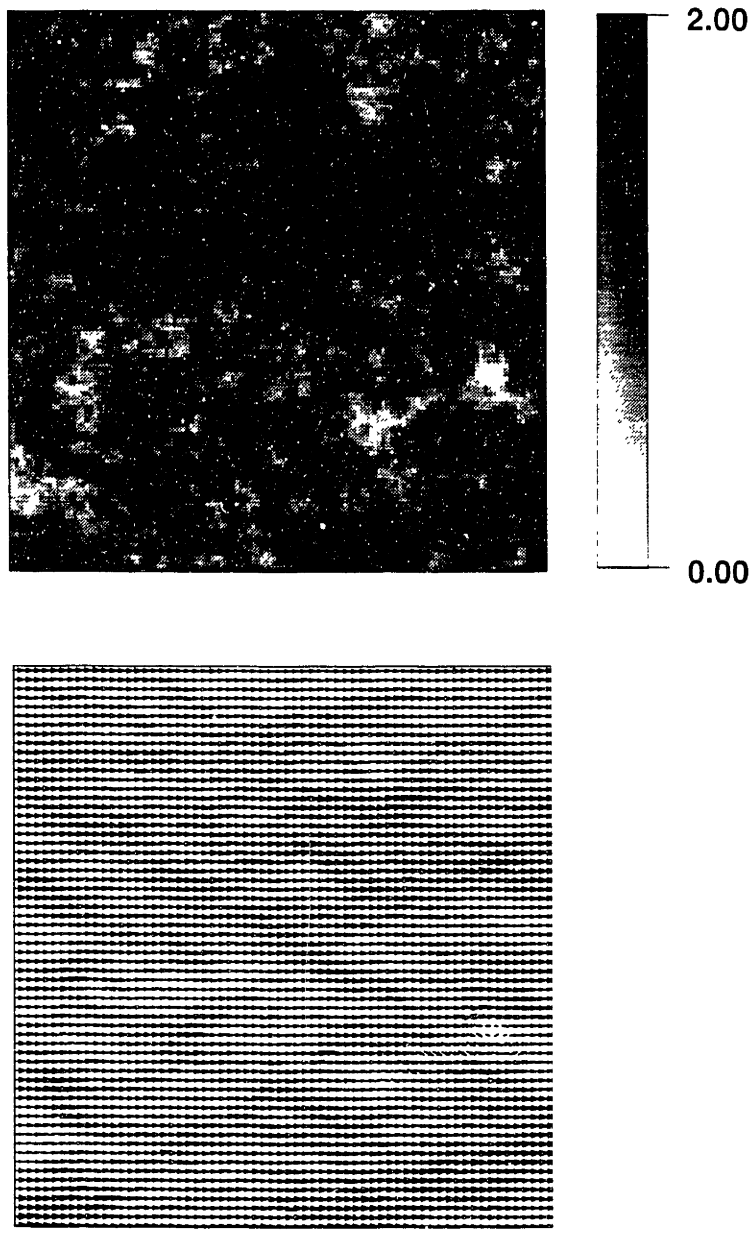

Figure 2-10: Isotropic permeability distribution generated by von Kármán correlation function (top) and the simulated fluid flow field for the random field (bottom). The correlation lengths of the distribution are $a_1 = a_2 = 3$, and the model size is 128×128.

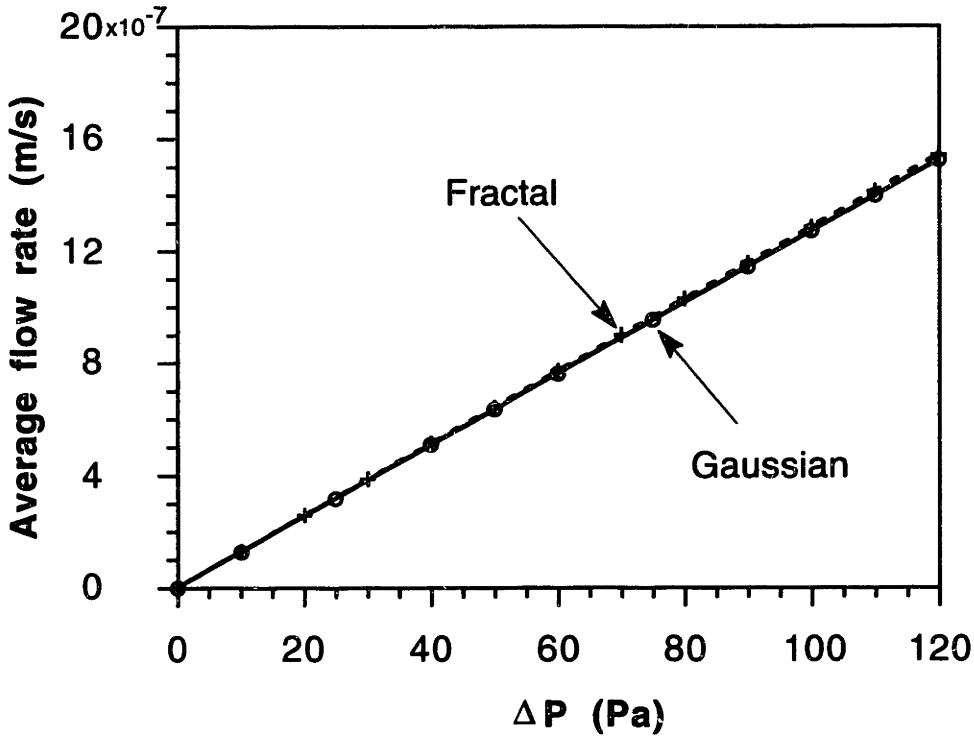

Figure 2-11: Flow rate *vs.* pressure gradient for the Gaussian (solid line with open circles) and von Kármán (dashed line with crosses) distributions shown in Figures 2-9 and 2-10. The slopes of the lines give the average permeabilities $\bar{\kappa}$ of the media. In both cases, the $\bar{\kappa}$ values are very close. The permeability difference is only 1%.

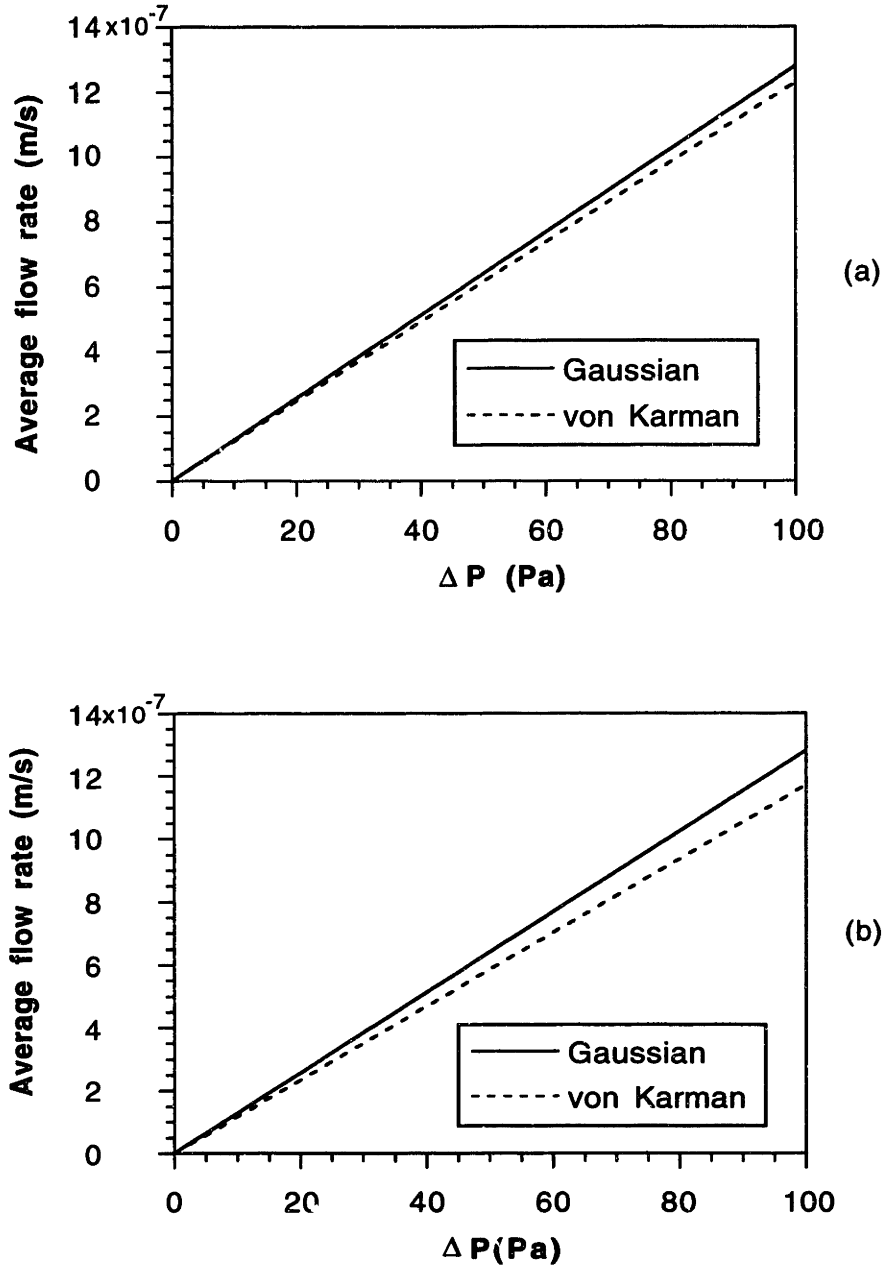

Figure 2-12: Same as Figure 2-11, but now the ratio of correlation length to the model length is increased. In (a), the ratio is about 0.047 and in (b), it is 0.078. The von Kármán distribution has a lower $\bar{\kappa}$ value than the Gaussian when correlation length increases. The differences between the two cases are about 4% in (a) and 9% in (b), respectively.

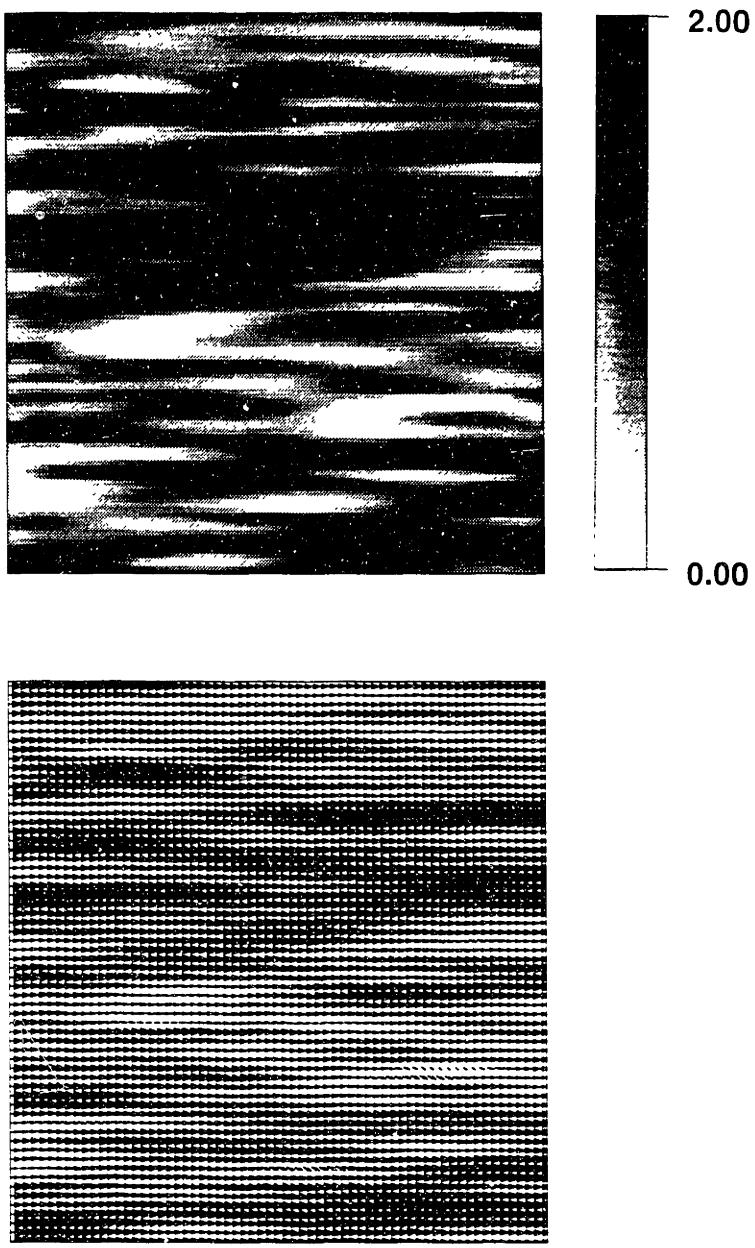

Figure 2-13: Aligned distributions with $\theta = 0°$, $45°$, and $90°$ calculated using Gaussian correlation functions. The correlation lengths are $a_1 = 20$ and $a_2 = 2$, respectively. Model lengths are $x_0 = y_0 = 128$. On this page, the top figure is the permeability model with $\theta = 0°$, the bottom figure is the simulated fluid flow field.

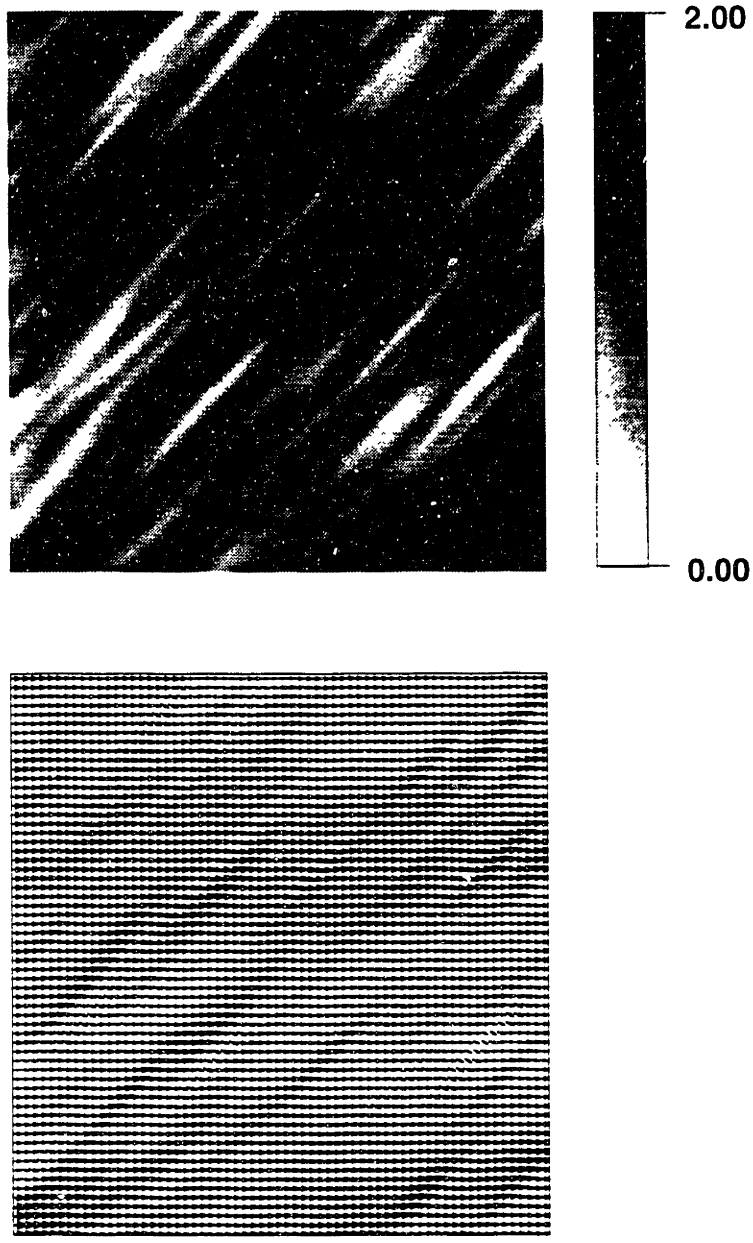

Figure 2-13 continued. The angle of alignment is $\theta = 45°$.

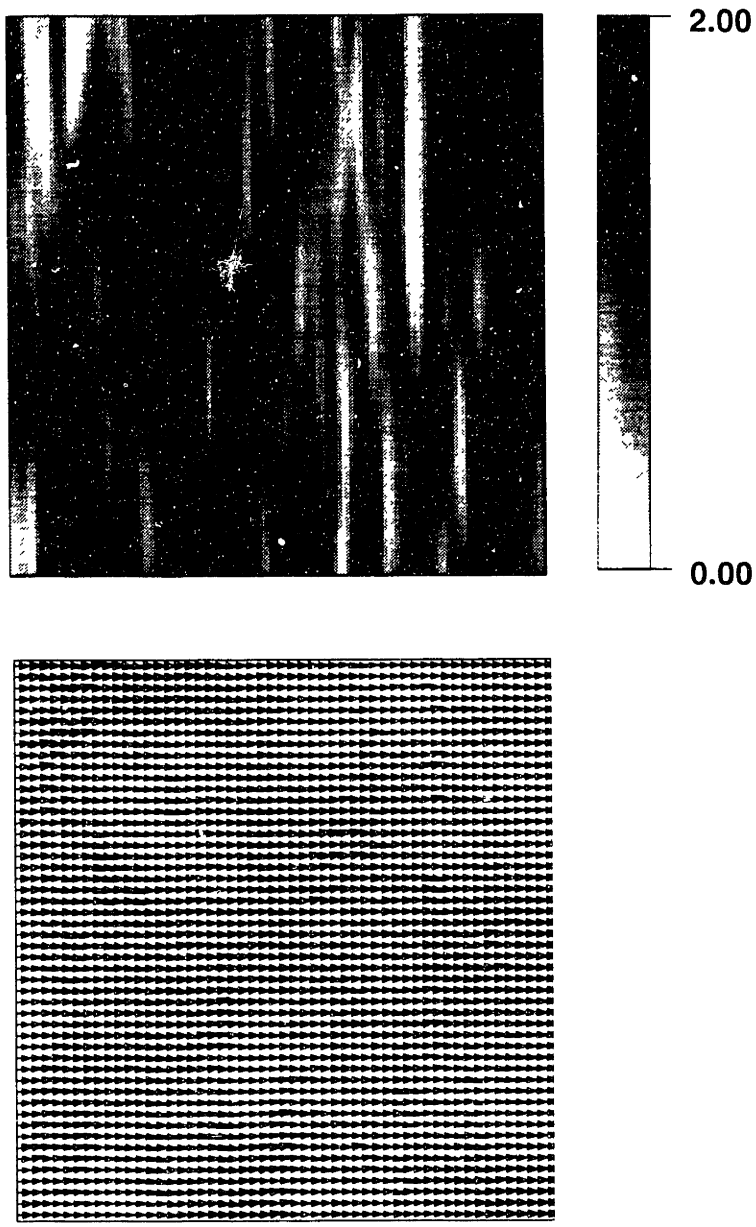

Figure 2-13 continued. The angle of lineation is $\theta = 90°$.

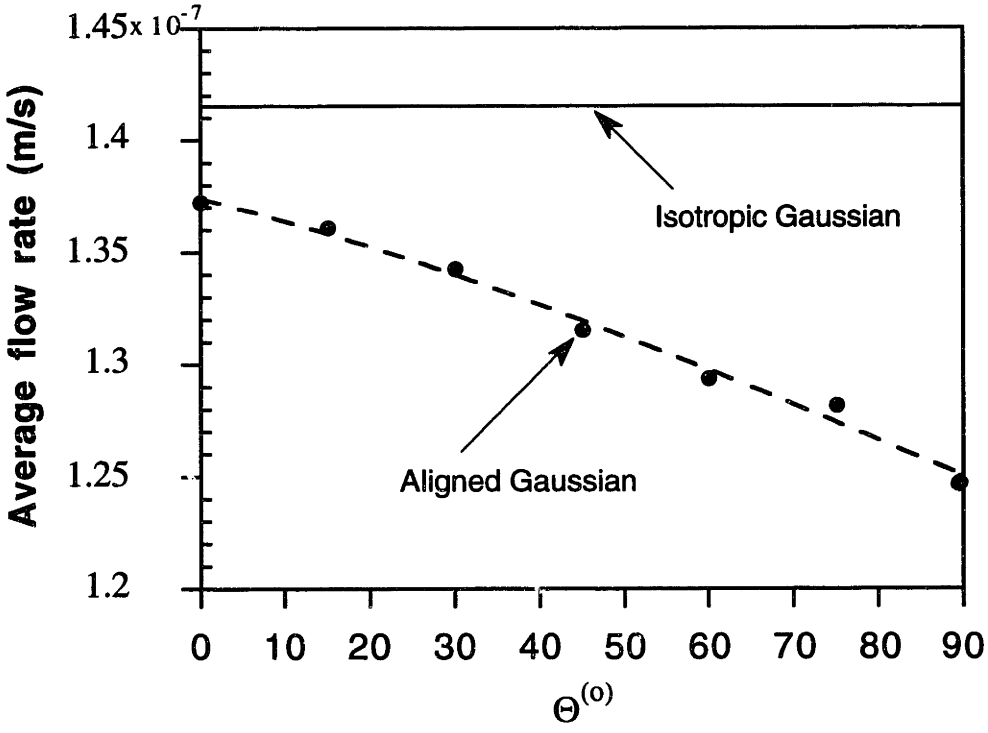

Figure 2-14: Average flow $\bar{q}$ *vs.* angle of lineation of permeability heterogeneities for the cases of Figure 2-13. The result of isotropic Gaussian ($a = 20$) is also plotted for comparison (solid line). Although permeability anisotropy is present, its magnitude is only about 10%

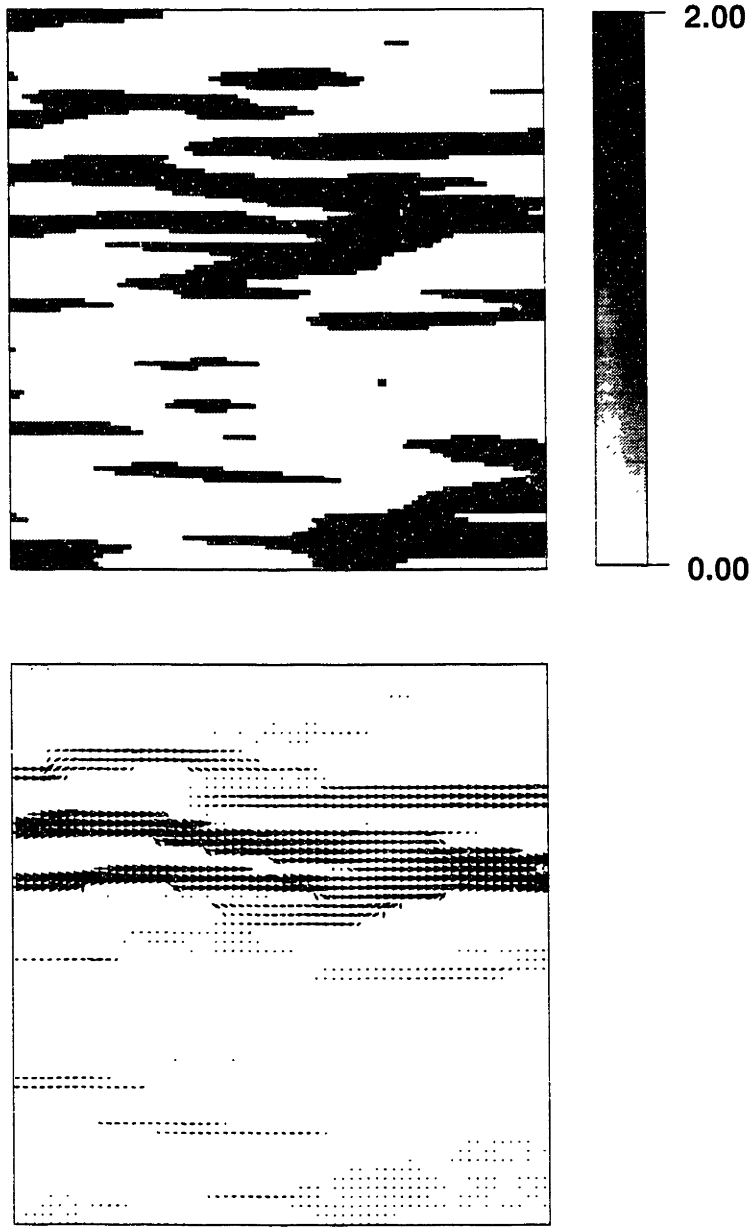

Figure 2-15: Flow channel models with $\theta = 0°$, 45°, and 90° calculated using Gaussian correlation functions and simulated flow fields. The correlation lengths are $a_1 = 20$, $a_2 = 2$. Model lengths are $x_0 = y_0 = 128$. On this page, the top figure is the flow channel model with $\theta = 0°$, the bottom figure is the calculated flow field.

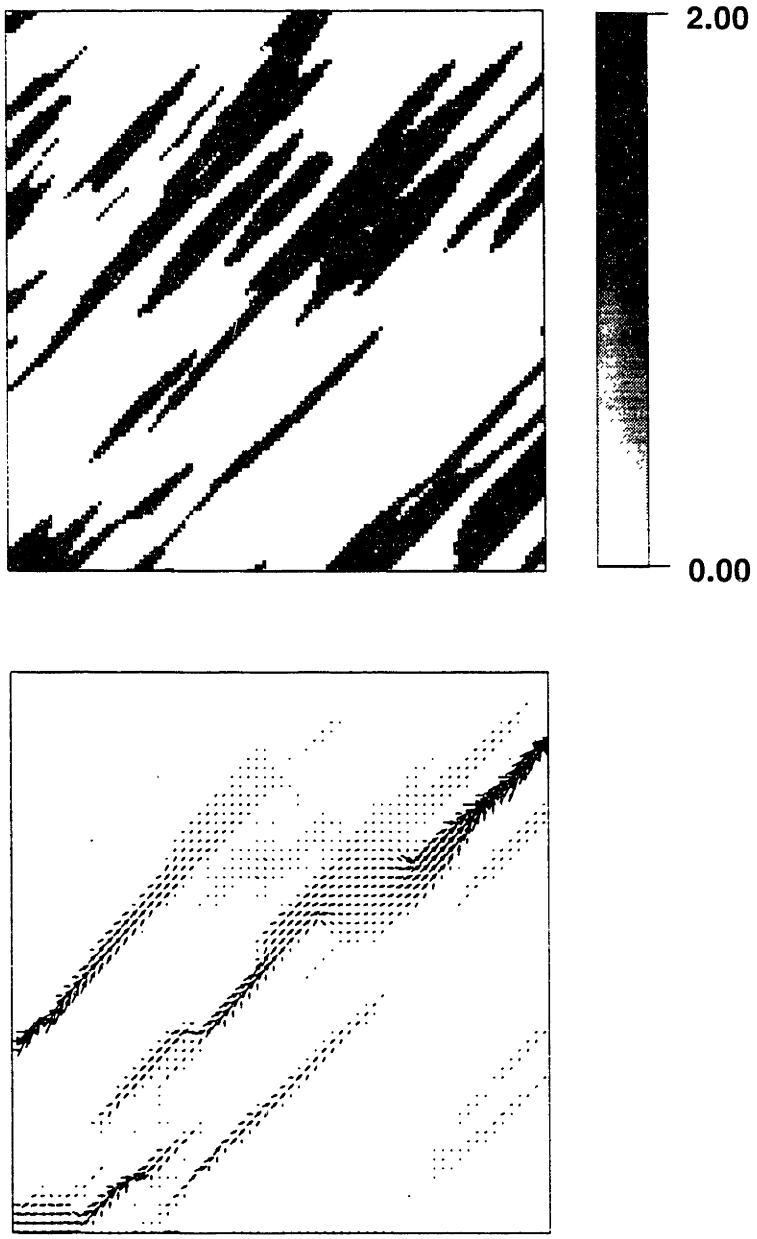

Figure 2-15 continued. The angle of lineation is $\theta = 45°$.

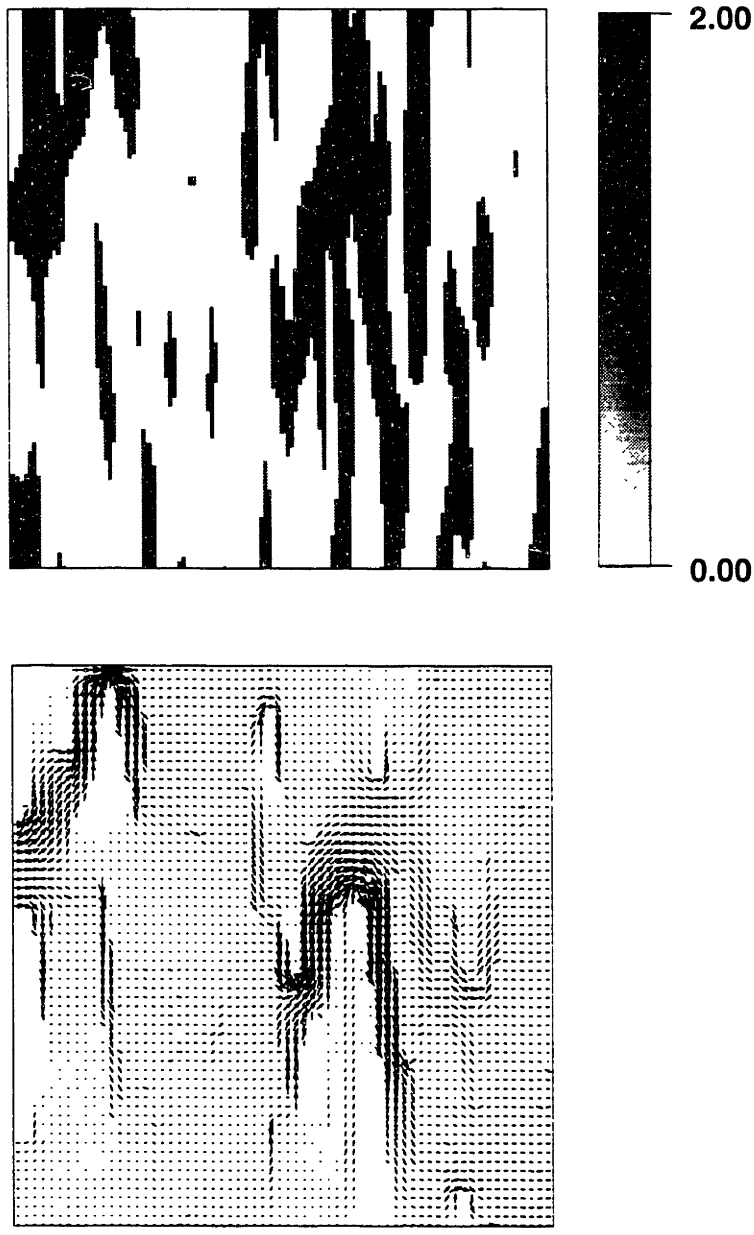

Figure 2-15 continued. The angle of lineation is $\theta = 90°$.

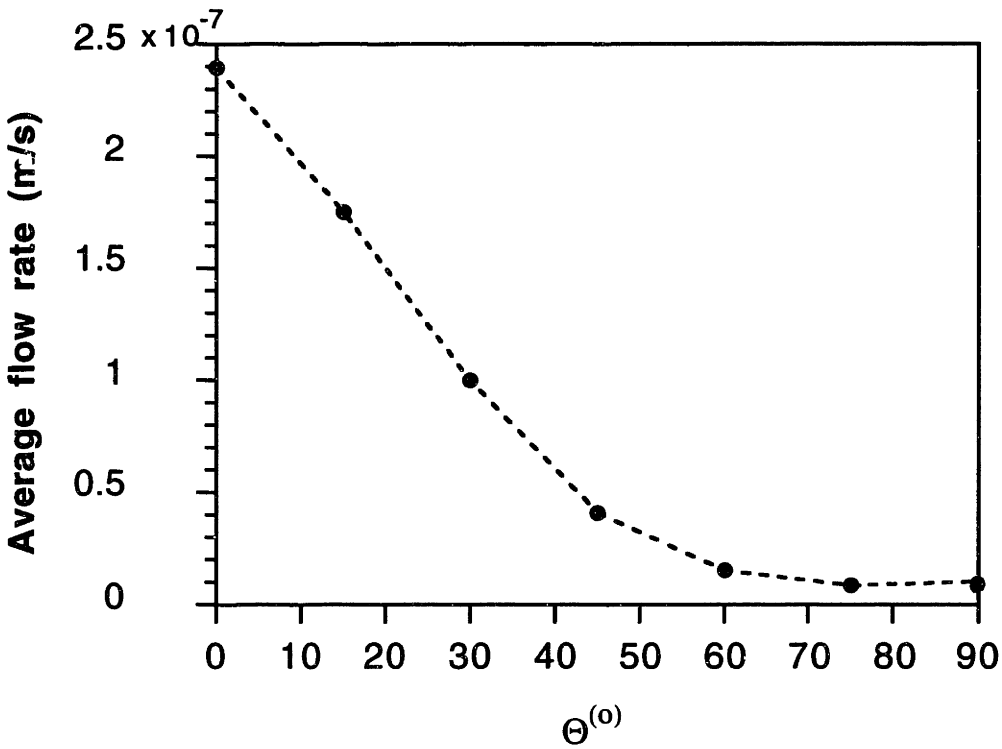

Figure 2-16: Average flow *vs.* angle θ for the models in Figure 2-15. In the case of flow channel models, $\bar{\kappa}$ values can have order of magnitude difference between $\theta = 0°$ and $\theta = 90°$, resulting in significant anisotropy (about 184%).

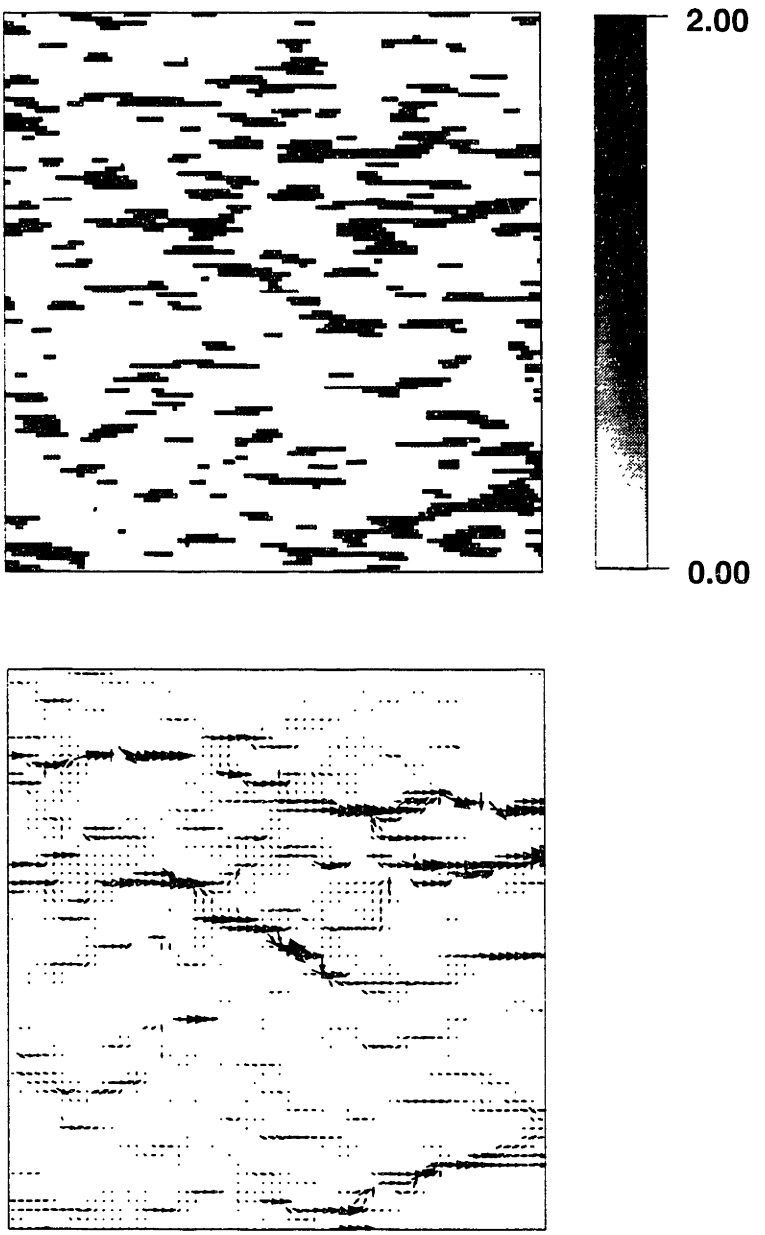

Figure 2-17: Same as Figure 2-15, but now the correlation lengths are reduced to $a_1 = 5$ and $a_2 = 1$, respectively. On this page, the top figure shows the permeability model with $\theta = 0°$, the bottom figure is the simulated flow field.

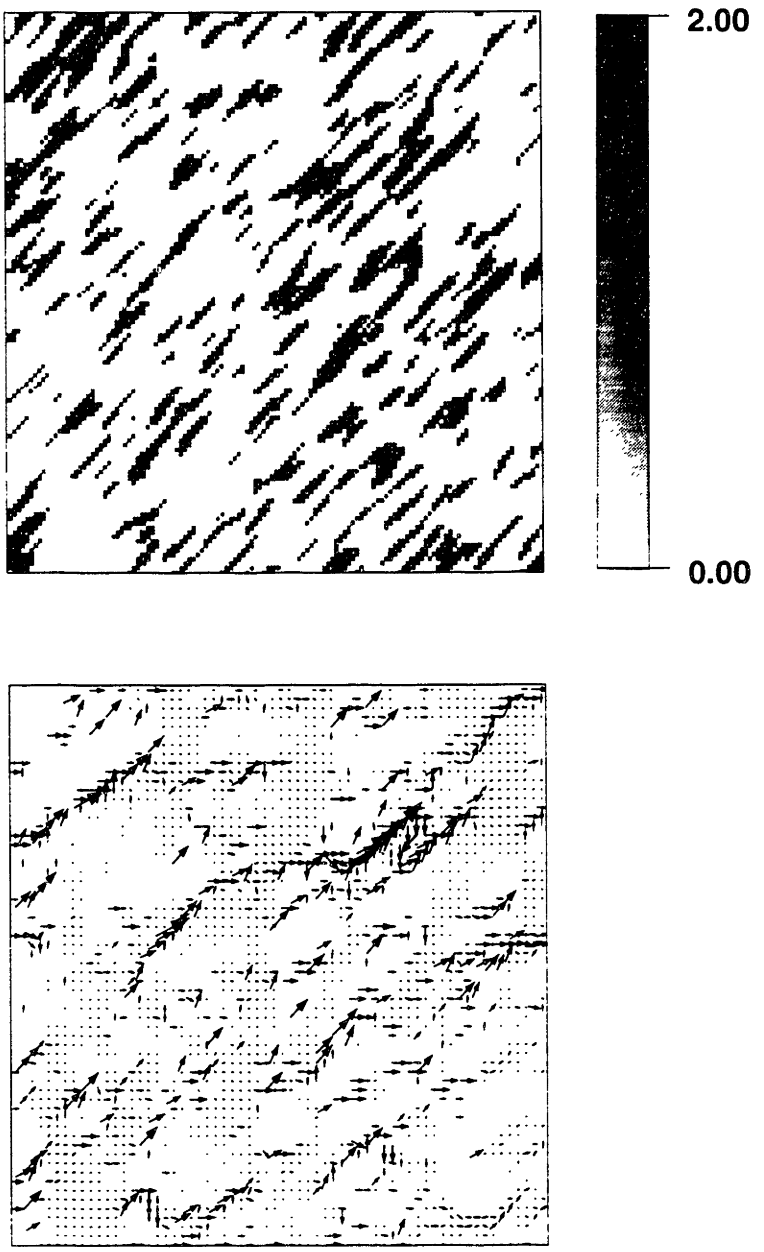

Figure 2-17 continued. The angle of lineation is $\theta = 45°$.

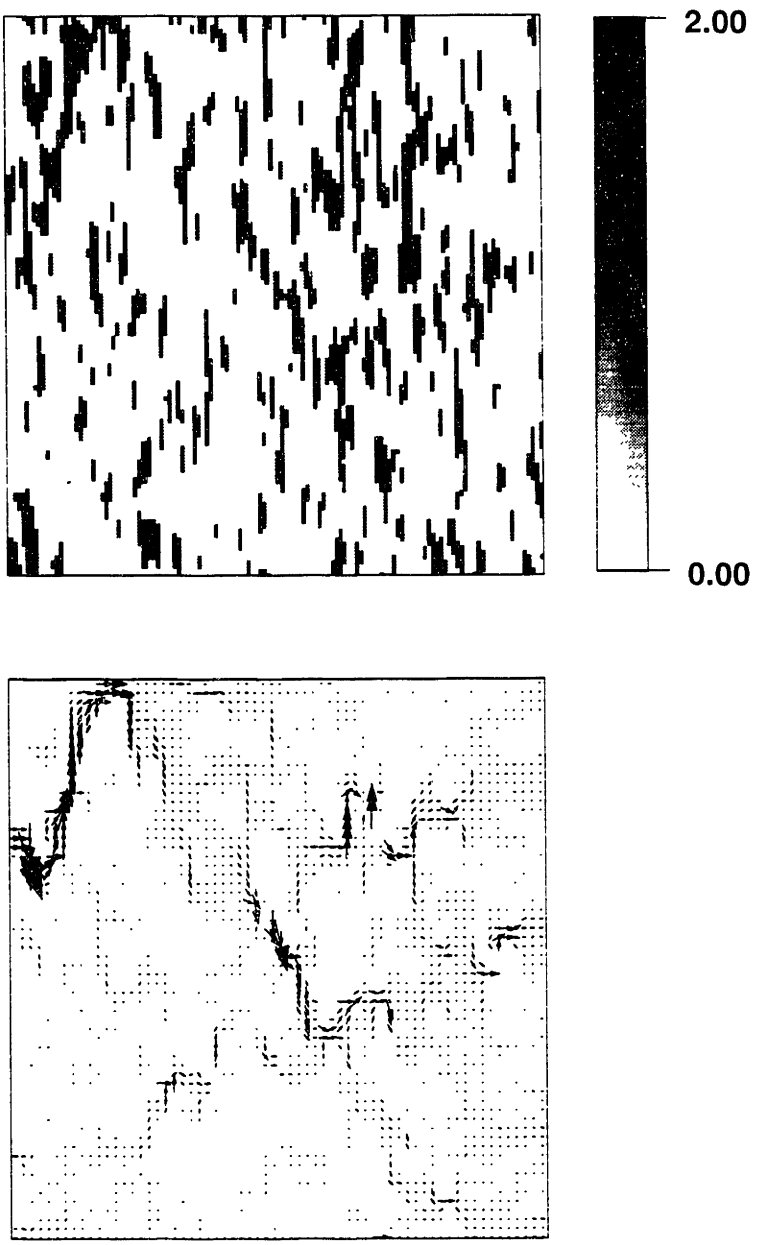

Figure 2-17 continued. The angle of lineation is $\theta = 90°$.

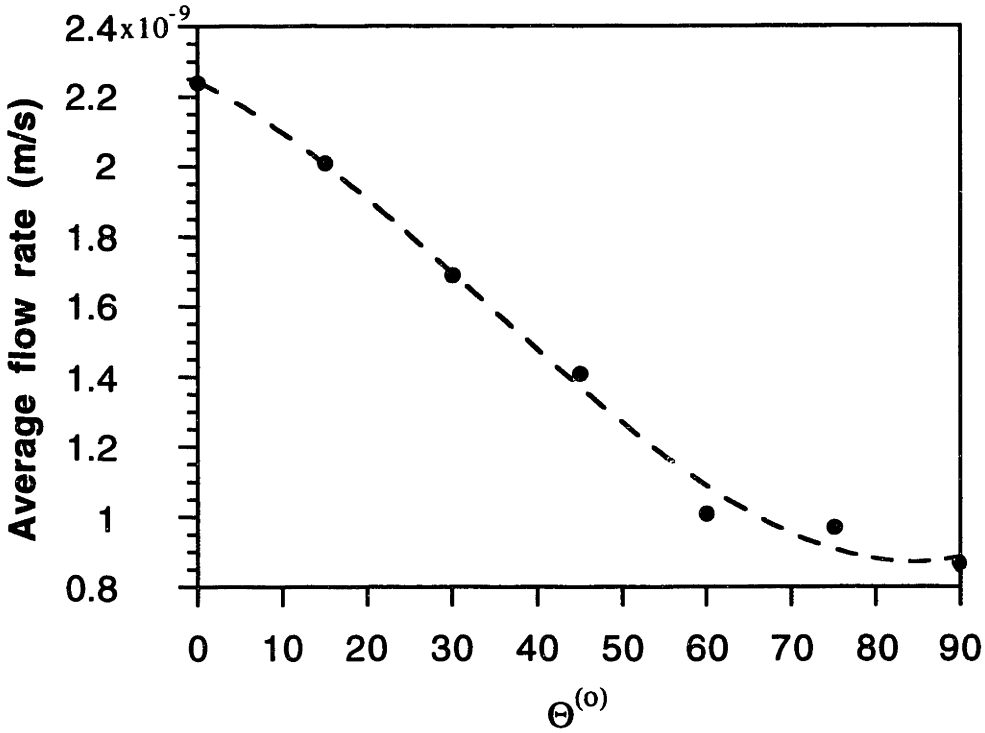

Figure 2-18: Average flow *vs.* angle θ for the models in Figure 2-17. The degree of anisotropy is reduced with reduction of the connectivity of the flow channels. The permeability difference between $\theta = 0°$ and $\theta = 90°$ is about 87%.

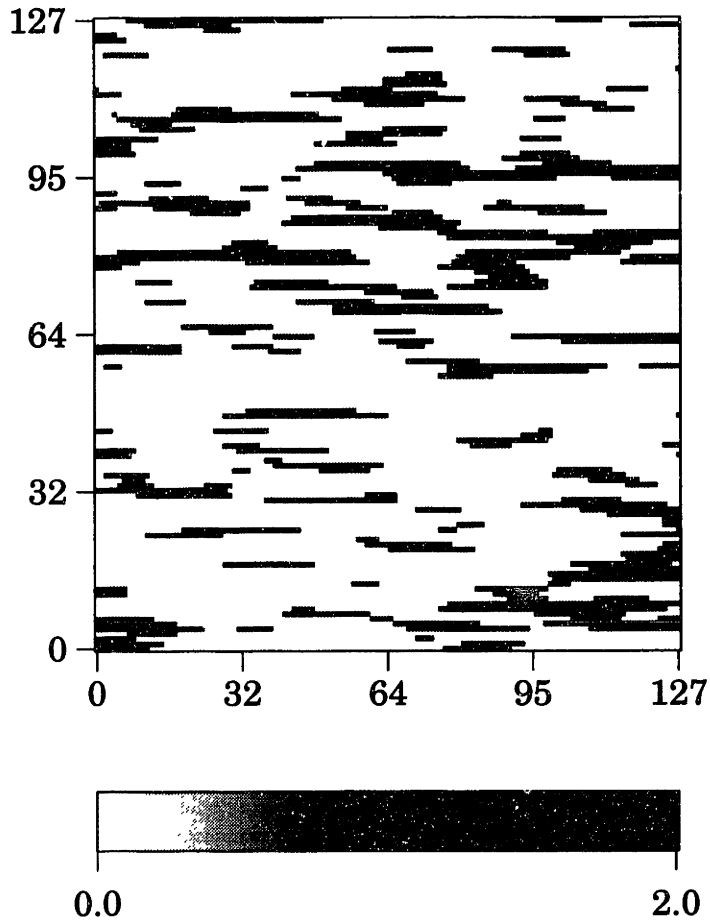

Figure 2-19: Flow channel model for testing the effects of model size on permeability anisotropy. The correlation lengths are $a_1 = 10$, $a_2 = 1$. Model size is 128×128.

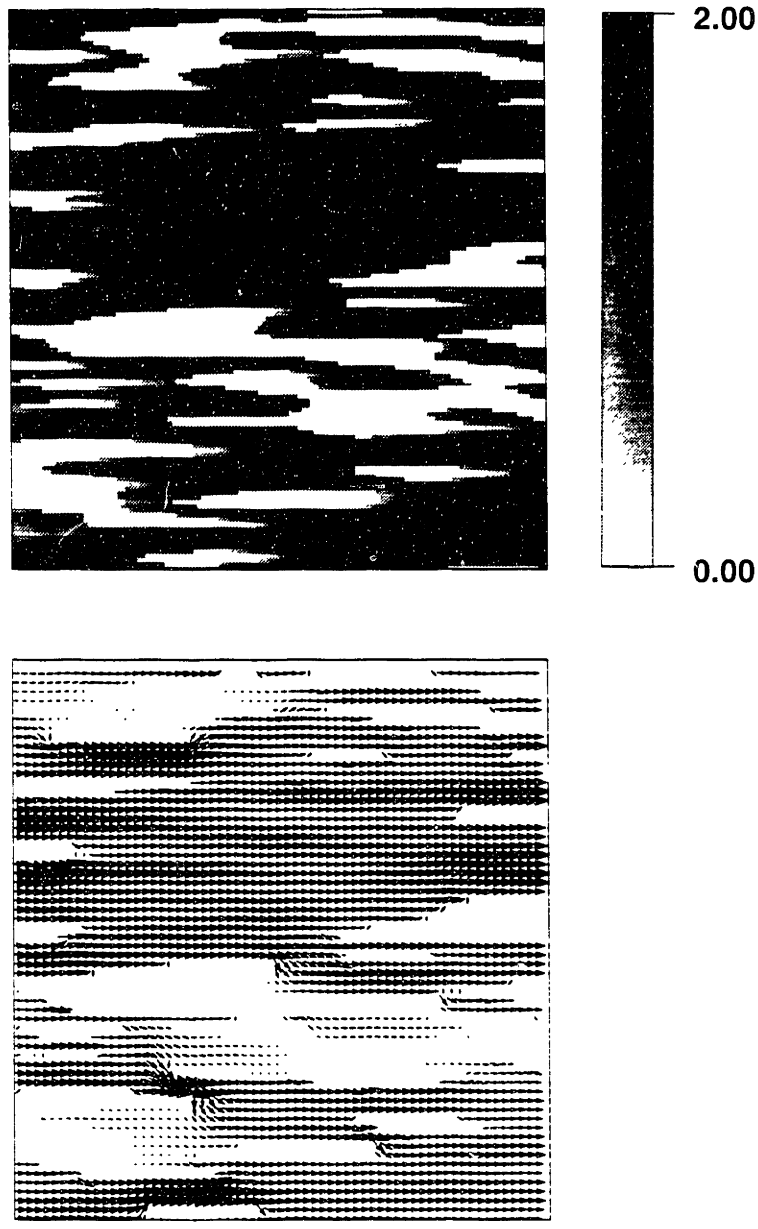

Figure 2-20: Aligned barriers models with $\theta = 0°$, $45°$, and $90°$ calculated using Gaussian correlation functions and calculated fluid flow fields. The correlation lengths and model lengths are the same as in Figure 2-15. On this page, the top figure is the permeability model with $\theta = 0°$, the bottom figure is the simulated flow field.

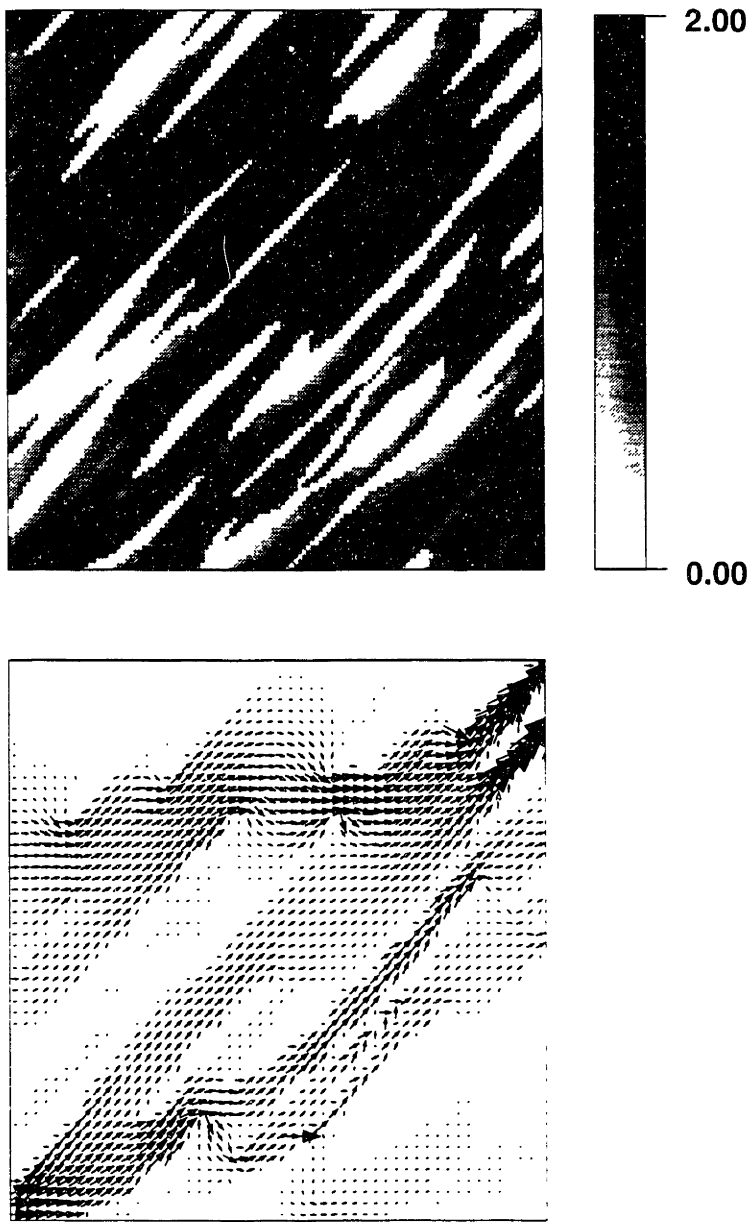

Figure 2-20 continued. The angle of lineation is $\theta = 45°$.

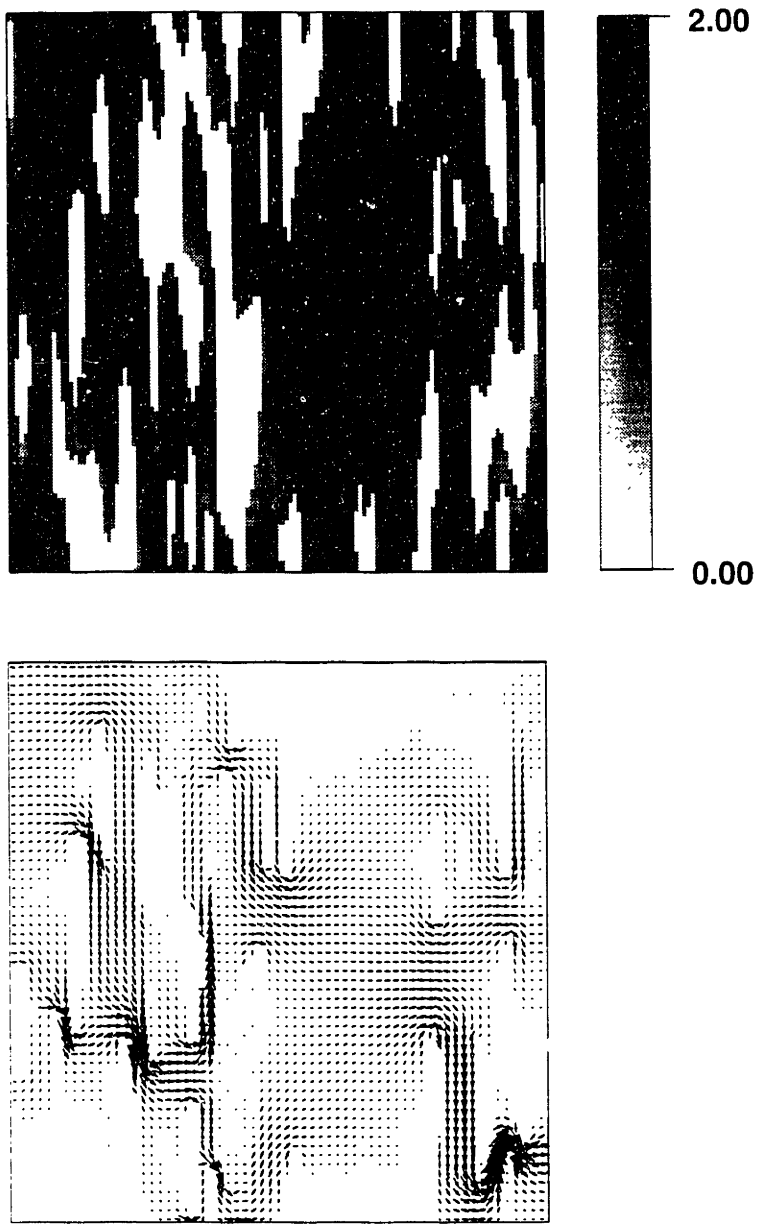

Figure 2-20 continued. The angle of lineation is $\theta = 90°$.

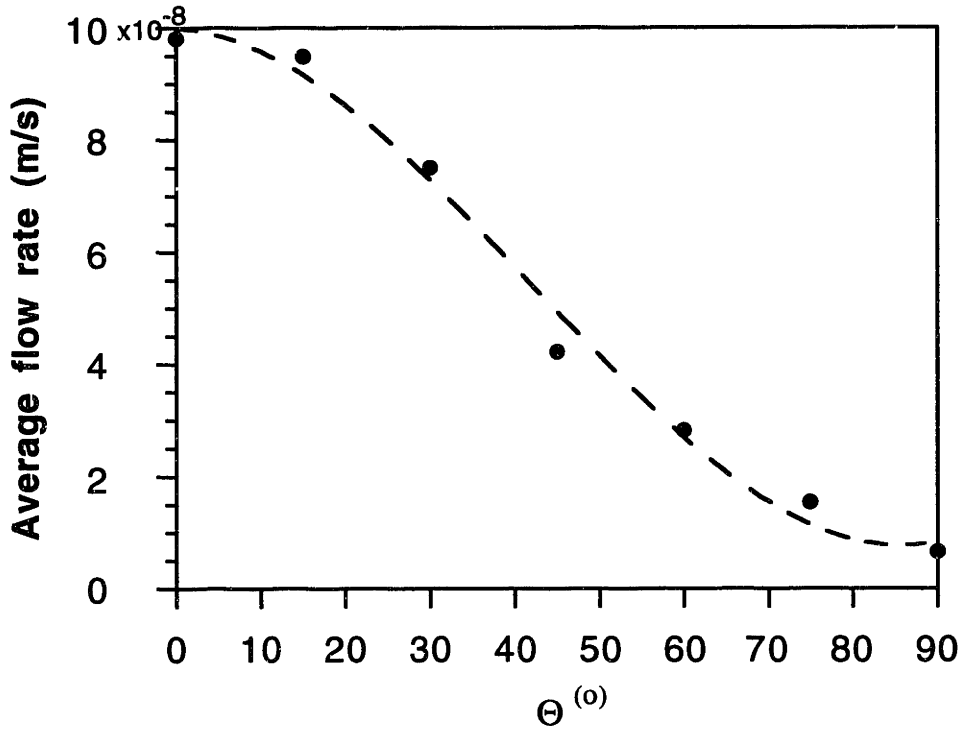

Figure 2-21: Average flow rate *vs.* angle θ for the models shown in Figure 2-20. The permeability anisotropy is about 175%.

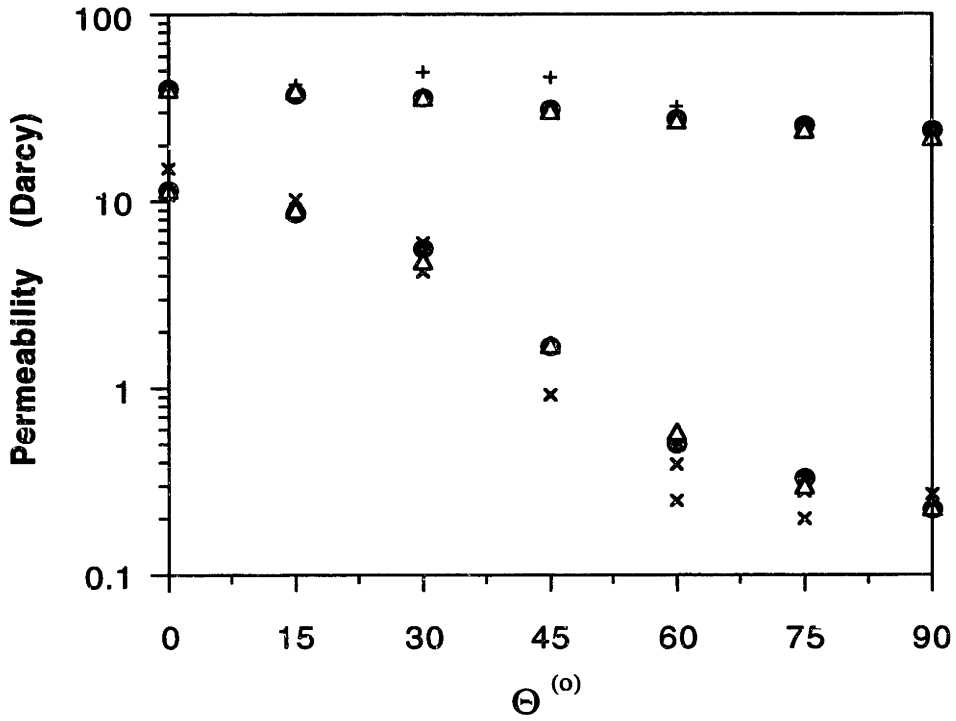

Figure 2-22: Theoretical (triangles and solid dots) and experimental (crosses + and ×) (Bernabé, 1991) results for two synthetic materials ($\kappa_{90}/\kappa_0 = 0.6$ and $\kappa_{90}/\kappa_0 = 0.02$). Triangles are the anisotropic finite difference modeling results obtained by Bernabé (1991). Solid dots are the finite difference modeling results of the thesis.

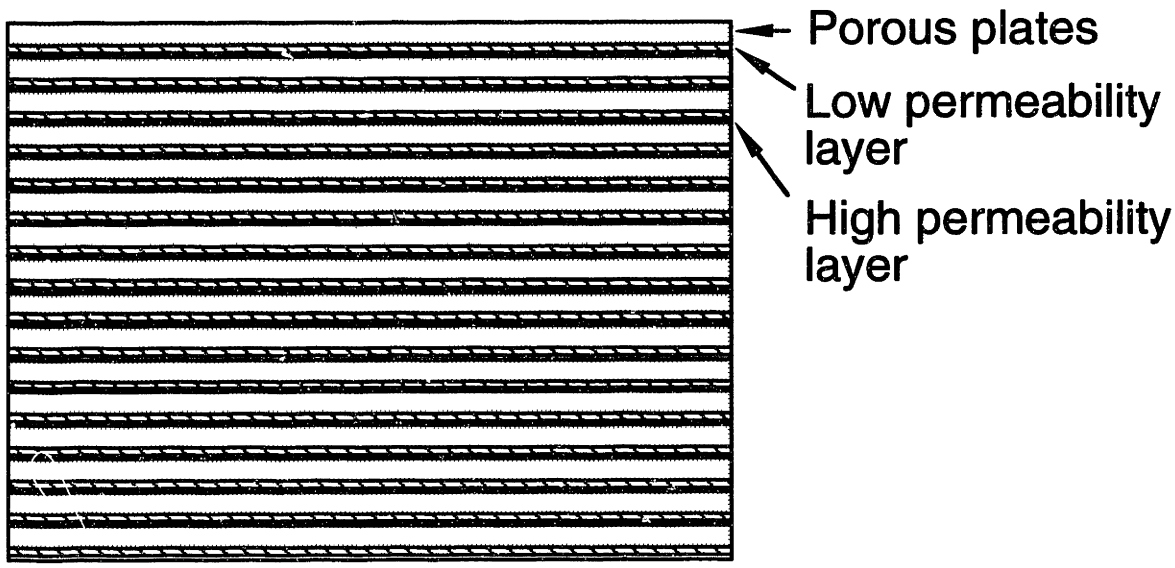

Figure 2-23: Stacked porous plates model used in the modeling of Bernabé's experimental data.

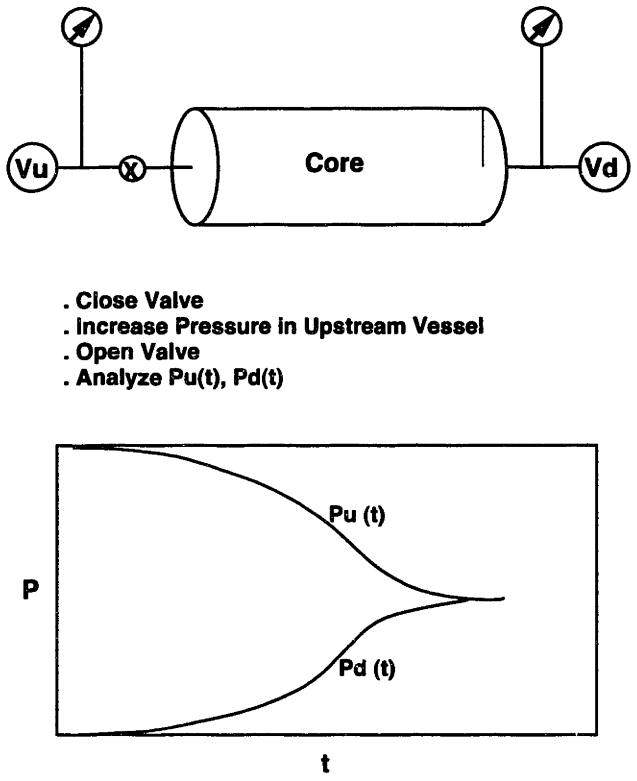

Figure 2-24: Pulse decay test methodology (from Kamath *et al.*, 1990).

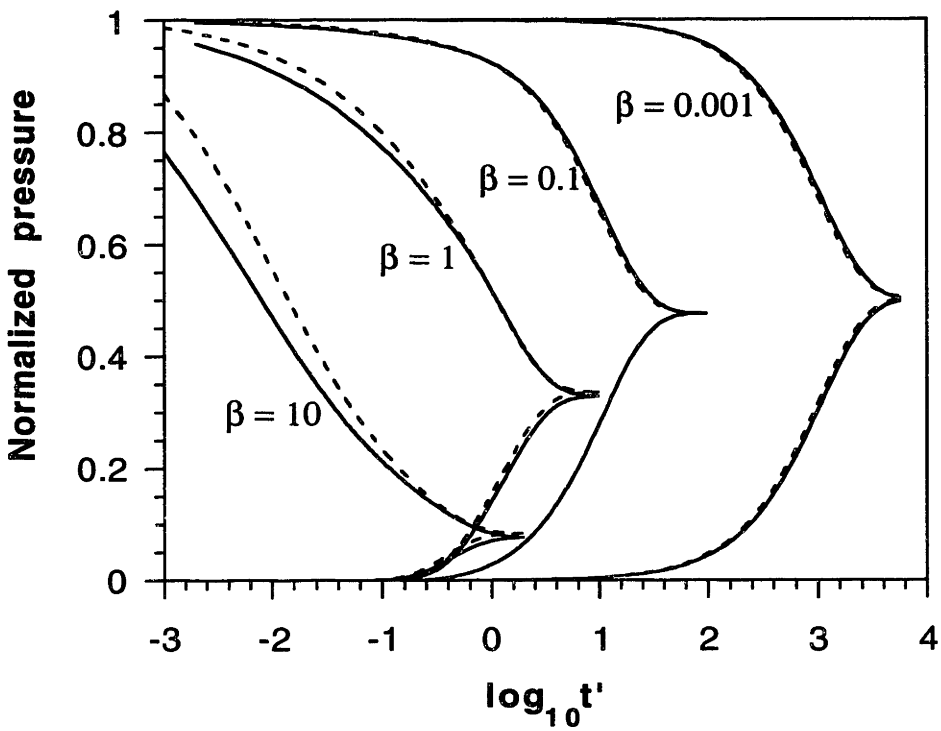

Figure 2-25: Pulse response curves for homogeneous (solid curves) and Gaussian (dashed curves) distributions.

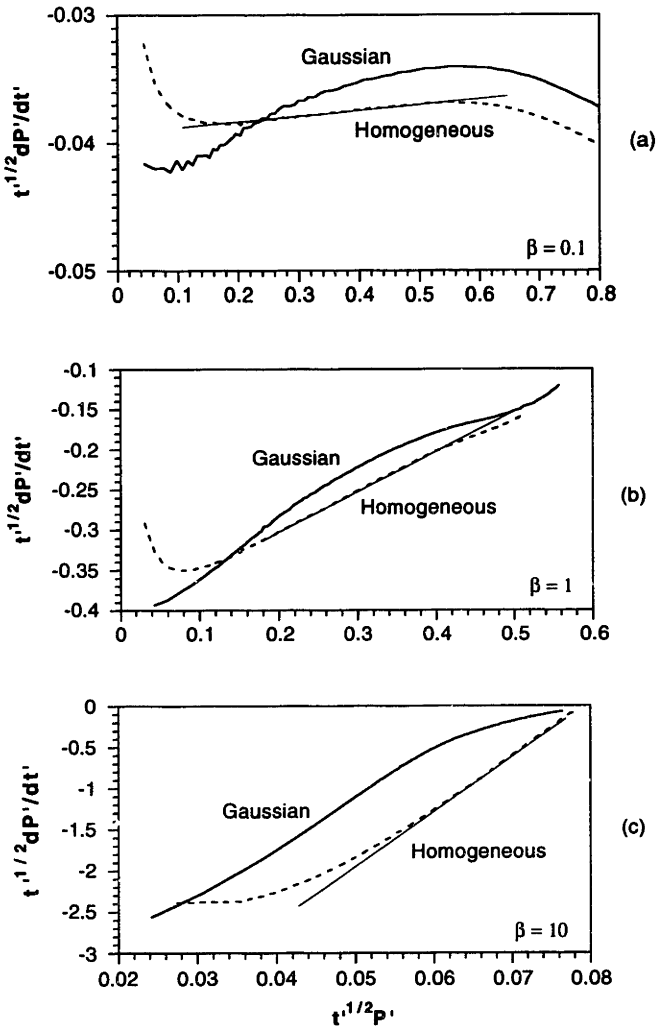

Figure 2-26: Comparison of early time solution for homogeneous and Gaussian distributions: (a) $\beta = 0.1$, (b) $\beta = 1$, and (c) $\beta = 10$. With increasing β, the slopes of the two solutions become similar.

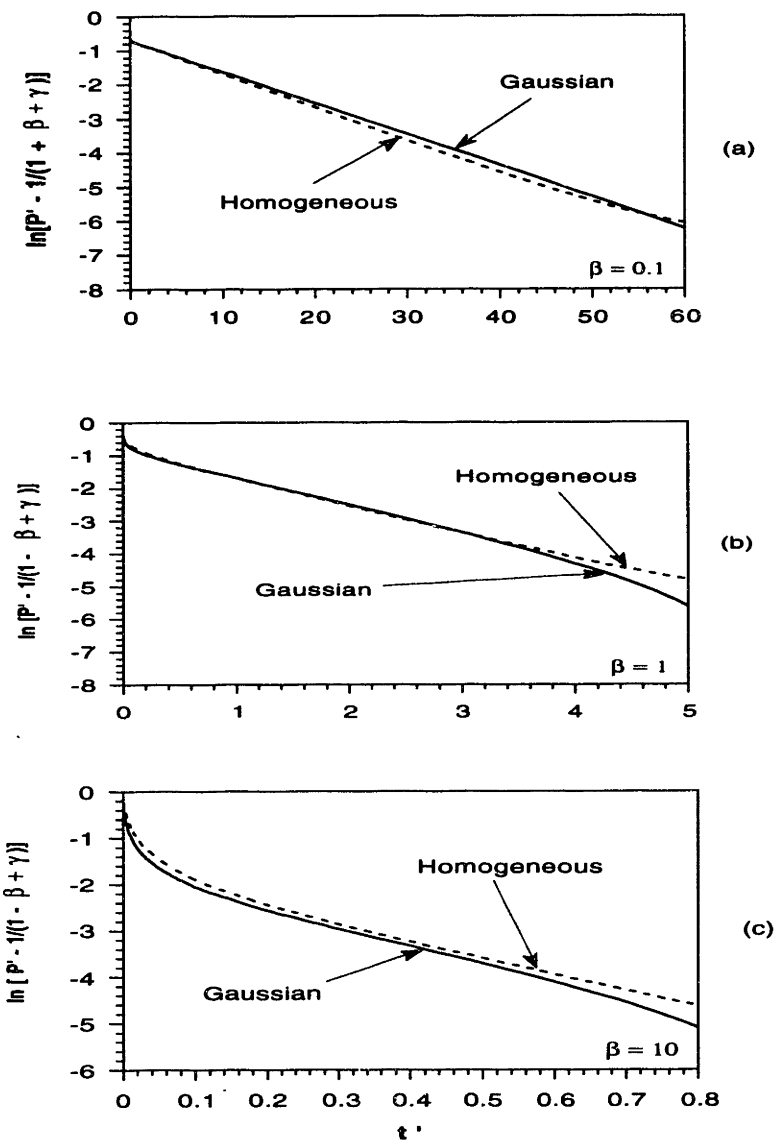

Figure 2-27: Comparison of late time solution for homogeneous and Gaussian distributions: (a) $\beta = 0.1$, (b) $\beta = 1$, and (c) $\beta = 10$. The slopes of the solutions are almost the same for the two distributions.

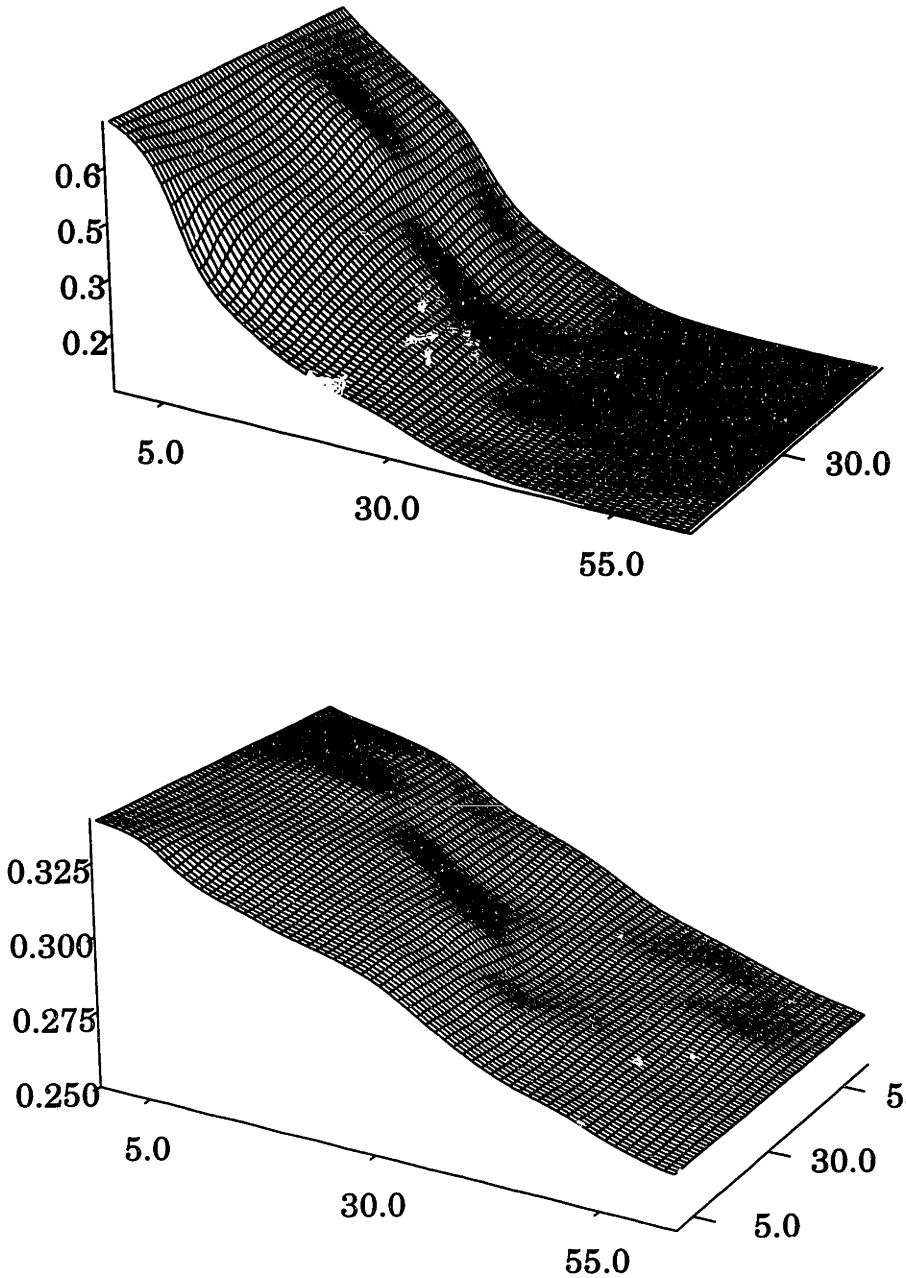

Figure 2-28: Pressure fields at early time (top figure, $t' = 0.1$) and late time (bottom figure, $t' = 3$). For the early time, the pressure has not reached the lower boundary. For the late time, the pressure has penetrated the lower boundary and the amplitudes are reduced. Notice the scale difference between the top and bottom figures.

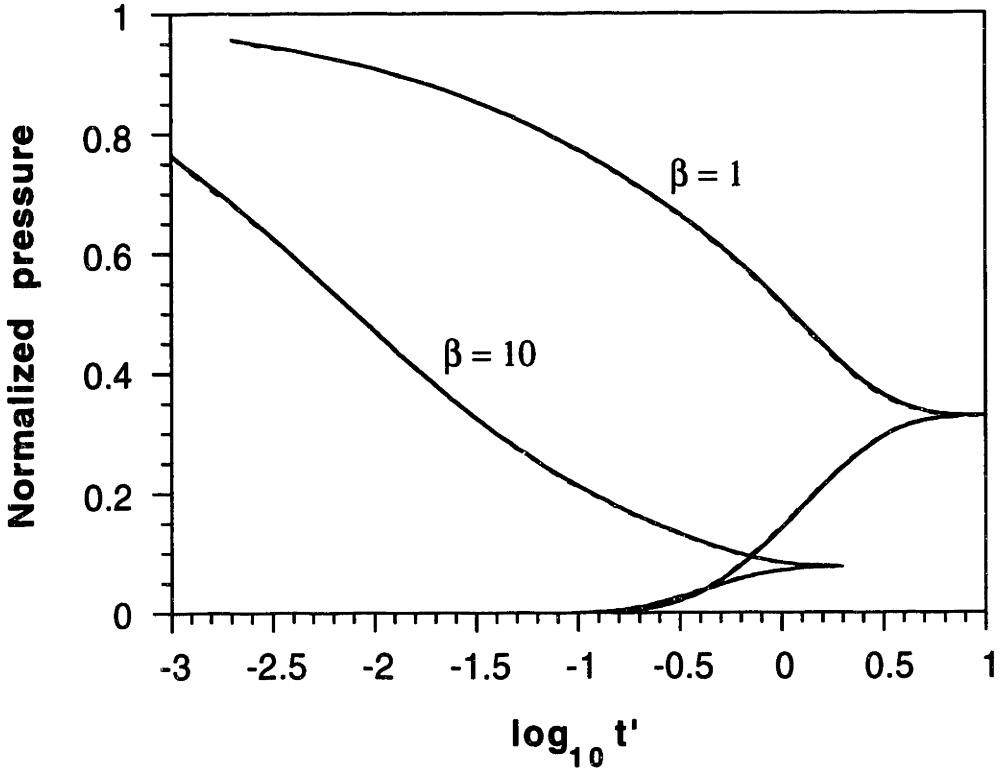

Figure 2-29: Comparison of pressure responses of Gaussian (solid curves) and von Kármán (dashed curves) heterogeneous distributions.

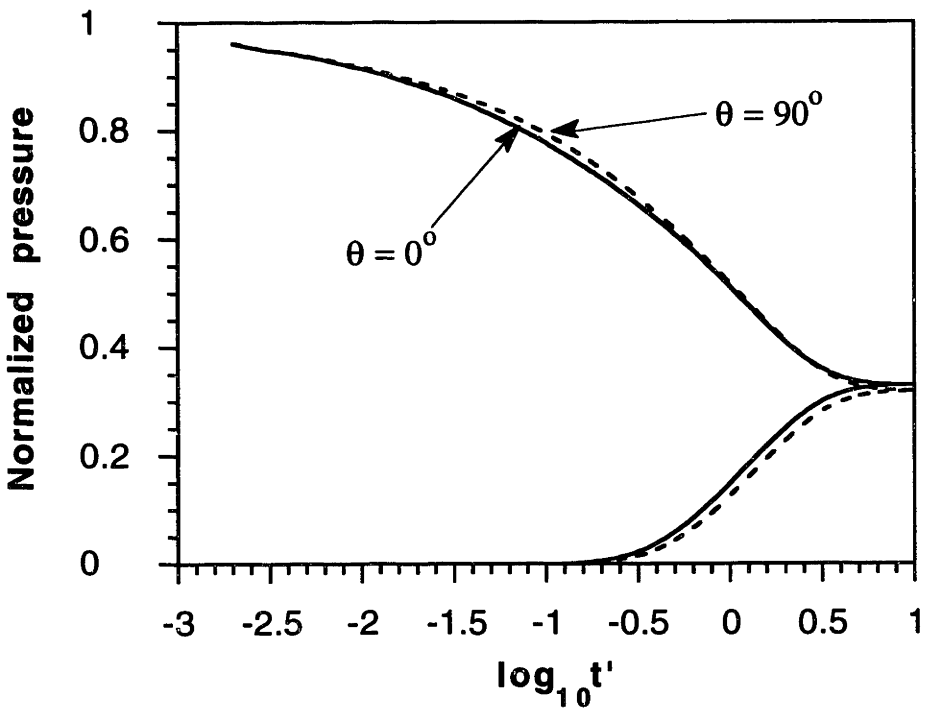

Figure 2-30: Pulse response curves of the aligned distributions at $\theta = 0°$ (solid curves) and $\theta = 90°$ (dashed curves) for $\beta = 1$.

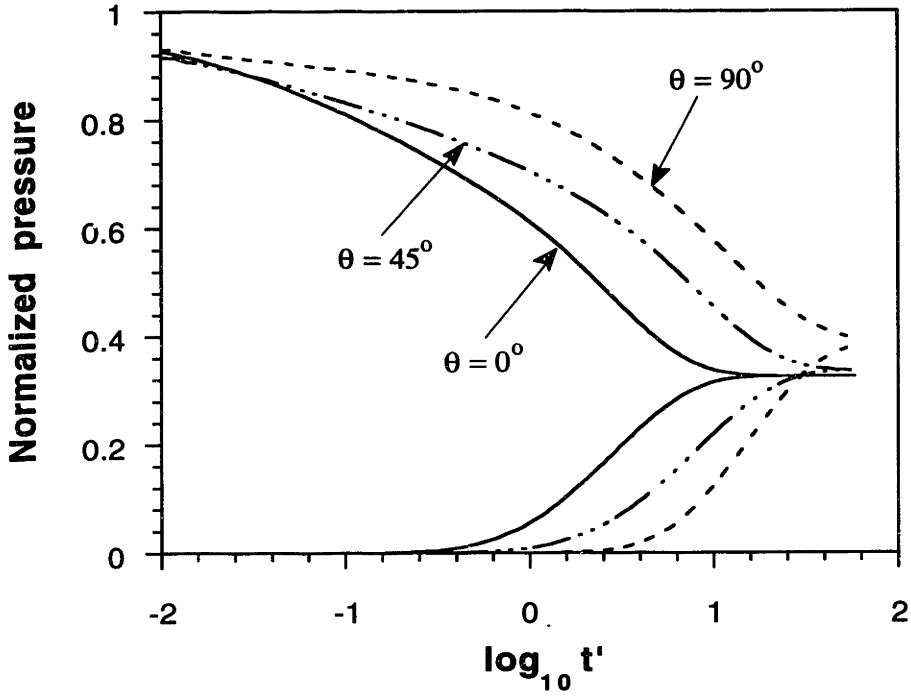

Figure 2-31: Pulse response curves of fractured medium at $\theta = 0°$, 45°, and 90°.

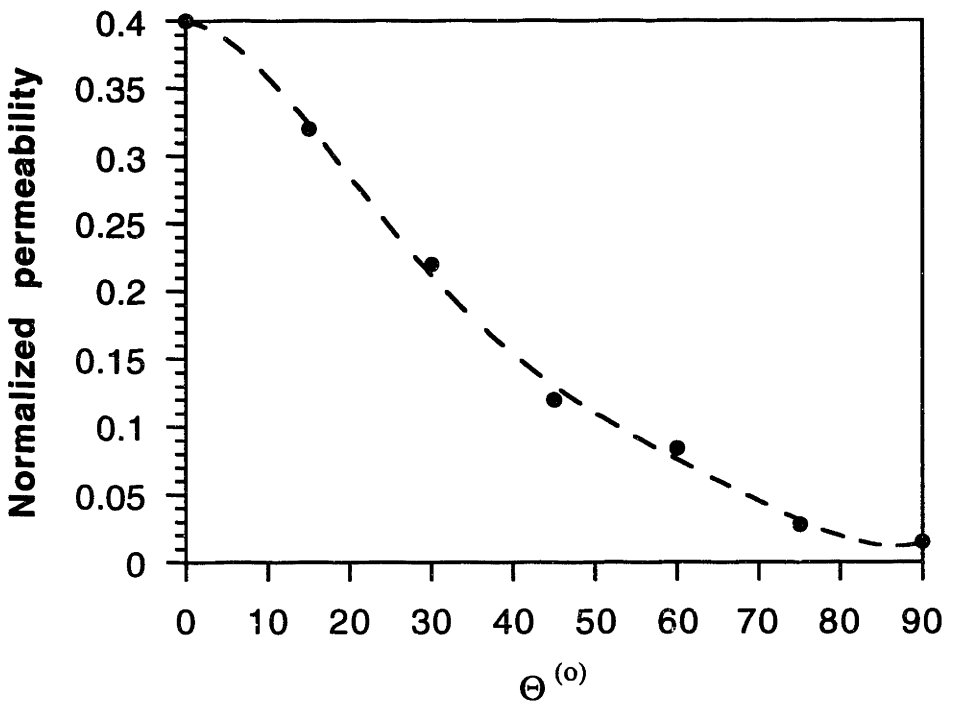

Figure 2-32: Normalized permeability of late time solution *vs.* fracture alignment angle θ.

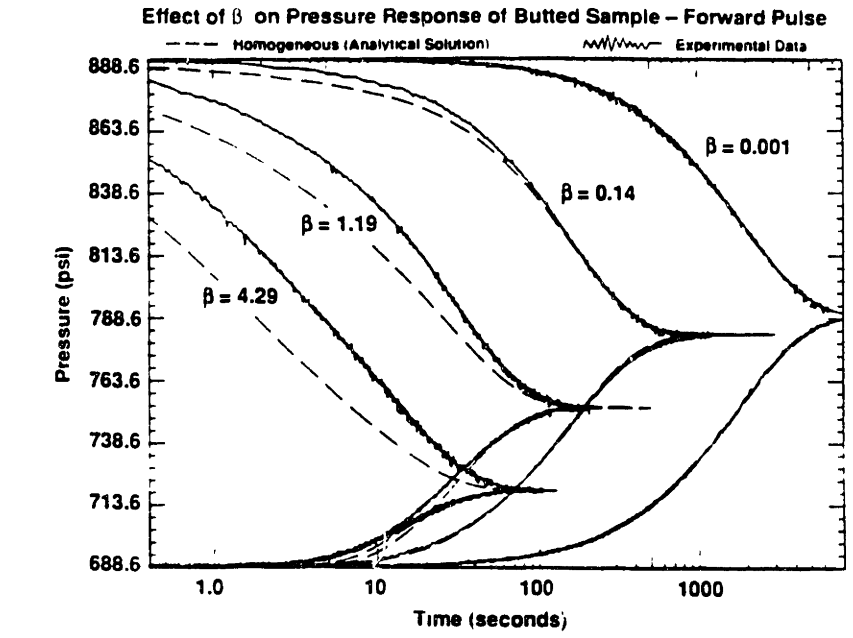

(a)

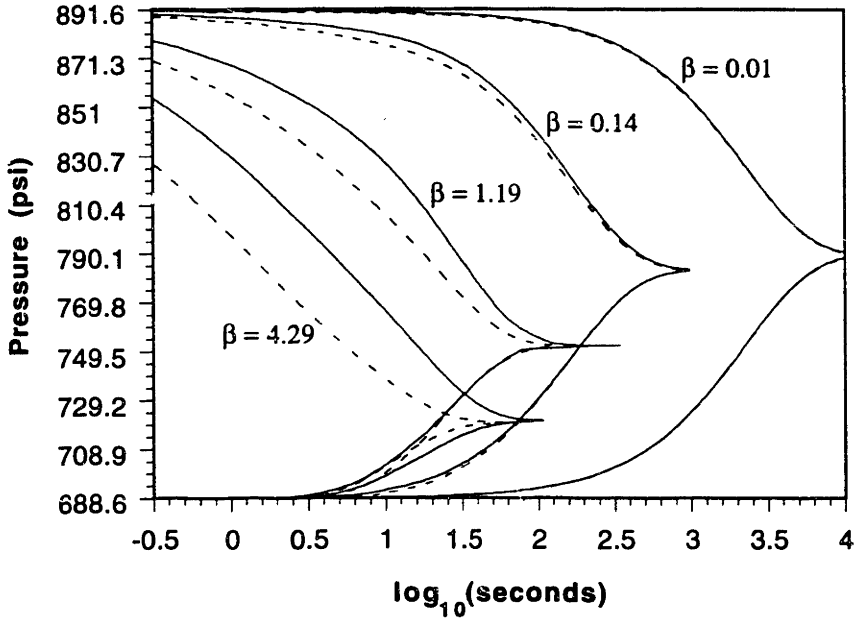

(b)

Figure 2-33: (a). Experimental pressure responses of butted sample together with the analytical solution for a homogeneous rock with same effective permeability (after Kamath *et al.*, 1990). (b). Finite difference modeling results for the same core samples. The dashed curves are the homogeneous rock results and solid curves are the butted core sample modeling results. In (a) the value of $\beta = 0.001$ may be a typo error and should be 0.01, as can be seen by comparing the corresponding responses in (a) and (b).

Chapter 3

Dynamic Fluid Flow in Heterogeneous Porous Media and Through a Single Fracture With Rough Surfaces

3.1 Introduction

Fluid flow in porous media is an important topic in the study of flow of oil or gas in petroleum reservoirs. In many applications where the fluid flow is time invariant, steady-state flow can be modeled in heterogeneous porous media using finite difference techniques as described in Chapter 2. When the fluid-driven source changes moderately with time, such as the pressure transient tests in a borehole (Melville *et al.*, 1991) and in laboratory measurements (Brace *et al.*, 1968; Kamath *et al.*, 1990; Bernabé, 1991), fluid flow can be modeled as a diffusion process in which the fluid transport properties such as permeability are still regarded as independent of time (or frequency) (see also Chapter 2). Moreover, in applications related to wave propagation, such as vertical seismic profiling and acoustic logging, fluid flow associ-

ated with the pressure disturbance caused by seismic wave propagation is dynamic in nature and may strongly depend on frequency. In fact, in these situations, the frequency-dependent flow becomes the Biot's slow wave (Biot, 1956a, b) in a porous medium.

To characterize the frequency-dependent fluid transport properties, Johnson *et al.* (1987) developed the theory of dynamic permeability. Applying the concept of dynamic permeability to the problem of acoustic logging in permeable porous formations, Tang *et al.* (1991b) showed that the dynamic permeability captures the frequency-dependent behavior of the Biot's slow wave and correctly predicts the effects of formation permeability on borehole Stoneley waves. The theory of dynamic permeability of Johnson *et al.* (1987) is formulated assuming the homogeneity of the porous medium. The natural geological medium, however, contains heterogeneities of various scales. It would be interesting to apply the dynamic permeability to the heterogeneous porous media to study the overall behavior of fluid flow through the media. In this study, we will extend the dynamic permeability of Johnson *et al.* (1987) to heterogeneous medium and model the dynamic fluid flow in the medium. A finite difference method will be developed to model the effects of heterogeneities.

A problem that has attracted much research interest is fluid flow through a rough-walled fracture or joint. Brown (1987, 1989) and Zimmerman *et al.* (1991) have modeled the steady-state fluid flow through the fracture and showed that the roughness of the fracture surfaces significantly affects the fluid flow when the surfaces are in contact. In the characterization of borehole fractures using acoustic logging (Paillet *et al.*, 1989; Hornby *et al.*, 1989; Cicerone, 1991; Toksöz *et al.*, 1992), the response of the fracture to the dynamic pressure set up by the logging waves is important for characterizing the fracture permeability. In this situation, fluid flow in fractures is dynamic in nature. Tang and Cheng (1989) have studied the dynamic flow through a plane fracture bounded by two parallel walls. Natural fracture surfaces, however, exhibit roughness (Brown, 1987). It is important to understand the effects of sur-

face roughness on the dynamic fluid flow in order to correctly model the dynamic response of natural fractures to borehole acoustic waves. Tang *et al.* (1991a) have shown that the theory of dynamic permeability, when applied to the parallel-wall fracture, is equivalent to the theory of fracture dynamic conductivity obtained from solution of viscous fluid flow in a plane fracture. Therefore, if we assume that the dynamic permeability for a parallel-wall fracture holds locally in a fracture, then we can use the finite difference method developed for heterogeneous porous media to model the dynamic flow in a rough-walled fracture.

In the following, we first discuss the theory of dynamic permeability and governing equations for the dynamic fluid flow. Then we develop a finite difference technique to solve the flow equation in the frequency domain. Finally, we apply the finite difference technique to study the dynamic flow in a heterogeneous medium and through a single fracture with rough surfaces.

3.2 Theory of Dynamic Fluid Flow

3.2.1 Dynamic permeability

Consider the dynamic response of a porous medium saturated with a viscous fluid and subjected to a small amplitude oscillatory pressure gradient across the medium. The response to the pressure gradient $\nabla P e^{-i\omega t}$ is conveniently defined in terms of the volumetric fluid velocity $\vec{\mathbf{v}}(\omega)$ of the porous medium. Assuming $\vec{\mathbf{v}}(\omega)$ is linearly related to ∇P at any frequency ω, we have

$$\vec{\mathbf{v}}(\omega) = -\frac{\kappa(\omega)}{\mu}\nabla P \ , \tag{3.1}$$

where μ is pore fluid viscosity. The frequency-dependent permeability $\kappa(\omega)$ is defined in Equation (3.1) by analogy with the steady-state ($\omega = 0$) definition (Scheidegger, 1974). In order to derive a governing equation for dynamic fluid pressure in the

frequency domain, we consider the following equation for transient flow

$$\frac{\partial P}{\partial t} = \nabla \cdot (\alpha \nabla P) \ . \tag{3.2}$$

In the frequency domain, α is a function of frequency if we use dynamic permeability $\kappa(\omega)$ to replace the static permeability κ_0. Also, by replacing $\frac{\partial P}{\partial t}$ with $-i\omega P$, we get

$$\nabla^2 P + \frac{i\omega}{\alpha(\omega)} P = 0 \ . \tag{3.3}$$

In deriving this equation, we have assumed that the medium is homogeneous. The dynamic pore fluid diffusivity $\alpha(\omega)$ is given by

$$\alpha(\omega) = \frac{\kappa(\omega) K_f}{\mu\phi(1+\xi)} \ , \tag{3.4}$$

where $\xi = \frac{K_f}{K_p}$ is the ratio of the pore fluid incompressibility K_f to the porous matrix incompressibility K_p. The functional form of ξ is given in Chang *et al.* (1988) and Norris (1989). Equation (3.3) can be regarded as a wave equation with a wavenumber $k = \sqrt{\frac{i\omega}{\alpha(\omega)}}$.

In the following, we describe the procedure for obtaining the frequency dependent dynamic permeability. For simplicity, we first assume that the porous solid is rigid [i.e., $\xi = 0$ ($K_p \to \infty$), a non-zero ξ value allows the correction for solid elasticity]. The low- and high-frequency limits of $\kappa(\omega)$ will first be established. Obviously, for low enough frequencies, the dynamic permeability approaches its d.c. value

$$\lim_{\omega \to 0} \kappa(\omega) = \kappa_0 \ , \tag{3.5}$$

where κ_0 is the real-valued, conventional Darcy permeability. In this low frequency range, fluid motion is slowly varying in time and follows a diffusion equation with a diffusivity $\alpha = \kappa_0 K_f / \mu\phi$.

In the limit of high frequencies, we shall use the high frequency characteristics of the pore fluid motion to establish the high frequency behavior of $\kappa(\omega)$. At very high frequencies, the viscous skin depth, $\delta = \sqrt{\frac{2\mu}{\rho_0 \omega}}$, eventually becomes much smaller than

the pore sizes. The Darcy flow is dominant only within a viscous layer of thickness δ at the pore walls. Therefore, except for the boundary layer of thickness δ, the fluid motion is characterized by wave propagation. The wave velocity, c, of this propagating wave mode in a (rigid) porous solid is well established (Johnson *et al.*, 1982; 1987), as given by

$$\lim_{\omega\to\infty} c(\omega) = \frac{\omega}{k_r(\omega)} = \frac{v_f}{\sqrt{\tau + C(-i\omega)^{-1/2})}} \quad , \tag{3.6}$$

where $k_r(\omega)$ is the real part of the wavenumber $k(\omega)$ [its imagenary part is $k_i(\omega)$]; v_f is the acoustic speed of the pore fluid; τ is the high frequency limit of the frequency-dependent tortuosity (Johnson *et al.*, 1987); and C is a constant to be determined.

By using the real and imaginary parts, $\kappa_r(\omega)$ and $\kappa_i(\omega)$, of the dynamic permeability and using Equation (3.4) (with $\xi = 0$), $k_r(\omega)$ and $k_i(\omega)$ can be expressed as

$$k_r^2(\omega) = \frac{\omega\mu\phi}{2\rho_0 v_f^2|\kappa|^2}(|\kappa| + \kappa_i) \tag{3.7}$$

$$k_i^2(\omega) = \frac{\omega\mu\phi}{2\rho_0 v_f^2|\kappa|^2}(|\kappa| - \kappa_i) \quad , \tag{3.8}$$

where $|\kappa| = [\kappa_r^2(\omega) + \kappa_i^2(\omega)]^{1/2}$ is the amplitude of $\kappa(\omega)$ and $k_r(\omega)$ is given by Equation (3.6). To find the high frequency behavior of $\kappa_r(\omega)$ and $\kappa_i(\omega)$, we also need to know $k_i(\omega)$, which will be obtained by evaluating energy dissipation in the fluid flow field. On a microscopic scale, $k_i(\omega)$ can be related to the exact microscopic velocity field $\vec{\mathbf{u}}(\vec{\mathbf{r}})$ as (Landau and Lifshitz, 1959)

$$k_i(\omega) = \frac{|\dot{E}_{mech}|}{S_0} \quad , \tag{3.9}$$

where S_0 is the energy flux density of the wave motion, which is equal to the high frequency speed of the wave, $v_f/\sqrt{\tau}$ [omitting the $C(i\omega)^{-1/2}$ term in Equation (3.6)], times the energy density:

$$S_0 = \frac{v_f}{\sqrt{\tau}}\frac{1}{2}\rho_0\frac{1}{V}\int_V |\vec{\mathbf{u}}_\mathbf{0}(\vec{\mathbf{r}})|^2 dV \quad . \tag{3.10}$$

where V is the volume of the porous solid; $\vec{\mathbf{u}}_0$ is the fluid velocity outside the viscous boundary layer in the bulk of pore fluid; and $\dot{E}_{mech}$ is the rate of viscous dissipation per unit volume

$$\dot{E}_{mech} = -\frac{1}{4}\mu\frac{1}{V}\int_V \left|\frac{\partial u_i}{\partial x_j} + \frac{\partial u_j}{\partial x_i}\right|^2 dV \ . \tag{3.11}$$

The fluid velocity field $\vec{\mathbf{u}}$ satisfies the linearized microscopic Navier-Stokes equation

$$-i\omega\rho_0\vec{\mathbf{u}} = -\nabla P + \mu\nabla^2\vec{\mathbf{u}} \ . \tag{3.12}$$

Taking the curl of Equation (3.12), we have

$$\nabla^2(\nabla\times\vec{\mathbf{u}}) + \frac{i\omega\rho_0}{\mu}(\nabla\times\vec{\mathbf{u}}) = 0 \ . \tag{3.13}$$

This equation indicates that the vorticity, $\nabla\times\vec{\mathbf{u}}$, obeys the diffusion equation with a diffusion length given by δ. Because δ is arbitrarily small at high enough frequencies, the walls of the pores appear to be flat at the scale of δ and the solution of Equation (3.13) for this situation is (Landau and Lifshitz, 1959)

$$\vec{\mathbf{u}}(\vec{\mathbf{r}}) = \vec{\mathbf{u}}_0(\vec{\mathbf{r}}_w)(1 - e^{iqy}) \ , \tag{3.14}$$

where y is a local coordinate measured from the pore wall at position $\vec{\mathbf{r}}_w$ into the bulk of the pore and $q = (i\omega\rho_0/\mu)^{1/2}$ is the viscous shear wavenumber. The velocity is zero at the pore walls and equal to $\vec{\mathbf{u}}_0$ outside the viscous boundary layer. Substituting Equation (3.14) into Equation (3.11), we get

$$\dot{E}_{mech} = -\frac{1}{2V}\left(\frac{1}{2}\mu\rho_0\omega\right)^{1/2}\int_{A_w} |\mathbf{u}_0(\vec{\mathbf{r}}_w)|^2 dA \ , \tag{3.15}$$

where A_w is the boundary walls of the surfaces. In the above expression, we have neglected the volume integral in the bulk of pores, which is small compared to the above expression at high frequencies (Johnson *et al.*, 1987). Using Equations (3.15) and (3.9), we obtain $k_i(\omega)$ as

$$\lim_{\omega\to\infty} k_i(\omega) = \left(\frac{1}{2}\frac{\omega\mu}{\rho_0\tau}\right)^{1/2}\frac{1}{v_f}\frac{2}{\Lambda} \ , \tag{3.16}$$

where the parameter Λ is given by

$$\frac{2}{\Lambda} = \frac{\int_{A_w} |\mathbf{u_0}(\vec{\mathbf{r}}_w)|^2 dA}{\int_V |\mathbf{u_0}(\vec{\mathbf{r}})|^2 dV} \quad . \tag{3.17}$$

Because $2/\Lambda$ is essentially the surface-pore-volume ratio of the pore-solid interface, Λ has the dimension of length and is used as a measure of the characteristic size of the pores. If we model the porous solid as a set of non-intersecting tubes, then Λ is approximately given as (Johnson *et al.*, 1987)

$$\Lambda = \left(\frac{8\tau\kappa_0}{\phi}\right)^{1/2} \quad . \tag{3.18}$$

In case of fracture-shaped pores, the number 8 should be replaced by 12.

Substituting the known $k_r(\omega)$ and $k_i(\omega)$ into Equations (3.7) and (3.8), we can determine the constant C in Equation (3.6) and find the high frequency limit of the dynamic permeability as

$$\lim_{\omega\to\infty} \kappa(\omega) = \kappa_r(\omega) + i\kappa_i(\omega) = \frac{i\mu\phi}{\tau\rho_0\omega}\left[1 - \left(\frac{i\mu}{\rho_0\omega}\right)^{1/2}\frac{2}{\Lambda}\right] \quad . \tag{3.19}$$

To connect the low- and high-frequency limits of $k(\omega)$, Johnson *et al.* (1987) wrote $\kappa(\omega)$ as

$$\kappa(\omega) = \frac{\kappa_0}{F(\omega) - \frac{i\tau\rho_0\omega\kappa_0}{\mu\phi}} \quad . \tag{3.20}$$

The function $F(\omega)$ has the following properties:

$$F(0) = 1 \tag{3.21}$$

$$\lim_{\omega\to\infty} F(\omega) = \frac{2\kappa_0\tau}{\Lambda\phi}\left[-\frac{i\omega\rho_0}{\mu}\right]^{1/2} \tag{3.22}$$

The simplest possible model for $F(\omega)$ is (Johnson *et al.*, 1987)

$$F(\omega) = \left\{1 - i\frac{4\tau^2\kappa_0^2\rho_0\omega}{\mu\Lambda^2\phi^2}\right\}^{1/2} \quad . \tag{3.23}$$

By combining this relation with $\Lambda = \left(\frac{8\tau\kappa_0}{\phi}\right)^{1/2}$, the dynamic permeability model is finally written as

$$\kappa(\omega) = \frac{\kappa_0}{\left(1 - \frac{i}{\beta}\tau\kappa_0\rho_0\omega/\mu\phi\right)^{\frac{1}{2}} - i\frac{\tau\kappa_0\rho_0\omega}{\mu\phi}} \quad , \tag{3.24}$$

where $\beta = 2$ is for a porous media, $\beta = 3$ is for a fracture. It is worthwhile to mention that Pride *et al.* (1993) evaluated the validity of Equation (3.24) using some variable cross section flow channel models. He found that Equation (3.24) gives very good description of the frequency-dependent fluid transport, although this model (mainly the imaginary part) may slightly deviate from the numerical modeling results at low to medium frequencies when the channel-wall slopes are large.

The above dynamic permeability model can be used to provide a simple and valid description of the frequency-dependent fluid motion. With the correction for the solid compressibility, ξ, Equation (3.13) can be used to model dynamic fluid motion in a poroelastic solid. As an example, we show the comparison of the dynamic fluid wave (i.e. Biot's slow wave) phase velocity $[c(\omega) = \omega/k_r(\omega)]$ and attenuation $[1/Q = 2k_i(\omega)/k_r(\omega)]$ calculated using the simple formula $k = \sqrt{i\omega/\alpha(\omega)}$ given by Equation (3.3) and the complete Biot's poroelastic theory. Figure 3-1 shows the comparison [velocity (a), attenuation (b)] for two solids. One is a hard porous solid. The other is a soft solid. The compressional, shear velocities and densities for the two fluid saturated solids are 4 km/sec, 2.3 km/sec, 2.4 g/cm^3, and 2.3 km/sec, 1.2 km/sec, 2.1 g/cm^3, respectively. The pore fluid is water. The porosity and permeability for the hard and soft solids are 0.15, 1 Darcy and 0.25, 1 Darcy, respectively. The tortuosity τ is 3 for both cases. It can be seen that the simple model results (solid curves) agree with the full theoretical results (dashed curves) very well. The two sets of results overlap in the hard solid case. In the soft solid case, there are only some slight differences between the two sets of results. This comparison shows that the simple model, coupled with the dynamic permeability theory, captures the essence of the frequency-dependent fluid flow motion.

3.2.2 Extending dynamic permeability to heterogeneous media

In this thesis, our primary interest is in the fluid flow in heterogeneous media. However, the dynamic permeability theory is formulated assuming homogeneity of the medium. It is therefore necessary to discuss how to incorporate heterogeneity variations into the dynamic permeability theory.

In the derivation of the dynamic permeability theory, Johnson *et al.* (1987) assumed that the scale of the space occupied by the porous medium is much greater than the sizes of the pores. In the present pore fluid flow problem, the porous medium is treated as a continuum medium. For a heterogeneous medium, there are three fundamental scales: the pore scale, characteristic scale, and macroscopic scale. The lengths of these scales differ by orders of magnitude. The characteristic length scale is the scale which represents the characteristic property of a local element (volume or area) in a porous medium. For the characteristic scale, the pore scale can be regarded as a microscopic scale. A characteristic element (volume or area), although it may be an infinitesimal volume (area) at the macroscopic scale, contains a great number of pores, such that the porous medium property of this element is the average value of many pores. Therefore, the dynamic fluid flow theory, obtained assuming medium homogeneity, can be applied locally to describe the dynamic fluid transport property of the characteristic element. Thus, when we refer to the dynamic fluid flow velocity at a point in the continuum porous medium, this flow velocity is not the velocity in a particular pore channel, but is the average velocity of a large number of pores in the characteristic element. Having defined the dynamic fluid transport properties at the characteristic scale, we can describe the variations at the macroscopic scale by using a spatially varying transport property, i.e., permeability $\kappa_0(\vec{\mathbf{x}})$

$$\kappa_0 = \kappa_0(\vec{\mathbf{x}})$$

By introducing the spatially varying permeability into Equation (3.24), the dynamic

permeability becomes

$$\kappa(\omega;\vec{\mathbf{x}}) = \frac{\kappa_0(\vec{\mathbf{x}})}{\left(1-\frac{i}{\beta}\tau\kappa_0(\vec{\mathbf{x}})\rho_0\omega/\mu\phi\right)^{\frac{1}{2}} - i\frac{\tau\kappa_0(\vec{\mathbf{x}})\rho_0\omega}{\mu\phi}} \quad . \tag{3.25}$$

In this formula, we assume that the other parameters do not change with spatial positions. In fact, changing the parameter β from 2 (round pores) to 3 (fractures) will not appreciably change the value of $\kappa(\omega;\vec{\mathbf{x}})$. The parameter τ only has moderate effects on the value of $\kappa(\omega;\vec{\mathbf{x}})$ at high frequencies. The effects of β and τ will be further discussed later in Chapter 5 along with the modeling of a laboratory data set. For a porous medium, the fluid density ρ and viscousity μ can be reasonably regarded as constants throughout the medium. Only porosity ϕ is most likely to change with spatial coordinates in a heterogeneous rock. We keep it a constant for two reasons. First, the ratio κ_0/ϕ always appears together in the fluid diffusivity $\alpha(\omega)$ [see Equations (3.4) and (3.25)]. Therefore, we may include the variation of ϕ in that of permeability κ_0 for simplicity. Second, in a real rock, the possible range of porosity change is not large ($0 < \phi < 0.5$). Whereas the value of permeability may vary by orders of magnitude.

In this chapter, we will investigate the behavior of the flow field over two-dimensional (2-D) heterogeneity distributions. To model the effects of the 2-D heterogeneities on the fluid flow, we assign a 2-D distribution for the permeability κ_0, i.e.,

$$\kappa_0 = \kappa_0(x,y) \quad .$$

In this way, the dynamic permeability [Equation (3.25)] is a function of both frequency and spatial coordinates x and y. Because of the spatial variation of κ_0, flow in the heterogeneous porous medium may exhibit different characteristics at different locations. For example, in regions where κ_0 is small, the flow is dominated by Darcy's flow, whereas in regions where κ_0 is high, dynamic effects may become significant and the flow becomes a propagational wave. Because $\kappa(\omega;x,y)$, as well as $\alpha(\omega;x,y)$,

change spatially, Equation (3.3) is written as

$$\frac{\partial}{\partial x}\left[\alpha(\omega;x,y)\frac{\partial P}{\partial x}\right]+\frac{\partial}{\partial y}\left[\alpha(\omega;x,y)\frac{\partial P}{\partial y}\right]+i\omega P=0 \ . \tag{3.26}$$

This equation, together with given boundary conditions, describes the fluid pressure fields in the 2-D heterogeneous porous medium for the given frequency ω. We choose to model the dynamic flow in the frequency domain because the dynamic permeability is defined as a function of frequency. This formulation allows us to study the flow behavior over different frequency ranges.

3.3 Finite Difference Modeling

For the finite difference modeling, it is convenient to use dimensionless variables. We introduce the dimensionless permeability κ' and spatial variables x' and y' as follows:

$$\begin{aligned} \kappa_0(x,y)=\kappa_{max}\kappa'(x,y) \qquad & 0<\kappa'<1 \\ x=L_x x' \qquad & 0<x'<1 \\ y=L_y y' \qquad & 0<y'<1 \ , \end{aligned}$$

where κ_{max} is the maximum permeability over the region of interest, x' and y' are the dimensionless variables in x and y directions, respectively. For a square 2-D grid, we assume $L_x=L_y=L$. We also introduce the characteristic frequency of the model

$$\omega_0=\frac{\kappa_{max}K_f}{\phi\mu L^2} \ . \tag{3.27}$$

The dimensionless frequency Ω is defined as

$$\Omega=\frac{\omega}{\omega_0} \ . \tag{3.28}$$

Using the dimensionless variables, Equation (3.25) becomes

$$\frac{\partial}{\partial x'}\left[A(\omega;x',y')\frac{\partial P}{\partial x'}\right]+\frac{\partial}{\partial y'}\left[A(\omega;x',y')\frac{\partial P}{\partial y'}\right]+i\Omega P=0 \ , \tag{3.29}$$

where the dimensionless dynamic permeability is

$$A(\omega; x', y') = \frac{\kappa'(x', y')}{\left(1 - \frac{i}{2}\tau\kappa_{max}\kappa'(x', y')\frac{\rho_0\omega}{\mu\phi}\right)^{1/2} - i\tau\kappa_{max}\kappa'(x', y')\frac{\rho_0\omega}{\mu\phi}} \quad . \tag{3.30}$$

It is interesting to note that, because the spatial variation of $\kappa'(x', y')$ in $A(\omega; x', y')$ is coupled with the frequency ω, $A(\omega; x', y')$ may have different distributions over the 2-D grids x' and y' at different frequencies.

Forward difference solution of Equation (3.29) (which is a Helmholtz type equation) is unstable, especially for large Ω values where the dynamic effects become significant. This can be shown by analyzing 1-D Helmholtz equation

$$\frac{d^2P}{dx^2} + \lambda^2 P = 0 \quad . \tag{3.31}$$

Substituting $P = P_0 e^{i\lambda x}$ (where $x = m\Delta x$, $m = 0, 1, 2, \cdots, M$) into Equation (3.31) and using the central difference $\frac{d^2P}{dx^2} = \frac{P_{m+1} - 2P_m + P_{m-1}}{\Delta x^2}$, we have the following stability equation:

$$\sin^2\left(\frac{\lambda\Delta x}{2}\right) = \left(\frac{\lambda\Delta x}{2}\right)^2 \quad . \tag{3.32}$$

This equation holds only when $\lambda\Delta x$ is small. In Equation (3.29), however, $\lambda = \sqrt{i\Omega}$ is large when Ω is large, Equation (3.32) cannot have a solution unless Δx is exceedingly small. We therefore use an iterative procedure to solve Equation (3.29). We write Equation (3.29) as

$$\frac{\partial}{\partial x'}\left[A(\omega; x', y')\frac{\partial P}{\partial x'}\right] + \frac{\partial}{\partial y'}\left[A(\omega; x', y')\frac{\partial P}{\partial y'}\right] + i\Omega P = \frac{\partial P}{\partial t'} \quad , \tag{3.33}$$

where t' is a dimensionless time. The steady-state solution of Equation (3.33) will be the solution of Equation (3.29), and the solution of Equation (3.33) will be unconditionally stable if we solve it using the Alternating Direction Implicit (ADI) scheme (Ferziger, 1981; Appendix A). The boundary conditions are specified by assigning a no-flow condition for $y' = 0$ and $y' = 1$, i.e.,

$$\frac{\partial P'}{\partial y'} = 0 \qquad \text{at } y' = 0 \text{ and } y' = 1 \quad . \tag{3.34}$$

The pressure spectrum $P_0(\omega)$ is assigned to the $x' = 0$ boundary. At $x' = 1$, the pressure is set to zero. The detailed finite difference solution procedure for Equation (3.33) and the given boundary conditions are described in Appendix A.

3.4 Testing the Finite Difference Algorithm

As a test of the numerical algorithm, we compare the finite difference results with the results from the analytical solution for the simple 1-D case [Equation (3.31)]. For the 1-D case, if we assign $P|_{x=0} = P_0$ and $P|_{x=L} = 0$, then the solution is

$$P(\omega; x) = P_0 \frac{\sin[\lambda(L - x)]}{\sin \lambda L} \quad , \tag{3.35}$$

where λ now equals $\sqrt{\frac{i\omega\phi\mu L^2}{\kappa(\omega)K_f}}$ for the dynamic flow problem. Figure 3-2 shows the comparison between the results of the finite difference algorithm and the analytical solution [Equation (3.35)], where the amplitude, the real and imaginary parts of the pressure spectrum $P(\omega; x)$ are plotted. The parameters used in the calculations are $\kappa_0 = 1$ Darcy, $\phi = 0.2$, $K = 2.25 \times 10^9$ Pa, and $\mu = 1.14 \times 10^{-3}$ Pa s. For the finite difference scheme, the pressure along the middle line $y' = L/2$ of the 2-D model is used. The two results are in almost exact agreement (the no-flow boundary condition at $y' = 0$ and $y' = 1$ makes the 2-D solution very close to the 1-D solution). The behavior of the dynamic flow pressure *vs.* distance is also demonstrated in Figure 3-2a through 3-2c for frequency = 100 Hz, 5000 Hz, and 20000 Hz cases. At low frequencies, the pressure $\sim x$ relation is approximately a linear function. As frequency increases the pressure decreases and becomes oscillatory, showing that the flow becomes a propagational wave and decays rapidly with distance.

3.5 Results for Heterogeneous Media

In Figures 2-3 and 2-4, we showed two heterogeneous distributions generated by Gaussian (Figure 2-3) and von Kármán (Figure 2-4) correlation functions. In Figure 3-3, we show the finite difference modeling results of dynamic fluid flow for those two distributions. The von Kármán distribution has a fractal dimension of $D = 2.5$ at small wavelengths (Frankel and Clayton, 1986), thus it is much rougher than the Gaussian distribution. In spite of the roughness, the fluid pressures for the two distributions are almost the same (Figure 3-3a and 3-3b for frequency = 1000 and 30000 Hz, respectively), showing that the dynamic flow is not sensitive to the roughness of the heterogeneities as long as the wavelength is greater than the small scale roughness. This is also true for the steady-state flow and the transient flow cases (Chapter 2).

To study the behavior of the heterogeneous porous medium in conducting the dynamic flow, we compute the flow rate q_x into the medium at the $x = 0$ boundary, as

$$q_x = \frac{1}{L_y} \int_0^{L_y} \left\{ \frac{\kappa(x,y)}{\mu} \frac{\partial P}{\partial x} \right\} \Bigg|_{x=0} dy \ . \tag{3.36}$$

In the logging situation, this flow corresponds to the dynamic flow into a formation due to the pressure disturbance of the acoustic logging waves. In the effective medium approach, a heterogeneous medium having random variations is often treated as an equivalent homogeneous medium whose property (i.e. permeability in this work) is the average property of the heterogeneous medium. We have calculated the flow rate for the heterogeneous medium (generated by Gaussian correlation function) and the homogeneous medium as a function of frequency using the same parameters as used in Figure 3-2. In Figure 3-4, we plot the ratio q_{hete}/q_{homo} *vs.* frequency for different correlation lengths (a = 3, 5, and 10, the model length is 64). Here q is the amplitude of the complex flow rate of Equation (3.36). If the behavior of the heterogeneous medium is the same as that of the equivalent homogeneous medium, the ratio q_{hete}/q_{homo} would plot as a horizontal line of height 1. However, this ra-

tio demonstrates a strong frequency-dependent behavior. At very low frequencies, q_{hete}/q_{homo} is always less than 1. As frequency increases, this ratio increases to reach a maximum. At very high frequencies, this ratio approaches a constant. The maximum lies within the transition region between the quasi-static and dynamic regimes and reflects the complexity of dynamic flow in heterogeneous media. The variation of q_{hete}/q_{homo} is also a function of the scale of the heterogeneities. This scale is governed by the correlation length a of the medium. As a increases the range of variation also increases. For example, the curve in Figure 3-4 for $a = 10$ case varies by more than 30% from zero frequency to the maximum, while for $a = 3$, this range is reduced to about 10%. It can be concluded that when the correlation length is very small, the heterogeneous medium will behave like an equivalent homogeneous medium.

The above results may be relevant to Stoneley wave logging in a heterogeneous formation. For an average permeability of 1 Darcy, the maximum of the flow ratio is around 5 kHz, within the frequency of Stoneley wave measurements. In addition, the borehole diameter is generally on the order of 0.2 m and is in many cases comparable to the scale of formation heterogeneities. When the q_{hete}/q_{homo} maximum lies within the frequency range of measurements, more flow will be conducted into a heterogeneous formation than into a homogeneous formation. It is therefore expected that the Stoneley wave propagation in the heterogeneous formation may experience more attenuation than in the homogeneous formation. These effects will be studied in detail in Chapters 4 and 5.

3.6 Dynamic Fluid Flow Through a Single Fracture with Rough Surfaces

We now apply the finite difference formulation for heterogeneous media to study the dynamic flow in a single fracture with rough surfaces. The roughness of a natural rock

surface has power spectra of the form $G(\Lambda) \sim \left(\frac{2\pi}{\Lambda}\right)^{-(7-2D)}$ (Brown, 1987), where Λ is the wavelength, and D is the fractal dimension of the surface and falls in the range $2.0 \leq D \leq 2.5$. For this thesis work, the fractal model is assumed to adequately describe the character of rock fractal surfaces. To form a fracture, two surfaces with the same fractal dimension of $D = 2.5$, but generated with different sets of random numbers were placed together (with one of them flipped over) at some fixed distance d_m between the mean planes of the two surfaces. Figure 3-5 shows the two surfaces. The local distance between the two surfaces gives the aperture distribution $d(x, y)$. The model surfaces are generated using Gaussian random distribution with a standard deviation σ and a von Kármán correlation function having a fractal dimension $D = 2.5$ (see Chapter 2). When $d_m = 4.24\sigma$, the two surfaces begin to contact each other. At the "contact", the local aperture $d(x, y)$ is set to zero assuming that the deformation of the contact are ignored (Brown, 1987). Figure 3-6 shows examples of the local aperture distribution generated with the two surfaces of Figure 3-5 at various d_m values [(a) $d_m = 10\sigma$ and (b) $d_m = 1\sigma$]. For a rough-wall fracture, a measure of aperture in terms of fluid flow is the mean aperture defined as (Brown, 1987)

$$\bar{d} = \frac{1}{L_x L_y} \int_0^{L_x} \int_0^{L_y} d(x, y) dx dy \quad . \tag{3.37}$$

The mean aperture represents the aperture available to the flow.

If we assume that $d(x, y)$ varies slowly in the plane of the fracture and that the permeability for a parallel plane fracture holds locally, we then have

$$\kappa_0(x, y) = \frac{d^2(x, y)}{12} \quad . \tag{3.38}$$

Equation (3.38) gives the static (zero-frequency) permeability distribution over the fracture plane. Applying the dynamic permeability locally, we have

$$\kappa(\omega; x, y) = \frac{d^2(x, y)/12}{[1 - i\omega\rho_0 d^2(x, y)/36\mu]^{1/2} - i\omega\rho_0 d^2(x, y)/12\mu} \quad . \tag{3.39}$$

where we have used $\tau = 1$ [straight flow at (x, y)] and $\phi = 1$ (aperture filled with fluid) in Equation (3.25). Tang *et al.* (1991b) showed that Equation (3.39) agrees

almost exactly with the theory of dynamic conductivity derived for a parallel-wall fracture. With the dynamic permeability distribution specified for each (x, y) using Equation (3.39), the finite difference technique of the previous section is applied to calculate the dynamic fluid flow over the 2-D grids for various frequencies and separations d_m/σ. The results are presented in the following.

For dynamic fluid flow through a rough-walled fracture, the measurable quantity is the average flow rate per unit fracture length into the fracture opening:

$$\bar{q} = \frac{1}{L_y} \int_0^{L_y} \left\{ d(x,y) \frac{\kappa(\omega; x, y)}{\mu} \frac{\partial P}{\partial x} \right\} \Big|_{x=0} dy \ , \tag{3.40}$$

where $\kappa(\omega; x, y)|_{x=0}$ is the fracture dynamic permeability of Equation (3.39) evaluated at $x = 0$. In the borehole situation, the average flow rate $\bar{q}$ represents the dynamic flow into a borehole fracture due to the acoustic wave excitation in the borehole.

For the finite difference modeling, we set $L_x = L_y = L = 0.2$m, the standard deviation $\sigma \approx 1.6\mu$m. The flow field through the fracture is computed at increasing frequency with d_m/σ equal to various values. As pointed out earlier, whether the flow motion in the fracture is steady or dynamic depends on whether the viscous skin depth $\delta = \sqrt{\frac{2\mu}{\rho\omega}}$ is large compared to the fracture aperture $\bar{d}$ (Johnson *et al.*, 1987). For water ($\mu = 1.14 \times 10^{-3}$ Pa s), δ is 19.05 μm at 1000 Hz and 3.48 μm at 30000 Hz. The two surfaces will begin to contact at about $4.26\sigma = 6.8$ μm. Comparing these numbers, we see that by varying d_m/σ and frequency, fluid flow in a rough-walled fracture can be simulated for both quasi-static and dynamic regimes. For each simulated pressure field, the pressure gradient at $x = 0$ is calculated and used in Equation (3.40) to compute the flow rate. For comparison with the parallel plate model, we compute the dynamic flow rate into a plane fracture using the dynamic fracture conductivity $\bar{c}(\omega; \bar{d})$ (Tang and Cheng, 1989)

$$\vec{\mathbf{q}} = \bar{c}(\omega; \bar{d}) \nabla P \ . \tag{3.41}$$

Assuming 1-D flow field along a fracture of length L, the pressure in the fracture

is given in Equation (3.35). We then have

$$\frac{\partial P}{\partial x}|_{x=0} = P_0(\omega)\lambda\frac{\cos\lambda L}{\sin\lambda L} \quad . \tag{3.42}$$

In addition, the dynamic conductivity in Equation (3.41) is calculated using Equation (6.12) of Tang and Cheng (1989) with $\bar{d}$ of Equation (3.37) as the aperture of the equivalent plane fracture.

Before we compare the results *vs.* frequency, we show the zero-frequency results calculated using the iterative finite difference algorithm. The results are shown as q_{rough}/q_{plane} *vs.* d_m/σ in Figure 3-7, where q_{rough} is the calculated rough-walled flow rate and q_{plane} is the cubic law flow rate calculated using Equations (3.41) and (3.42) with $\omega = 0$, and with the plane fracture thickness equal to $\bar{d}$ of the rough-walled fracture. The ratio of the mean plane separation d_m over standard deviation of the roughness is the standardized separation between the mean planes of the two fracture surfaces. As shown in Figure 3-7, for small separations, q_{rough} is significantly reduced compared with q_{plane} because of the contacting of the rough surfaces. As d_m/σ increases to 10, q_{rough}/q_{plane} approaches 1. The overall behavior of q_{rough}/q_{plane} agrees with the results calculated by Brown (1987) for the steady flow case.

Next, we compare the results for $d_m/\sigma = 1$, 3, 6, and 10 and for frequencies ranging from 0 to 30000 Hz. Figure 3-8 shows the calculated rough-walled fracture flow rate q_{rough} (solid dots) and the parallel plane fracture flow rate q_{plane} (dashed curves) calculated using Equation (3.41) and (3.42) with the plane fracture aperture equal to $\bar{d}$. As seen from Figure 3-8, the flow rate shows strong frequency dependence (or dynamic effects). The rough-walled fracture flow rate is smaller than that of the equivalent plane fracture. This difference demonstrates that the effects of the fracture surface roughness is to reduce the fluid flow in static as well as dynamic regimes. In the high-frequency dynamic regime, the ratio q_{rough}/q_{plane} increases to approach 1 as the fracture aperture increases. For example, at 30000 Hz, the ratios for $d_m/\sigma = 1$, 3, 6, and 10 are 0.66, 0.68, 0.82, and 0.92, respectively. The high-frequency results are analogous to the results of electrical current through a fracture

modeled by Brown (1989), because in both cases the local fracture conductivities of both the high-frequency fluid flow and electrical current are linearly proportional to the local aperture (see Brown, 1989; Tang and Cheng, 1989).

3.7 Conclusions

In this chapter, we modified the dynamic permeability theory by introducing the medium heterogeneity in the formulation. We have developed a finite difference algorithm for simulating dynamic fluid flow in the frequency domain for an arbitrarily heterogeneous porous medium. A heterogeneous medium behaves differently from a homogeneous medium, especially at low to medium frequencies. At medium frequencies, the heterogeneous medium conducts more flow than the homogeneous one, depending on the scale of the heterogeneities. In the logging situation, since the formation may contain various heterogeneities, the heterogeneous flow behavior may cause some discrepancy between the field observation and the theoretical prediction from Biot's theory for a homogeneous medium.

Applying the finite difference technique to study the dynamic fluid flow through a single fracture with rough surfaces, we have demonstrated the effects of surface roughness on the dynamic flow. For dynamic as well as steady flow cases, the surface roughness reduces the amount of fluid flow through the fracture in the static and dynamic regimes. When the separation between the two fracture surfaces is about 10 times that of the standard deviation of the roughness, the behavior of the rough-wall fracture approaches that of a parallel plane fracture.

The finite difference technique developed here can find useful applications in the study of Stoneley wave propagation in a heterogeneous porous formation. For example, by developing the frequency-dependent finite difference algorithm in cylindrical coordinates, we can study the propagation of borehole Stoneley waves in relation to

the dynamic fluid flow into a heterogeneous porous formation. We can also model the Stoneley wave reflection and transmission across a natural fracture zone having a heterogeneous permeability distribution. This will be discussed in detail in the following two chapters.

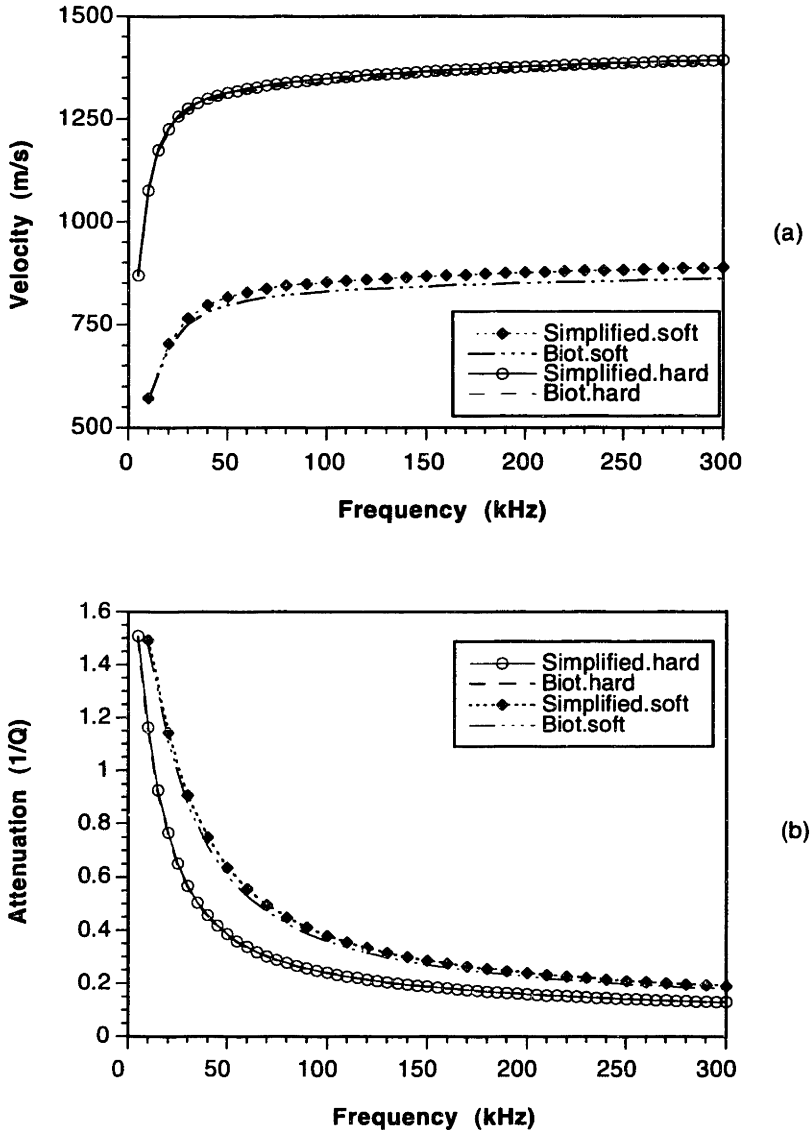

Figure 3-1: Comparison of the simple model and Biot's model results for a hard and soft porous solid, (a) phase velocity and (b) attenuation. The two model results agree almost exactly in the hard solid case and differ only slightly in the soft solid case.

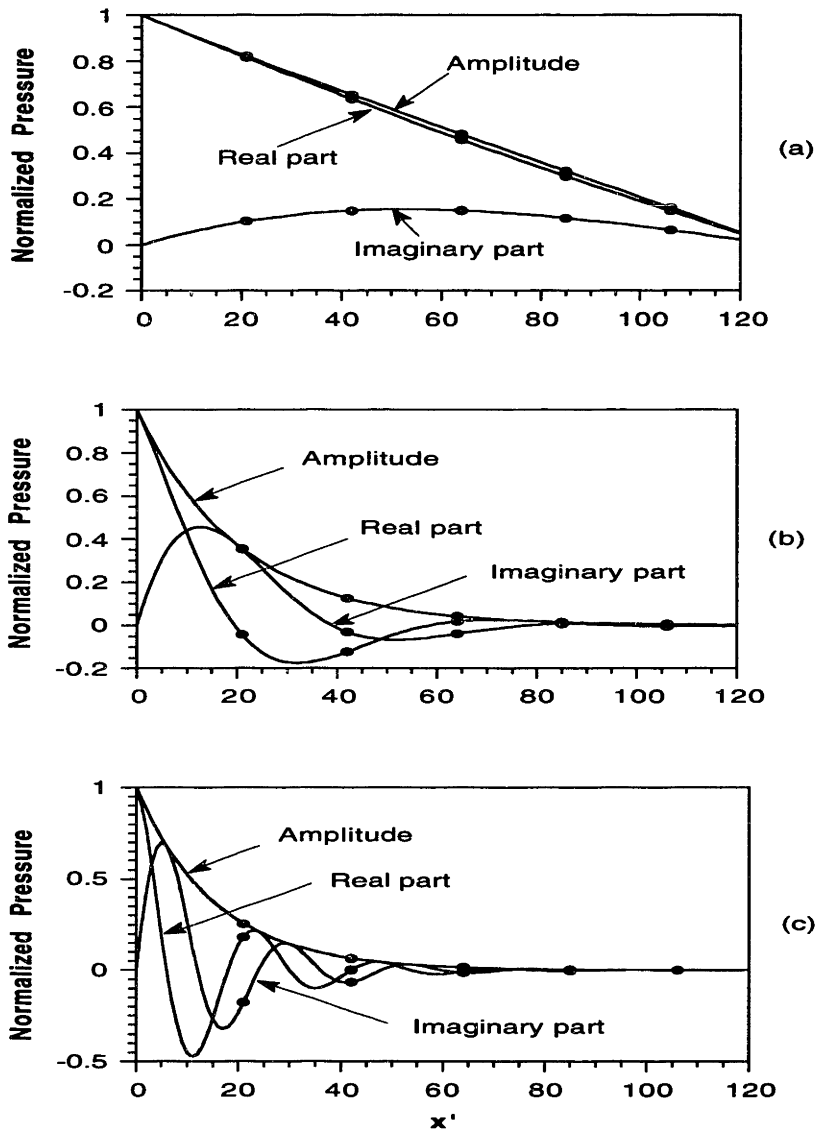

Figure 3-2: Comparison of finite difference pressure decay curves along model length x' (dashed curves with dots) with 1-D analytical results (solid curves) for a homogeneous distribution at various frequencies. The frequencies are (a) 100 Hz, (b) 5000 Hz, and (c) 20 kHz.

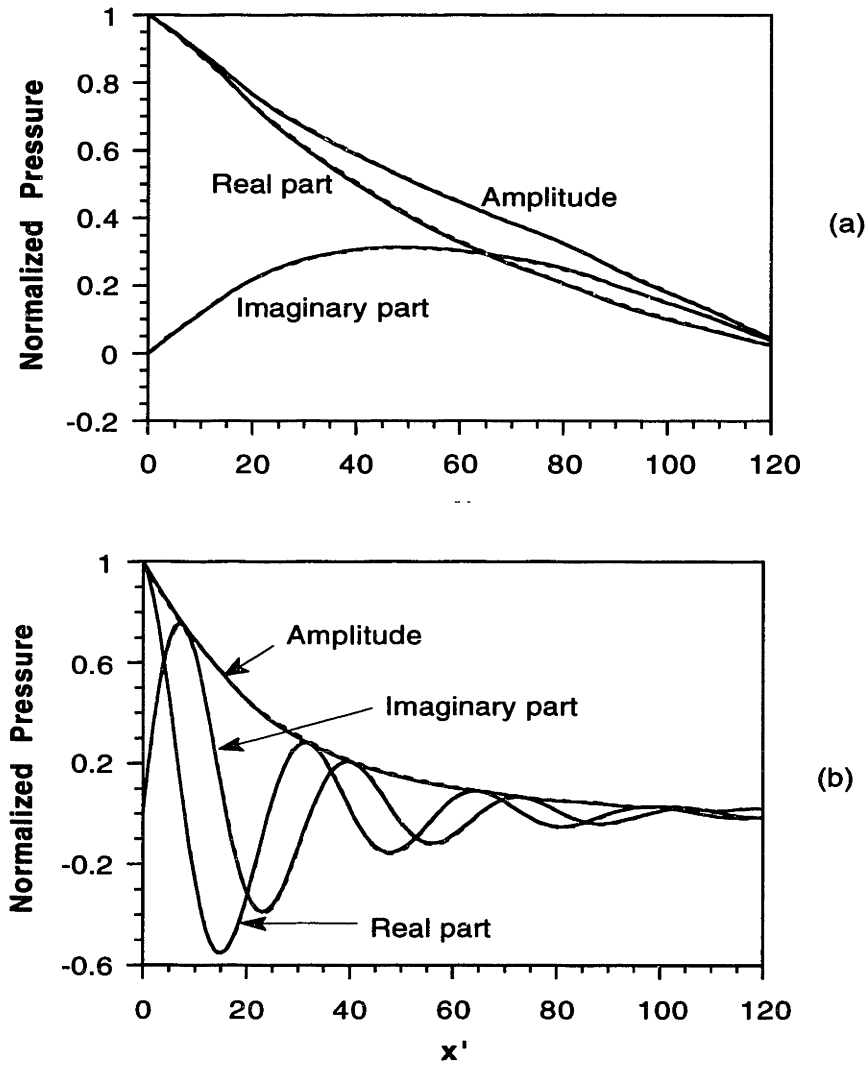

Figure 3-3: Pressure decay curves for Gaussian (solid curves) and von Kármán (dashed curves) distributions showing in Figure 2-3 and 2-4 at (a) 1 kHz and (b) 30 kHz, respectively.

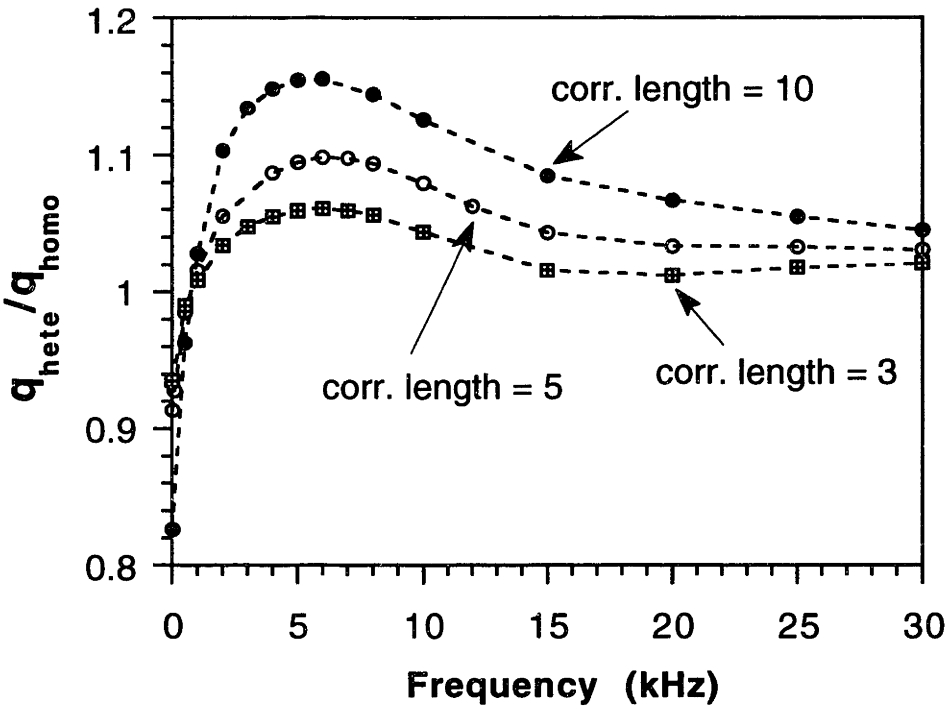

Figure 3-4: Fluid flow ratios through a heterogeneous and homogeneous medium as functions of frequency.

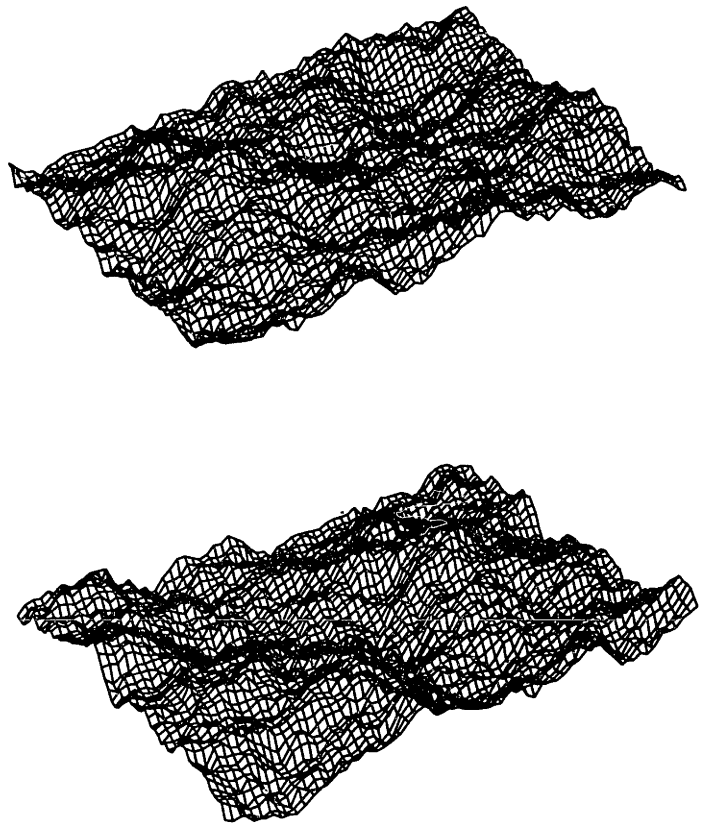

Figure 3-5: Rough surfaces representing the fracture walls. A fracture is formed by placing the two surfaces together (with one of them flipped over).

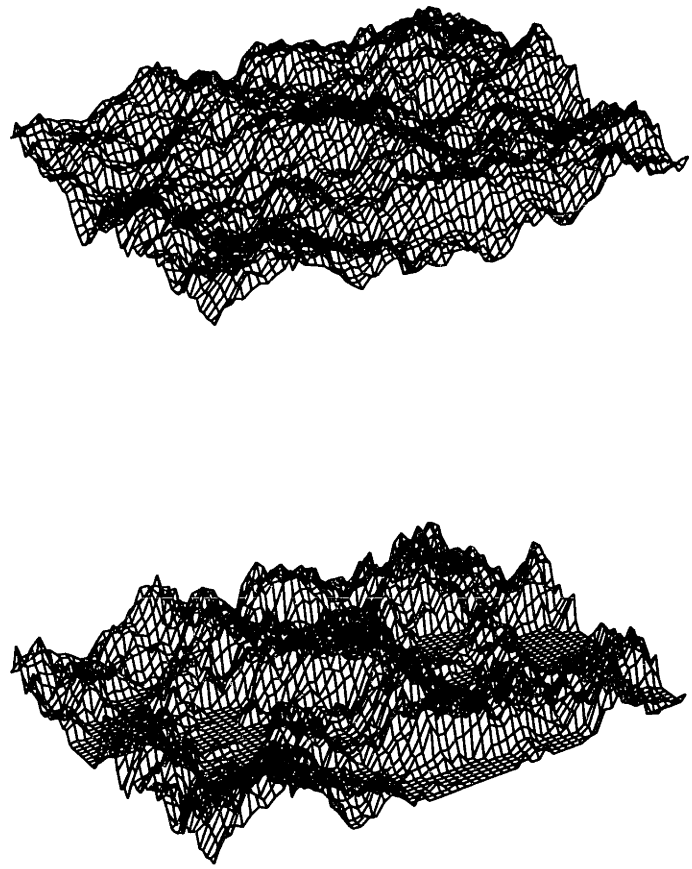

Figure 3-6: Examples of local aperture distribution formed using the two rough surfaces in Figure 3-5 with $d_m/\sigma = 10$ (a) and 1 (b).

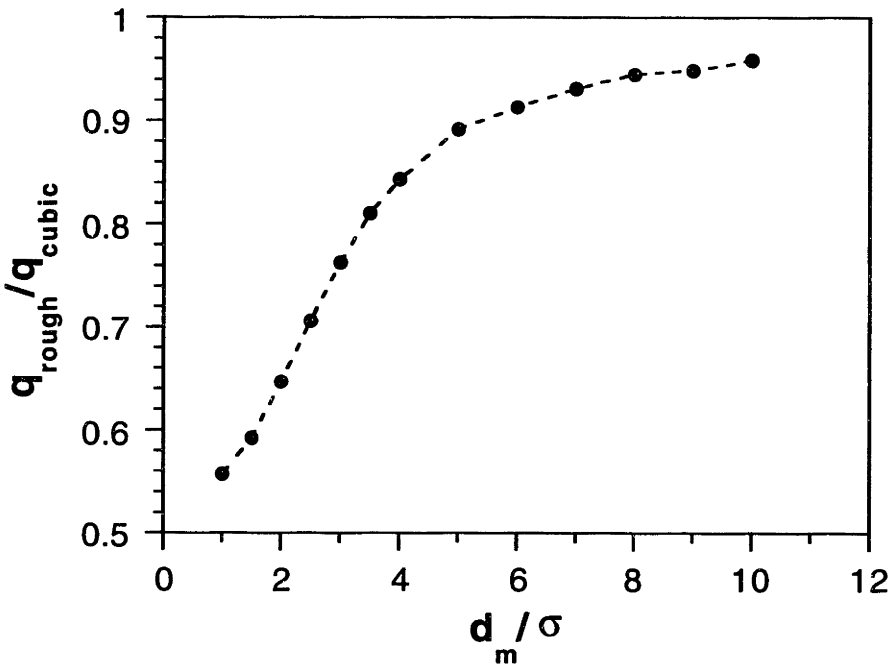

Figure 3-7: Comparison of fluid flow through a rough-walled fracture and a parallel plane wall fracture at zero frequency.

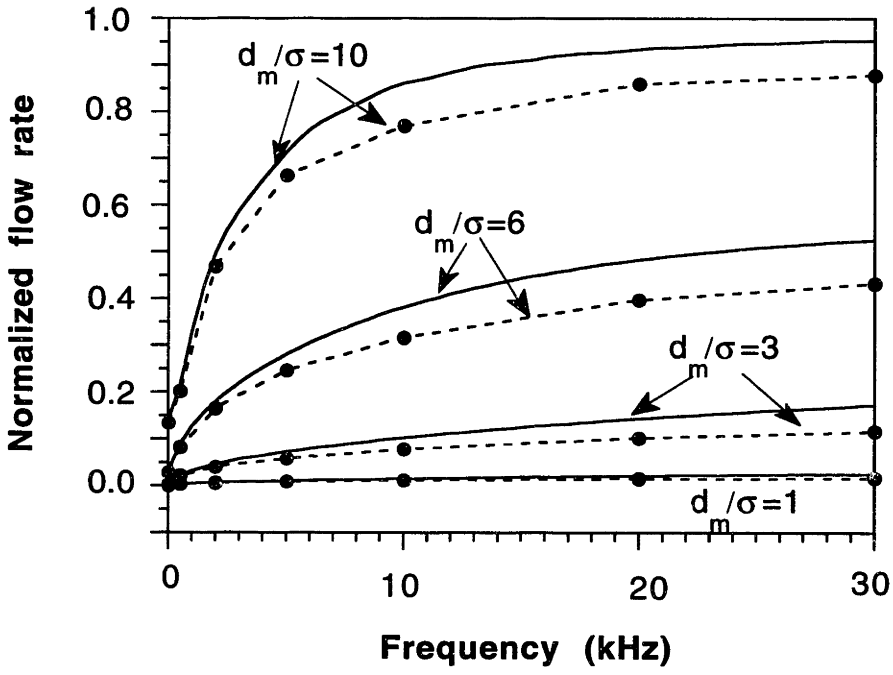

Figure 3-8: Fluid flow rate (scaled) *vs.* frequency for rough-walled (dashed curves with dots) and plane (solid curves) fractures at various standard separations (d_m/σ).

Chapter 4

Stoneley Wave Propagation in Heterogeneous Permeable Porous Formations

4.1 Introduction

Stoneley waves in open boreholes are sensitive to formation permeability. Intensive research has been carried out to study the effects of permeability on Stoneley waves (Rosenbaum, 1974; Schmitt *et al.*, 1988; Cheng *et al.*, 1987; Chang *et al.*, 1988; Tang *et al.*, 1991b). In most of the previous studies, permeability distribution in the formation was assumed homogeneous. In many situations, however, permeability changes in the formation. For example, the damaged borehole wall due to drilling results in higher permeability of the immediate surrounding formation than the virgin formation. Schmitt (1989) studied the effects of a damaged zone, where the permeability is moderately different from that of the virgin formation. Mud filtration into the formation may also change the formation flow property along the radial direction. The random variation of the porous formation is also an example of heterogeneous permeability. Because of the heterogeneous formation flow properties, the propa-

gation of borehole Stoneley waves will be modified compared to the homogeneous case. Therefore, the study of Stoneley wave propagation in the presence of heterogeneous formation permeability will illustrate the influence of the heterogeneities on the Stoneley wave propagation data and help develop methods for characterizing these heterogeneities.

The effective technique to handle medium heterogeneities is the finite difference method. However, the application of this technique with Biot's poro-elastic theory (Biot, 1956a, b) to model acoustic wave propagation in porous boreholes is still a topic of research. The difficulty lies in the coupling of the pore fluid motion (i.e. the Biot's slow wave) with the motion of the elastic solid and the strong dispersive nature of the slow wave. Two recent developments have made it possible to model the effects of formation permeability heterogeneities on borehole Stoneley wave propagation. One such development is the theory of dynamic permeability (Johnson *et al.*, 1987), which provides a simple way to calculate the frequency-dependent (or dynamic) fluid transport property of the slow wave. In Chapter 3, we have shown that the theory can be modified to describe the slow wave behavior in heterogeneous media by introducing a spatially-variable dynamic permeability. The second development is the simplified Biot-Rosenbaum model for Stoneley wave propagation in porous boreholes (Tang *et al.*, 1991b). In this simplified model, the interaction of the borehole Stoneley wave with the porous formation is decomposed into two parts. One is the interaction with the motion of the formation elastic solid (equivalent elastic formation) and the other is with the pore fluid flow. The advantage of this decomposition is that, given the solution of the elastic problem, one can solve the pore fluid flow problem for the heterogeneous porous formation independent of the elastic problem. The combination of the two situations will give the solution for Stoneley wave propagation in the formation with heterogeneous permeability.

The behavior of dynamic fluid flow in heterogeneous porous media has been modeled in Chapter 3 for the Cartesian coordinates. Because of the dispersive nature of

the fluid motion, an iterative finite difference technique was developed to compute the flow field in the frequency domain. For the present borehole geometry, we need to solve the dynamic fluid flow problem for the cylindrical coordinate system. The iterative finite difference technique for the cylindrical system will be developed in this chapter. With this technique, the borehole Stoneley wave propagation in the presence of various formation permeability heterogeneities will be studied.

4.2 Theory of Stoneley Wave Propagation in Permeable Boreholes

In this section, we review the simplified model for Stoneley wave propagation in porous boreholes (Tang *et al.*, 1991b) in order to show how we can incorporate the dynamic fluid flow in a heterogeneous formation into this theory. As a result, we can compute the effects of heterogeneity on Stoneley wave propagation.

Consider a cylindrical borehole volume ΔV of height L and radius R surrounded by a permeable porous formation. To study the wave motion in $\Delta V = \pi R^2 L$, we apply the equation of mass conservation for a small amplitude wave motion (Tang and Cheng, 1989)

$$-\oint_S \vec{\mathbf{v}} \cdot \vec{\mathbf{n}} ds = \frac{i\omega}{\rho_f v_f^2} \int_{\Delta V} -P dV \quad , \tag{4.1}$$

where ρ_f is fluid density and v_f is acoustic speed of fluid , P is fluid pressure, $\vec{\mathbf{v}}$ is the fluid particle velocity, *i.e.*, $\vec{\mathbf{v}} = -i\omega\vec{\mathbf{U}}$, where $\vec{\mathbf{U}}$ is fluid displacement, ω is angular frequency, S is the surface enclosing ΔV. The normal $\vec{\mathbf{n}}$ to S is directed outwards from ΔV. The physical meaning of this equation is that the net fluid flow into ΔV equals the dynamic compression of the fluid volume. For the cylindrical volume ΔV, the axial (z-direction) flux can be calculated. At $z = 0$, the flux is $i\omega U_z(0)\pi R^2$. At $z = L$, it is $-i\omega U_z(L)\pi R^2$, where U_z is the axial fluid displacement. In the radial direction, the fluid displacement includes two contributions. The first is the displacement of

an equivalent elastic formation, given by U_e. The second is the fluid flow into the permeable formation, given by U_f. The equivalent elastic formation is characterized by parameters v_p, v_s, and ρ. They are the compressional wave velocity, shear wave velocity, and density of the fluid-saturated porous rock, respectively. Using the fluid fluxes, we can write Equation (4.1) as

$$[U_z(L) - U_z(0)]\pi R^2 + [U_e + U_f]2\pi RL = -\frac{\pi R^2 L}{\rho_f v_f^2} P \quad . \tag{4.2}$$

Dividing Equation (4.2) by $\pi R^2 L$ and using

$$U_z = \frac{1}{\rho_f \omega^2} \frac{dP}{dz} \tag{4.3}$$

and the approximation

$$\frac{U_z(L) - U_z(0)}{L} \approx \frac{dU_z}{dz} \quad , \tag{4.4}$$

we obtain an 1-D Stoneley wave equation for the borehole pressure P,

$$\frac{d^2P}{dz^2} + \left[\frac{\omega^2}{v_f^2} + \frac{2\rho_f\omega^2}{R}\frac{U_e}{P} + \frac{2\rho_f\omega^2}{R}\frac{U_f}{P}\right] P = 0 \quad . \tag{4.5}$$

Equation (4.5) shows that the Stoneley wave has a wavenumber given by

$$k = \sqrt{\frac{\omega^2}{v_f^2} + \frac{2\rho_f\omega^2}{R}\frac{U_e}{P} + \frac{2\rho_f\omega^2}{R}\frac{U_f}{P}} \quad . \tag{4.6}$$

This equation indicates that the Stoneley wave propagation in a porous borehole is affected by formation elastic displacement U_e and the pore fluid flow U_f. If the borehole wall is impermeable, i.e. $U_f = 0$, then the Stoneley wavenumber becomes

$$k_e = \sqrt{\frac{\omega^2}{v_f^2} + \frac{2\rho_f\omega^2}{R}\frac{U_e}{P}} \quad . \tag{4.7}$$

This wavenumber is the Stoneley wavenumber for the equivalent elastic formation (Tang and Cheng, 1993). Specifically, k_e is computed from the following borehole dispersion equation (Cheng *et al.*, 1982)

$$\frac{I_0(fR)}{fI_1(fR)} = \frac{\rho}{\rho_0 l}\left\{\frac{2v_s lg}{\omega^2}\left[\frac{1}{gR} + \frac{2v_s^2}{c^2}\frac{K_0(gR)}{K_1(gR)}\right]\left(\frac{k_e^2}{k_s^2} - 1\right)^2 \frac{K_0(lR)}{K_1(lR)}\right\} \tag{4.8}$$

with the radial wavenumbers l, g, and f given as

$$l = \sqrt{k_e^2 - k_p^2}\,, \quad g = \sqrt{k_e^2 - k_s^2}\,, \quad f = \sqrt{k_e^2 - k_f^2}\,, \tag{4.9}$$

where, $k_p = \omega/v_p$, $k_s = \omega/v_s$, $k_f = \omega/v_f$; I_0 and I_1 are the first kind, K_0 and K_1 are the second kind modified Bessel functions of order zero and one, respectively; ρ_f and v_f are the bore fluid density and velocity, respectively. The formation compressional velocity v_p, shear velocity v_s, and density ρ are those of the saturated rock. The wavenumber k_e is found by locating the root of Equation (4.8) corresponding to the Stoneley mode for each given frequency (Cheng and Toksöz, 1981).

The objective of this chapter is: given the solution for the elastic problem, compute the formation flow U_f due to heterogeneous permeability and study its effects on the Stoneley wave propagation using the following equation

$$k = \sqrt{k_e^2 + \frac{2\rho_f\omega^2}{R}\frac{U_f}{P}}\,. \tag{4.10}$$

That is, if we can compute the flow per unit pressure U_f/P into the formation of a given permeability distribution, then we can substitute the U_f/P value and the given k_e into Equation (4.10) to obtain the Stoneley wavenumber for the heterogeneous permeability formation. From this wavenumber, the Stoneley wave attenuation (expressed as $1/Q$) and phase velocity are computed using

$$\begin{cases} 1/Q &= 2\dfrac{Im(\bar{k})}{Re(\bar{k})} \\ v_{st} &= \dfrac{\omega}{Re(\bar{k})} \end{cases}\,. \tag{4.11}$$

4.3 Dynamic Fluid Flow in Cylindrical Coordinates

In this chapter, we consider the case where the formation permeability varies in the radial and azimuthal directions. As a result, the fluid flow U_f at the borehole wall

varies azimuthally. In this case, we compute the net flow into the formation by using

$$\overline{U}_f = \frac{1}{2\pi}\int_0^{2\pi} U_f(\theta)d\theta \quad . \tag{4.12}$$

The dynamic fluid flow in heterogeneous permeability media is described by the following equation (see Chapter 3)

$$\nabla \cdot [\alpha(\omega;\vec{\mathbf{x}})\nabla p] + i\omega p = 0 \quad , \tag{4.13}$$

where p is dynamic pressure associated with pore fluid motion,

$$\alpha(\omega;\vec{\mathbf{x}}) = \frac{\kappa(\omega;\vec{\mathbf{x}})K_f}{\phi\mu(1+\xi)} \tag{4.14}$$

is dynamic pore fluid diffusivity, $\kappa(\omega;\vec{\mathbf{x}})$ = dynamic permeability, K_f = fluid incompressibility, ϕ = porosity, μ = fluid viscosity, and ξ is a correction for solid matrix compressibility (Norris, 1989). In this chapter, we neglect the effect of solid compressibility (i.e., $\xi = 0$). This effect is minor because the fluid is much more compressible than the rock. The fluid diffusivity $\alpha(\omega;\vec{\mathbf{x}})$ is a function of both frequency and the spatial position $\vec{\mathbf{x}}$. This happens if the dynamic permeability (Johnson *et al.*, 1987)

$$\kappa(\omega;\vec{\mathbf{x}}) = \frac{\kappa_0(\vec{\mathbf{x}})}{\left(1 - \frac{i}{2}\tau\kappa_0(\vec{\mathbf{x}})\rho_0\omega/\mu\phi\right)^{\frac{1}{2}} - i\frac{\tau\kappa_0(\vec{\mathbf{x}})\rho_0\omega}{\mu\phi}} \tag{4.15}$$

is a function of both the frequency ω and the spatial position, while the static permeability $\kappa_0(\vec{\mathbf{x}})$ varies with $\vec{\mathbf{x}}$. In Equation (4.15), τ is tortuosity of the porous medium, ρ_0 the pore fluid density.

For the borehole configuration, the cylindrical coordinates are most convenient to use. In this chapter, we investigate a two-dimensional (2-D) case where the permeability variation is in the radial (r) and azimuthal (θ) directions, i.e.,

$$\kappa_0(\vec{\mathbf{x}}) = \kappa_0(r,\theta) \quad . \tag{4.16}$$

In the cylindrical system, Equation (4.13) becomes

$$\frac{\partial}{\partial r}\left(\alpha(r,\theta)\frac{\partial p}{\partial r}\right) + \frac{\alpha(r,\theta)}{r}\frac{\partial p}{\partial r} + \frac{1}{r^2}\frac{\partial}{\partial\theta}\left(\alpha(r,\theta)\frac{\partial p}{\partial\theta}\right) + \alpha(r,\theta)\frac{\partial^2 p}{\partial z^2} + i\omega p = 0 \quad . \tag{4.17}$$

Due to the excitation of a propagating borehole Stoneley wave e^{ikz} [(as first order perturbation, e^{ikz} can be replaced by $e^{ik_e z}$, see Tang *et al.*, (1991b)], the pore fluid pressure can be written as

$$p(r,\theta,z) = p(r,\theta)e^{ik_e z} \quad . \tag{4.18}$$

By substituting Equation (4.18) into Equation (4.17), Equation (4.17) becomes

$$\frac{\partial}{\partial r}\left(\alpha\frac{\partial p}{\partial r}\right) + \frac{\alpha}{r}\frac{\partial p}{\partial r} + \frac{\alpha}{r^2}\frac{\partial}{\partial \theta}\left(\alpha\frac{\partial p}{\partial \theta}\right) + (i\omega - \alpha k_e^2)p = 0 \quad . \tag{4.19}$$

Equation (4.19) is the 2-D partial differential equation of dynamic flow for the heterogeneous permeability distribution $\kappa_0(r,\theta)$. Because Equation (4.19) is a Helmholtz type equation, an iterative method (see Chapter 3) based on the Alternating Direction Implicit (ADI) finite difference algorithm (Ferziger, 1981; Appendix A) is used to solve the equation. The boundary conditions for the problem are

$$p(r,\theta)|_{r=R} = P \quad \text{(pressure continuity)} \tag{4.20}$$

$$p(r,\theta)|_{r=\infty} = 0 \quad \text{(radiation condition)} \quad . \tag{4.21}$$

In the numerical simulation, we need to specify two imaginary boundaries in θ direction ($\theta = 0$ and $\theta = 2\pi$) with the periodic boundary condition, as

$$p(r,\theta)|_{\theta=0} = p(r,\theta)|_{\theta=2\pi}. \tag{4.22}$$

Figure 4-1 shows the boundary conditions used in the numerical modeling. The detailed finite difference solution procedure of Equation (4.19) together with the boundary conditions [Equations (4.20), (4.21), and (4.22)] is described in Appendix B.

From the finite difference solution, we can compute the pressure distribution $p(\omega; r, \theta)$ over the (r, θ) grid. The fluid flow at the borehole wall is computed using the modified Darcy's law (Tang *et al.*, 1991b)

$$-i\omega\overline{U}_f = -\frac{1}{2\pi}\int_0^{2\pi}\left\{\frac{\kappa(\omega;r,\theta)}{\mu}\frac{dp(r,\theta)}{dr}|_{r=R}\right\}d\theta \quad , \tag{4.23}$$

where $\frac{dp(r,\theta)}{dr}$ is numerically evaluated from the calculated pressure field at the borehole wall. Because U_f is proportional to the borehole pressure P, the ratio $U_f/p|_{r=R} = U_f/P$ is independent of the magnitude of P. Substituting U_f/P into Equation (4.10), the Stoneley wavenumber can be calculated. From the wavenumber, the Stoneley wave attenuation and phase velocity can be calculated using Equations (4.11).

4.4 Numerical Simulation Results

In this section, we present the finite difference simulation results for various permeability distributions surrounding the borehole. For all the calculations below, we first calculate the elastic problem using the saturated rock properties: $v_p = 4000$ m/sec, $v_s = 2300$ m/sec, and $\rho = 2.16$ g/cm^3. The Stoneley wavenumber k_e for the equivalent elastic formation is calculated using the borehole dispersion equation [Equation (4.8)]. The borehole fluid density and velocity are $\rho_f = 1$ g/cm^3 and $v_f = 1500$ m/sec, respectively. The borehole radius is 0.1 m. For simplicity, we assume that the elastic properties for the various heterogeneous permeability distributions are the same, so that the same k_e is used for the following cases. In all the cases below, the pore fluid properties are: $K_f = 2.25$ GPa, $\rho_0 = 1$ g/cm^3, $\mu = 1.14$ cp, porosity $\phi = 0.3$, and tortuosity $\tau = 3$.

4.4.1 Homogeneous permeability – A test of the numerical algorithm

We first present the simulation result for a homogeneous permeable formation surrounding the borehole. This example, together with the existing analytical solution, offers a test of the validity and accuracy of the finite difference simulation algorithm.

For homogeneous permeability, the solution to Equation (4.19) becomes

$$p(r) = \frac{K_0(r\sqrt{-i\omega/\alpha + k_e^2})}{K_0(R\sqrt{-i\omega/\alpha + k_e^2})} \quad , \tag{4.24}$$

and the Stoneley wavenumber for the permeable formation is (Tang *et al.*, 1991b)

$$k = \sqrt{k_e^2 + \frac{2i\rho_f\omega\phi}{R\mu}\sqrt{-\frac{i\omega}{\alpha} + k_e^2}\frac{K_1(R\sqrt{-i\omega/\alpha + k_e^2})}{K_0(R\sqrt{-i\omega/\alpha + k_e^2})}} \quad , \tag{4.25}$$

where α is given by Equations (4.14) and (4.15). In Equations (4.24) and (4.25), K_0 and K_1 are the zero and first order of modified Bessel functions of the second kind. The Stoneley wave velocity and attenuation calculated using Equations (4.11) agree with the results calculated with the full Biot theory very well (Tang *et al.*, 1991b), although in this much simplified theory, the coupling between the elastic motion and the dynamic flow [i.e. the coupling between the fast (compressional and shear) waves and the slow wave] is not fully considered. This tells us that if the dynamic fluid flow in heterogeneous permeability porous media can be accurately modeled using the finite difference technique, then the effects of the heterogeneous permeability on the Stoneley wave propagation can be calculated using the simple formula given in Equation (4.10).

Figure 4-2 shows the comparison between the Stoneley wave phase velocity (a) and attenuation (b) calculated using the analytical solution [Equations (4.24 and (4.25)] and those using the finite difference method. These results are calculated for the frequency range of $0 \sim 5$ kHz, in which most Stoneley wave measurements are made. The formation permeability is 1 Darcy. For simplicity, the effects due to solid matrix compressibility are neglected [i.e. $\xi = 0$ in Equation (4.14)] when calculating both the analytical and finite difference results. The results for the two approaches agree very well. This comparison demonstrates the validity and accuracy of the finite difference technique. In the case of a heterogeneous permeability distributions where an analytical solution is difficult to find, we will rely on the finite difference method to calculate the Stoneley wave propagation.

4.4.2 Random permeability distributions

In a geological porous medium, the permeability of the medium may fluctuate from place to place. These fluctuations can be modeled by describing the medium as having a random permeability distribution. In Chapter 3, we have modeled the dynamic pore fluid flow in such a random medium. It is interesting to investigate how this random variation of formation permeability affects the borehole Stoneley wave propagation and how the random permeability heterogeneities can best be characterized using Stoneley wave measurements.

The method of generating 2-D random variations in Cartesian coordinates were described in Chapter 2. Figure 4-3 shows an example of the random permeability distribution with a borehole of 0.2 m diameter at the center. The distribution is generated with a Gaussian correlation function which has a correlation length of 0.08 m. The standard deviation of the random field is 20% of the mean value (average of the random field). It can be seen that the permeability varies significantly in the formation surrounding the borehole. It is interesting to see how this permeability fluctuation affects the Stoneley wave propagation in the borehole and how the results compare with those calculated with the constant permeability distribution.

For calculating the dynamic pore fluid flow in the cylindrical coordinates, the permeability distribution in Cartesian coordinates are mapped into cylindrical coordinates using

$$\kappa_0(x,y) \overset{x=r\cos\theta, y=r\sin\theta}{\longrightarrow} \kappa_0(r,\theta) \quad . \tag{4.26}$$

For the distribution $\kappa_0(x,y)$ in the equally-spaced grids (x,y), its mapping into the (r,θ) coordinates are distributed over a (r,θ) grid that is not equally-spaced. But our finite difference algorithm requires an equally-spaced gird. This problem is solved by interpolating the mapped values of $\kappa_0(r,\theta)$ to the finite difference grids.

Figure 4-4 shows the finite difference simulation of pore fluid presure amplitude distribution at 100 Hz together with the permeability distribution of Figure 4-3. The correlation length of this distribution is 0.08 m, and the mean permeability is 1 Darcy.

For a constant permeability distribution, the pressure contours should be circular in shape. The non-circular shape of the pressure contours in Figure 4-4 demonstrates the effects of the heterogeneous permeability. The Stoneley wave phase velocity and attenuation for the heterogeneous permeability in Figure 4-3 are shown in Figure 4-5. For the fixed correlation length and mean permeability, the calculation is performed for two fluctuation values, one is 20% (dashed curves), the other is 38% (solid - dashed curves). The results are plotted *vs.* frequency together with those calculated using a constant permeability that equals the mean value of the random permeability distribution (solid curves). Both Stoneley velocity dispersion and attenuation for the random permeability are somewhat higher than those for the constant permeability case. The 20% curves are closer to the constant permeability curve, while the 38% case shows more attenuation and dispersion than the constant permeability case. This is consistent with the result of Chapter 3 which shows that a heterogeneous formation may conduct more dynamic flow than the homogeneous formation of the same average permeability (see Figure 3-4).

The results for the heterogeneous formation do not deviate significantly from those for the homogeneous formation. This happens because the Stoneley wave tends to average out the azimuthal permeability variation [see Equation (4.23)], such that the random permeability medium behaves like a constant permeability medium. The important implication of this is that, for Stoneley waves measured in formations with randomly fluctuating permeability, the analytical solution for the constant permeability medium [Equation (4.24)] is a good description, if we regard the constant permeability κ_0 as the mean permeability of the random medium. To account for the increased attenuation and dispersion, we can interpret the medium as a homogeneous one having a slightly higher permeability than the mean permeability of the actual random medium.

4.4.3 Layered model

We discuss an interesting situation in which the permeability distribution has a plane, layered structure and the borehole axis is parallel to the layering. We may encounter this situation in a horizontal well drilled through a formation with fine horizontal layering.

We first study the case where the permeability varies smoothly across the layers. We model this by generating the random permeability distributions using flat-ellipse-shaped Gaussian correlation function, in which the correlation length in the major axis direction is much greater than that along the minor axis direction. The procedure is described in detail in Chapter 2. Figure 4-6 shows the configuration of the borehole in the smoothly varying layered media. The correlation length in the elongated direction is 0.23 m, whereas that in the direction normal to the layering is 0.05 m. The standard deviation of permeability is 38%. The mean permeability is 1 Darcy. The calculated Stoneley wave velocity and attenuation are shown in Figure 4-7 (a) and (b) (solid curves), respectively. The results calculated using the constant permeability (1 Darcy) are also plotted. As for the isotropic random-permeability distribution cases (Figure 4-5), the results for the layered permeability distribution are not very different from those of the constant permeability.

Next we study the case in which the layers have strong permeability contrast, such as the sand-shale sequences. We generate this model using a random repetition of layers with low and high permeabilities (they are 0.01 and 2 Darcy, respectively, see Chapter 2). The thicknesses of the layers obey a Poisson distribution (Kerner, 1992). Figure 4-8 shows the configuration of the borehole in the layered medium with alternating permeabilities. The calculated Stoneley wave velocity and attenuation are shown in Figure 4-9 (a) and (b) (solid curves), respectively. The results for the average permeability (1 Darcy) are also shown (dashed curves). Again, the layered model results are very similar to those for constant permeability.

The simulations for the layered permeability models show that the Stoneley wave

propagation is not sensitive to the anisotropy in the permeability distribution. This can be expected since the Stoneley wave sums the effects of pore fluid flow at a borehole wall in all azimuthal directions [see Equation (4.23)]. If the high and low permeability regions alternate around the borehole wall, as is the case for the above two examples, then the effects of the heterogeneous permeability formation affects the borehole Stoneley wave in much the same way as does a homogeneous formation having the average permeability of the heterogeneous formation.

4.4.4 Mud filtration model

In a mud-filled borehole, the filtration (or invasion) of mud into the porous formation may result in the replacement or mixing of mud with formation saturant fluid, resulting in the change of fluid flow properties in the radial direction. For example, if the viscosity of mud is different from that of the virgin saturant fluid, the fluid mobility (expressed as κ_0/μ) may decrease or increase away from the borehole, assuming that μ equals mud viscosity at the borehole wall and the formation saturant fluid viscosity far from borehole. Alternatively, this change of fluid mobility may also be modeled as change of permeability, if we fix viscosity μ as a constant and vary permeability. Therefore, we model the mud filtration effects using the variable permeability model.

We consider two simple cases as shown in Figure 4-10. One is that the permeability increases linearly from 0.1 Darcy at borehole wall ($r = R = 0.1$ m) to a value of 1 Darcy at $r = 1$ m (viscousity decreases in a radial direction, top figure in Figure 4-10). The other case is that the permeability decreases linearly from a value of 1 Darcy at the borehole wall ($r = R = 0.1$ m) to 0.1 Darcy at $r = 1$ m (viscosity increases, bottom figure in Figure 4-10). Figure 4-11 shows the modeled Stoneley wave dispersion (a) and attenuation (b) as functions of frequency. For comparison, the results for constant permeabilities 0.1 and 1 Darcy are also plotted. In general, the behaviors of the Stoneley wave velocity and attenuation for the linear permeabil-

ity model are similar to those of the constant permeability case. Because the fluid flow penetration depth is very small, the attenuation and dispersion of the variable permeability model are very close to those calculated with the constant permeability having a value equal to that of the borehole wall. For the increasing permeability (0.1 - 1) model, the results are almost the same as those calculated with the constant permeability of 0.1 Darcy. For the decreasing permeability (1 - 0.1) model, the results differ only slightly from the constant permeability (1 Darcy) model at higher frequencies. These results suggest that for permeability decreasing or increasing smoothly from the borehole, the Stoneley wave is mainly sensitive to the permeability of the immediate formation surrounding the borehole.

4.4.5 Damaged zone model

During the drilling of a borehole, the drilling process can change the physical properties of the formation close to the borehole wall. For example, due to the drilling damage, vertical micro fractures and fissures may exist at the borehole wall, resulting in the immediate surrounding formation having much higher permeability than the virgin formation. An example is illustrated in Figure 4-12. As will be shown below, this high permeability contrast produces significant effects on the Stoneley wave propagation.

The first example considered is a case in which the permeability difference between the borehole wall layer and the virgin formation is moderate. The damaged zone is modeled as a porous layer of 5 cm thick. The zone and the formation are assumed to have the same porosity and are water saturated. The permeability for the layer and the formation are 1.0 and 0.3 Darcy, respectively. Figure 4-13 shows the calculated dispersion and attenuation curves, in comparison with the results calculated for the constant permeability of 1.0 and 0.3 Darcy. At low frequencies, the velocity and attenuation are sensitive to the virgin formation permeability. Particularly for the

attenuation, the attenuation value tends to approach that calculated for the virgin permeability at very low frequencies. As frequency increases, the results approach those for the damaged zone, becoming representative of the inner layer properties. These results are similar to those obtained by Schmitt (1989) using the full Biot theory. For the case of moderate permeability contrast, the behavior of Stoneley wave propagation is not significantly different from the Stoneley wave behavior in a formation of constant permeability, except at very low frequencies.

The next two examples correspond to strong permeability contrast cases in which the inner layer permeability is very high (10 Darcy). This high permeability could result from vertical micro fractures surrounding the borehole wall, when the wall is intensely damaged. The zone thickness is assumed to be 0.11 m. The results are calculated with virgin formation permeability equal to 1 and 0.1 Darcy, respectively. Figure 4-14 shows the dispersion (a) and attenuation (b) curves for the first case (virgin permeability = 1 Darcy). For comparison, the results for the constant permeabilities (1 and 10 Darcy, respectively) are also plotted. Figure 4-15 shows the results for the second case (virgin permeability = 0.1 Darcy). The results for the two very different virgin permeability cases show similar behavior. At very low frequencies, the Stoneley wave attenuation is very close to those of the virgin formation. As frequency increases, the attenuation increases significantly, and then decreases to approach the attenuation from the inner layer, showing a well defined peak in the frequency range between $0 \sim 3$ kHz. Even more interesting, in the $0 \sim 1$ kHz frequency range, the Stoneley wave velocity is much lower than the elastic (non-permeable) results, compared to the homogeneous model results. As a result, the Stoneley velocity in this frequency range exhibits a very significant velocity decrease (around 1 kHz, this dispersion is about 20%, relative to the non-permeable case). As the frequency increases further, the velocity crosses the elastic formation velocity curve, and then approaches the velocity calculated with the inner layer permeability (the attenuation also shows the same trend), indicating that the inner layer properties control the Stoneley wave

propagation at high frequencies.

To further demonstrate the relative importance of the inner layer and virgin formation properties, we plot the dynamic pressure field as the function of radial distance for two extreme frequencies, 100 Hz and 5 kHz. Figure 4-16 shows the real and imaginary parts of the complex pressure fields for the 100 Hz (a) and 5 kHz (b) cases. For the very low frequencies, the dynamic fluid flow pressure can penetrate the inner layer to a depth of about 0.7 m into the formation [Figure 4-16 (a)]. This explains why the results at very low frequencies are sensitive to the virgin formation. At high frequencies, the dynamic flow is effective only close to the borehole wall [Figure 4-16 (b)]. This shows that the Stoneley wave propagation will primarily be controlled by the inner layer properties at high frequencies. The significant Stoneley wave velocity dispersion (velocity decrease or travel time delay) and attenuation peak in the frequency range of common Stoneley wave measurements could be easily measured. Therefore, the dispersion and attenuation characteristics could be used as a diagnostic of near borehole wall damage or fractures.

4.5 Conclusions

For the first time, the effects of various types of formation heterogeneous permeability on the borehole Stoneley waves have been investigated. The approach was based on an iterative finite difference technique developed for cylindrical coordinates. Because the dynamic fluid flow effects are most effective in the region around the borehole, the Stoneley wave samples the effective (or average) permeability of the immediate surrounding formation (see our modeling of random permeability formation). Because the Stoneley wave sums the effects of pore fluid flow in all azimuthal directions, it is not sensitive to the permeability anisotropy (or azimuthal variation of pore fluid flow in the formation). This has been evidenced by our modeling of Stoneley wave

propagation in layered porous media. In most cases, the behavior of Stoneley waves in a variable permeability formation is very similar to their behavior in a homogeneous permeability formation. This demonstrates that the analytical solution for the homogeneous permeability formation [Equation (4.24)] provides a very useful method for calculating the effective permeability of the heterogeneous formation surrounding the borehole, although the calculated permeability may be (slightly or moderately) higher than the average permeability of the formation depending on the degree of variation of the heterogeneity (see Figure 4-5).

The most likely case in which the formation permeability heterogeneities will have significant effects on the Stoneley wave propagation is the damaged zone case where the damaged borehole wall has much higher permeability than the virgin formation due to fissures or micro-fractures existing in the borehole wall. As predicted by our modeling, this damaged, highly permeable wall can be detected by the significant delay in Stoneley wave arrival (up to 20% relative to non-permeable formation) and attenuation peak in the frequency range of common Stoneley wave measurements.

Boundary Conditions:

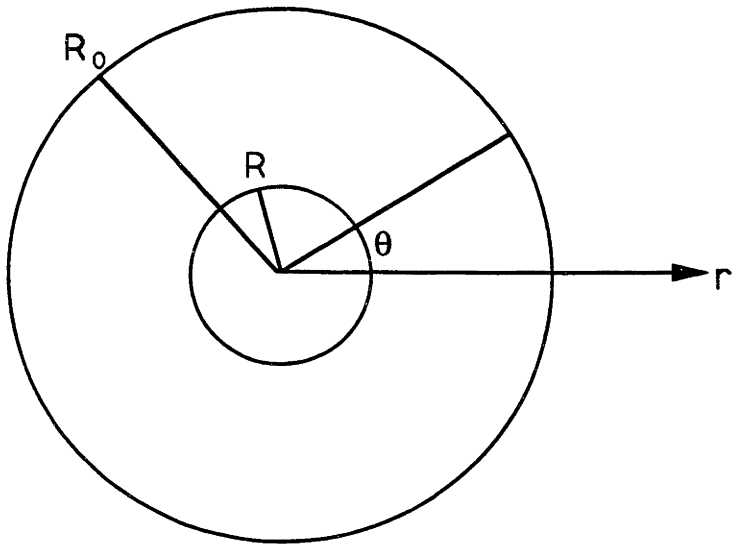

$$\begin{cases} P(R,\theta) = P_0 \\ P(R_0,\theta) = 0 \\ P(r,0) = P(r,2\pi) \end{cases}$$

Figure 4-1: Boundary conditions used in the numerical simulation.

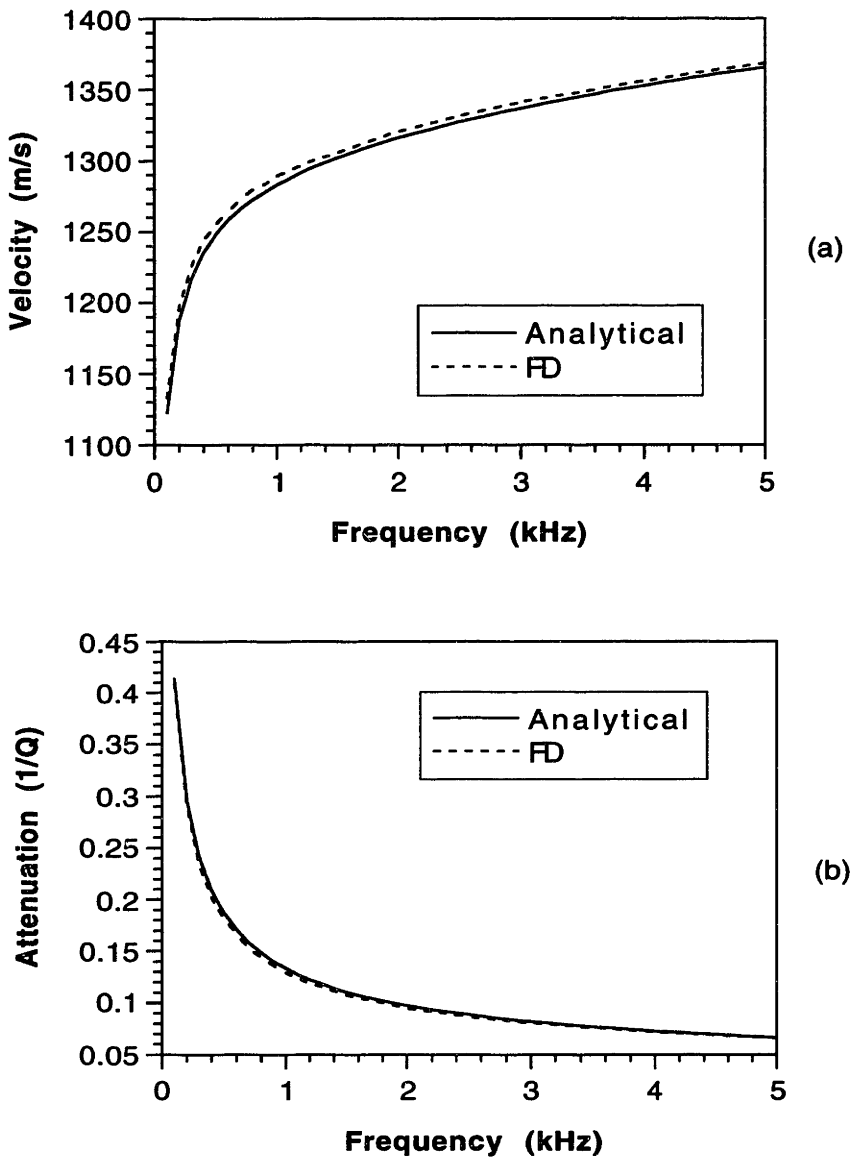

Figure 4-2: Comparison between analytical (solid curves) and finite difference (dashed curves) results: (a) Stoneley wave velocity, (b) Stoneley wave attenuation.

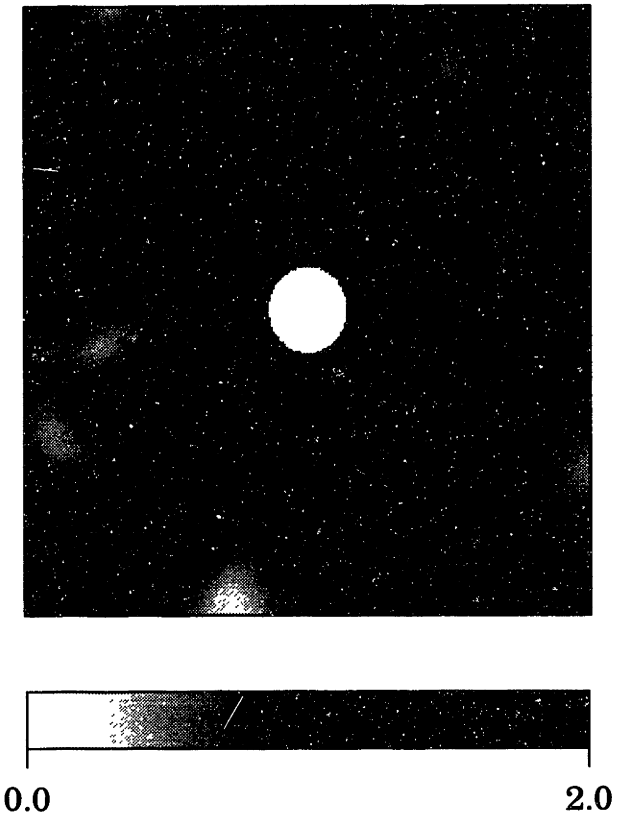

Figure 4-3: Random permeability variation around a borehole.

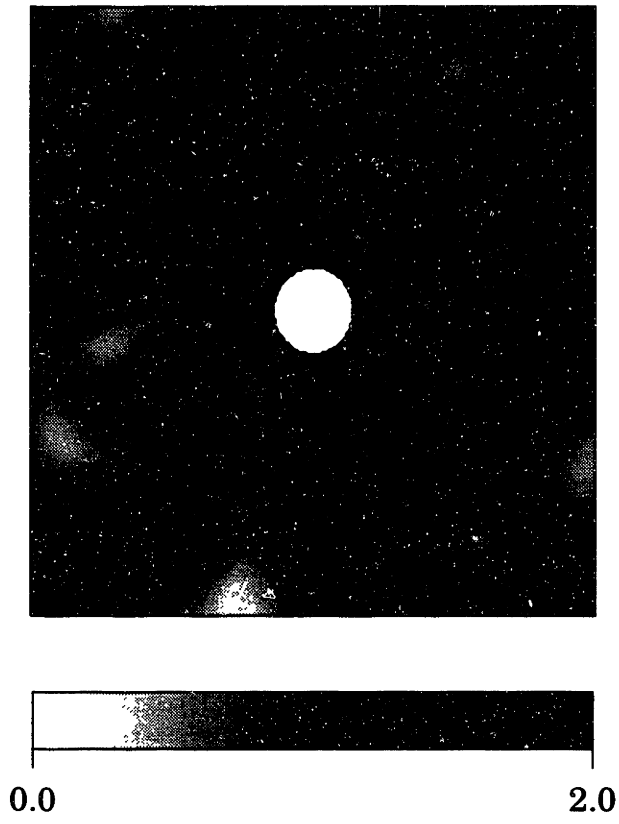

Figure 4-4: Contours of the amplitude of dynamic pore fluid pressure in the formation shown in Figure 4-3 at 100 Hz.

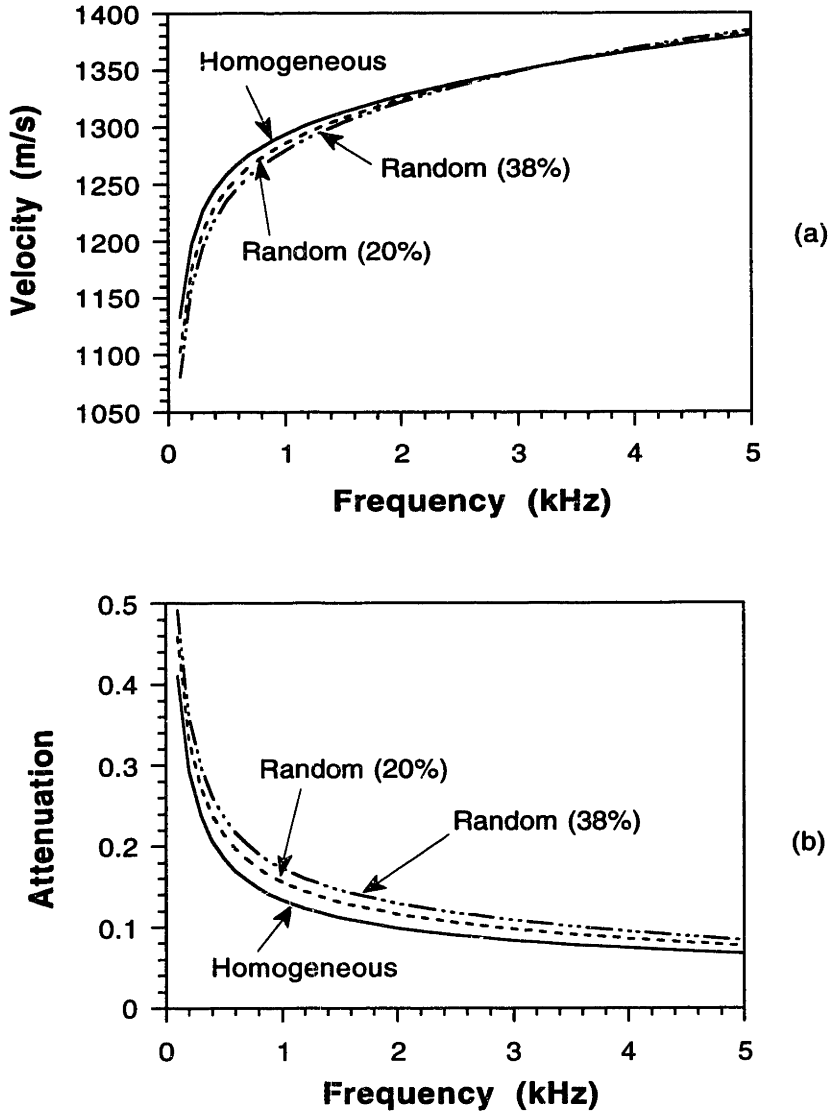

Figure 4-5: Stoneley wave velocity (a) and attenuation (b) due to the random permeability variation. For comparison, the results for the equivalent homogeneous permeability are also plotted.

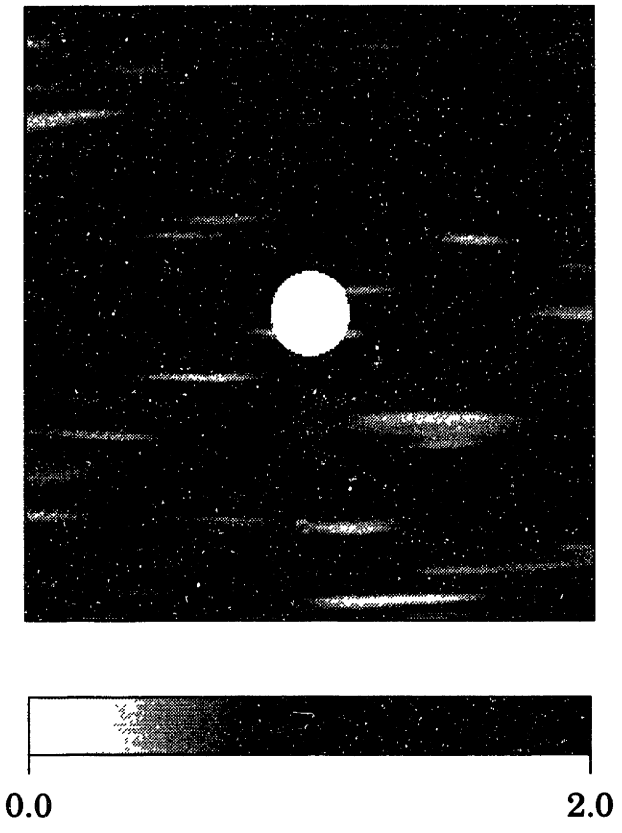

Figure 4-6: Lineated permeability distribution (anisotropy) surrounding a borehole. The lineation is smoothly varying.

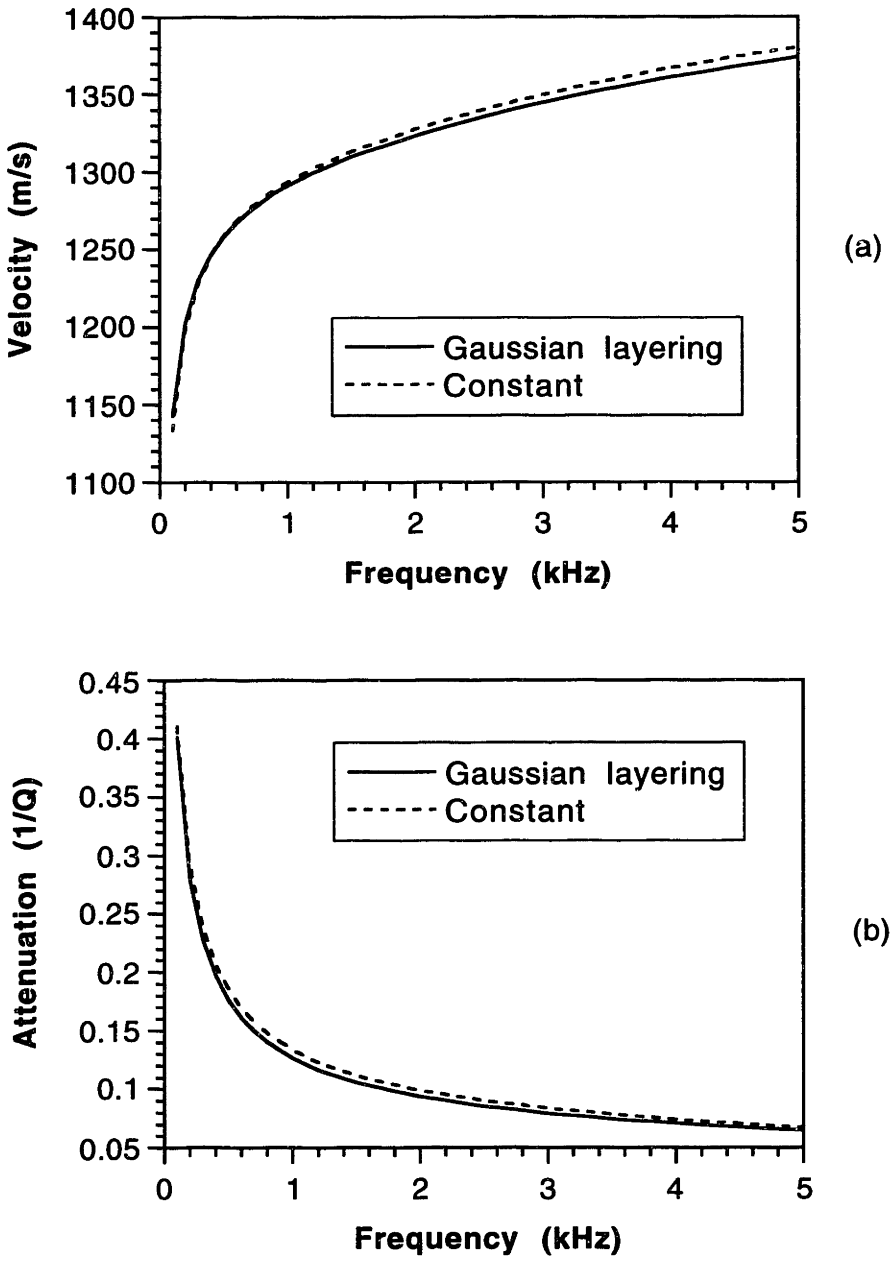

Figure 4-7: Stoneley wave velocity (a) and attenuation (b) due to the lineated permeability variation of Figure 4-6 (solid curves). The results of the equivalent constant permeability are also plotted (dashed curves).

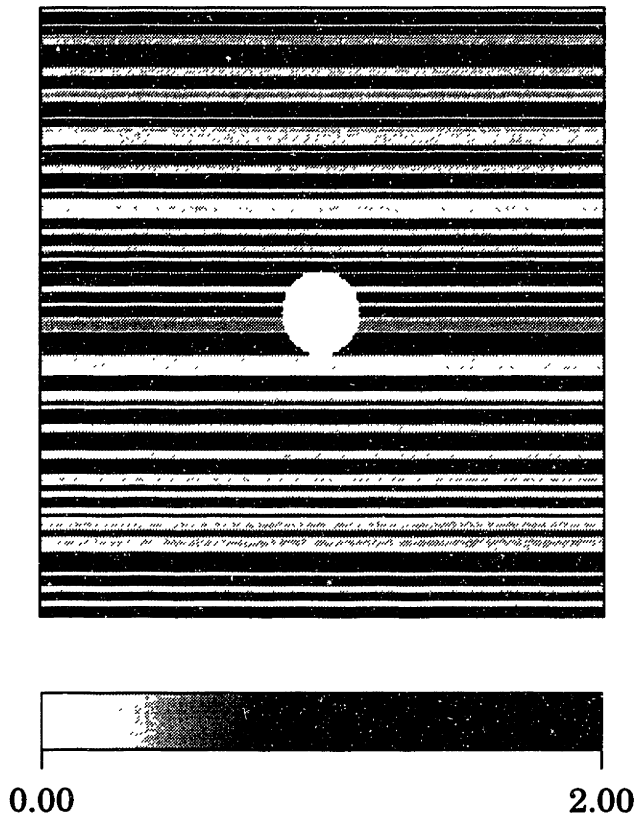

Figure 4-8: 1-D Poisson permeability distribution surrounding a borehole.

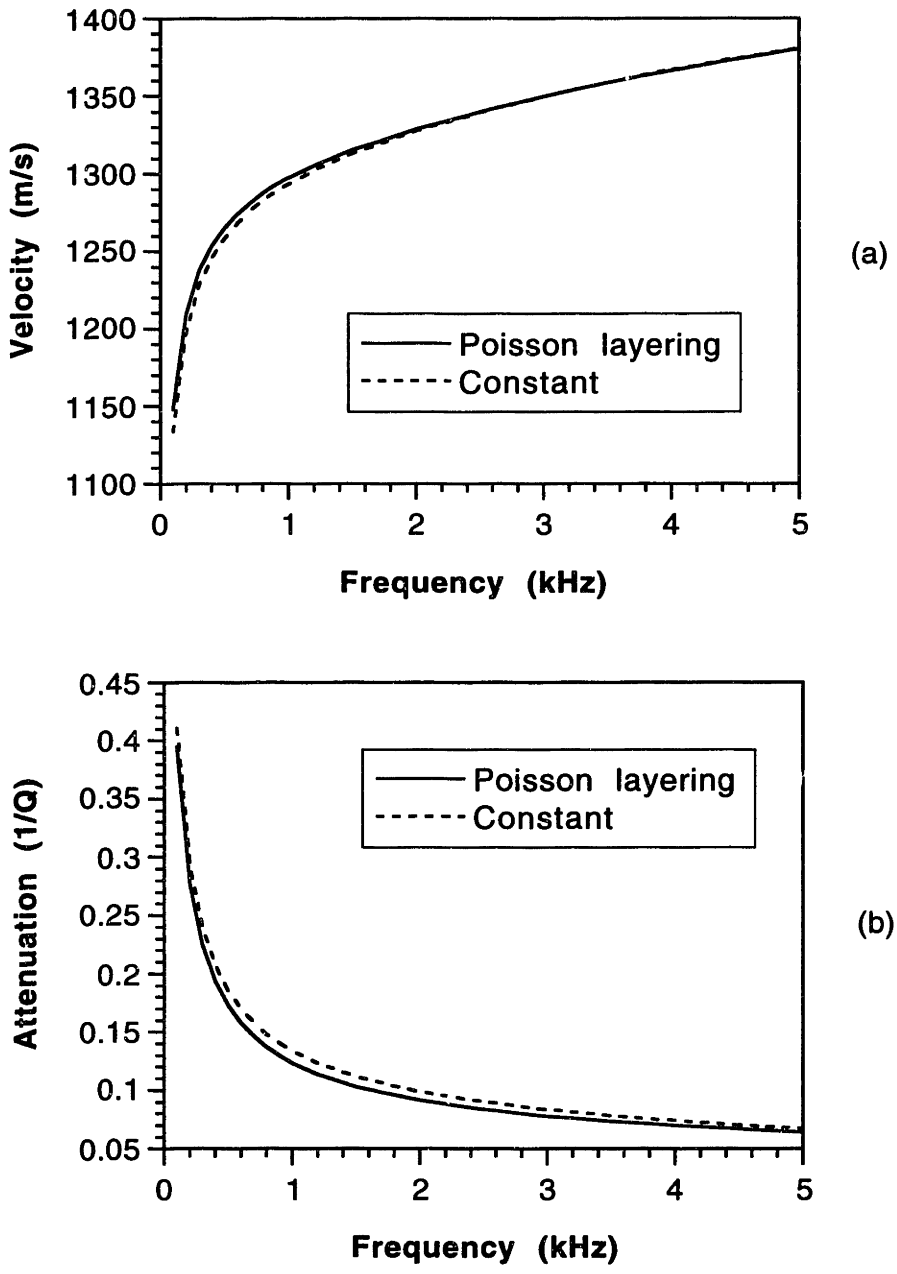

Figure 4-9: Stoneley wave velocity (a) and attenuation (b) due to the layered permeability variation of Figure 4-8 (solid curves). The results of the equivalent constant permeability are also plotted (dashed curves).

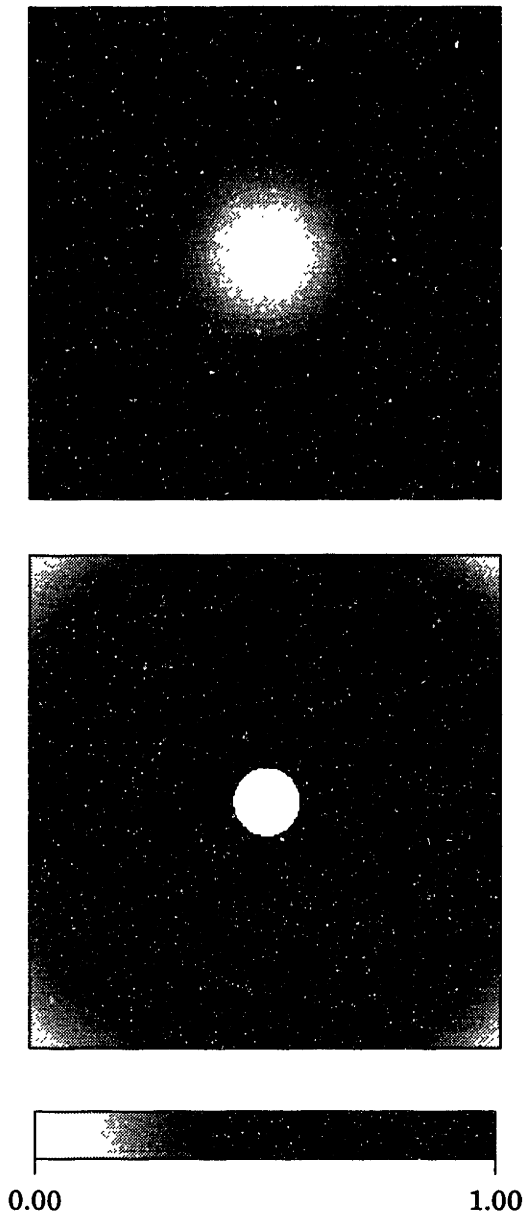

Figure 4-10: Linearly increasing (upper figure) and decreasing (lower figure) permeability models. The borehole is in the middle of the formation.

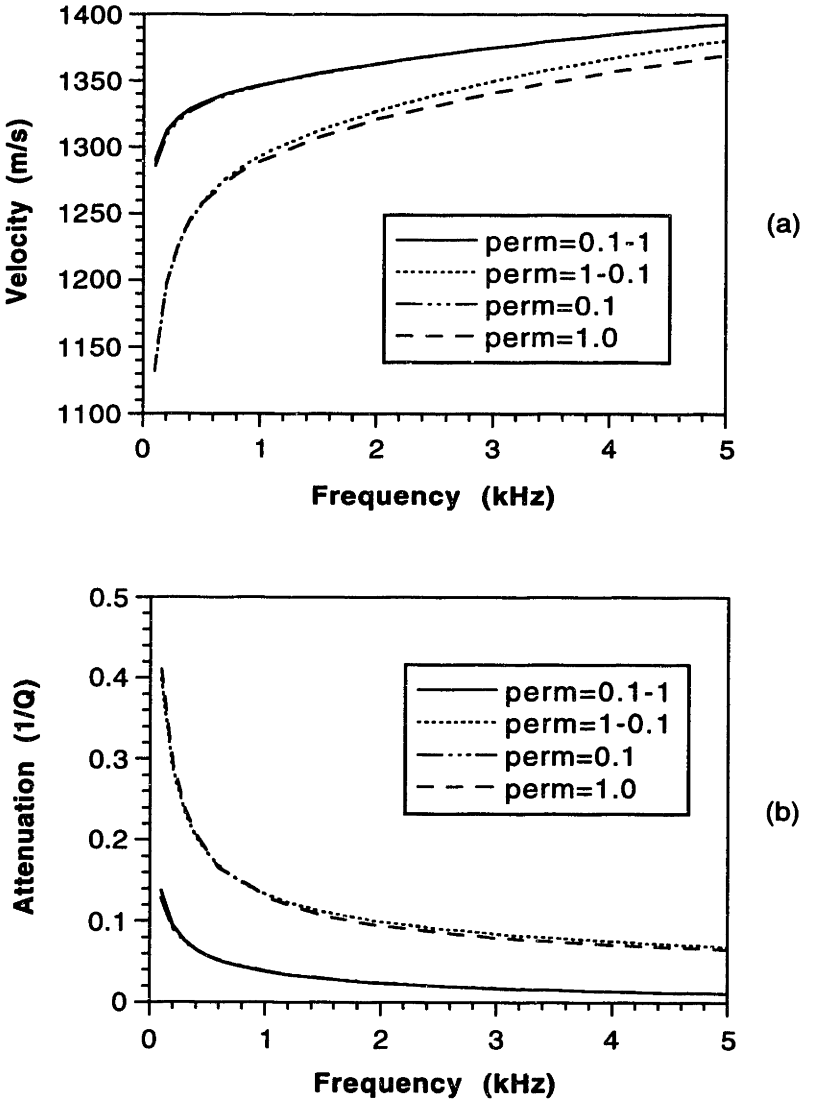

Figure 4-11: Stoneley wave velocity (a) and attenuation (b) due to the linearly increasing and/or decreasing permeability variation of Figure 4-10. The results of the equivalent constant permeability are also plotted.

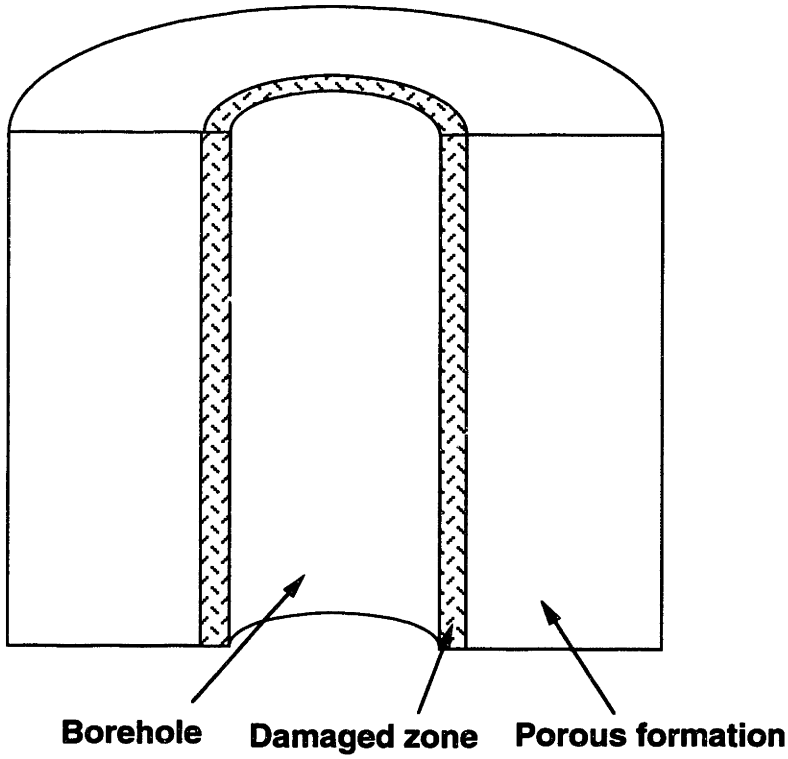

Figure 4-12: Modeling of a damaged borehole wall as a high permeability layer immediately surrounding the borehole.

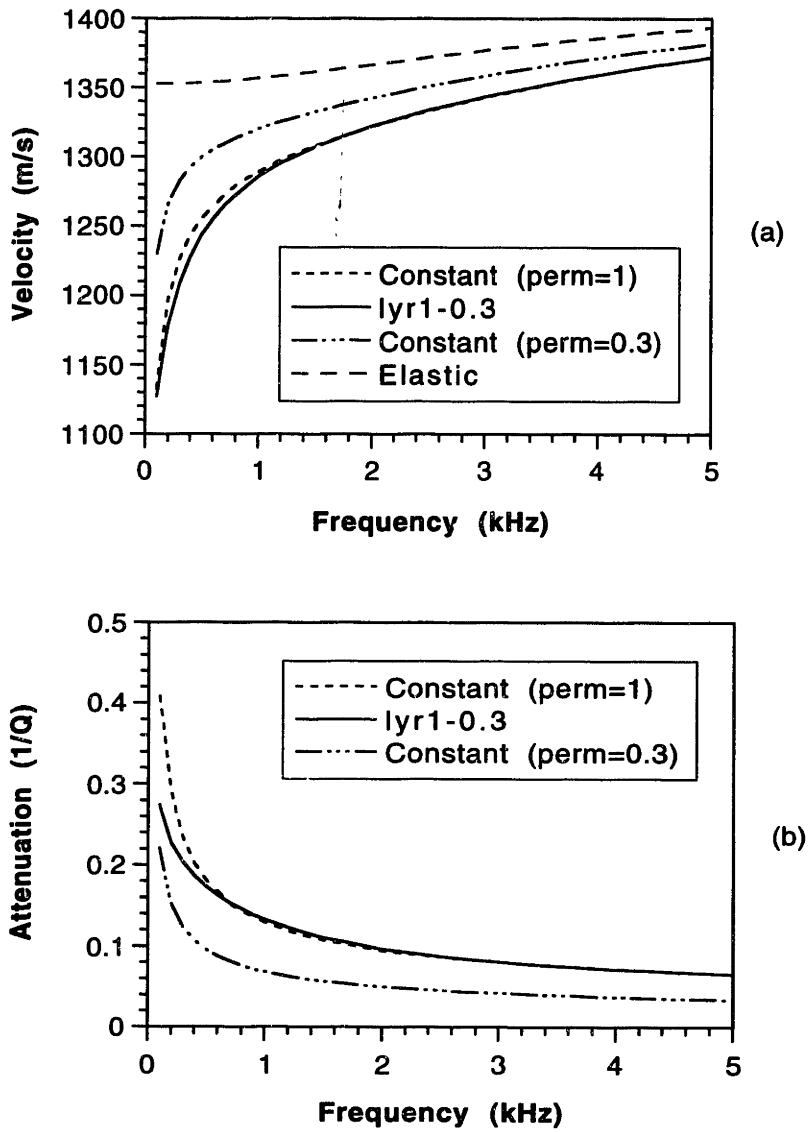

Figure 4-13: Stoneley wave velocity (a) and attenuation (b) for the damaged zone model shown in Figure 4-12. The inner layer permeability is 1 Darcy and the virgin formation permeability is 0.3 Darcy.

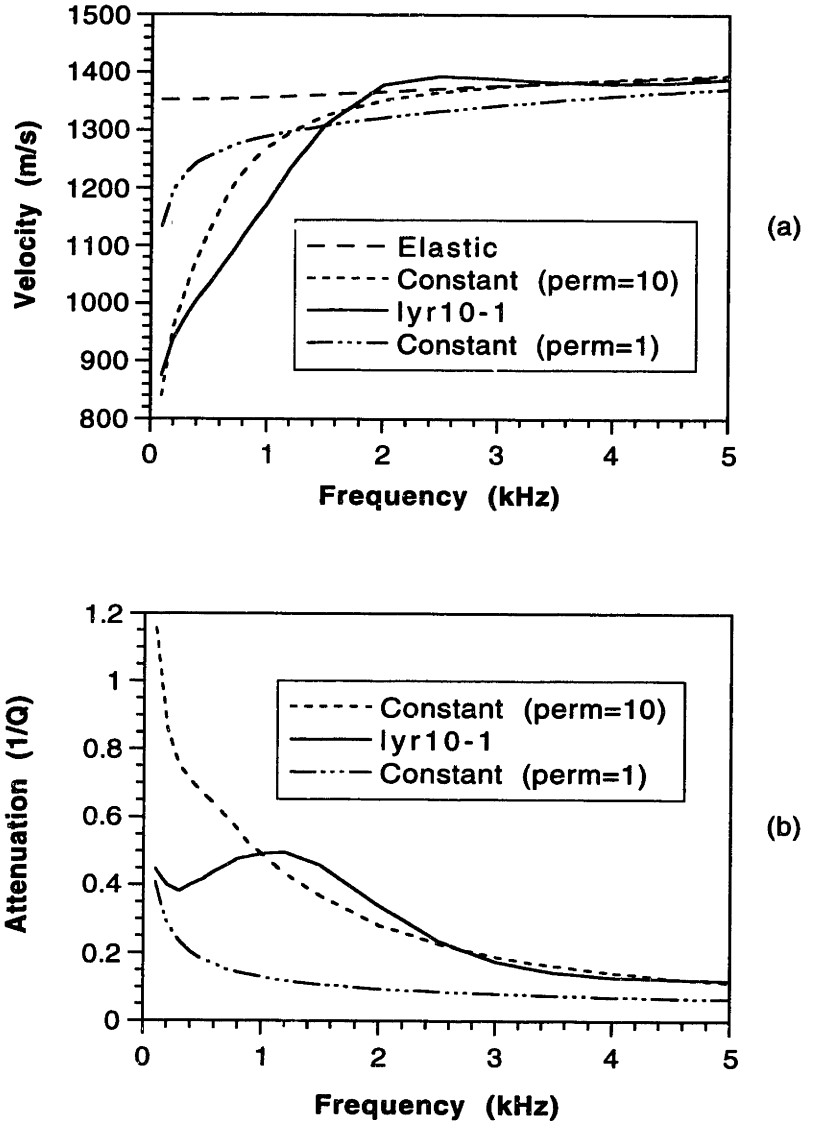

Figure 4-14: Stoneley wave velocity (a) and attenuation (b) for the damaged zone model shown in Figure 4-12. The inner layer permeability is 10 Darcy and the virgin formation permeability is 1 Darcy.

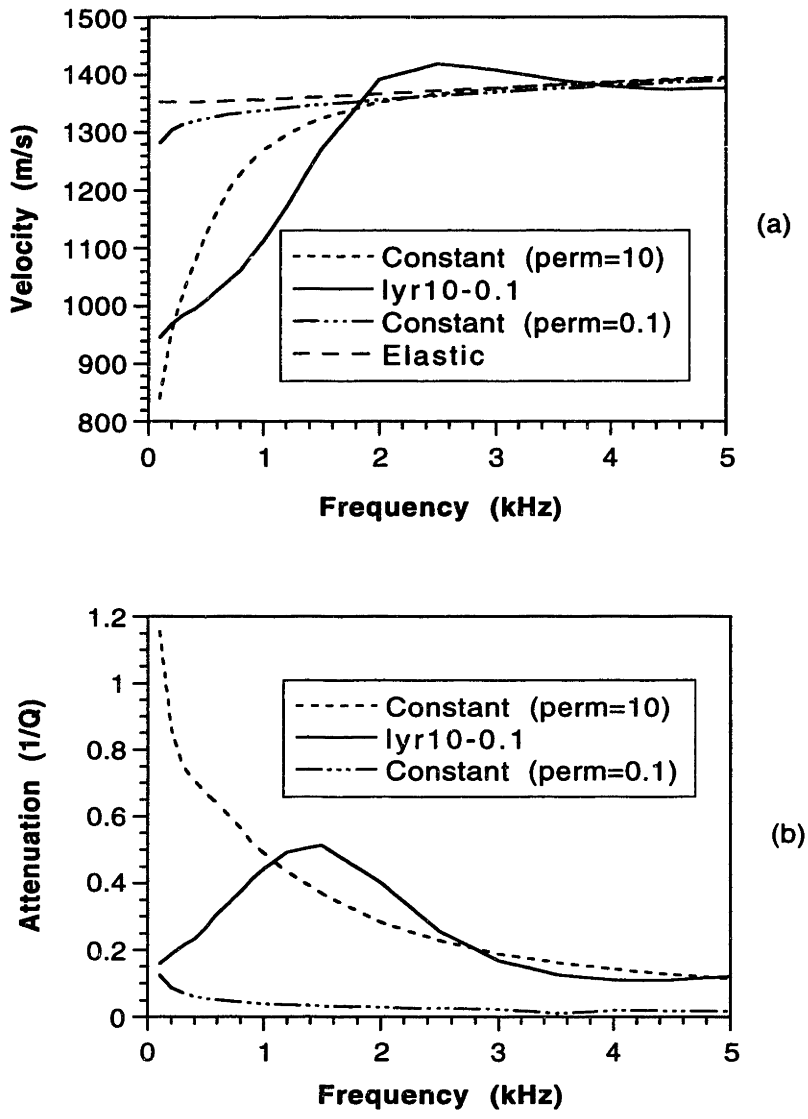

Figure 4-15: Stoneley wave velocity (a) and attenuation (b) for the damaged zone model shown in Figure 4-12. The inner layer permeability is 10 Darcy and the virgin formation permeability is 0.1 Darcy.

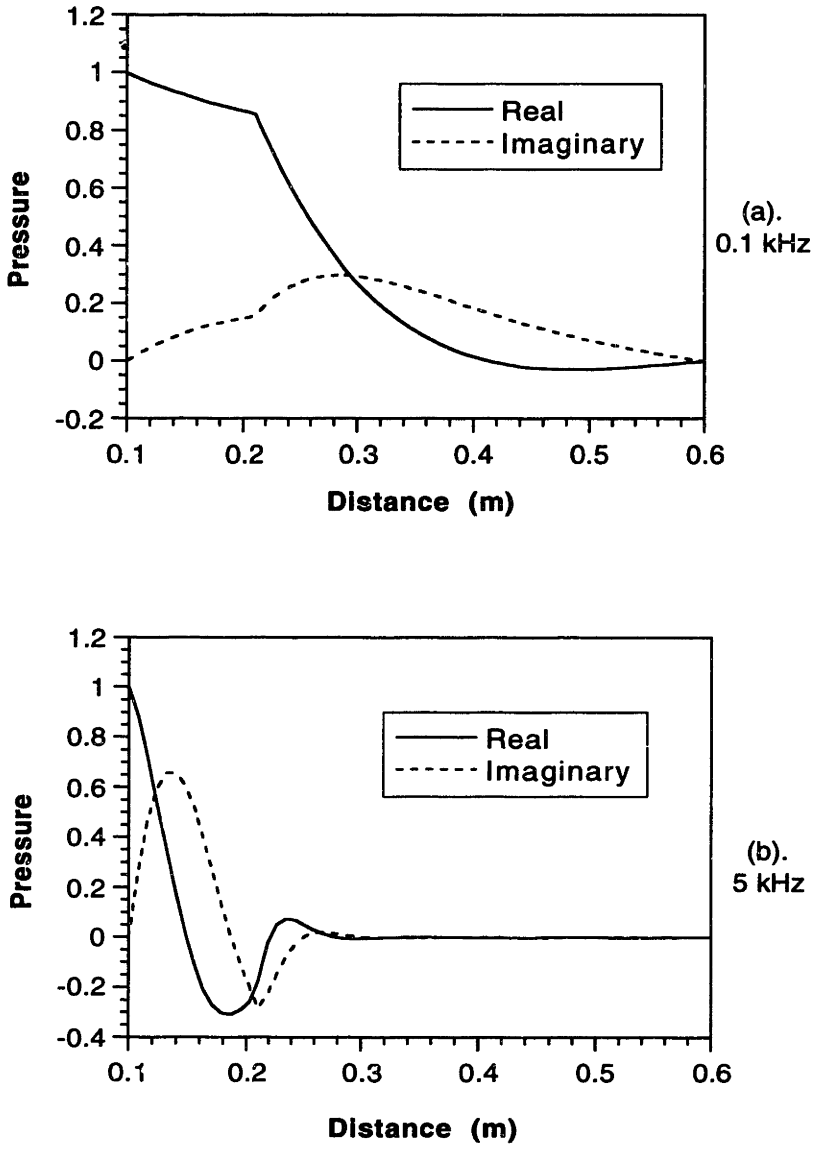

Figure 4-16: Amplitude of formation dynamic pore fluid pressure for the damaged zone model as a function of radial distance: (a) frequency = 100 Hz, (b) frequency = 5 kHz.

Chapter 5

Stoneley wave Propagation Across Heterogeneous Zones

5.1 Introduction

In Chapter 4, we have studied the effects of radial and azimuthal variations of formation permeability on the borehole Stoneley wave propagation. In this chapter, we will study the situation where the permeability varies in vertical (or borehole axial) and radial directions. This situation is commonly encountered in acoustic logging applications. For example, vertical layering of sedimentary rocks often results in formation sequences that consist of permeable and non-permeable layers (e.g. sand-shale sequences). Even in formations that are considered homogeneous, permeability values measured from well bores often show considerable variations. In many situations, formation permeability heterogeneity is due to fractures and/or permeable zones that intersect the borehole. The characterization of these permeability heterogeneities and the determination of their fluid transmissivity are very important tasks in acoustic logging applications (Paillet, 1984; Tang and Cheng, 1993), in which the borehole Stoneley wave is commonly used as a primary means for formation permeability studies.

The effects of vertical formation permeability heterogeneity variation on Stoneley wave propagation have been studied by numerous authors. Hornby et al. (1989), Tang and Cheng (1989), and Güler and Toksöz (1987) have studied the propagation of Stoneley waves across borehole fractures. Tang and Cheng (1993) presented a theory which can be used to study the effects of the permeable zone as well as those of fractures. Kostek (1991), by using a finite difference approach, studied the effects of multiple borehole fractures on Stoneley wave propagation. In this chapter, we will study a more general case in which the formation permeability can have arbitrary variations along the vertical as well as radial directions. As a result, permeability heterogeneities of interest, such as sand-shale sequences, heterogeneous permeable layers, multiple fractures *etc.*, can be analyzed. The results of these numerical studies will not only demonstrate the effects of the permeability heterogeneities on the borehole Stoneley waves, but also can be used to provide bases for detecting and characterizing these heterogeneities using Stoneley wave measurements.

As discussed in Chapter 4, the effects of formation heterogeneity can be studied using a simplified Biot model approximation (Tang *et al.*, 1991b). By decomposing the problem into the elastic and flow problems, we can solve the pore fluid flow problem for the heterogeneous porous formation independent of the elastic problem. The combination of the solution for the elastic and flow problems will give the solution for Stoneley wave propagation with heterogeneous permeability.

The behavior of dynamic fluid flow in heterogeneous porous media has been modeled in Chapter 3. Because of the dispersive nature of the flow motion, an iterative finite difference technique was developed to compute the flow field in the frequency domain. For the present borehole geometry, we need to solve the dynamic fluid flow problem for the cylindrical coordinate system. The iterative finite difference technique for the cylindrical system has been developed in Chapter 4 to investigate dynamic fluid flow in formations with radial and azimuthal permeability variations. In this chapter, the formation permeability will vary along the borehole axial and radial di-

rections. Therefore, the iterative finite difference technique used in Chapter 4 will be modified for the axial and radial coordinates system. Furthermore, because of heterogeneity variation along the axial direction and the resulting axial variation of Stoneley wave propagation, we will employ a propagator matrix method to compute the Stoneley wave propagation across the permeability heterogeneities.

The effects of the borehole permeability heterogeneity on the Stoneley wave propagation can be reflected from the transmission loss (or attenuation) and reflection from the heterogeneity boundaries. Both laboratory and field studies have provided such evidence. In the laboratory, the effects of heterogeneity on Stoneley wave propagation has been noticed by Winkler *et al.*, (1989). They evaluated the theory of Stoneley wave propagation in porous boreholes using laboratory experiments and found excellent agreement between theory and experiment for 3 out of 4 data sets. However, they reported that for one data set the data disagree with the results predicted using the homogeneous model theory. They suggested that either sample heterogeneity or the limitation of the dynamic permeability theory at the low frequency and high frequency transition was the cause.

In the field study, effects of permeability heterogeneity are commonly encountered in acoustic logging across fractures or fracture zones. Even in isolated fracture zones, the permeability may have significant variations and these variations can have important effects on the Stoneley wave propagation. Such a case was observed by Paillet (1984), who reported an acoustic logging data set across a permeable fracture zone. The data set shows non-symmetric patterns for Stoneley wave attenuation and reflection at the upper and lower boundaries of the fracture zone. Although Tang *et al* (1991a) have used a homogeneous permeability layer to model the fracture zone and explained the significant Stoneley wave attenuation and reflection, the homogeneous layer cannot model the heterogeneity variation within the zone and cannot explain the non-symmetric patterns of the data.

With the numerical analysis developed in this chapter, we will carry out modeling

studies on the laboratory data set of Winkler *et al.* (1989) and the field data set of Paillet (1984). These studies will demonstrate the effects of formation heterogeneity on Stoneley wave propagation and the applicability of the numerical technique in handling formation heterogeneities.

5.2 Stoneley Wave Propagation in a Formation with Variable Permeabilities

As shown in Chapter 4, for a Stoneley wave propagating in a permeable porous borehole, the interaction of the Stoneley wave with the formation can be decomposed into two parts (Tang *et al.*, 1991b). The first is the interaction with an equivalent elastic formation, and the second is the interaction with the dynamic fluid flow into the formation. The Stoneley wave can be described by the following one-dimensional wave equation [Equation (4.5)]:

$$\frac{d^2P}{dz^2} + \left[\frac{\omega^2}{v_f^2} + \frac{2\rho_f\omega^2}{R}\frac{U_e}{P} + \frac{2\rho_f\omega^2}{R}\frac{U_f}{P}\right]P = 0 \ , \tag{5.1}$$

with the Stonely wavenumber k given by

$$k = \sqrt{\frac{\omega^2}{v_f^2} + \frac{2\rho_f\omega^2}{R}\frac{U_e}{P} + \frac{2\rho_f\omega^2}{R}\frac{U_f}{P}} \ . \tag{5.2}$$

This equation indicates that the Stoneley wave propagation in a porous borehole is affected by the formation elastic displacement U_e and the pore fluid flow displacement U_f. If the borehole wall is impermeable, i.e. $U_f = 0$, then the Stoneley wavenumber can be written as

$$k_e = \sqrt{\frac{\omega^2}{v_f^2} + \frac{2\rho_f\omega^2}{R}\frac{U_e}{P}} \ . \tag{5.3}$$

Given elastic properties of the fluid-saturated rock, k_e is found by solving the borehole dispersion equation [Equation (4.8)]. Because the objective of the present study is to investigate the effects of permeability variation, we neglect the variation of the elastic

properties and assume a spatially invariable k_e for the formation. For the given elastic properties of the fluid-saturated formation, k_e can be calculated using Equation (4.8). With k_e known, the Stoneley wavenumber in a permeable borehole is

$$k = \sqrt{k_e^2 + \frac{2\rho_f \omega^2}{R}\frac{U_f}{P}} \quad . \tag{5.4}$$

Equation (5.4) is valid only for a formation with homogeneous permeability. For a formation with heterogeneous permeability that can change with the axial distance z, U_f will also vary with z. In this case, we discretize the borehole (along the axial direction) into equally-spaced intervals. Within each small interval, permeability can be regarded as homogeneous and Equation (5.4) can be used to calculate the Stoneley wavenumber for the interval. To find this vertically variable $k(z)$, we will use the finite difference method to solve for $U_f(z)$. The overall effects of the permeability variation will be calculated using a propagator matrix technique.

5.2.1 Dynamic fluid flow in radial and axial coordinates system

The dynamic fluid flow in heterogeneous permeability media is described by the following equation (see Chapter 3)

$$\nabla \cdot [\alpha(\omega; \vec{\mathbf{x}}) \nabla p] + i\omega p = 0 \quad , \tag{5.5}$$

where p is dynamic pressure associated with pore fluid motion,

$$\alpha(\omega; \vec{\mathbf{x}}) = \frac{\kappa(\omega; \vec{\mathbf{x}}) K_f}{\phi \mu (1 + \xi)} \tag{5.6}$$

is dynamic pore fluid diffusivity, K_f = fluid incompressibility, ϕ = porosity, μ = fluid viscosity, and ξ is a correction for solid matrix compressibility (Norris, 1989). The fluid diffusivity $\alpha(\omega; \vec{\mathbf{x}})$ is a function of both frequency and the spatial position $\vec{\mathbf{x}}$. This happens if the dynamic permeability of Johnson *et al.* (1987) is a function of

the spatial position when the static permeability $\kappa_0(\vec{\mathbf{x}})$ varies with $\vec{\mathbf{x}}$:

$$\kappa(\omega;\vec{\mathbf{x}}) = \frac{\kappa_0(\vec{\mathbf{x}})}{\left(1-\frac{i}{2}\tau\kappa_0(\vec{\mathbf{x}})\rho_0\omega/\mu\phi\right)^{\frac{1}{2}} - i\frac{\tau\kappa_0(\vec{\mathbf{x}})\rho_0\omega}{\mu\phi}} \quad . \tag{5.7}$$

In Equation (5.7), τ is tortuosity of the porous medium, ρ_0 the pore fluid density.

For the borehole configuration, the cylindrical coordinates are most convenient to use. In this study, we investigate a two and half dimensional (2.5D) case where the permeability variation is in the radial (r) and vertical (z) directions, i.e.,

$$\kappa_0(\vec{\mathbf{x}}) = \kappa_0(r,z) \quad , \tag{5.8}$$

but the pore fluid flow takes place in the 3-D space. In the cylindrical system, Equation (5.5) becomes

$$\frac{\partial}{\partial r}\left(\alpha(r,z)\frac{\partial p}{\partial r}\right) + \frac{\alpha(r,z)}{r}\frac{\partial p}{\partial r} + \frac{\partial}{\partial z}\left(\alpha(r,z)\frac{\partial p}{\partial z}\right) + i\omega p = 0 \tag{5.9}$$
$$(r > R \text{ and } 0 < z < L) \quad ,$$

where R is the borehole radius and $z = 0$ and $z = L$ represent the lower and upper boundaries of the heterogeneous formation, respectively. The boundary conditions for Equation (5.9) are described below.

The boundary condition at the borehole wall is the continuity of pressure, i.e., the borehole Stoneley wave pressure should equal the pore fluid pressure at the borehole wall. However, the Stoneley wave pressure is not known at this stage. We therefore use a perturbation approach. We assume that the Stoneley wave pressure can be decomposed into two parts. The first is the zero order term $p_0 e^{ik_e z}$, which corresponds to the equivalent elastic (or non-permeable) formation, with p_0 being the pressure amplitude. The second part is a perturbation term due to the porous formation fluid flow. The borehole Stoneley wave pressure is then written as

$$p = p_0 e^{ik_e z} + p_1 \quad . \tag{5.10}$$

Compared with the pore fluid flow due to $p_0 e^{ik_e z}$, the pore fluid flow associated with p_1 is a higher order perturbation because p_1 itself is the first order perturbation.

Therefore, for a first order perturbation theory (i.e., the simplified Biot model of Tang *et al.*, 1991b), we assign the known zero order Stoneley wave pressure function $p_0 e^{ik_e z}$ as the boundary condition for the pore fluid flow pressure at the borehole wall,

$$p(R,z) = p_0 e^{ik_e z} \quad , \qquad (0 < z < L) \tag{5.11}$$

together with the radiation condition

$$p(r = \infty, z) = 0 \tag{5.12}$$

and the no-flow boundary conditions

$$\frac{\partial p(r, z = 0)}{\partial z} = \frac{\partial p(r, z = L)}{\partial z} = 0 \ . \tag{5.13}$$

With these boundary conditions, Equation (5.9) is solved using the iterative finite difference technique (see Appendix C) to give the pore pressure distribution over the (r, z) grid. The fluid flow at the borehole wall is computed using the modified Darcy's law (Tang *et al.*, 1991b)

$$-i\omega U_f(z) = -\frac{\kappa(\omega; r, z)}{\mu} \frac{dp(r,z)}{dr}\bigg|_{r=R} \ . \tag{5.14}$$

Note this flow is a function of z because of the permeability variation. The pressure gradient is numerically evaluated from the calculated pressure field at the borehole wall. With this flow field, the Stoneley wave propagation will be perturbed. We then add this perturbation to the elastic Stoneley wavenumber k_e to give the Stoneley wave number in the heterogeneous formation using Equation (5.4)

$$k(z) = \sqrt{k_e^2 + \frac{2\rho_f \omega^2}{R} \frac{U_f(r,z)}{p(r,z)}\bigg|_{r=R}} \ . \tag{5.15}$$

Because the flow field at the borehole boundary ($r = R$) varies with z, the resulting permeable formation Stoneley wavenumber is also a function of z. The effects of this variable wavenumber on the Stoneley wave propagation will be addressed in the following.

5.2.2 Propagation using the propagator matrix method

To calculate the effects of the heterogeneous fluid flow field on the Stoneley wave propagation, we use the propagator matrix technique (Aki and Richards, 1980). For the present problem, we only consider the change of the Stoneley wave amplitude due to fluid flow effects. Other effects, like the scattering of the Stoneley wave into compressional and shear waves at heterogeneity boundaries, are neglected. Although these scattering effects are present (Peng, 1994), they are second order effects compared to the fluid flow effects, especially at low frequencies. For the wavenumber $k(z)$ given in Equation (5.15), the borehole Stoneley wave pressure $p(z)$ and vertical displacement $u(z)$ are

$$p(z) = \rho_f \omega^2 A(z) e^{ik(z)z} \tag{5.16}$$

$$u(z) = ik(z) A(z) e^{ik(z)z} \ , \tag{5.17}$$

where $A(z)$ is the as-yet-to be determined amplitude coefficient, $A(z)e^{ik(z)z}$ representing the Stoneley wave displacement potential. To our advantage, the finite difference grid along the z-direction discretizes the borehole into equally-spaced layers of thickness δz. The continuity conditions for pressure and displacement are then applied to each interface between the adjacent layers. At each boundary, a 2×2 boundary condition matrix D is calculated which can be used to propagate the displacement-pressure vector $[u, p]^T$ along the borehole axis. For example, at $z = z_n$, D is given as

$$D_n(z_n) = \begin{pmatrix} e^{ik(z_n)z_n} & e^{-ik(z_n)z_n} \\ \\ \dfrac{i\rho_f\omega^2}{k(z_n)} e^{ik(z_n)z_n} & \dfrac{-i\rho_f\omega^2}{k(z_n)} e^{-ik(z_n)z_n} \end{pmatrix} . \tag{5.18}$$

The propagation of the vector $[u, p]^T$ across the discretized borehole layers is expressed as

$$\begin{pmatrix} u \\ p \end{pmatrix}_{z=0} = \left(\prod_{n=1}^{N} D_n(z_n) D_n^{-1}(z_{n-1}) \right) \begin{pmatrix} u \\ p \end{pmatrix}_{z=L} = G \begin{pmatrix} u \\ p \end{pmatrix}_{z=L} , \tag{5.19}$$

where N is the number of finite difference grid along z-direction, L is the total propagation length, and G is the notational simplification of the matrix product in Equation (5.19). Using the expression of D, the propagation matrix of layer n is written as

$$D_n(z_n)D_n^{-1}(z_{n-1}) = \begin{pmatrix} cos[k(z_n)\delta z] & sin[k(z_n)\delta z]\frac{k_n}{\rho_f\omega^2} \\ -sin[k(z_n)\delta z]\frac{\rho_f\omega^2}{k_n} & cos[k(z_n)\delta z] \end{pmatrix} , \qquad (5.20)$$

where $k_n = k(z_n)$ is the Stoneley wavenumber at $z = z_n$ computed using Equation (5.15).

Using the propagator matrix technique, the transmission and reflection of a Stoneley wave due to a heterogeneous permeable structure can be calculated. Let a Stoneley wave $A_0^+ e^{ik_e z}$ approach from $z < 0$ onto the upper boundary of the heterogeneous zone (z = 0). Upon interacting with the structure, part of the wave energy will be reflected back, propagating in the negative z direction as given by $A_0^- e^{-ik_e z}$. Across the lower boundary at $z = L$, there is only the transmitted wave, given by $A_N^+ e^{ik_N z}$, where k_N is the Stoneley wavenumber for the formation located adjacent to the $z = L$ boundary. k_N can be taken as k_e, assuming that the formations above and below the heterogeneous formation are the same. Therefore, the displacement and pressure at $z = 0$ and $z = L$ are

$$\begin{cases} u = ik_e(A_0^+ - A_0^-) \\ p = \rho_f\omega^2(A_0^+ + A_0^-) \end{cases} \qquad (z = 0) \qquad (5.21)$$

and

$$\begin{cases} u = ik_e A_N^+ e^{ik_e L} \\ p = \rho_f\omega^2 A_N^+ e^{ik_e L} \end{cases} \qquad (z = L) \ , \qquad (5.22)$$

respectively.

Equations (5.21) and (5.22) are related using the propagator matrix method

[Equation (5.19)],

$$\begin{pmatrix} ik_e(A_0^+ - A_0^-) \\ \rho_f\omega^2(A_0^+ + A_0^-) \end{pmatrix} = \begin{pmatrix} g_{11} & g_{12} \\ g_{21} & g_{22} \end{pmatrix} \begin{pmatrix} ik_e A_N^+ e^{ik_e L} \\ \rho_f\omega^2 A_N^+ e^{ik_e L} \end{pmatrix} , \tag{5.23}$$

where g_{ij} (i,j = 1, 2) is the element of G. Solving this equation, we find the transmission and reflection coefficients for the pressure field,

$$\begin{aligned} Trs &= \frac{p^+|_{z=L}}{p^+|_{z=0}} \\ &= \frac{(ik_e g_{11} + \rho_f\omega^2 g_{12})(\rho_f\omega^2 g_{22} - ik_e g_{21}) - (ik_e g_{21} + \rho_f\omega^2 g_{22})(\rho_f\omega^2 g_{12} - ik_e g_{11})}{ik_e(\rho_f\omega^2 g_{22} - ik_e g_{21}) - \rho_f\omega^2(\rho_f\omega^2 g_{12} - ik_e g_{11})} \end{aligned} \tag{5.24}$$

$$\begin{aligned} Ref &= \frac{p^-|_{z=0}}{p^+|_{z=0}} \\ &= \frac{\rho_f\omega^2(ik_e g_{11} + \rho_f\omega^2 g_{12}) - ik_e(ik_e g_{21} + \rho_f\omega^2 g_{22})}{ik_e(\rho_f\omega^2 g_{22} - ik_e g_{21}) - \rho_f\omega^2(\rho_f\omega^2 g_{12} - ik_e g_{11})} \quad . \end{aligned} \tag{5.25}$$

Therefore, by using the finite difference method to compute the fluid flow effects for the heterogeneous formation, and the propagation matrix method to calculate the propagation for the spatially variable Stoneley wavenumber $k(z)$, Stoneley wave propagation across an arbitrarily heterogeneous permeable structure can be modeled. This allows us to model the effects of such heterogeneity structures as multiple permeable zones, sand-shale (permeable and non-permeable) sequences, or any permeable structure with varying permeability values.

In formations where the scale of permeability variation is small compared to the wavelength, the propagator matrix method can be used to obtain an equivalent Stoneley wave number for the heterogeneous formation. In the heterogeneous formation, the transmitted Stoneley wave at $z = L$ is $A(L)e^{ik(L)L}$ where $k(L)$ is computed using the finite difference method and $A(L)$ is computed using the propagator matrix method. Assume that this wave can be approximated by a wave $A_0 e^{i\bar{k}L}$, where A_0 is the wave amplitude at $z = 0$ and $\bar{k}$ is the equivalent Stoneley wavenumber. Equating $A_0 e^{i\bar{k}L}$ with $A(L)e^{ik(L)L}$, we have

$$\bar{k} = k(L) - \frac{i}{L} ln\left(\frac{A(L)}{A_0}\right) \quad . \tag{5.26}$$

From this equivalent wavenumber, the Stoneley wave attenuation $1/Q$ and phase velocity v_{st} are computed using

$$\begin{cases} 1/Q &= 2\dfrac{Im(\bar{k})}{Re(\bar{k})} \\ v_{st} &= \dfrac{\omega}{Re(\bar{k})} \end{cases} . \tag{5.27}$$

5.3 Numerical Simulation Results

In this section, we present the finite difference simulation results for various permeability heterogeneities along a vertical borehole. For all the calculations below, we first calculate the elastic problem using the saturated rock properties: $v_p = 4000$ m/s, $v_s = 2300$ m/s, and $\rho = 2.16$ g/cm^3. The Stoneley wavenumber k_e for the equivalent elastic formation is calculated using the borehole dispersion equation (Cheng and Toksöz, 1981). The borehole fluid density and velocity are $\rho_f = 1$ g/cm^3 and $v_f = 1500\ m/s$, respectively. The borehole radius is 0.1 m. For simplicity, we assume that the elastic properties for the various heterogeneous permeability distributions are the same, so that the same k_e is used for the following cases. In all the cases below (unless specified), the pore fluid properties are: $K_f = 2.25\ GPa$, $\rho_0 = 1$ g/cm^3, $\mu = 1.14 \times 10^{-3}$ Pa s, porosity $\phi = 0.2$, and tortuosity $\tau = 3$.

5.3.1 Homogeneous permeability – A test of the numerical algorithm

We first present the simulation result for a homogeneous permeable formation surrounding the borehole. This example, together with the existing analytical solution, offers a test of the validity and accuracy of the finite difference simulation algorithm.

Figure 5-1 shows the comparison between the Stoneley wave phase velocity (a) and attenuation (b) calculated using the analytical solution [Equation (4.24)] and

those using the finite difference method, and equivalent wave number formula [Equation (5.26)] for a homogeneous permeability model. These results are calculated for the frequency range of $0 \sim 5$ kHz in which most Stoneley wave measurements are performed. The formation permeability is 1 Darcy. For simplicity, the effects due to solid matrix compressibility are neglected [i.e. $\xi = 0$ in Equation (5.6)] when calculating both the analytical and finite difference results. The results for the two difference approaches agree very well. This comparison demonstrates the validity and accuracy of the finite difference technique. Therefore, in the case of a heterogeneous permeability distributions where an analytical solution is difficult to find, we will use the finite difference method to calculate the Stoneley wave propagation.

5.3.2 Variable permeability models

In the field acoustic logging applications, the formation permeability is usually heterogeneous. For example, the permeability may fluctuate from place to place due to random variations. The permeability may have cyclic variations due to sand-shale sequences. The effects of these heterogeneity variations on the borehole Stoneley wave propagation are studied here. In this section, we assume that the logging tool is within the heterogeneous formation and we will analyze the average Stoneley wave attenuation and velocity dispersion characteristics using Equations (5.26) and (5.27).

In Figures 5-2, 5-3, and 5-4, three formation permeability heterogeneity models are shown. They are a 2-D random variation with a Gaussian correlation function (Figure 5-2), a 1-D random variation along borehole axial direction with Gaussian correlation function (Figure 5-3), and a permeable and non-permeable layer model generated using the Poisson process (see Chapter 2). All the three models have same average permeability of 1 Darcy. For the continuous models, the standard deviation of the variation is 30%. For the discontinuous model, the permeability contrast between high and low permeability layers is 100:1. For the borehole Stoneley wave, the axial

propagation distance is much greater than the depth of fluid motion penetration in the radial direction. We therefore set the axial and radial model dimensions as 10 m and 0.5 m, respectively. In Figures 5-2, 5-3, and 5-4, the models are shown only for a 5 m section in axial direction and 0.3 m in radial direction. In these figures, the calculated dynamic fluid pressure amplitude distributions for those heterogeneous models are also plotted. The frequency for the fluid motion is 1 kHz. As can be seen from these figures, the formation fluid pressure distributions are distinctly different from one another because of the different heterogeneity variations. The 2-D random model shows considerable fluid pressure variation in both radial and axial directions. The 1-D model shows less axial variations. For the discontinuous model, the fluid motion is largely concentrated in the high permeability layers.

The effects of the heterogeneity variations are now analyzed. We use Equations (5.26) and (5.27) to calculate the average Stoneley wave phase velocity and attenuation for these heterogeneity models and plot the results in Figures 5-5a (velocity) and 5-5b (attenuation) in the frequency range of 0 - 5 kHz. For comparison, the results for a homogeneous formation with a constant permeability of 1 Darcy is also shown. A very interesting feature of these results is that, despite the considerable difference in the heterogeneity variations, the average Stoneley wave attenuation and velocity dispersion are very close to the homogeneous model results. Only the discontinuous model results show appreciably lower attenuation and velocity dispersion than the homogeneous model results.

The difference between the discontinuous model and the continuous model results becomes very significant when formation permeability is high. To demonstrate this, we have re-calculated the Stoneley wave attenuation and phase velocity for the same heterogeneous models shown in Figures 5-2, 5-3, and 5-4 by increasing the average model permeability from 1 Darcy to 10 Darcy and keeping other parameters (porosity, tortuosity, *etc.*) unchanged. The results are shown in Figure 5-6 for the Stoneley wave velocity (Figure 5-6a) and attenuation (Figure 5-6b). The continuous heterogeneous

model results, despite some small differences, are still close to the homogeneous model results. However, the discontinuous model results show significant difference from the continuous and homogeneous model results. The velocity is higher than those from the other models in the frequency range of 0 - 2 kHz and the attenuation is significantly lower than those from the other models.

The difference between discontinuous and continuous permeability models at high permeabilities can be explained based on the behavior of dynamic permeability. In both models, the Stoneley wave propagation sums all the fluid flow effects over the same model length. In the discontinuous model, only the high permeability layers contribute to the Stoneley wave attenuation and dispersion. However, although the permeability of the permeable layers is twice that of the mean permeability, the attenuation value due to these layers is not doubled. This can be seen from analyzing the dynamic permeability. At high permeability values, the amplitude of dynamic permeability is always less than the static permeability as can be seen by the inequality $|\kappa(\omega)| < \kappa_0$ $(\omega > 0)$, the larger the static permeability κ_0 is, the smaller $|\kappa(\omega)|$ is compared to κ_0 [see Equation (5.7)]. Therefore, compared to the continuous model, the high permeability layers in the discontinuous model will contribute less to the attenuation and dispersion when averaged over the same propagation length. For the continuous model, because there is no significant permeability contrast, the average result will be more or less close to the homogeneous result.

5.4 Stoneley Wave Propagation Across Heterogeneous Permeable Structures

In this section, we study Stoneley wave propagation across various heterogeneous permeable structures. This is an important problem for the characterization of formation permeability using borehole Stoneley wave measurements. A theory has been

presented by Tang and Cheng (1993) to model borehole fractures as a highly permeable zone. This theory is able to explain the observed Stoneley wave transmission and reflection at fractures. A drawback of this model is that it uses a homogeneous permeability layer to model the permeable zone and therefore neglects the permeability variation within the zone. In reality, a natural permeable structure may contain various heterogeneous structures. With the heterogeneous propagation theory developed in this chapter, we can study the effects of the heterogeneity structures and compare the similarity and difference between the simple homogeneous model and the heterogeneity structure model.

5.4.1 Comparison with homogeneous permeable zone model

According to Tang and Cheng (1993), the Stoneley wave transmission and reflection coefficients due to a homogeneous permeable layer are given by

$$Trs = \frac{4k_1k_2e^{-ik_2L}}{(k_1+k_1)^2e^{-ik_2L}-(k_1-k_2)^2e^{ik_2L}} \tag{5.28}$$

$$Ref = \frac{2i(k_2^2-k_1^2)sin(k_2L)}{(k_1+k_2)^2e^{-ik_2L}-(k_1-k_2)^2e^{ik_2L}} \ , \tag{5.29}$$

where k_1 is the Stoneley wavenumber outside the permeable zone, k_2 is the permeable zone Stoneley wavenumber, and L is the zone thickness. In fact, the simple homogeneous permeable model results can be derived as the special case for the propagator matrix results [Equations (5.24) and (5.25)]. Therefore, the analytical results presented in Equations (5.28) and (5.29) can be used to test the validity and accuracy of the finite difference and propagator matrix approach developed in this study.

Figure 5-7 compares the transmission and reflection coefficients computed using the analytical results [Equations (5.28) and (5.29)] and the numerical simulation results [Equations (5.24) and (5.25)]. The permeable zone has a porosity 0f 0.3, tortuosity of 3, permeability of 5 Darcy, and a thickness of 0.5 m. As can be seen

from Figure 5-7, the results from the analytical approach and the numerical approach agree very well. Only at frequency beyond 5 kHz, do the two transmission coefficients differ slightly. This comparison shows the validity and accuracy of our numerical modeling. In the case of a heterogeneous permeability structure, we can use our numerical technique to compute the Stoneley wave transmission and reflection due to the structure.

5.4.2 Double permeable layers

A permeable zone encountered in acoustic logging may consist of multiple permeable structures. The permeable zone with multiple structures results in some complex features compared to the single permeable layer model. For simplicity, we model the effects for a double permeable layer model (Figure 5-8). In this model two permeable layers, each having a permeability of 10 Darcy, porosity of 0.3, and thickness of 0.15 m are separated by a non-permeable formation of thickness 0.2 m. The high permeability value (10 Darcy) used here is based on the conclusion of Tang and Cheng (1993) that fracture zones can be modeled as high permeability layers.

The numerical finite difference technique, together with the propagator matrix method, is applied to model the Stoneley wave propagation across the double layer structure. The transmission and reflection coefficients calculated using the numerical method are plotted in Figure 5-9 for the frequency range from 0 to 5 kHz. For comparison, the results calculated for a single layer of thickness 0.3 m with the same permeability and porosity as the double layer model are also plotted (dashed curves). Although the double layer model and the single layer model have the same fluid transmissivity (permeability $\times$ thickness), the double layer model results show more complex features compared with the single layer results. The transmission coefficient for the double layer model is somewhat lower than the single layer result due to the interaction of the two permeable layers. This interaction is especially pronounced

for the reflection coefficient, resulting in the significant variation of the reflected wave amplitude in the frequency range being modeled. Moreover, in the frequency range of 2 to 3 kHz, the reflection coefficient can reach a peak value of 0.3, which is significantly higher than the value of the single layer result. Note that this peak occurs at the frequency corresponding to the half wavelength of the Stoneley wave, indicating that the constructive interference between the two layers occurs arrond this frequency. The high amplitude reflected Stoneley wave events on an acoustic waveform log may be helpful in detecting two major fractures that are close to each other. It is also interesting to note that the transmission and reflection coefficients for the two layer and single layer models converge at very low frequencies, indicating that at very long wavelengths the Stoneley wave cannot resolve the structure of a heterogeneous zone, but is sensitive only to the overall fluid transmissivity of the zone.

5.4.3 Multiple layer structure

We study the effects of a permeable zone that consists of a sequence of permeable and non-permeable layers. The thicknesses of these layers are small compared to the Stoneley wavelength of interest. Figure 5-10 show an example of such a model. The model is generated using a random repetition of layers of low and high permeabilities (they are 20 and 0.1 Darcy, respectively). The average thickness of the layers is 0.025 m, and thicknesses of the layers obey the Poisson distribution (see Chapter 2).

The calculated Stoneley wave transmission and reflection coefficients are shown in Figure 5-11, together with the results for a single layer of the same thickness 0.4 m and a cumulative permeability of 10 Darcy. Compared to the homogeneous layer results, the Stoneley wave transmission coefficient is significantly higher when frequency is higher than 2 kHz, and the reflection coefficient shows some complex features. The smaller transmission loss of the multiple layer model is consistent with the smaller average attenuation of the model shown in Figure 5-6, which is due to the same cause

we discussed in relation to Figure 5-6. The reflection coefficient is very different from the homogeneous model result at higher frequences (> 2 kHz). It decreases, then increases with frequency, showing that at high frequencies the reflection from the multiple layered zone is very sensitive to the fine structure of the zone. At low frequencies (< 1 kHz) the homogeneous and heterogeneous model results approach each other. Compared to the double layer model results at low frequencies, we see again that very low frequency Stoneley waves see only the overall fluid transmissivity of a permeable zone, regardless of the fine structure of the zone.

5.4.4 Random permeability structure

We now study the case where the permeability within the permeable zone can have random but continuous variations. We model this situation using the 1-D continuous random model generated using the 1-D Gaussian correlation function (see Chapter 2). The permeability variation is shown in Figure 5-12 which has an average value of 10 Darcy and a standard deviation of 28%. This permeability variation is assigned to a permeable zone 0.4 m thick with a porosity value of 0.3. Figure 5-13 shows the resulting Stoneley wave transmission and reflection coefficients across the heterogeneous zone. For comparison, we also plot the results (dashed curves) calculated using a homogeneous layer model [Equations (5.28) and (5.29)], in which we used the average permeability of 10 Darcy and the same thickness of 0.4 m for the layer.

Despite the considerable permeability variation within the permeable zone, the heterogeneous model results are not very different from the homogeneous model results, except the transmission and reflection coefficients for the heterogeneous model are a little higher than the homogeneous model result beyond 2 kHz. At low frequencies, especially approaching the zero frequency, the results from both models converge towards each other. This convergence occurs at higher frequency than the previous double layer and multiple layer models.

5.4.5 Model comparison

To further investigate the similarity and difference of Stoneley wave propagation across the different heterogeneity models, we plot the Stoneley wave amplitude change *vs.* distance across the permeable zone in Figure 5-14 for these models. The amplitude *vs.* distance curves are calculated for a 5 kHz Stoneley wave by using the propagator matrix method to compute the transmitted wave amplitude [Equation (5.24)] at each finite difference grid inside the permeable zone.

We compare three situations: (1) the multiple layer structure given in Figure 5-10; (2) the random permeability variation model given in Figure 5-12; and (3) the homogeneous layer model. The parameters for all three models are the same (i.e. same porosity, thickness, and average permeability, *etc.*). As shown in Figure 5-14, when the Stoneley wave enters the permeable zone, the amplitude begins to decrease. For the random permeability model, although the heterogeneous variation is evident on the amplitude, the overall result (solid line) is not very different from the homogeneous model result, because of the continuous permeability variation. For the multiple layer model, which has a discontinuous permeability variation, the amplitude *vs.* distance curve is distinctly different from the homogeneous and the continuous model results. The amplitude is attenuated in the permeable layer, but remains constant in the non-permeable layers, resulting in a step-like decrease of the wave amplitude. As a result, the total amplitude reduction is less than those of the other two models. This result is also consistent with the Stoneley wave attenuation results plotted in Figure 5-6 which shows that for the same average permeability the discontinuous permeability model has lower attenuation than those from the continuous models.

In the following application section, we will use heterogeneous permeability models to study the laboratory and field Stoneley wave data, which could not be explained using the homogeneous model theory. For the laboratory data set, we will show that only the discontinuous permeability model can explain the data very well.

5.5 Application to Acoustic Logging Data from heterogeneous formations

5.5.1 Data from laboratory experiments

Winkler *et al.* (1989) were the first to perform laboratory experiments to evaluate Biot's theory for acoustic propagation in a porous borehole. Four samples were measured in their experiments. Three were synthetic materials made of resin-cemented glass beads (sample A, B, and C). One was a rock sample: Berea sandstone (sample S.S.). All these samples were cylindrical in shape with a diameter of 15.2 cm for the synthetic samples and 21.6 cm for the Berea sandstone sample. A borehole was drilled along the sample axis. The diameter of the hole was 1.06 cm for the synthetic samples and 0.93 cm for the rock sample. They showed the experimental results on Stoneley wave propagation in those permeable porous materials. For three samples (samples A, C, and S.S.), they found excellent agreement between theory and experiment (Winkler *et al.*, 1989). However, for one sample (sample B), the measured Stoneley wave velocity and attenuation were found to significantly deviate from the theoretical prediction. In a recently published paper, Tang *et al.* (1991a) applied the simplified Stoneley propagation model to Winkler *et al.*'s (1989) experimental data. Again, they found excellent agreement between theory and experiment for the three samples (A, C, and S.S.) and disagreement for sample B. The sample and fluid properties of sample B are summerized in Table I for reference. The comparison between the modeling results of Tang *et al.* (1991a) and experimental data is shown in Figure 5-15, in which both the Stoneley wave attenuation and velocity dispersion are over-estimated by the theory. Winkler *et al.* (1989) suggested that the discrepancy between the theory and experiment may be due to either the heterogeneities in the sample, or the limitation of the Biot's dynamic fluid flow (i.e. slow wave) model. With the theory of Stoneley wave propagation in heterogeneous formations developed here, we can test the first hypothesis by modeling the laboratory data using heterogeneous

permeability models.

We first checked the effects of model parameters on the data fitting using the homogeneous theory. We change the tortuosity value from 1 to 3. The velocity and attenuation change moderately at higher frequencies but the results cannot fit the data (Figure 5-16). Figure 5-17 shows the modeling results for permeability equals to 1 Darcy and 5 Darcy cases. The 1 Darcy curves have smaller discrepancy with the data. But the theory and data still do not agree in the medium frequency range. Figure 5-18 shows the modeling results for porosity equals to 0.15 and 0.35 cases. For the 0.15 porosity case, the theory fits the velocity data but not the attenuation. We also test the β value in Equation (3.24). The results for $\beta = 2$ (round pores) and $\beta = 3$ (fractures) are almost identical. Because the homogeneous model theory cannot explain the data, we turn to the use of heterogeneous models.

We use the measured parameters given in Table I. From the measured rock and fluid density, velocity, and incompressibility, we calculated the solid rock frame compressibility correction term ξ using the formula of Norris (1989), which gives $\xi = 0.264$, We use this ξ in Equation (5.6) for numerical modeling. From the formation and fluid acoustic properties and borehole diameter, we calculate the equivalent elastic formation Stoneley wave number k_e using the elastic wave theory (Cheng and Toksöz, 1981), which is also given in Equation (4.8).

We now discuss the choice of heterogeneous permeability models. The constraint on these models is that the average permeability must equal the permeability value (2.3 Darcy) measured from the sample. A natural model choice is the random medium model which has a mean value of 2.3 Darcy and the permeability fluctuates around this value with specified deviation (i.e. continuous model described in Chapter 2). However, the modeling results in Figures 5-5 and 5-6 indicate that the continuous permeability model results do not differ greatly from the homogeneous model results. On the other hand, the discontinuous permeability model results in these figures (especially Figure 5-6) show significantly less attenuation and dispersion compared

with the homogeneous model results, as is also the case for the data shown in Figure 5-15. We therefore use a set of 1-D discontinuous models to study the experimental data. For comparison, both the continuous and discontinuous models will be tested against the measured data.

In our modeling, the numerical model length L is taken as 0.2 m, which is approximately the array aperture spanned by the scanning receiver in the experiment (Winkler *et al.*, 1989). The radial model size is about 10 times that of the borehole diameter. The continuous permeability model is generated using an 1-D Gaussian correlation function. The continuous heterogeneous variations have a mean of 2.3 Darcy and a standard deviation of 30% (Figure 5-3). The discontinuous permeability models are generated using the Poisson process with various thickness values ranging from 0.004 m (50 layers) to 0.1 m (2 layers). The high permeability layers have a permeability value of 4.6 Darcy, while the low permeability layers 0.01 Darcy, the average is about 2.3 Darcy.

The modeled Stoneley wave velocity and attenuation results from both continuous and discontinuous models are shown together with the measured data in Figure 5-19. As expected from our previous modeling experience, the continuous model results do not differ significantly from the homogeneous model results. However, the discontinuous model results agree with the data quite well. The simplest 2-layer model results only slightly differ from the multilayer model results. We average the Stoneley wave velocity and attenuation curves for 30 discontinuous 1-D Poisson models and plot them against the data in Figure 5-20. The error bars on the curves represent one standard deviation obtained from all the modeling results. There is an excellent agreement between the modeling results and the data. It is worthwhile to note that this agreement holds for both phase velocity and attenuation. It is also worthwhile to emphasize that the same excellent agreement is seen for the different 1-D Poisson models with different average layer thickness used in the numerical modeling. In these models, about 50% of the formation has high permeability, and the other 50%, low

permeability.

Our numerical modeling results is consistent with the hypothesis that the sample heterogeneity may be the cause of discrepancy between the experimental data and the theory for a homogeneous formation. Our model requires that some portions of the borehole are very permeable and the other portions are impermeable, similar to the Poisson layering models used in the numerical modeling. We cannot independently verify whether this is the case.

5.5.2 Data from URL-M11 well

In this section, we apply the theory of Stoneley wave propagation across permeability heterogeneities to the acoustic logging data obtained from URL-M11 well (Paillet, 1984). This example demonstrates that the numerical modeling of the logging data not only will help determine the fluid transmissivity of a permeable fracture zone, but also assesses the distribution of permeability across the fracture zone.

The data set was obtained in a borehole (M11 well) at the Underground Research Laboratory (URL) located on the southern edge of the Canadian shield in Southeastern Manitoba, Canada. A major isolated fracture zone was detected at a depth of about 188 m in this borehole. Figure 5-21 shows the televiewer log, the Stoneley waveform data, and the Stoneley amplitude log data (open circles) in the vicinity of the fracture. In this figure, the modeling synthetic Stoneley waveform and amplitude log (solid line) of Tang *et al.* (1991a) using the simple homogeneous permeability layer model [Equations (5.28) and (5.29)] are also shown. The isolated fracture appeared in a single sub-horizontal band on the televiewer log, but additional high resolution televiewer logs indicated that this fracture was actually composed of several subparallel fractures. The logging waveforms were obtained using a sparker source at 5 kHz, the borehole and the tool diameters were 15.2 and 5.1 cm, respectively. The source-receiver spacing was 2.14 m.

As seen from the logging waveforms, the Stoneley waves are significantly attenu-

ated across the fractures. A Stoneley wave reflection at the top can also be observed, as indicated by the line drawn on the observed waveform log in Figure 5-21, which marks the moveout of the reflected waves. A feature that is of special interest in this study is that the field data do not have a clearly traceable down-going reflection, whereas the homogeneous layer theory of Tang *et al.* (1991a) predicts a symmetric pattern for the up-going and down-going reflections (see the synthetic waveforms in Figure 5-21). The non-symmetric nature inherent in the logging data can also be seen from the Stoneley wave transmission log across the fracture zone.

The Stoneley wave transmission log is measured as the amplitude deficit or attenuation across the fractures. This measurement has long been used in fracture detection and characterization (Paillet, 1980). To compute the attenuation, one first applies a window that contains Stoneley arrivals. Then the mean square wave energy (sum of the square of each sampled wave amplitude within the window) is computed and modified by a half cosine taper. The attenuation or transmission log is measured from the amplitude deficit - the "representative" percentage decrease of the average wave energy in the time window over the vertical distance of one source-receiver separation. The transmission log obtained in this way gives a measure of the square of transmission coefficient around the measurement frequency (Tang *et al.*, 1991a).

The amplitude deficit log in Figure 5-21 was modeled by Tang *et al.* (1991a) using the homogeneous layer model [Equations (5.28) and (5.29)]. The model parameters were: permeability = 2.5 Darcy, porosity = 0.35, and layer thickness = 0.4 m (measured from the width of the fracture zone image on the televiewer log). The synthetic Stoneley waveform log was also computed using these parameters. The overall match between the calculated deficit log (solid line) and the measured data (open circles) is quite good, especially for the upper part of the zone. Both logs show an average deficit of about 82% across the zone, which provides a measure of the overall fluid transmissivity across the fracture zone. The major difference between the two logs is at the lower part of the zone. The calculated amplitude shows a sharp decrease at

the top (which is confirmed by the data). However, the amplitude decrease at the bottom part of the deficit log is more gradual, while the calculated log from the homogeneous layer model predicts a sharp decrease. The sharp amplitude decrease at the top and the gradual decrease at the bottom, together with the fact that the reflection is seen clearly at the top but not at the bottom, led Paillet (1984) to hypothesize that the permeable fracture zone may have a non-uniform permeability distribution, and that the bottom part of the zone may be less permeable than the top part. With the heterogeneous permeable zone theory developed in this study, we can test this hypothesis by modeling the Stoneley wave transmission and reflection data using a variable permeability model for the fracture zone.

Although various permeability models can be chosen to model the Stoneley wave data, we use a simple permeability distribution model as shown in Figure 5-22. In this model, the permeability is assumed to attain its maximum at the top boundary, and smoothly varies to zero at the bottom boundary $z = L = 0.4$ m. This variation is given as $\kappa(z) = \kappa_0[1 + cos(\frac{z}{L}\pi)]$ where κ_0 is chosen by requiring that $\frac{1}{L}\int_0^L \kappa(z)dz =$ 2.5 Darcy, which gives $\kappa_0 = 2.5$ Darcy. In this way, the total fluid transmissivity of the fracture zone remains the same as the homogeneous layer model of Tang *et al.*, (1991a). The top boundary has a sharp permeability contrast while the bottom boundary has no permeability contrast (Figure 5-22). In our numerical modeling, the other parameters used are the same as in the homogeneous layer model. In addition, because of the presence of the logging tool, we use an effective borehole radius calculated using $\bar{R} = \sqrt{R^2 - R_{tool}^2}$.

For the permeability model in Figure 5-22, two numerical modeling experiments were performed. In the first experiment, the incident Stoneley wave approaches the heterogeneous zone from the bottom boundary (z = L) where there is no permeability contrast. This experiment is performed to simulate the logging operation of the acoustic logging tool that is being pulled towards the fracture zone from below the zone. For the second experiment, we let the incident Stoneley wave approach the

model from the top boundary ($z = 0$), where there is a sharp permeability contrast. This experiment is performed to simulate the acoustic logging tool that has just passed through the fracture zone and is being pulled away from the zone. The downgoing Stoneley wave from the source will interact with the fracture zone and the resulting reflection will be recorded by the receiver.

Figure 5-23 shows the calculated transmission and reflection coefficients for the two numerical modeling experiments in the frequency range of $0 \sim 8$ kHz. The transmission coefficients for the two experiments are very close and are around the value of 0.43 at about 5 kHz. This will produce an amplitude deficit value of about $(1 - 0.43^2) \times 100\% \approx 0.82\%$, in very good agreement with the measured value on the amplitude log. However, the reflection coefficients for the two experiments differ greatly at higher frequencies, although they approach each other towards the zero frequency (this suggests that the reflection data of very low frequency tube waves is not sensitive to the structure of the permeable zone, same as shown in Figures 5-9, 5-11, and 5-13). For the Stoneley wave approaching the top boundary of the fracture zone (sharp permeability contrast boundary), the reflection coefficient is about 0.1, which is about the same order of magnitude as the observed reflected Stoneley wave amplitude shown in Figure 5-21. For the Stoneley wave approaching the bottom boundary (zero permeability contrast boundary), the reflection coefficient value around 5 kHz is only about 0.02. Given the noise level in the measured Stoneley waveform data in Figure 5-21, reflected waves with such a small amplitude cannot be visually identified. Thus, the variable permeability model shown in Figure 5-22 can model the reflection data very well.

To model the transmission data, we again need to use the finite difference method and the propagator matrix formulation result given in Equation (5.19). When the receiver of the logging tool enters the fracture zone (source below receiver), the Stoneley wave is attenuated because of the propagation loss due to permeability. This amplitude loss can be modeled by computing the Stoneley wave amplitude reduction from

the bottom boundary to the receiver (assuming wave incidence from the bottom). In this way, amplitude loss as a function of the receiver location can be modeled. Similarly, when the source enters the permeable zone (receiver above the zone), the Stoneley wave amplitude *vs.* source location can be simulated by computing the amplitude reduction from the top boundary to the source (assuming wave incidence from the top boundary using reciprocity).

We use again the same variable permeability model shown in Figure 5-22. The simulated amplitude log (solid curve) for the permeability model in Figure 5-22 is plotted in Figure 5-24 with the measured amplitude log (dots) and the homogeneous layer model result (dashed curve).

Although our simulation result is modeled in the frequency domain for the central wave frequency of 5 kHz, the overall amplitude decrease across the fracture zone is not different from the time domain measurement of the waveforms. The major improvement by our heterogeneous permeability model is at the lower portion of the amplitude deficit log. Both the numerical result and the data show the same gradual change of amplitude at the bottom boundary of the fracture zone, while the homogeneous model result shows the same sharp amplitude change as at the top boundary. Therefore, by using the variable permeability model, we successfully explain that the gradual amplitude change at the lower boundary is due to the small permeability for the lower portion of the zone as compared to the upper portion. Thus, in addition to the agreement for the reflection data, the good agreement between theory and the transmission data again supports the interpretation of the fracture zone permeability distribution, as given by the variable permeability model (Figure 5-22).

The numerical modeling results confirm the hypothesis that the bottom part of the URL M11 well fracture zone is less permeable than the top part. This example also demonstrates how the numerical modeling approach can be used to assess the borehole permeability heterogeneity from logging data.

5.6 Conclusions

An effective numerical analysis method has been developed to handle Stoneley wave propagation through borehole heterogeneities. This technique is based on finite difference modeling of dynamic fluid flow in heterogeneous formation and the propagation matrix method for wave propagation in 1-D heterogeneous medium.

This technique can be used to calculate the effective Stoneley wave attenuation and velocity dispersion if the wave propagation distance is within the heterogeneous formation. When the heterogeneity variation is confined to a zone whose thickness is small compared to the propagation distance, the technique can be used to calculate the Stoneley wave transmission across the permeable zone and the reflection from the zone.

For continuous permeability variations, the cumulative Stoneley wave attenuation and velocity dispersion can be well described by a homogeneous permeability model having the average properties of the heterogeneous medium. For discontinuous variations, significant deviation from the homogeneous model results exists only when the medium has high permeability. The numerical modeling results demonstrate that, for most situations (low to medium permeability), the homogeneous model theory can be reliably used to obtain average permeability of a heterogeneous permeable formation.

For Stoneley wave transmission and reflection at a heterogeneous permeable structure, the transmitted wave amplitude is controlled by the overall fluid transmissivity of the structure, although some discrepancy may arise depending on the structure of the heterogeneities. Reflection, on the other hand, is most sensitive to the structure of the heterogeneities. However, at very low frequencies, both transmission and reflection are controlled by the overall fluid transmissivity of the structure, irrespective of the distribution of heterogeneities within the structure. This shows that the low frequency tube wave can be used as an effective means to measure fluid transmissivity of the permeable structure. The Stoneley wave reflection at higher frequencies can be used to detect heterogeneity variation within the structure.

The numerical modeling results have been verified by both laboratory experimental data and field acoustic logging data. Thus, for problems concerning acoustic logging in heterogeneous porous formations, the numerical method can be effectively used to help determine formation permeability heterogeneities and their fluid transmissivity.

Table I. Physical properties of sample B in Winkler *et al.*'s (1989) experiments

$\phi(\%)$	κ_0(mD)	τ	ρ_0(kg/m^3)	μ(cp)	V_f(m/s)	ρ_e(kg/m^3)	V_p(m/s)	V_s(m/s)
22.9	2300	2.4	934	9.34	999	1960	2930	1610

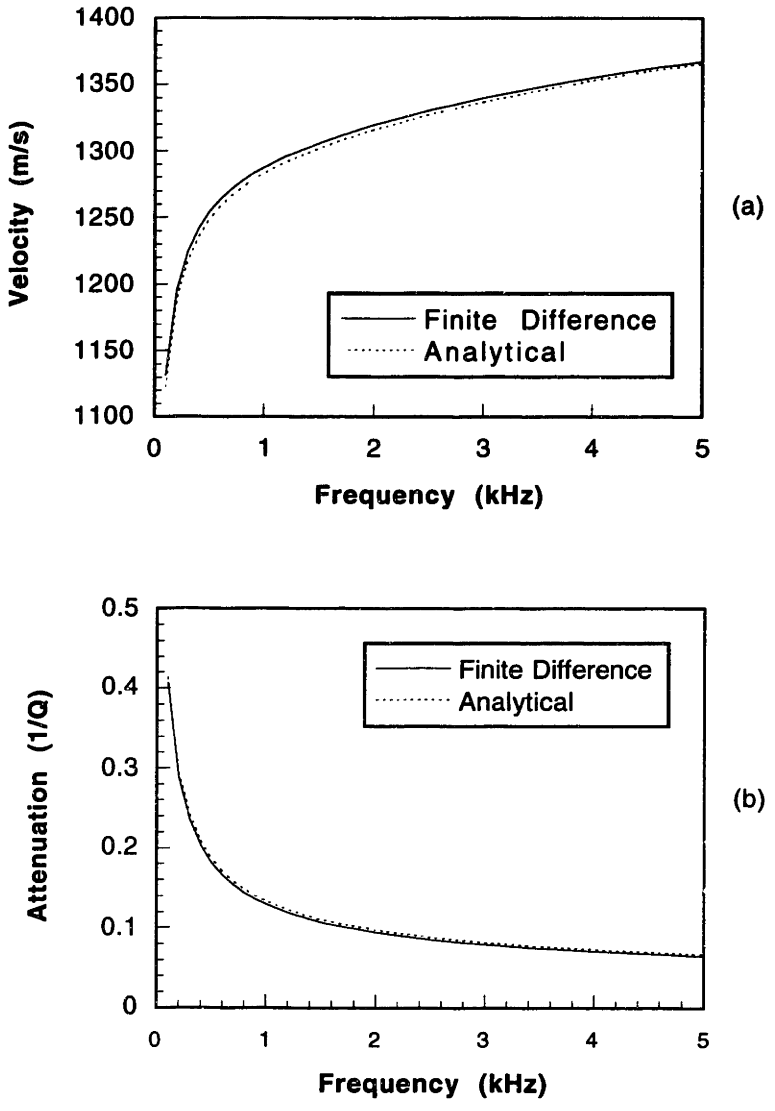

Figure 5-1: Comparison between analytical (dashed curves) and finite difference (solid curves) results: (a) Stoneley wave velocity, (b) Stoneley wave attenuation.

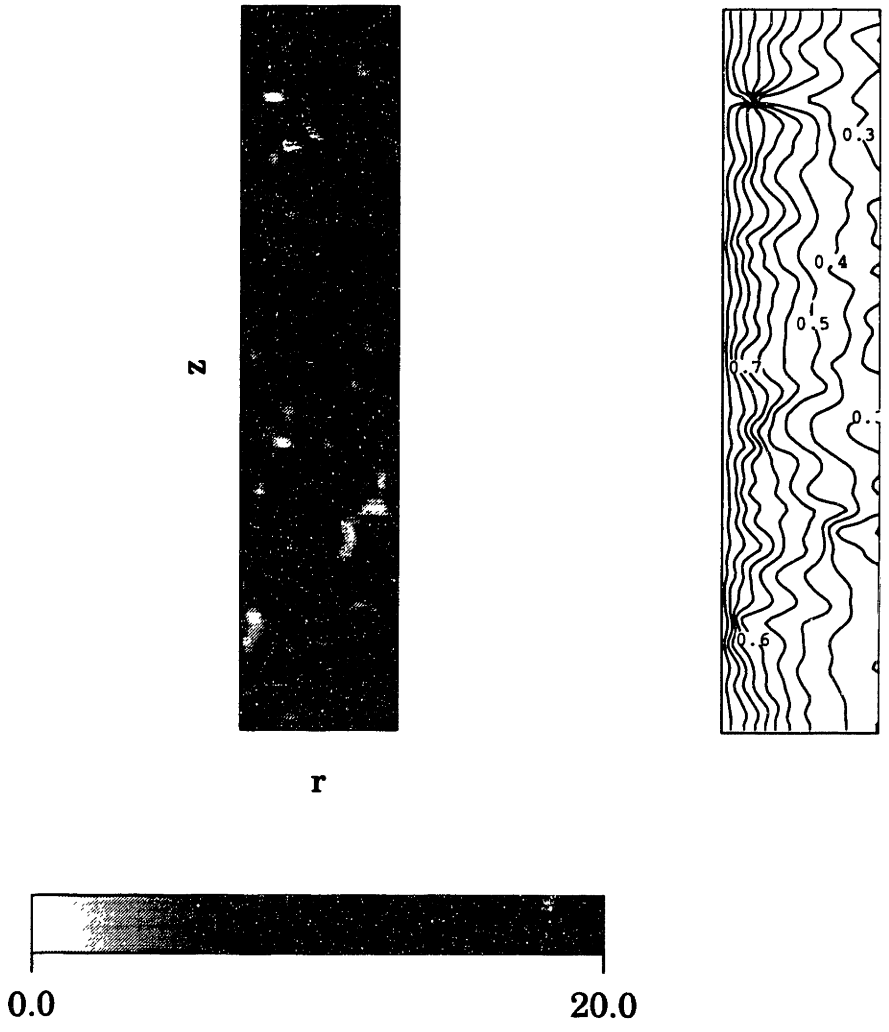

Figure 5-2: Random permeability model (left) generated using 2-D Gaussian correlation function and simulated pore fluid pressure contour (right) in the formation for a 1000 Hz Stoneley wave. The model dimensions are: 10 m in the z-direction and 0.5 m in the r-direction. Permeability ranges from 0 - 20 Darcy.

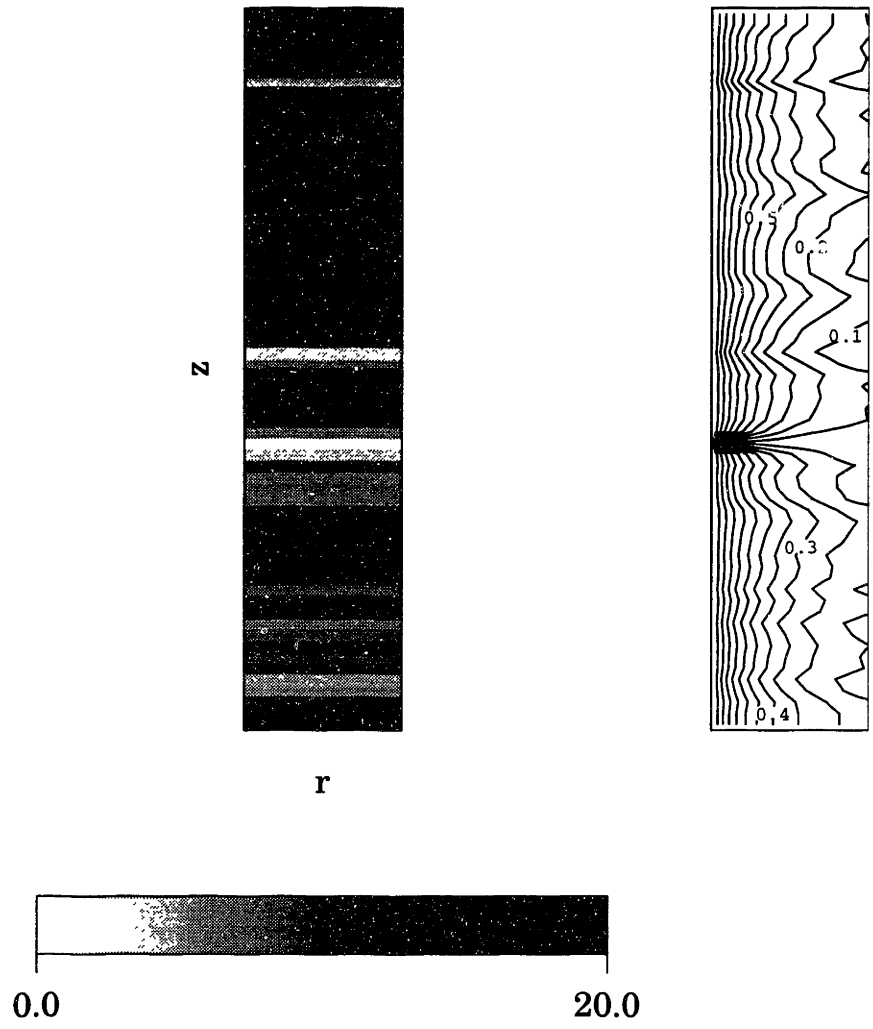

Figure 5-3: 1-D permeability model (left) with a Gaussian correlation function and simulated pore fluid pressure contour (right) for a 1000 Hz Stoneley wave. Model dimensions are the same as in Figure 5-2.

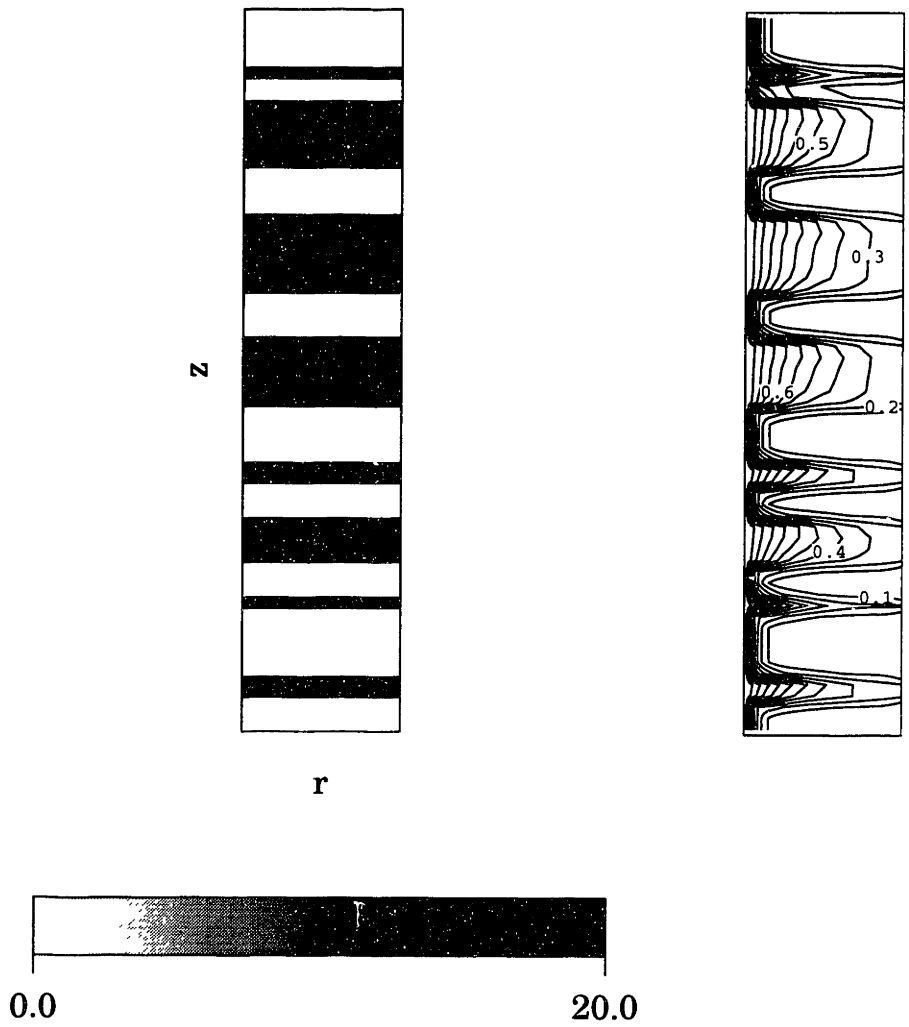

Figure 5-4: Cyclic permeability model (left) and the simulated pore pressure contour (right) for a 1000 Hz Stoneley wave. Model dimensions are the same as in Figure 5-2.

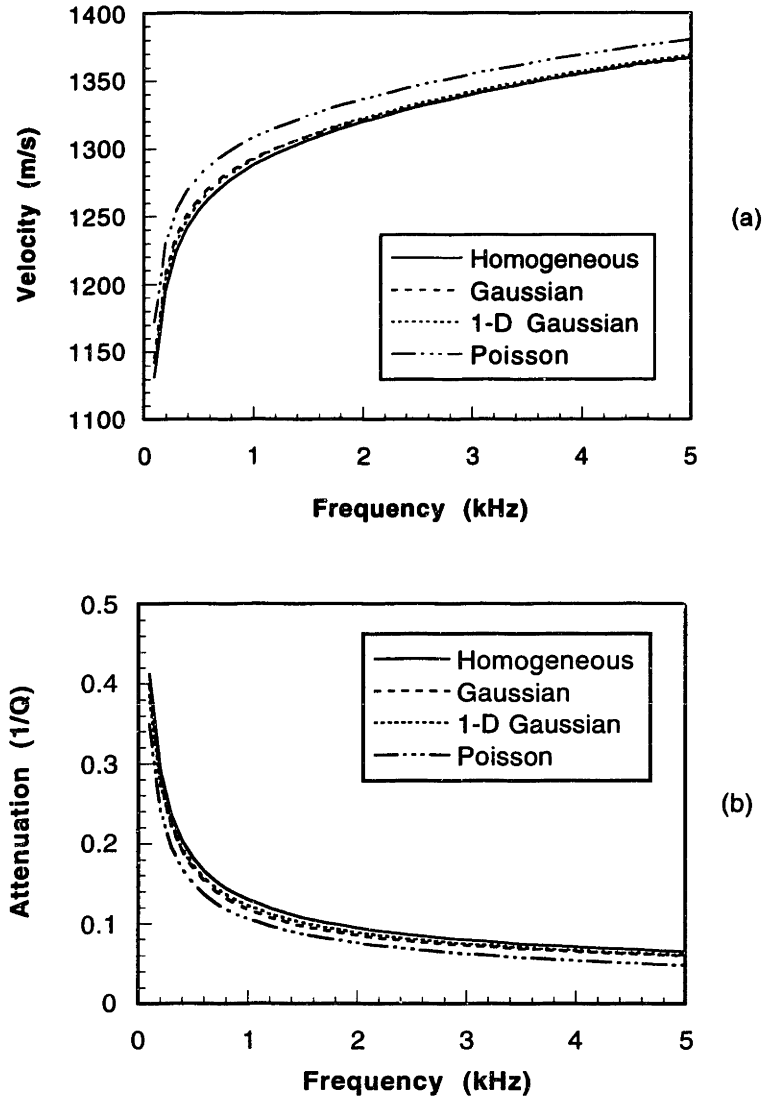

Figure 5-5: Stoneley wave phase velocity (a) and attenuation (b) curves for different heterogeneous permeability models. The average permeability of the models is 1 Darcy.

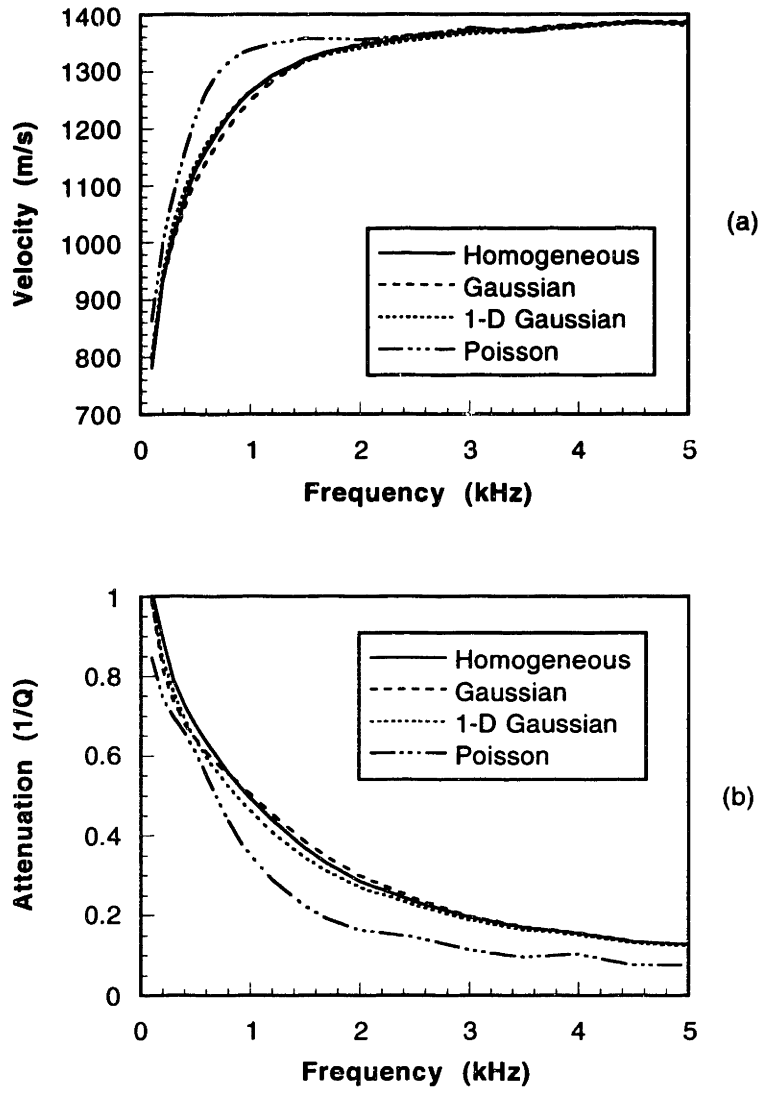

Figure 5-6: Stoneley wave phase velocity (a) and attenuation (b) curves for different heterogeneous permeability models. The average permeability of the models is 10 Darcy.

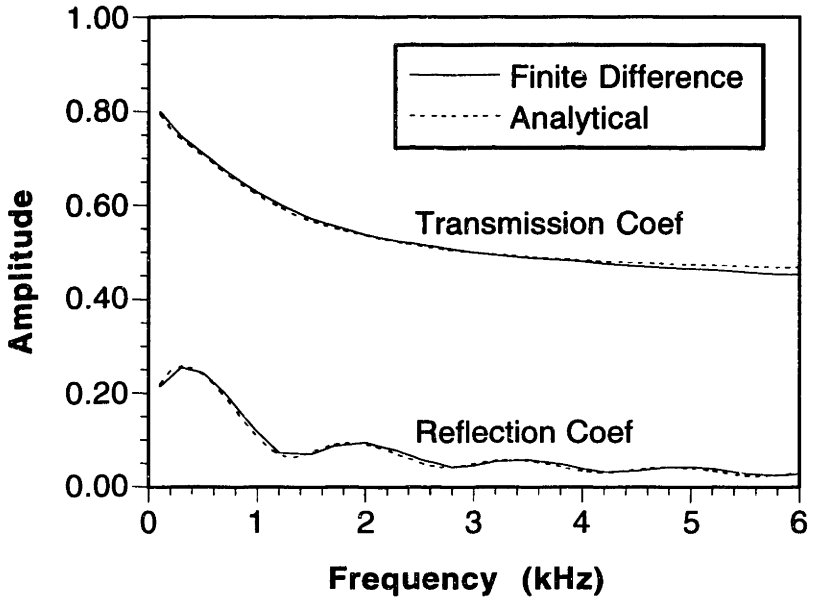

Figure 5-7: Testing the results of numerical modeling of Stoneley wave transmission and reflection coefficients across a permeable zone (solid curves) using the analytical solution results (dashed curves).

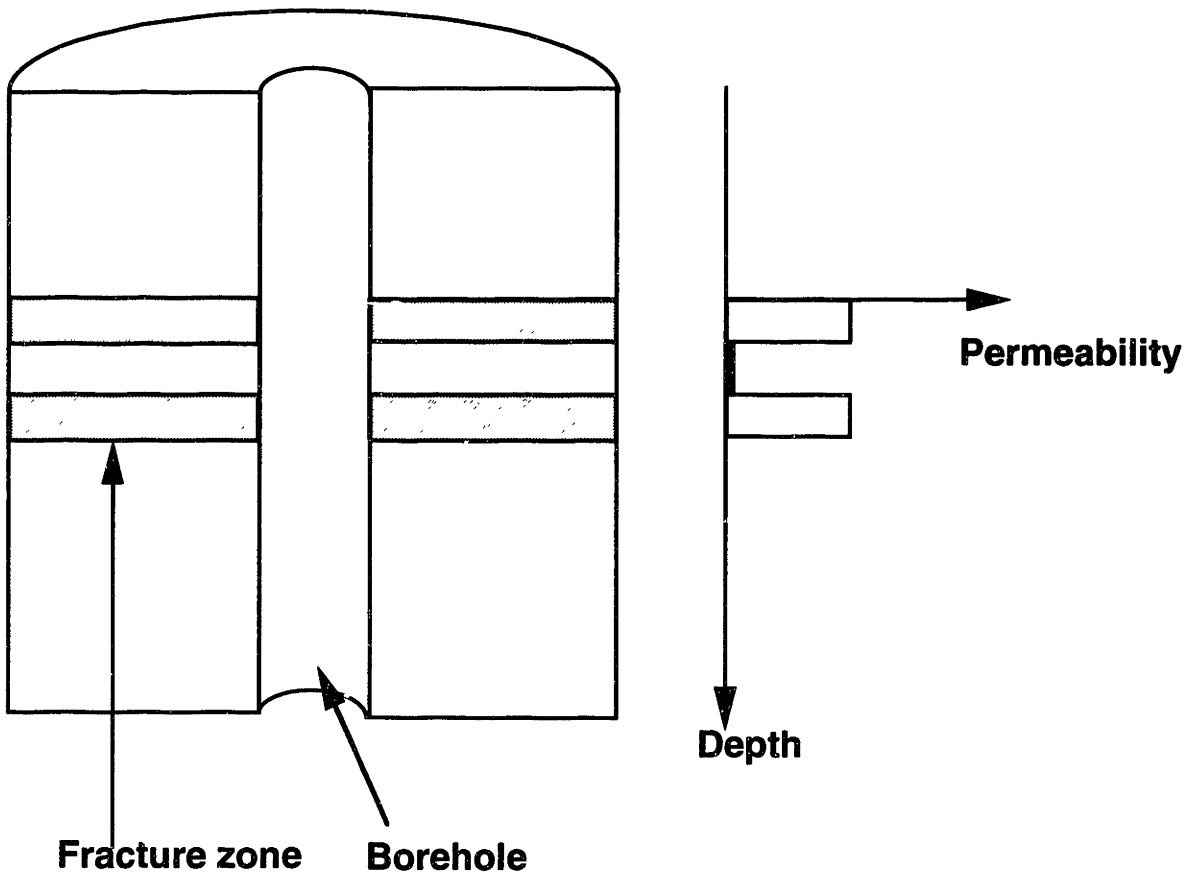

Figure 5-8: Double permeability layer model for modeling Stoneley wave propagation. Two layers of 10 Darcy permeability with 0.15 m thickness and separated by a non-permeable formation of 0.2 m thick.

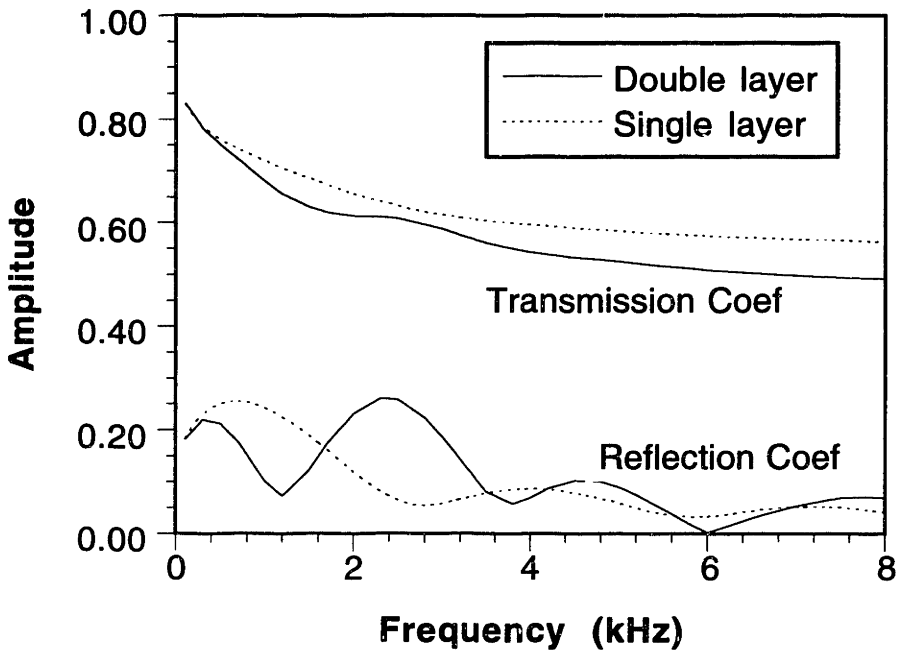

Figure 5-9: Stoneley wave transmission and reflection coefficients (solid curves) for the double layer model shown in Figure 5-8. For comparison, the results for a homogeneous layer with cumulative thickness of 0.3 m and 10 Darcy permeability are also shown (dashed curves). The two results agree only in the low frequency limit.

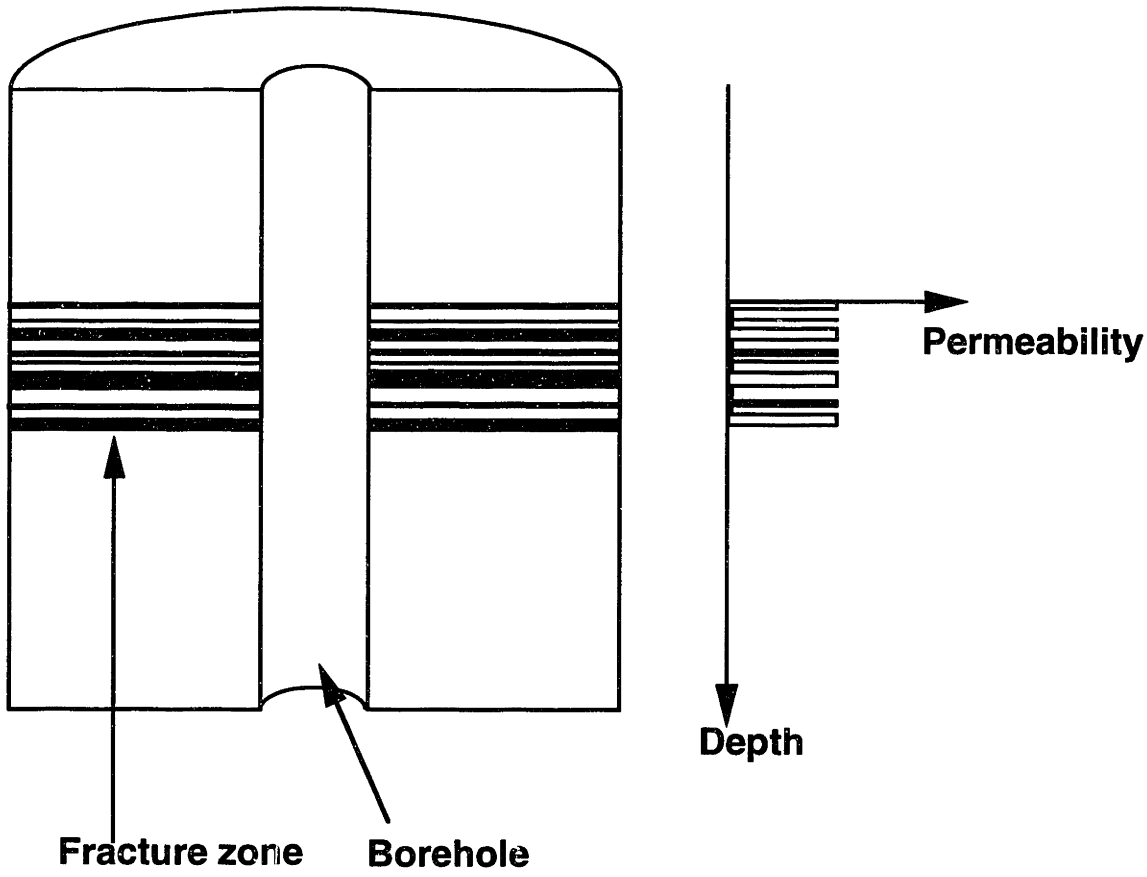

Figure 5-10: Multiple layer permeable zone model. The thickness and average permeability of the zone are 0.4 m and 10 Darcy, respectively.

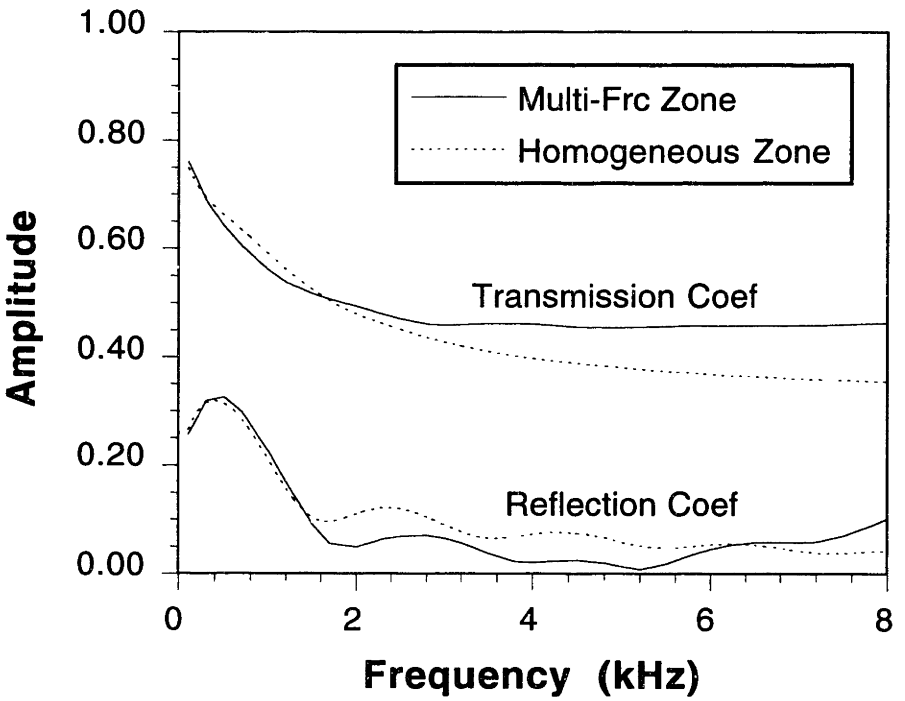

Figure 5-11: Stoneley wave transmission and reflection coefficients for the multiple layer zone model (solid curves) shown in Figure 5-10. For comparison, the results for a homogeneous zone of thickness 0.4 m and permeability 10 Darcy are also shown (dashed curves).

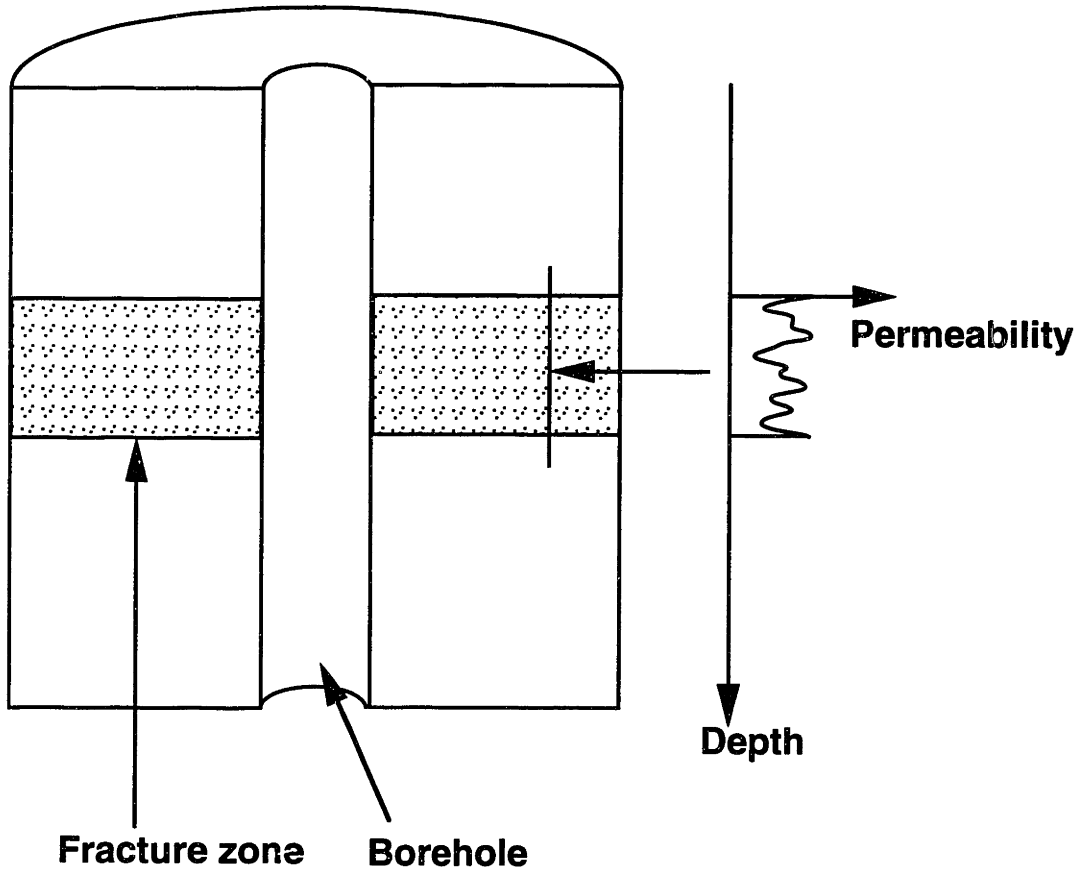

Figure 5-12: Permeability zone model with random permeability variation along borehole axial direction. The variation is characterized by Gaussian correlation function. The average permeability of the model is 10 Darcy.

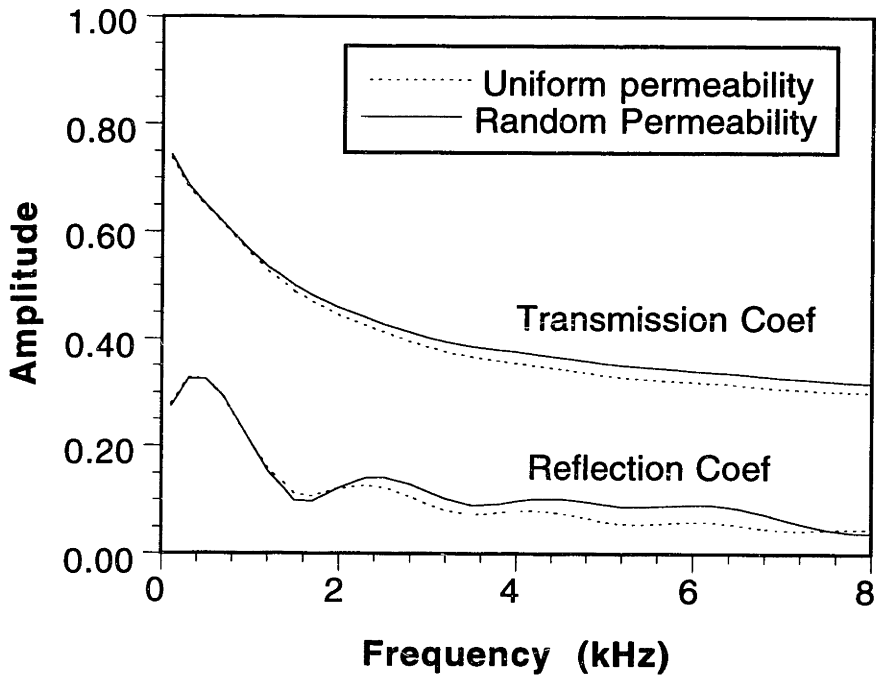

Figure 5-13: Stoneley wave transmission and reflection coefficients (solid curves) for the random permeability model of Figure 5-12. The results for a uniform permeability (10 Darcy) layer are also shown (dashed curves).

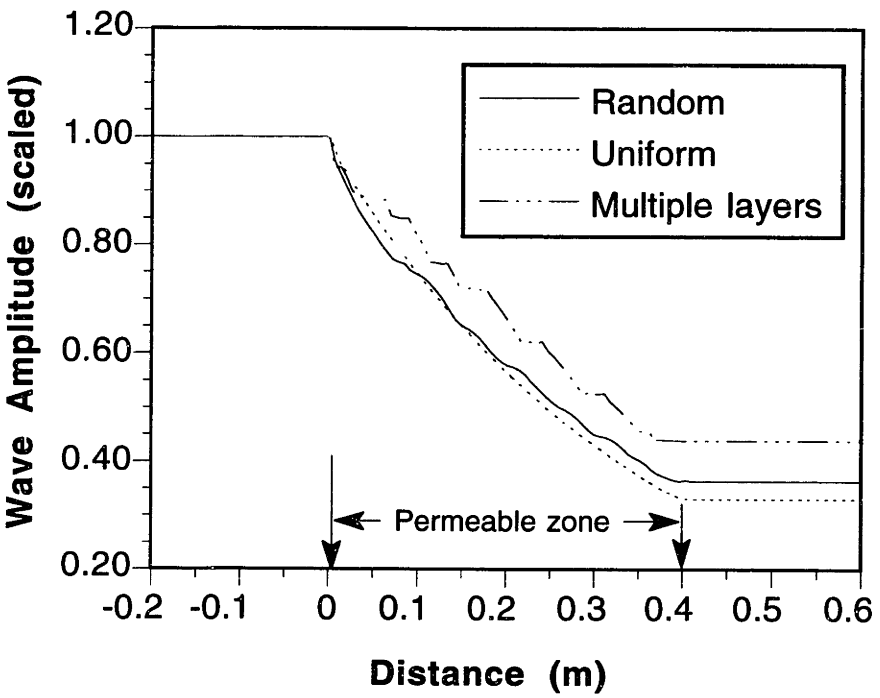

Figure 5-14: Comparison of Stoneley wave (5 kHz) amplitude variation across a 0.4 m permeable zone for homogeneous model (dashed curve), random permeability model (solid curve), and the multiple layer model (solid-dashed curve).

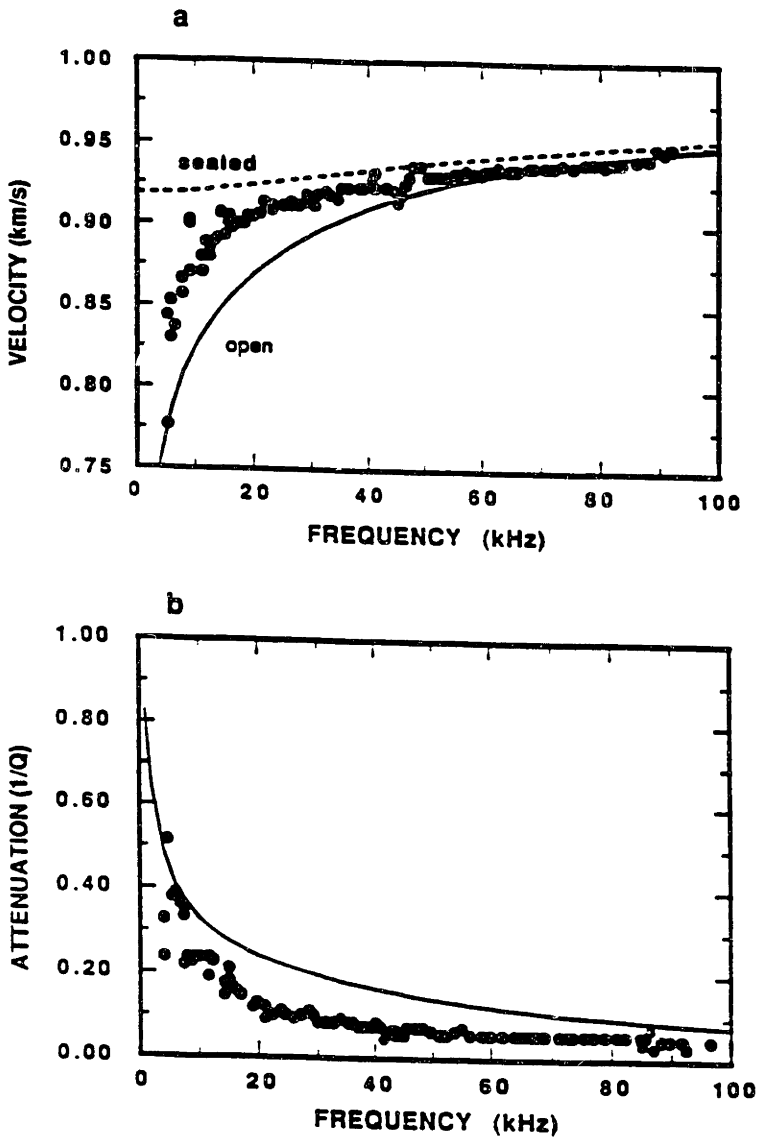

Figure 5-15: Winkler *et al.*'s (1989) experimental Stoneley wave velocity (a) and attenuation (b) data for sample B (dots) and the theoretical predictions calculated using a homogeneous formation model (from Tang *et al.*. 1991a). There is a significant discrepancy between the data and homogeneous model theory.

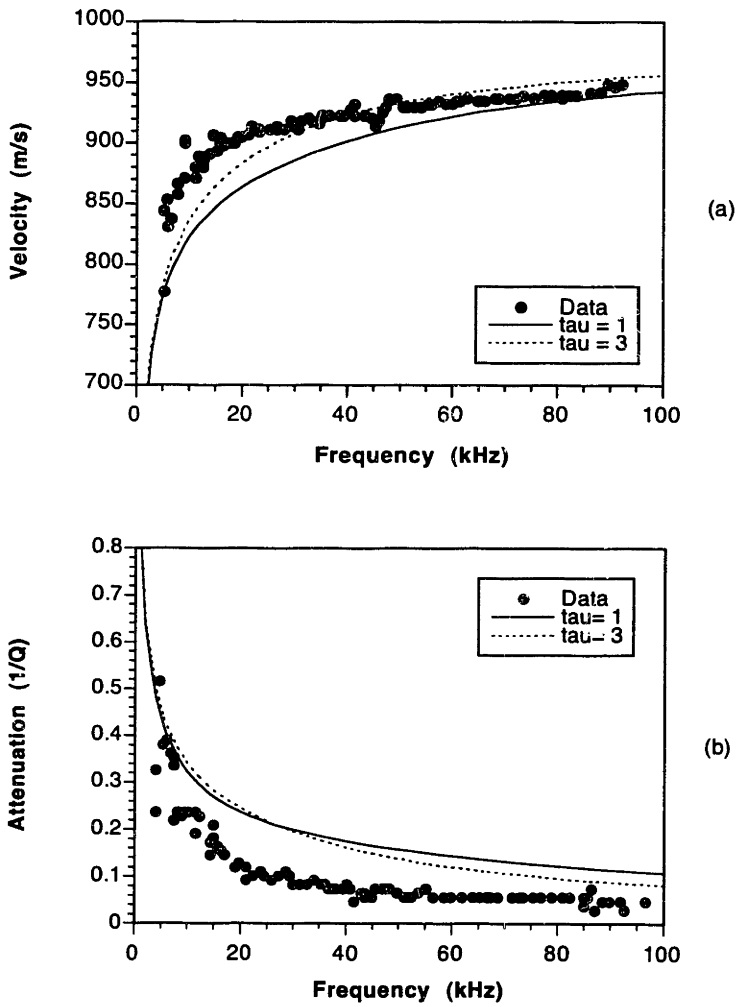

Figure 5-16: Modeling of Stoneley wave velocity (a) and attenuation (b) for $\tau = 1$ and $\tau = 3$ cases. Neither value fits the data.

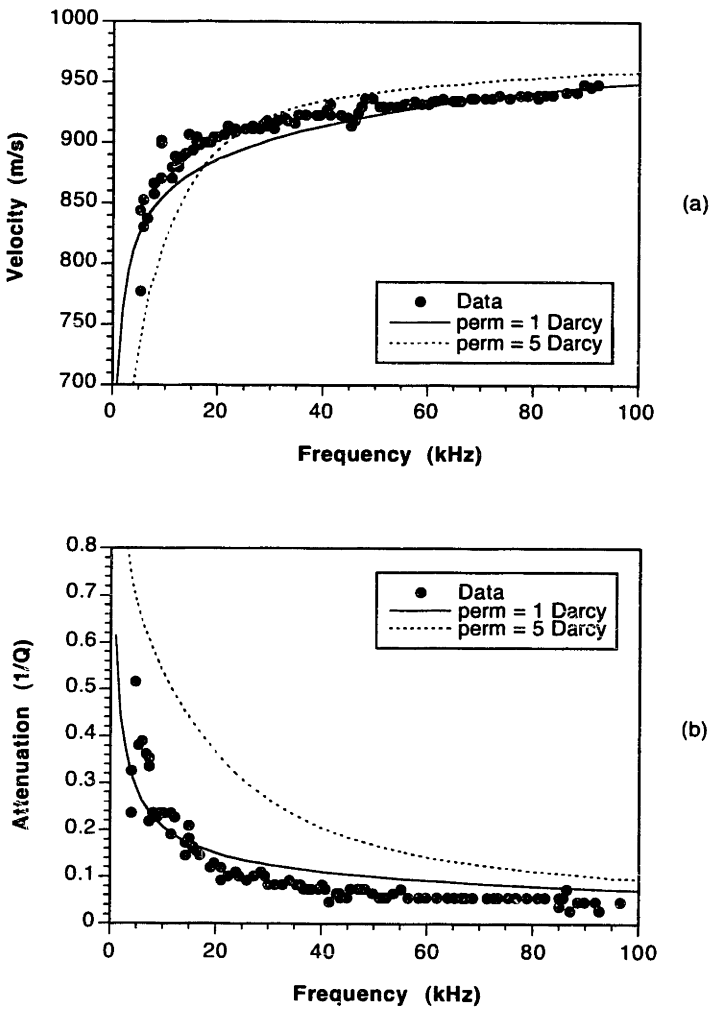

Figure 5-17: Modeling the effects of permeability on the Stoneley wave velocity (a) and attenuation (b) for 1 and 5 Darcy cases. The 1 Darcy permeability value results in smaller discrepancy between theory and data. But the theoretical results still do not fit the data well.

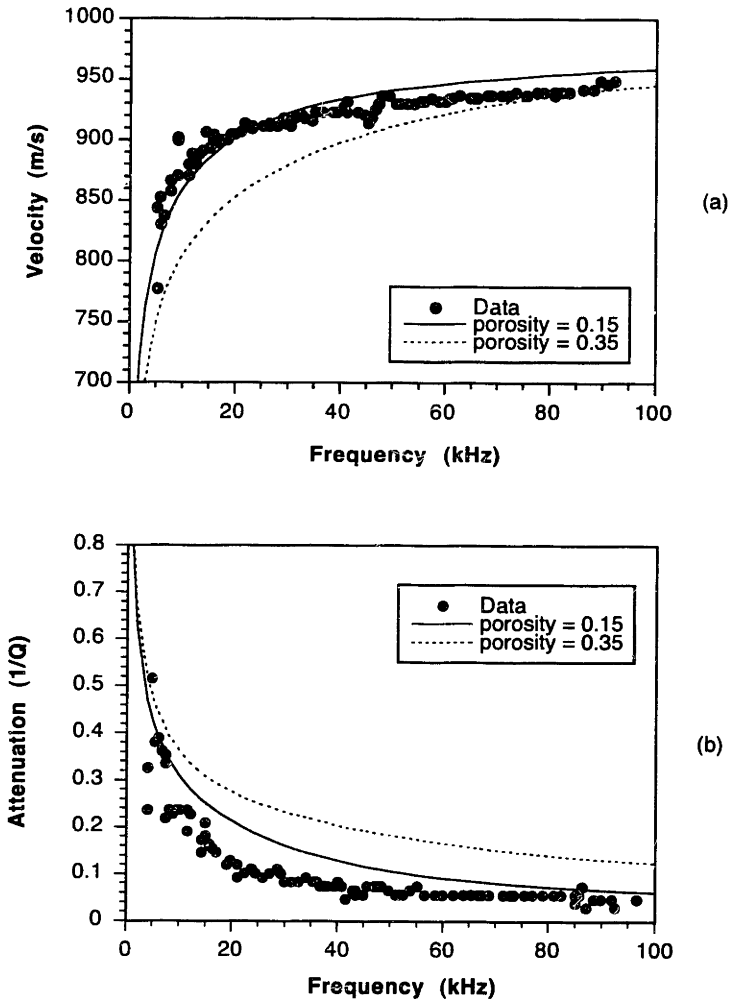

Figure 5-18: Modeling of Stoneley wave velocity (a) and attenuation (b) data for porosity ϕ equals 0.15 and 0.35. The $\phi = 0.15$ case fits the velocity data but not the attenuation.

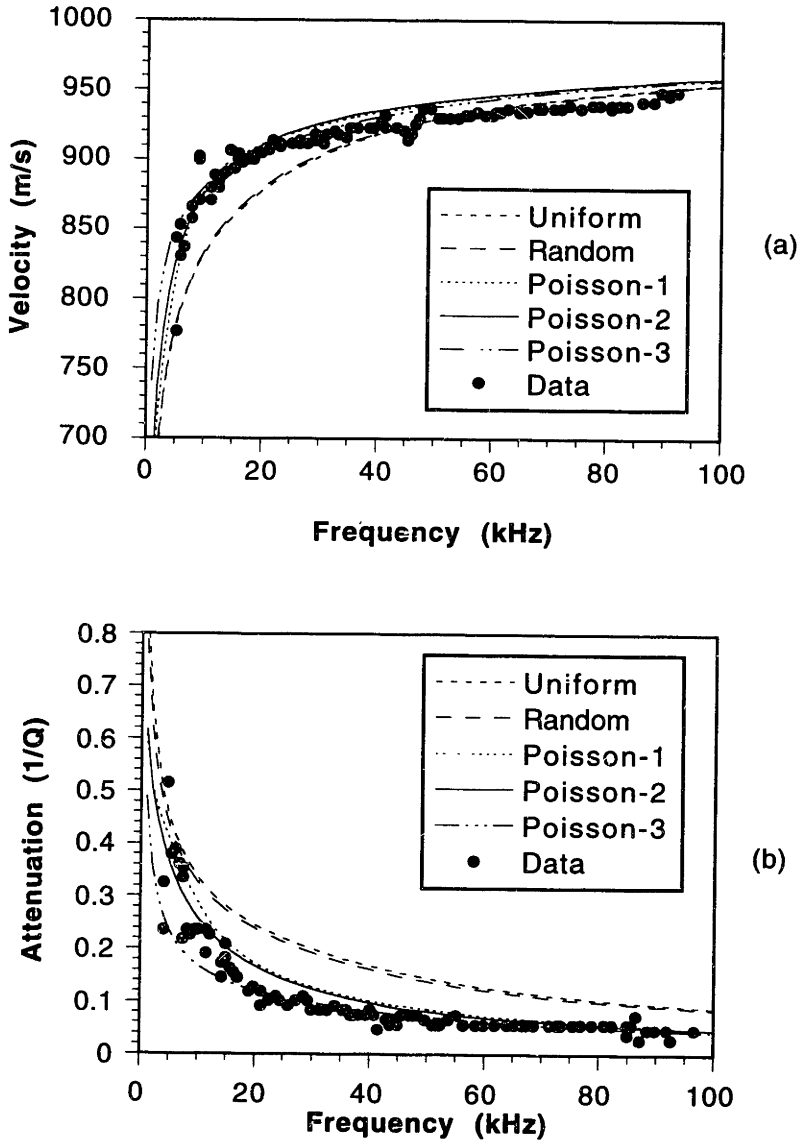

Figure 5-19: Comparison of the experimental Stoneley wave velocity (a) and attenuation(b) data (dots) with the theoretical modeling results using continuous (random) and discontinuous models. For the discontinuous models, Poisson-1 is for a model with 50 layer, Poisson-2, 20 layers, and Poisson-3, 2-layers.

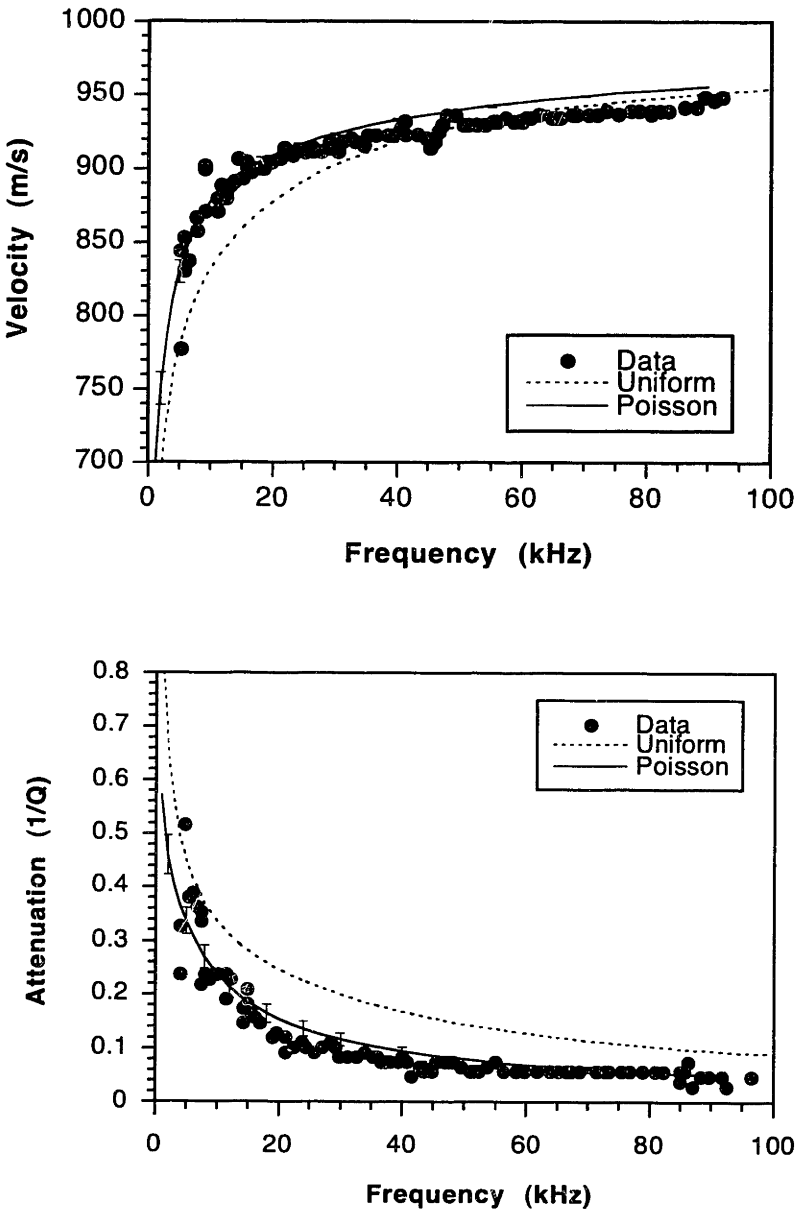

Figure 5-20: Comparison of the experimental Stoneley wave velocity (a) and attenuation (b) data (dots) with the theoretical modeling results (solid curves) using the discontinuous permeability layer model. The error bars represent one standard deviation obtained from 30 modeling results. These is an excellent agreement between data and theory for both velocity and attenuation.

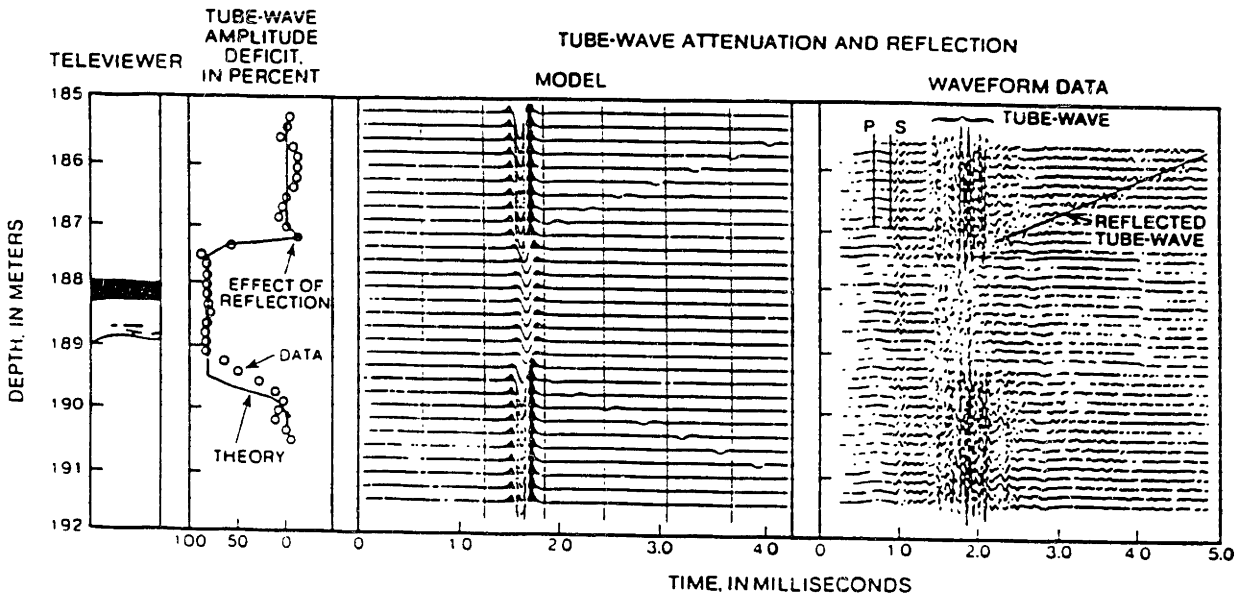

Figure 5-21: Stoneley waveforms, amplitude log, and televiewer log for the URL-M11 well around 188 m (After Paillet and Cheng, 1991). The theoretical modeling results of Tang *et al.* (1991a) are also shown in this figure.

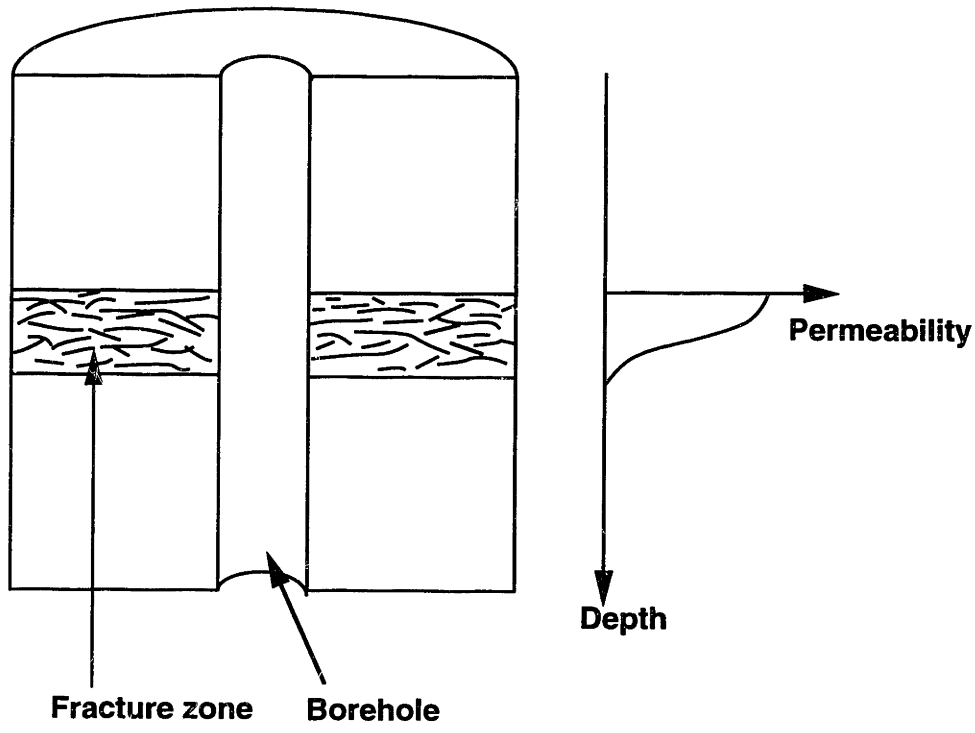

Figure 5-22: Variable permeability model for the URL-M11 fracture zone. The permeability is the highest (2.5 Darcy) at the top boundary, and decreases to attain a zero value at the lower boundary.

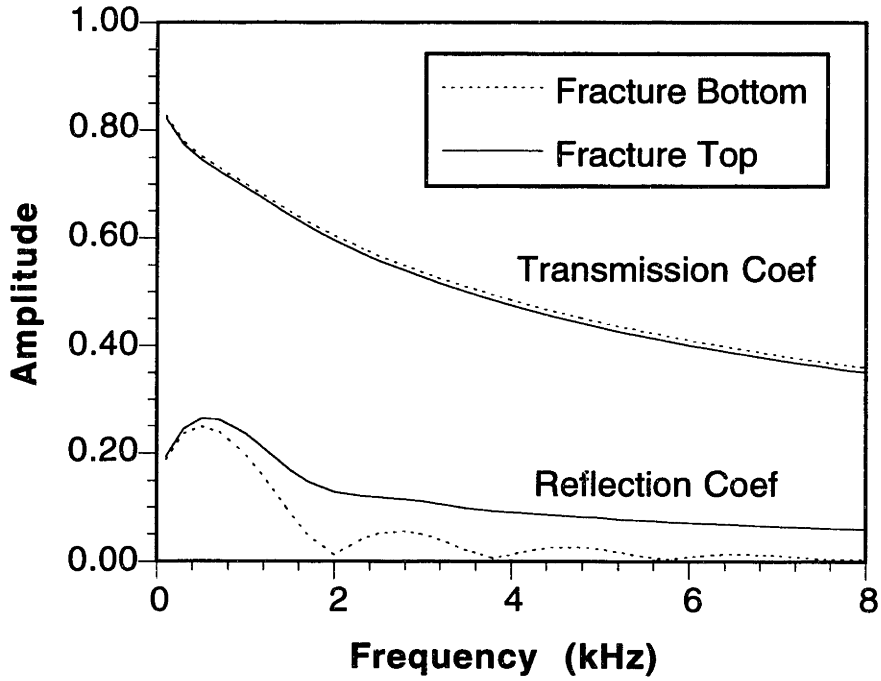

Figure 5-23: Simulated Stoneley wave transmission and reflection coefficients using the model shown in Figure 5-22. The dashed (solid) curves correspond to the situation in which the logging tool is below (above) the fracture zone and the wave is incident from the bottom (top) of the fracture zone. The transmission coefficients for the two cases are very close, while the reflection coefficient from the fracture top boundary is much greater than that from the bottom boundary. This agrees with the non-symmetric reflection patterns of the fracture zone (Figure 5-21).

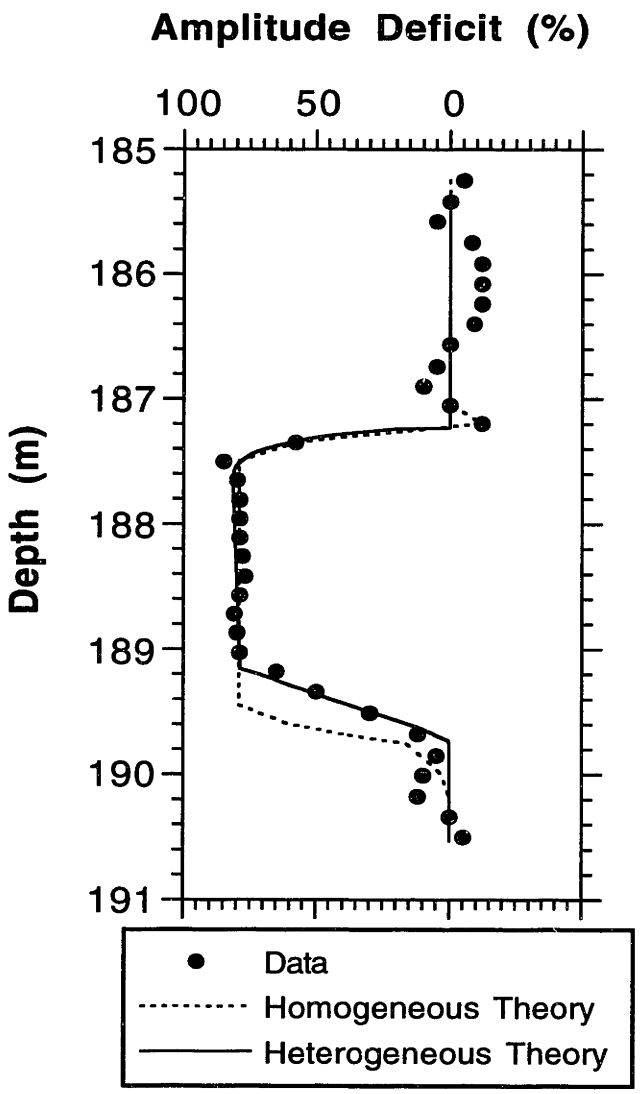

Figure 5-24: Amplitude deficit log from the measured Stoneley wave (5 kHz) data (dots), the homogeneous layer modeling (dashed curve), and the heterogeneous permeability zone modeling. For the same fluid transmissivity, both theories match the portion of the data where the attenuation is the greatest (fracture zone between source and receiver). However, for the lower portion of the amplitude deficit log where receiver is within the fracture zone, only the heterogeneous model results agree with the data.

Chapter 6

Summary and Conclusions

The purpose of this thesis was to study how the heterogeneity variations of a porous medium affect the steady, transient, and dynamic fluid flow properties. The topics under this thesis study cover a broad range of interest and are related to different areas of applications including laboratory pressure transients and borehole acoustic logging. The reason that these topics can be systematically studied using a unified approach is due to the fact that the fluid transport properties (steady, pressure transient, and dynamic fluid flow) obey the same fundamental physics of mass conservation and are included by a unified mathematical formulation. As shown in Appendix A, all these physical phenomena are described by a partial differential equation [Equation (A.1)]. This allows us to apply the numerical finite difference analysis method (e.g., ADI) to model these different fluid transport phenomena in heterogeneous porous media.

Two types of heterogeneity models have been used to simulate permeability variations commonly encountered in porous rock formations. One is the transitional (or continuous) models, and the other is the cyclic (discontinuous) models (Kerner, 1992). The major difference between the two models is that the continuous models do not have significant permeability contrast whereas that contrast is very significant in the discontinuous models. We have described the procedure for generating these models. As we have demonstrated in this thesis, these two types of models have quite different

effects on the fluid transport properties.

The relationship between permeability heterogeneity and permeability anisotropy was studied in the steady state (Darcy flow) case using the (continuous and discontinuous) random permeability models. Because of the effects of heterogeneous and anisotropic structures on oil and gas reservoir production, it is important to understand how these structures affect fluid transport properties. Specifically, the relationship between heterogeneity and fluid transport anisotropy was investigated. From the numerical modeling studies on various continuous and discontinuous lineated heterogeneity models, we draw an important conclusion that permeability contrast between low- and high-permeability regions in the formation is the key factor controlling the degree of fluid flow anisotropy. This conclusion is in support of the study results of several researchers on various rock and formation types (Lake, 1988; Haldorsen and Lake, 1984; Long *et al.*, 1982), especially the experimental results of Bernabé (1992). It is worthwhile to mention that another important factor affecting anisotropy is the scale size (or connectivity) of the heterogeneities. In general, large size heterogeneities tend to produce strong permeability anisotropy, while small sizes, despite the presence of large permeability contrast, only produce small to moderate permeability anisotropy. This conclusion also supports the results of Lake (1988) who showed that small scale heterogeneities (micro cracks, elongated grains) cannot produce significant permeability anisotropy, while large scale heterogeneities (sand-shale sequences and oriented fractures) with large permeability contrast result in strong anisotropy.

The conclusions obtained from the study of static fluid flow properties also hold true for transient fluid flow. Moreover, transient flow has some additional effects. An important phenomenon seen from our numerical modeling is that the transient fluid flow, being a time-dependent flow phenomenon, may reflect heterogeneities of different penetration depths. For example, the early time portion of the pressure transient sees heterogeneity effects of the formation close to the presure source, while the late time portion can detect heterogeneity variations deeper into the formation. This result

may provide some insight in the interpretation of borehole pressure transient tests made in situ.

Because of the importance in obtaining formation permeability from borehole acoustic logging waves (i.e., Stoneley wave), this thesis is primarily concerned with fluid flow under dynamic wave (borehole acoustic wave) excitations and its applications to borehole acoustic logging studies. Based on two recent developments [the theory of dynamic permeability of Johnson *et al.*, (1987) and the simplified Biot model for borehole Stoneley wave propagation (Tang *et al.*, 1991b)], we developed numerical finite difference analysis methods to model the effects of formation permeability heterogeneity on the borehole Stoneley wave propagation. The validity of the finite difference method in modeling the dynamic fluid transport is studied in Chapter 3. The acoustic logging applications of the numerical method were studied in detail in Chapters 4 and 5.

In Chapter 4, we studied the case where the permeability variation is in the borehole radial and azimuthal directions. We have simulated the effects of various continuous and discontinuous permeability heterogeneity models. A major finding is that, because the Stoneley wave sums the effects of pore fluid flow in all azimuthal directions, it is not sensitive to the azimuthal permeability variation or anisotropy. In other words, the heterogeneous formation behaves like an equivalent homogeneous formation. The important result of this finding is that one can use the Stoneley wave propagation theory for a homogeneous permeable porous formation to estimate the effective (or average) permeability of a heterogeneous formation. The only case in which the permeability heterogeneity has large effects on the Stoneley waves is the damaged borehole situation where the borehole wall has significantly higher permeability than the virgin formation. We showed that such a damaged wall results in a peaked Stoneley wave attenuation and significant wave velocity dispersion in the frequency range of Stoneley wave measurements, thus providing the theoretical basis for detecting the borehole damage using Stoneley wave measurements.

In acoustic logging applications, the most common situation of permeability variation is along the borehole axial direction, as can be seen for vertical layering of sand-shale sequences and borehole fractures. This case was studied in Chapter 5. To account for the variation along the wave propagation path, we combine the finite difference technique with a propagator matrix method. The resulting numerical method can be used to compute the equivalent Stoneley wave attenuation and velocity of a heterogeneous formation, or to calculate the wave transmission and reflection at a heterogeneous permeable zone. As before, the continuous and discontinuous permeability models were used for the simulation. We found that the continuous model results are very close to the homogeneous model results. Only the discontinuous model can produce significant differences between the homogeneous and heterogeneous models, although the two models may have the same (average) properties.

For Stoneley wave transmission and reflection at a heterogeneous structure, we found that the transmitted wave amplitude is controlled by the overall fluid transmissivity of the structure and that the reflection is most sensitive to the heterogeneity structures. However, at very low frequencies, both transmission and reflection are controlled by the overall fluid transmissivity of the zone, irrespective of the distribution of the heterogeneities. These results can be used to provide methods for characterizing the fluid transmissivity of a permeable zone using Stoneley wave measurements. We have tested our numerical methods using data from laboratory and field Stoneley wave measurements. We demonstrated that only the heterogeneous models can explain the data well. The numerical modeling technique can be used in interpreting acoustic data logged in heterogeneous formations.

Further research in the above areas can be followed in a number of aspects. An immediate work will be to include attenuation of Stoneley waves due to formation anelasticity and borehole fluid (drilling mud). In order to interpret permeability from Stoneley wave attenuation, we need to correct for Stoneley wave attenuation caused by these factors. Another major aspect is to extend the numerical algorithm

to a 3-dimensional heterogeneous medium. With the availability of high speed, large memory computers, this extension can be achieved without much difficulty. Other aspects include multi-phase flow in the static, transient, and dynamic flow problems.

References

Ababou, R., *Three dimensional flow in random porous media*. Ph. D. Thesis, **MIT**, MA, 1988.

Aki, K. and P.G. Richards, *Quantitative Seismology*, W.H. Freeman and Co., New York, 1990.

Bear, L., *Dynamics of Fluids in Porous Media*, Elsevier, New York, 1972.

Begg, S. H., R. R. Carter, and P. Dranfied, Assigning effective values to simulator gridblock parameters for heterogeneous reservoirs, *SPE Reservoir Eng.*, **4**, 455-463, 1989.

Bernabé, Y., A wide range parameter for use in rock physics, *Int. J. Rock Mech. Sci. & Geomech. Abstr.*, **24**, 309-315, 1987.

Bernabé, Y., On the measurement of permeability in anisotropic rocks. *Fault Mechanism and Transport Properties of Rocks: The Brace Volume* edited by T. F. Wong and B. Evans, Academic Press, London, 147-167, 1992.

Biot, M. A., Theory of propagation of elastic waves in a fluid-saturated porous solid, I: Low frequency range, *J. Acoust. Soc. Am.* **28**, 168-178, 1956a.

Biot, M. A., Theory of propagation of elastic waves in a fluid-saturated porous solid, II: Higher frequency range, *J. Acoust. Soc. Am.* **28**, 179-191, 1956b.

Brace, W. F., J. B. Walsh, and W. T. Frangos, Permeability of granite under high pressure, *J. of Geophys. Res.*, **73**, 2225-2236, 1968.

Bracewell, R., *The Fourier Transform and its Applications*, McGraw-Hill, New York, 1978.

Bredehoeft, J. D. and S. S. Papadopulos, A method for determining the hydraulic properties of tight formations, *Water Resour. Res.*, **16**, 233-238, 1980.

Brown, S., Flow through rock joints: the effects of surface roughness, *J. Geophys., Res.*, **92**, 1337–1347, 1987.

Brown, S., Transport of fluid and electric current through a single fracture, *J. Geophys., Res.*, **94**, 9429–9438, 1989.

Burns, D. R. and C. H. Cheng, Determination of in-situ permeability from tube wave velocity and attenuation, *Trans., Soc. Prof. Well Log Analysis, 27th Ann. Log. Symp.*, paper KK, 1986.

Chang, S.K., H.L. Liu, and D.L. Johnson, Low frequency tube waves in permeable rocks, *Geophysics*, **53**, 519-527, 1988.

Charrette, E. E., *Elastic Wave Scattering in Laterally Inhomogeneous Media*, Ph. D. Thesis, **MIT**, MA, 1991.

Cheng, C.H. and M.N. Toksöz, Elastic wave propagation in a fluid -filled borehole and synthetic acoustic logs: *Geophysics*, **46**, 1042-1053, 1981.

Cheng, C. H., M. N. Toksöz, anb M. E. Willis, Determination of in-situ attenuation from full-waveform acoustic logs, *J. Geophys. Res.*, **87**, 5447-5484, 1982.

Cheng, C. H., J. Z. Zhang, and D. R. Burns, Effects of in-situ permeability on the propagation of Stoneley (tube) waves in a borehole, *Geophysics*, **52**, 1297-1289, 1987.

Cicerone, R. D., *Detection and Characterization of In-situ Fracture in the Earth from Vertical Seismic Profiling Data*, Ph. D. Thesis, **MIT**, MA, 1991.

Dagan, G., Statistical theory of groundwater flow and transport: pore to laboratory, laboratory to formation, and formation to regional scale, *Water resours. Res.*, **22**, 1986.

Desbarats, A. J., Numerical estimation of effective permeability in sand-shale formations, *Water Resour. Res.*, **23**, 273-286, 1987.

Deutsch, C., Calculating effective absolute permeability in sandstone/shale sequences, *SPE Formation Evaluation*, **4**, 343-348, 1989.

Ferziger, J. H., *Numerical Methods for Engineering Applications*, John Wiley & Sons, Inc., New York, 1981.

Frankel, A., and R. Clayton, Finite difference simulations of seismic scattering: implications for the propagation of short-period seismic waves in the crust and models of crustal heterogeneity, *J. Geophys. Res.*, **91**, 6465–6489, 1986.

Gibson, R. L., Jr., and M. N. Toksöz, Permeability estimation from velocity anisotropy in fractured rock, *J. Geophys. Res.*, **95**, 15643–15655, 1990.

Güler, F. and M. N. Toksöz, Ultrasonic laboratory study of full waveform acoustic logs in boreholes with fractures, *M.I.T. Full Waveform Acoustic Logging Consortium Annual Report*, 1987.

Haldorsen, H. H. and L. W. Lake, A new approach to shale management in field scale problems, *Soc. Pet. Eng. J.*, **24**, 447-457, 1984.

Hornby, B. E., D. L. Johnson, K. H. Winkler, and R. A. Plumb, Fracture evaluation using reflected Stoneley-wave arrivals, *Geophysics*, **54**, 1274-1288, 1989.

Hvorslev, M. J., Time lag and soil permeability in ground water observations, *Bulletin No. 36, U. S. Army Engineer*, Waterways Experiment Station, Vicksburg, Mississippi, 1951.

Jenkins, G. M. and D. G. Watts, *Spectral Analysis and its Applications*, Holden-Day, Inc., San Francisco, 1968.

Johnson, D. L., T. J. Plona, C. Scala, F. Pasierb, and H. Kojima, Tortuosity and acoustic slow waves, *Phys. Rev. Lett.*, **49**, 1840-1844, 1982.

Johnson, D. L., J. Koplik, and R. Dashen, Theory of dynamic permeability and tortuosity in fluid-saturated porous media, *J. Fluid Mech.*, **176**, 379-402, 1987.

Kamath, J, R. E. Boyer, and F. M. Nakagawa, Characterization of core scale heterogeneities using laboratory pressure transients, *Society of Petroleum Engineers*, 475– 488, 1990.

Kerner, C., Anisotropy in sedimentary rocks modeled as random media, *Geophysics*, **57**, 564–576, 1992.

Kostek, S. Borehole acoustic wave propagation in the presence of fractures: A finite difference approach, *SEG* **61th** *Ann. Intl. Mtg. & Expo. Expanded Abst.* Houston, Taxas, 1991.

Kwicklis, E. M. and R. W. Healy, Numerical investigation of steady liquid water flow in a variably saturated fracture network, *Water Resours. Res.*, **29(12)**, 1993.

Lake, L. W., The origin of anisotropy, *J. Pet. Tech.*, **40**, 395-396, 1988.

Landau, L. D. and E. M. Lifshitz, *Fluid Mechanics*, Pergamon, 1959.

Long, C. S., J. S. Remer, C. R. Wilson, and P. A. Witherspoon, Porous media equivalents for networks of discontinuous fractures, *Water Resour. Res.*, **18**(3), 645-658, 1982

Long, C. S., and P. A. Witherspoon, The relationship of the degree of interconnection to permeability in fracture networks, *J. Geophys. Res.*, **90**, 3087–3098, 1985.

Melville, J.G., F.J. Molz, O. Güven, and M.A. Widdowson, Multilevel slug tests with comparisons to tracer data, *Ground Water*, **29**, 897- 907, 1991.

Norris, A. N., Stoneley-wave attenuation and dispersion in permeable formations, *Geophysics*, **54**, 330-341, 1989.

Oda, M., Permeability tensor for discontinuous rock masses, *Geotech.*, **35**(4), 483-495, 1985.

Oppenheim, A. V., ed, *Applications of Digital Signal Processing*, Englewood Cliffs, N. J., Prentice-Hall, 1978.

Paillet, F. L., Acoustic propagation in the vicinity of fractures which intersect a fluid-filled borehole, *Trans., Soc. Prof. Well Log Analysts,* **21th** *Ann. Symp.*, paper DD, 1980.

Paillet, F. L., Field test of a low-frequency sparker source for acoustic waveform logging, *M.I.T., Full Waveform Acoustic Logging Consortium Annual Report*, 207-228, 1984.

Paillet, F. L. and C. H. Cheng, *Acoustic Waves in Boreholes - The Theory and Application of Acoustic Full-Waveform Logs*, CRC Press, 264p, 1991.

Paillet, F. L., C. H. Cheng, and X. M. Tang, Theoretical models relating acoustic tube-wave attenuation to fracture permeability - reconciling model results with field data, *Trans., Soc. Prof. Well Log Analyst,* **30th** *Ann Symp*, 1989.

Peng, C., *Borehole Effects on Downhole Seismic Measurements*, Ph.D. Thesis, **MIT**, MA, 1993.

Pride, S. R., F. D. Morgan, and A. F. Gangi, Drag forces of porous-medium acoustics, *Physical Review B*, **47**, No. 9, 4964-4978, 1993.

Priestly, M. B., *Spectral Analysis and Time Series*, Academic Press, San Diego, 1981.

Rosenbaum, J.H., Synthetic microseismograms: logging in porous formations, *Geophysics*, **39**, 14-32., 1974

Rothman, D. H., Cellular-automaton fluids: A model for flow in porous media, *Geophysics*, **53**, 509–518, 1987.

Scheidegger, A. E., *The physics of flow through porous media*, Univ. Toronto Press, Toronto, 1974.

Schmitt, D. P., M. Bouchon, and G. Bonnet, Full-waveform synthetic acoustic logs in radially semiinfinite saturated porous media, *Geophysics,* **53**, 807-823, 1988.

Schmitt, D. P., Acoustic multipole logging in transversely isotropic poroelastic formations: *J. Acoust. Soc. Am.*, **86**, 2397-2421, 1989.

Smith, L. and R. A. Freeze, Stochastic analysis of steady state groundwater flow in a bounded domain, 2. Two-dimensional simulations, *Water Resours. Res.*, **15**(6), 1979.

Stephen, R., F. Pardo-Casas, and C. H. Cheng, Finite difference synthetic acoustic logs, *Geophysics*, **50**, 1588-1609, 1985.

Tang, X. M. and C. H. Cheng, A dynamic model for fluid flow in open borehole fractures, *J. Geophys. Res.*, **94**, 7567-7576, 1989.

Tang, X. M., C. H. Cheng, and F. L. Paillet, Modeling Stoneley wave propagation across in-situ fractures, *Trans.* **36th** *Soc. Prof. Well Log Analysis*, 1991a.

Tang, X. M., C. H. Cheng, and M. N. Toksöz, Dynamic permeability and borehole Stoneley waves: A simplified Biot-Rosenbaum model, *J. Acous. Soc. Am.*, **90**, 1632-1646, 1991b.

Tang, X. M. and C. H. Cheng, Borehole Stoneley wave propagation across heterogeneous and permeable structures, *Geophysical Prospecting*, **41**, 165-187, 1993.

Thompson, M.E., Numerical simulation of solute transport in rough fractures, *J. Geophys. Res.*, **96**, 4157–4166, 1991.

Toksöz, M. N., C. H. Cheng, and R. D. Cicerone, Fracture detection and characterization from hydrophone VSP data, *Fault Mechanics and Transport Properties of Rocks*, edited by Evans, B., Academic Press, 389-414, 1992.

Winkler, K. W., H. L. Liu, and D. L. Johnson, Permeability and borehole Stoneley waves: Comparison between experiment and theory, *Geophysics*, **54**, 66-75, 1989.

Zeigler, T. W., Determination of rock mass permeability, *Technical Report S-76-2, U. S. Army Engineer*, Waterways Experiment Station, Vickburg, Mississippi, 1976.

Zimmerman, R. W., S. Kumar, and G. S. Bodvarsson, Lubrication theory analysis of the permeability of rough-walled fractures, *Int. J. Rock. Mech. Min. Sci. & Geomech. Abstr.*, **28**, 325-331, 1991.

Appendix A

Finite Difference Solution of Parabolic Equation Using ADI Method

A.1 ADI technique

In this appendix, we consider the solution of the following parabolic equation using a stable Alternating Direction Implicit (ADI) technique in a Cartesian coordinate system:

$$\nabla \cdot (E \nabla \Psi) + G\Psi = \frac{\partial \Psi}{\partial t} . \tag{A.1}$$

where E and G are coefficients that vary with spatial coordinates $\vec{\mathbf{x}}$, ∇ is gradient operator, and t is time. Many important problems, such as steady-state fluid flow, transient fluid flow, and dynamic fluid flow, *etc.*, are described by Equation (A.1) as follows:

Static flow:

Compare Equation (A.1) with Equation (2.14), if we set $G = \frac{\partial \Psi}{\partial t} = 0$, E = fluid diffussivity α, and Ψ = fluid pressure P, Equation (A.1) becomes the governing equation for static pore pressure. The solution to the static flow problem is equivalent

to the solution of Equation (A.1) at infinite time. Finding this solution at infinite time using ADI method in essence is equivalent to the iterative procedure used in the SOR method (see Chapter 2).

Pressure transient:

Compare Equation (A.1) with Equation (2.33), if we set $G = 0$, $E =$ fluid diffusivity α, and $\Psi =$ fluid pressure P, Equation (A.1) becomes the governing equation for the pressure transient.

Dynamic fluid flow:

Compare Equation (A.1) with Equation (3.33), if we let Ψ represent the complex dynamic pore fluid pressure P, E the dynamic fluid diffusivity $A(\omega, \vec{x})$ and $G = i\Omega$, Equation (A.1) becomes identical to Equation (3.33), whose steady-state solution gives the dynamic fluid transport for the given frequency ω.

The ADI technique solves Equation (A.1) in a rectangular domain. Here we describe the solution procedure in the 2-D case, where coefficients E and G are functions of x and y. Following the ADI algorithm, we rewrite Equation (A.1) as

$$\Psi_t = \Lambda_1 \Psi + \Lambda_2 \Psi \ , \tag{A.2}$$

where

$$\begin{cases} \Psi_t &= \dfrac{\partial \Psi}{\partial t} \\ \Lambda_1 &= \dfrac{\partial}{\partial x}\left[E(x,y)\dfrac{\partial P}{\partial x}\right] + G\Psi \\ \Lambda_2 &= \dfrac{\partial}{\partial y}\left[E(x,y)\dfrac{\partial \Psi}{\partial y}\right] \end{cases} . \tag{A.3}$$

We discretize Equation(A.2) using the Crank-Nicolson scheme, which is the center difference scheme about time $t = (n + 1/2)\Delta t$. By using the Taylor expansion and taking the first order approximation, Equation (A.2) becomes

$$\frac{\Psi^{n+1} - \Psi^n}{\Delta t} = \frac{1}{2}(\Lambda_1 \Psi^{n+1} + \Lambda_1 \Psi^n) + \frac{1}{2}(\Lambda_2 \Psi^{n+1} + \Lambda_2 \Psi^n) \ . \tag{A.4}$$

Equation (A.4) can further be written as

$$\left(I - \frac{\Delta t}{2}\Lambda_{1h}\right)\left(I - \frac{\Delta t}{2}\Lambda_{2h}\right)\Psi^{n+1} = \left(I + \frac{\Delta t}{2}\Lambda_{1h}\right)\left(I + \frac{\Delta t}{2}\Lambda_{2h}\right)\Psi^n \ , \tag{A.5}$$

where Λ_{1h} and Λ_{2h} represent the following operators:

$$\Lambda_{1h}\Psi = \frac{1}{\Delta x^2}\left[B_{i+1,j}(\Psi_{i+1,j}-\Psi_{i,j}) - B_{i,j}(\Psi_{i,j}-\Psi_{i-1,j})\right] + G_{i,j}\Psi_{i,j} \quad \text{(A.6)}$$

$$\Lambda_{2h}\Psi = \frac{1}{\Delta y^2}\left[C_{i,j+1}(\Psi_{i,j+1}-\Psi_{i,j}) - C_{i,j}(\Psi_{i,j}-\Psi_{i,j-1})\right] \quad \text{(A.7)}$$

with

$$\begin{cases} B_{i,j} = \dfrac{E(i,j)+E(i+1,j)}{2} \\ C_{i,j} = \dfrac{E(i,j)+E(i,j+1)}{2} \end{cases}, \quad \text{(A.8)}$$

and $i = 0, 1, 2, \cdots, I$; $j = 0, 1, 2, \cdots, J$.

Equation (A.5) can be solved using the Peaceman-Rachford algorithm (Ferziger, 1981). This algorithm consists of splitting Equation (A.5) into two separate equations by using an intermediate function $\Psi^{n+1/2}$:

$$\left(I - \frac{\Delta t}{2}\Lambda_{1h}\right)\Psi^{n+1/2} = \left(I + \frac{\Delta t}{2}\Lambda_{2h}\right)\Psi^{n} \quad \text{(A.9)}$$

$$\left(I - \frac{\Delta t}{2}\Lambda_{2h}\right)\Psi^{n+1} = \left(I + \frac{\Delta t}{2}\Lambda_{1h}\right)\Psi^{n+1/2} \ . \quad \text{(A.10)}$$

Substituting Equations (A.6) and (A.7) into Equations (A.9) and (A.10) results in

$$\begin{aligned} &-\frac{\Delta t}{2\Delta x^2}B_{i,j}\Psi^{n+1/2}_{i-1,j} + \left[1 + \frac{\Delta t}{2\Delta x^2}(B_{i,j}+B_{i+1,j}) - \frac{\Delta t}{2}G_{i,j}\right]\Psi^{n+1/2}_{i,j} \\ &\quad -\frac{\Delta t}{2\Delta x^2}B_{i+1,j}\Psi^{n+1/2}_{i+1,j} \\ &= \frac{\Delta t}{2\Delta y^2}C_{i,j}\Psi^{n}_{i,j-1} + \left[1 + \frac{\Delta t}{2\Delta y^2}(C_{i,j+1}+C_{i,j})\right]\Psi^{n}_{i,j} \\ &\quad +\frac{\Delta t}{2\Delta y^2}C_{i.j+1}\Psi^{n}_{i,j+1} \ , \end{aligned} \quad \text{(A.11)}$$

$$\begin{aligned} &-\frac{\Delta t}{2\Delta y^2}C_{i,j}\Psi^{n+1}_{i,j-1} + \left[1 + \frac{\Delta t}{2\Delta y^2}(C_{i,j}+C_{i+1,j})\right]\Psi^{n+1}_{i,j} \\ &\quad -\frac{\Delta t}{2\Delta y}C_{i+1,j}\Psi^{n+1}_{i,j+1} \\ &= \frac{\Delta t}{2\Delta x^2}B_{i,j}\Psi^{n+1/2}_{i-1,j} + \left[1 + \frac{\Delta t}{2\Delta x^2}(B_{i,j+1}+B_{i,j}) + \frac{\Delta t}{2}G_{i.j}\right]\Psi^{n+1/2}_{i,j} \\ &\quad +\frac{\Delta t}{2\Delta y^2}C_{i.j+1}\Psi^{n+1/2}_{i+1,j} \ . \end{aligned} \quad \text{(A.12)}$$

The advantage of the ADI method can be seen from Equations (A.11) and (A.12). Suppose at $t = n\Delta t$, Ψ^n is known for all $x = i\Delta x$ and $y = j\Delta y$ ($n = 0$ is determined

by the initial condition), so that the terms on the right-hand side of Equation (A.11) are known. Equation (A.11) now becomes one-dimensional (1-D) difference equation for $\Psi^{n+1/2}$ in the x-direction, which can be solved to find $\Psi^{n+1/2}$ with the given boundary conditions at $x = 0$ and $x = I\Delta x$. Once $\Psi^{n+1/2}$ is found, the terms on the right-hand side of Equation (A.12) are known. Equation (A.12) is now another 1-D difference equation for Ψ^{n+1} in the y-direction and can be solved with the given boundary conditions at $y = 0$ and $y = J\Delta y$. In this way, the unknown function at $(n + 1)$ step Ψ^{n+1} is found. This procedure can be repeated iteratively to find the solution at any given time $t = n\Delta t$. For this procedure the Peaceman-Rachford ADI algorithm is unconditionally stable and has a second-order accuracy in both time and space. Since the matrix expressions of Equations (A.11) and (A.12) have a triangular form, they can be efficiently solved using the Thomas algorithm (Ferziger, 1981).

A.2 Solution with different boundary conditions

We now describe the solution procedure that incorporates the boundary conditions. Specifically, we will discuss three types of boundary conditions. They are the first kind, second kind, and periodic boundary conditions. In the finite difference form, the boundary conditions are given in terms of Ψ^n and Ψ^{n+1}. For the intermediate function $\Psi^{n+1/2}$, we need to find its boundary condition using the prescribed values of Ψ^n and Ψ^{n+1} at the boundary. To do this, we start from Equations (A.9) and (A.10). From Equation (A.9), we have

$$\frac{\Delta t}{2}\Lambda_{1h}\Psi^{n+1/2} = \Psi^{n+1/2} - \left(I + \frac{\Delta t}{2}\Lambda_{2h}\right)\Psi^n \quad . \tag{A.13}$$

Substitute Equation (A.13) into Equation (A.10), we get

$$\Psi^{n+1/2} = \frac{1}{2}\left[(I - \frac{\Delta t}{2}\Lambda_{2h})\Psi^{n+1} + (I + \frac{\Delta t}{2})\Psi^n\right] \quad . \tag{A.14}$$

At $i = 0$ and $i = I$, Ψ^n and Ψ^{n+1} are prescribed by the boundary conditions. Therefore, using Equation (A.14) $\Psi^{n+1/2}_{0,j}$ and $\Psi^{n+1/2}_{I,j}$ can be obtained. Now the problem is to solve Equations (A.11) and (A.12) with appropriate boundary conditions.

Equations (A.11) and (A.12) have the form of

$$U_i\Phi_{i-1} + V_i\Phi_i + W_i\Phi_{i+1} = R_i \qquad i = 1, 2, \cdots, I-1 \tag{A.15}$$

where U_i, V_i, and W_i are the coefficients of $\Psi_{i-1,j}^{n+1/2}$, $\Psi_{i,j}^{n+1/2}$, and $\Psi_{i+1,j}^{n+1/2}$ in the left-hand side of Equation (A.11) or the coefficients of $\Psi_{i-1,j}^{n+1}$, $\Psi_{i,j}^{n+1}$, and $\Psi_{i+1,j}^{n+1}$ in the left-hand side of Equation (A.12); R_i is the right-hand side terms of Equation (A.11) or (A.12), and Φ_i can be either $\Psi_{i,j}^{n+1/2}$ or $\Psi_{i,j}^{n+1}$. Equation (A.15) is a tridiagonal system, which, together with appropriate boundary conditions, can be solved using the Thomas algorithm (Ferziger, 1981).

A.2.1 First kind boundary condition

For the first kind boundary condition, the value of the unknown function Φ is assigned to the boundary. For example,

$$\Phi(0) = \Phi_0 \quad \text{and} \quad \Phi(I) = \Phi_I \tag{A.16}$$

Now the problem is to solve Equation (A.15) for boundary conditions (A.16). By using Gaussian elimination, we want to replace Equation (A.15) by relationship of the form

$$\Phi_i = s_{i+1}\Phi_{i+1} + q_{i+1} \qquad i = 1, 2, \cdots, I-1 \ , \tag{A.17}$$

where s_{i+1} and q_{i+1} are to be determined.

Substituting Equation (A.17) into (A.15) for Φ_{i-1}, we have

$$U_i(s_i\Phi_i + q_i) + V_i\Phi_i + W_i\Phi_{i+1} = R_i \tag{A.18}$$

or

$$\Phi_i = -\frac{W_i}{U_i s_i + V_i}\Phi_{i+1} + \frac{R_i - U_i q_i}{U_i s_i + V_i} \ . \tag{A.19}$$

Compare (A.19) with (A.17), we must have

$$\begin{cases} s_{i+1} = -\dfrac{W_i}{U_i s_i + V_i} \\ q_{i+1} = \dfrac{R_i - U_i q_i}{U_i s_i + V_i} \end{cases} \tag{A.20}$$

for consistency of the formulas. Thus if we know s_1 and q_1, then we can calculate s_i and q_i for i greater than 1. Together with given Φ_I, we can calculate Φ_i ($i = 1, 2, \cdots, I-1$) using Equation (A.19).

The values of s_1 and q_1 are obtained from the boundary conditions [Equation (A.16)]. At $i = 0$, we have

$$\Phi_0 = s_1 \Phi_1 + q_1 = \beta_0 \ . \tag{A.21}$$

These conditions are consistent if $s_1 = 0$ and $q_1 = \beta_0$. Then s_i and q_i can be computed using Equation (A.20). With $\Phi_I = \beta_I$, Equation (A.19) is used to calculate the value of Φ_{I-1}, which is then back substituted to calculate Φ_{I-2} using the same equation. In this way Φ_i ($i = 1, 2, \cdots, I-1$) can all be obtained.

A.2.2 Second kind boundary condition

For the second kind boundary condition, the value of derivative of the unknown function Φ is assigned at the boundaries. The procedure for solving Equation (A.15) with this kind of boundary condition is the same as for the first kind of boundary condition except that the determination of s_1 and q_1 in Equation (A.21) needs some modification.

In terms of the finite difference scheme, the second kind boundary condition at $i = 0$ can be written as

$$\Phi_0 = \Phi_1 + \gamma_0 \ . \tag{A.22}$$

Compare Equation (A.22) with Equation (A.17) for the $i = 0$ (boundary) case, we should have $s_1 = 1$ and $q_1 = \gamma_0$. At the $i = I$ boundary, we have

$$\Phi_I = \Phi_{I-1} + \gamma_I \ . \tag{A.23}$$

On the other hand, the relation

$$\Phi_{I-1} = s_I \Phi_I + q_I \tag{A.24}$$

also holds. We combine Equations (A.23) and (A.24) to obtain

$$\Phi_I = \frac{q_I + \gamma_I}{1 - s_I} \quad . \tag{A.25}$$

Note that if $s_I = 1$, Φ_I can not be defined and the system with this boundary condition is singular. This situation is not considered in the present problem.

After Φ_I is found using Equation (A.25), the solution of Equation (A.15) is obtained by back-substitution using Equation (A.19), in much the same way as in the previous first kind boundary condition case.

A.2.3 Periodic boundary condition

If the unknown function repeats itself after a period of x_L in the x-direction, we can solve Equation (A.15) with a periodic boundary condition. Consider the system

$$U_i\Phi_{i-1} + V_i\Phi_i + W_i\Phi_{i+1} = R_i \quad , \qquad i = 1, \cdots, I \tag{A.26}$$

with periodic boundary condition

$$\Phi_0 = \Phi_I \quad \text{and} \quad \Phi_{I+1} = \Phi_1 \tag{A.27}$$

The solution to this periodic system can be found by solving three non-periodic systems for the entire domain from $i = 1$ to I:

$$\begin{cases} U_i\zeta_{i-1} + V_i\zeta_i + W_i\zeta_{i+1} = R_i \\ \zeta_0 = 0 \\ \zeta_{I+1} = 0 \end{cases} , \tag{A.28}$$

$$\begin{cases} U_i\eta_{i-1} + V_i\eta_i + W_i\eta_{i+1} = 0 \\ \eta_0 = 1 \\ \eta_{I+1} = 0 \end{cases} , \tag{A.29}$$

and

$$\begin{cases} U_i\xi_{i-1} + V_i\xi_i + W_i\xi_{i+1} = 0 \\ \xi_0 = 0 \\ \xi_{I+1} = 1 \end{cases} . \tag{A.30}$$

Systems (A.28), (A.29), and (A.30) can be solved using the approach we have described earlier in the first kind boundary condition case. The solution to the periodic system can be constructed as

$$\Phi_i = \zeta_i + g\eta_i + h\xi_i \quad . \tag{A.31}$$

We choose g and h to guarantee the periodicity. For $\Phi_0 = \Phi_I$, we have

$$\zeta_0 + g\eta_0 + h\xi_0 = g = \zeta_I + g\eta_I + h\xi_I \quad . \tag{A.32}$$

For $\Phi_{I+1} = \Phi_1$, we have

$$\zeta_{I+1} + g\eta_{I+1} + h\xi_{I+1} = h = \zeta_1 + g\eta_1 + h\xi_1 \quad . \tag{A.33}$$

These are two equations with two unknowns g and h. The solution is

$$\begin{cases} g = \dfrac{\zeta_I(1-\xi_1) + \zeta_1\xi_I}{D} \\ h = \dfrac{\zeta_I\eta_1 + \zeta_1(1-\eta_I)}{D} \end{cases} , \tag{A.34}$$

where $D = (1-\eta_I)(1-\xi_1) - \eta_1\xi_I$.

Appendix B

Finite Difference Solution for Dynamic Fluid Flow in (r, θ) Coordinates

In problems related to borehole acoustic logging, it is convenient to use the cylindrical coordinate system. The fluid flow pressure in the heterogeneous formation is given by Equation (4.19). In the cylindrical coordinates, fluid flow occurs in the region

$$\begin{aligned} R < \quad & r \quad < R_0 \\ 0 < \quad & \theta \quad < 2\pi \quad , \end{aligned}$$

where R is bore radius and R_0 is the outer radius of the region, at which the flow effectively vanishes because of the radiation condition. It is convenient to non-dimensionalize the governing equation [Equation (4.19)]. We use the dimensionless variables r' $(0 < r' < 1)$ and θ' $(0 < \theta' < 1)$ and the transformation

$$\begin{cases} r = R + (R_0 - R)r' \\ \theta = 2\pi\theta' \quad . \end{cases} \tag{B.1}$$

The spatially varying dynamic fluid diffusivity $\alpha(\omega; r, \theta)$ may also be non-dimensionalized using

$$\alpha = \frac{\kappa(\omega; r, \theta) K_f}{\mu\phi} = \alpha_0 \cdot \alpha'(\omega; r, \theta) \ , \tag{B.2}$$

where

$$\alpha_0 = \frac{\kappa_{max} K_f}{\mu\phi} \ , \tag{B.3}$$

and

$$\alpha' = \frac{\gamma(r, \theta)}{\left[1 - \frac{i}{2}\tau\kappa_{max}\gamma(r, \theta)\frac{\rho_f\omega}{\mu\phi}\right]^{1/2} - i\tau\kappa_{max}\gamma(r, \theta)\frac{\rho_f\omega}{\mu\phi}} \ , \tag{B.4}$$

where κ_{max} is the maximum permeability in the model, $\gamma(r, \theta) = \frac{\kappa(r, \theta)}{\kappa_{max}}$ is the dimensionless permeability distribution. $\alpha'(\omega; r, \theta)$ is now the dimensionless diffusivity that is a function of both frequency and spatial position. The non-dimensionalized governing equation [from Equation (4.19)] becomes

$$\frac{\partial}{\partial r'}\left(\alpha'\frac{\partial p}{\partial r'}\right) + \frac{R_0 - R}{R + (R_0 - R)r'}\alpha'\frac{\partial p}{\partial r'} + \frac{(R_0 - R)^2}{4\pi^2[R + (R_0 - R)r']^2}\frac{\partial}{\partial\theta'}\left(\alpha'\frac{\partial p}{\partial\theta'}\right) + (i\Omega - \alpha' k_e'^2)p = 0 \ , \tag{B.5}$$

where $\Omega = \frac{\omega}{\alpha_0}(R_0 - R)^2$ is the dimensionless frequency and $k_e' = (R_0 - R)^2 k_e$.

Because the straightforward center difference solution of Equation (B.5) is unstable (see Chapter 3), we solve Equation (B.5) using an iterative finite difference technique. We find the solution for the following equation

$$\Gamma p = \frac{\partial p}{\partial t'} \ , \tag{B.6}$$

where Γ is the left hand side of Equation (B.5), and t' is a dimensionless time. The solution of Equation (B.6) can be computed iteratively with increasing t' to approach the steady state, at which the solution of Equation (B.6) will be the solution of (B.5). Equation (B.6) can be solved using ADI method which is unconditionally stable for Equation (B.6) type equations (Ferziger, 1981). Using the ADI finite difference

method, we discretize the dimensionless variables r', θ' and t' using

$$\begin{cases} r' = i\Delta r' & i = 0, 1, 2, \cdots, I \quad \Delta r' = 1/I \\ \theta' = j\Delta\theta' & j = 0, 1, 2, \cdots, J \quad \Delta\theta' = 1/J \\ t' = n\Delta t' & n = 0, 1, 2, \cdots, N \end{cases} \tag{B.7}$$

For practical purposes $\Delta t'$ can be chosen to be $\sqrt{(\Delta r')^2 + (\Delta\theta')^2}/2$. To use the ADI method, we need to re-write Equation (B.6) in the form of Equation (A.2) of Appendix A,

$$p_{t'} = \Lambda_1 p + \Lambda_2 p \ , \tag{B.8}$$

where,

$$\begin{cases} \Lambda_1 p = \dfrac{\partial}{\partial r'}\left(\alpha' \dfrac{\partial p}{\partial r'}\right) + \dfrac{R_0 - R}{R + (R_0 - R)r'} \alpha' \dfrac{\partial p}{\partial r'} + \left(i\Omega - \alpha' k_e'^2\right) p \\ \\ \Lambda_2 p = \dfrac{(R_0 - R)^2}{4\pi^2 [R + (R_0 - R)r']^2} \dfrac{\partial p}{\partial \theta'}\left(\alpha' \dfrac{\partial p}{\partial \theta'}\right) \end{cases} \tag{B.9}$$

Equation (B.8) is then written into the ADI form by using an intermediate function $p^{n+1/2}$,

$$\left(I - \frac{\Delta t'}{2}\Lambda_{1h}\right) p^{n+1/2} = \left(I + \frac{\Delta t'}{2}\Lambda_{2h}\right) p^n \tag{B.10}$$

$$\left(I - \frac{\Delta t'}{2}\Lambda_{2h}\right) p^{n+1} = \left(I + \frac{\Delta t'}{2}\Lambda_{1h}\right) p^{n+1/2} \ . \tag{B.11}$$

Where I is unit matrix; Λ_{1h} and Λ_{2h} are finite difference operators, which, when operated on p, can be written as:

$$\begin{aligned} \Lambda_{1h} p \ = \ & \frac{1}{\Delta r'^2}\Big[(B_{i,j} - D_{i,j}) p_{i-1,j} - \Big(B_{i,j} + B_{i+1,j} - D_{i,j}^{(1)} \\ & -(i\Omega - A_{i,j} k_e'^2)\Delta r'^2\Big) p_{i,j} + B_{i+1,j} p_{i+1,j}\Big] \end{aligned} \tag{B.12}$$

$$\Lambda_{2h} p \ = \ D_{i,j}^{(2)} \frac{1}{\Delta\theta'^2}\left[C_{i,j} p_{i,j-1} - (C_{i,j} + C_{i,j-1}) p_{i,j} + C_{i,j+1} p_{i,j+1}\right] \ , \tag{B.13}$$

where

$$\begin{cases} A_{i,j} &= \alpha'_{i,j} \\ B_{i,j} &= \dfrac{A_{i,j}+A_{i-1,j}}{2} \\ C_{i,j} &= \dfrac{A_{i,j}+A_{i,j-1}}{2} \\ D^{(1)}_{i,j} &= \dfrac{(R_0-R)B_{i,j}\Delta r'}{[R+(R_0-R)(r'_{i,j}+r'_{i-1,j})/2]} \\ D^{(2)}_{i,j} &= \dfrac{(R_0-R)^2}{4\pi^2[R+(R_0-R)r'_{i,j}]^2} \end{cases} \tag{B.14}$$

Therefore, the ADI finite difference form of Equations (B.10) and (B.11) is

$$\begin{aligned} &-\mu_1(B_{i,j}-D^{(1)}_{i,j})p^{n+1/2}_{i-1,j}+\left[1+\mu_1\left(B_{i,j}+B_{i+1,j}-D^{(1)}_{i,j}\right.\right. \\ &\quad\left.\left.-(i\Omega-A_{i,j}k'^2_e)\Delta r'^2\right)\right]p^{n+1/2}_{i,j}-\mu_1 B_{i+1,j}p^{n+1/2}_{i+1,j} \\ &\quad=\mu_2 D^{(2)}_{i,j}p^n_{i,j-1}+\left[1-\mu_2 D^{(2)}_{i,j}(C_{i,j}+C_{i,j+1})\right]p^n_{i,j}+\mu_2 D^{(2)}_{i,j}C_{i,j+1}p^n_{i,j+1} \end{aligned} \tag{B.15}$$

$$\begin{aligned} &-\mu_2 D^{(2)}_{i,j}C_{i,j}p^{n+1}_{i,j-1}+\left[1+\mu_2 D^{(2)}_{i,j}(C_{i,j}+C_{i,j+1})\right]p^{n+1}_{i,j}-\mu_2 D^{(2)}_{i,j}C_{i,j+1}p^{n+1}_{i,j+1} \\ &\quad=\mu_1\left(B_{i,j}-D^{(1)}_{i,j}\right)p^{n+1/2}_{i-1,j}+\left[1-\mu_1\left(B_{i,j}+B_{i+1,j}-D^{(1)}_{i,j}\right.\right. \\ &\qquad\left.\left.-(i\Omega-A_{i,j}k'^2_e)\Delta r'^2\right)\right]p^{n+1/2}_{i,j}+\mu_1 B_{i+1,j}p^{n+1/2}_{i+1,j} \end{aligned} \tag{B.16}$$

where

$$\mu_1=\frac{\Delta t'}{2\Delta r'^2} \qquad \text{and} \qquad \mu_2=\frac{\Delta t'}{2\Delta\theta'^2}$$

These equations are similar to the ADI form finite difference equations (Equations (A.11) and (A.12)] in Appendix A, except that the dynamic fluid pressure function p is a complex variable because of the complex permeability.

The boundary conditions at radial direction are the continuity of borehole pressure with pore pressure p at the borehole wall and the radiation condition at infinity which states that pore pressure p should vanish at large radial distance ($R_0 >> R$). These results in

$$p(0,j)=P_0\ , \qquad \text{and} \qquad p(I,j)=0\ . \tag{B.17}$$

The boundary condition at azimuthal direction is the periodic condition

$$p(r,0)=p(r,2\pi)\ . \tag{B.18}$$

Equations (B.15) and (B.16), together with the given boundary conditions, are solved using the procedures describe in Appendix A.

Appendix C

Finite Difference Solution for Dynamic Fluid Flow in (r, z) Coordinates

In borehole acoustic logging in formations whose heterogeneity variation is in the radial (r) and vertical (z) directions, the (r, z) coordinates finite difference scheme is used to solve for the fluid flow in the heterogeneous medium. For the cylindrical system, the governing equation is given by Equation (5.9):

$$\frac{\partial}{\partial r}\left(\alpha(r,z)\frac{\partial p}{\partial r}\right)+\frac{\alpha(r,z)}{r}\frac{\partial p}{\partial r}+\frac{\partial}{\partial z}\left(\alpha(r,z)\frac{\partial p}{\partial z}\right) \quad + \quad i\omega p = 0 \qquad \text{(C.1)}$$

$$(R < r < R_0 \text{ and } 0 < z < L)$$

where R is the borehole radius, R_0 is a large radial distance ($R_0 >> R$) at which p is effectively zero, and $z = 0$ and $z = L$ represent the lower and upper boundaries of the heterogeneous formation, respectively.

Using the procedure leading to Equation (B.5), Equation(C.1) is non-dimensionalized to become

$$\frac{\partial}{\partial r'}\left(\alpha'\frac{\partial p}{\partial r'}\right)+\frac{R_0-R}{R+(R_0-R)r'}\alpha'\frac{\partial p}{\partial r'}+\frac{(R_0-R)^2}{L^2}\frac{\partial}{\partial z'}\left(\alpha'\frac{\partial p}{\partial z'}\right)+i\Omega p=0 \quad \text{(C.2)}$$

where

$$\alpha' = \frac{\gamma(r,z)}{\left[1 - \frac{i}{2}\tau\kappa_{max}\gamma(r,z)\frac{\rho_f\omega}{\mu\phi}\right]^{1/2} - i\tau\kappa_{max}\gamma(r,z)\frac{\rho_f\omega}{\mu\phi}} \quad , \tag{C.3}$$

is the non-dimensionalized dynamic fluid diffusivity, $\gamma(r,z) = \frac{\kappa(r,z)}{\kappa_{max}}$ is the dimensionless permeability distribution in the (r,z) coordinates, κ_{max} is the maximum permeability in the model, and $\Omega = \omega(R_0 - R)^2/\alpha_0$, where $\alpha_0 = \frac{\kappa_{max}K_f}{\mu\phi}$ is the maximum fluid diffusivity in the model. The dimensionless spatial variables are given by

$$\begin{aligned} r' &= \frac{r-R}{R_0-R} \qquad (0 < r' < 1) \\ z' &= z/L \qquad (0 < z' < 1) \end{aligned}$$

Solution of Equation (C.2) can be obtained as the steady-state solution of the following equation,

$$\Gamma p = \frac{\partial p}{\partial t'} \tag{C.4}$$

where Γp is the left hand side of Equation (C.2), and t' is a dimensionless time. The steady-state solution is found by employing a stable iterative procedure using the ADI method. The variables r', z', and t' are discretized as

$$\begin{cases} r' = i\Delta r' & i = 0,1,2,\cdots,I \quad \Delta r' = 1/I \\ z' = j\Delta z' & j = 0,1,2,\cdots,J \quad \Delta z' = 1/J \\ t' = n\Delta t' & n = 0,1,2,\cdots,N \end{cases} \tag{C.5}$$

where $\Delta t'$ can be chosen as $\sqrt{(\Delta r'^2 + \Delta z'^2)}/2$.

To use the ADI method to solve Equation (C.4), we re-write this equation in the form of

$$p_{t'} = \Lambda_1 p + \Lambda_2 p \ . \tag{C.6}$$

where,

$$\begin{cases} \Lambda_1 p = \dfrac{\partial}{\partial r'}\left(\alpha'\dfrac{\partial p}{\partial r'}\right) + \dfrac{R_0 - R}{R + (R_0 - R)r'}\alpha'\dfrac{\partial p}{\partial r'} + i\Omega p \\ \\ \Lambda_2 p = \dfrac{(R_0 - R)^2}{L^2}\dfrac{\partial p}{\partial z'}\left(\alpha'\dfrac{\partial p}{\partial z'}\right) \end{cases} \tag{C.7}$$

The ADI finite difference form of Equation (C.6) is

$$\left(I - \frac{\Delta t'}{2}\Lambda_{1h}\right) p^{n+1/2} = \left(I + \frac{\Delta t'}{2}\Lambda_{2h}\right) p^n \tag{C.8}$$

$$\left(I - \frac{\Delta t'}{2}\Lambda_{2h}\right) p^{n+1} = \left(I + \frac{\Delta t'}{2}\Lambda_{1h}\right) p^{n+1/2} \quad . \tag{C.9}$$

where Λ_{1h} and Λ_{2h} are finite difference operators:

$$\begin{aligned} \Lambda_{1h}p &= \frac{1}{\Delta r'^2}\left[(B_{i,j} - D_{i,j})p_{i-1,j} - (B_{i,j} + B_{i+1,j} - D^{(1)}_{i,j}\right. \\ &\quad \left. -i\Omega\Delta r'^2)p_{i,j} + B_{i+1,j}p_{i+1,j}\right] \qquad \text{(C.10)} \\ \Lambda_{2h}p &= D^{(2)}_{i,j}\frac{1}{\Delta z'^2}\left[C_{i,j}p_{i,j-1} - (C_{i,j} + C_{i,j-1})p_{i,j} + C_{i,j+1}p_{i,j+1}\right] \quad , \qquad \text{(C.11)} \end{aligned}$$

where

$$\left\{ \begin{array}{lcl} A_{i,j} &=& \alpha'_{i,j} \\ B_{i,j} &=& \dfrac{A_{i,j} + A_{i-1,j}}{2} \\ C_{i,j} &=& \dfrac{A_{i,j} + A_{i,j-1}}{2} \\ D^{(1)}_{i,j} &=& \dfrac{(R_0 - R)B_{i,j}\Delta r'}{[R + (R_0 - R)(r'_{i,j} + r'_{i-1,j})/2]} \\ D^{(2)}_{i,j} &=& \dfrac{(R_0 - R)^2}{L_2} \end{array} \right. \tag{C.12}$$

Therefore, the finite difference form of Equations (C.10) and (C.11) is

$$\begin{aligned} &-\mu_1(B_{i,j} - D^{(1)}_{i,j})p^{n+1/2}_{i-1,j} + \left[1 + \mu_1\left(B_{i,j} + B_{i+1,j} - D^{(1)}_{i,j}\right.\right. \\ &\qquad \left.\left. -i\Omega\Delta r'^2)\right]p^{n+1/2}_{i,j} - \mu_1 B_{i+1,j}p^{n+1/2}_{i+1,j} \qquad \text{(C.13)} \\ &= \mu_2 D^{(2)}_{i,j}p^n_{i,j-1} + \left[1 - (C_{i,j} + C_{i,j+1})\mu_2 D^{(2)}_{i,j}\right]p^n_{i,j} + \mu_2 D^{(2)}_{i,j}C_{i,j+1}p^n_{i,j+1} \end{aligned}$$

$$\begin{aligned} &-\mu_2 D^{(2)}_{i,j}C_{i,j}p^{n+1}_{i,j-1} + \left[1 + \mu_2 D^{(2)}_{i,j}(C_{i,j} + C_{i,j+1})\right]p^{n+1}_{i,j} - \mu_2 D^{(2)}_{i,j}C_{i,j+1}p^{n+1}_{i,j+1} \\ &= \mu_1(B_{i,j} - D^{(1)}_{i,j})p^{n+1/2}_{i-1,j} + \left[1 - \mu_1\left(B_{i,j} + B_{i+1,j} - D^{(1)}_{i,j}\right.\right. \qquad \text{(C.14)} \\ &\quad \left.\left. -i\Omega\Delta r'^2)\right]p^{n+1/2}_{i,j} + \mu_1 B_{i+1,j}p^{n+1/2}_{i+1,j} \end{aligned}$$

where

$$\mu_1 = \frac{\Delta t'}{2\Delta r'^2} \qquad \text{and} \qquad \mu_2 = \frac{\Delta t'}{2\Delta z'^2}$$

The boundary conditions for the problem are given in Equations (5.11), (5.12), and (5.13), which in the finite difference form, are given by

$$\begin{cases} p(0,j) = p_0 e^{ik_e \Delta z' j} \\ p(R_0,j) = 0 \ . \end{cases} \qquad (0 < j < J) \qquad \text{(C.15)}$$

and

$$\begin{cases} p(i,0) = p(i,1) \\ p(i,J-1) = p(i,J) \end{cases} \qquad (0 < i < I) \qquad \text{(C.16)}$$

The finite difference Equations (C.13) and (C.14), together with the boundary conditions, are solved using the procedures described in Appendix A.